Solvent Effects in Metal-Organic Framework Activation, Resolvation, Synthesis, and Linker Exchange

by

Ryan Adam Dodson

A dissertation submitted in partial fulfillment
of the requirements for the degree of
Doctor of Philosophy
(Chemistry)
in the University of Michigan
2021

Doctoral Committee:

Professor Adam J. Matzger, Chair
Assistant Professor Andrew P. Ault
Assistant Professor Ashley N. Bucsek
Assistant Professor Charles C. L. McCrory

Ryan A. Dodson

radodson@umich.edu

ORCID iD: 0000-0003-3866-1763

Acknowledgements

I would first like to thank Professor Adam Matzger for his guidance and mentorship throughout my time in graduate school. He has taught me an incredible amount about research, teaching, and learning in the past four and a half years. I have been grateful for his near-constant availability, his exceptional responsiveness, and his hands-on approach to training. I have been equally grateful for his willingness to let students take charge and ownership of their own work – his ability to balance both of these aspects of mentorship is something I hope to emulate moving forward with my career. I am also thankful for my other scientific mentors who helped me get where I am today: Professor Charles Taylor at Pomona College, who started me on my path into Chemistry and instilled in me both academic curiosity and an openness to learn by doing, and Dr. Kathryn Berchtold and Dr. Rajinder Singh at Los Alamos National Laboratory, who taught me how to approach research as a career and how to think more like an engineer. I owe a great debt to each of them. I would also like to thank my committee members – Professor Andrew Ault, Professor Charles McCrory, and Professor Ashley Bucsek – for their support throughout my graduate career

I have had the privilege of working with a number of highly talented, encouraging individuals, whose time and generosity I heavily relied on, especially at the beginning of my degree. In and around the Pratt and Ault labs, I owe thanks to Dr. Rebecca Craig, Dr. Amy Bondy, Dr. Jessica Axson, Dr. Rachel Kirpes, Dr. Stephen McNamara, Dr. Peter Peterson, Dr. Matt Gunsch, Ryan Cook, Dr. Nate May, Dr. Katie Kolesar, and Megan Connor. Moving across the country to start in a new program is an isolating experience, and they welcomed me into their

community and helped make Ann Arbor feel more like a home. In the Matzger lab, I was incredibly fortunate to have had the chance to spend so much time with Dr. Derek Frank and Dr. Ren Wiscons; Derek and Ren taught me something new nearly every day, and were (and are) both exceptional friends and brilliant scientists. I also have had the privilege of knowing, working with, and learning from many other students and postdocs from the Matzger lab, both those who have already left the lab – Dr. Jon Bennion, Dr. Kyle McDonald, Dr. Jialiu Ma, Dr. Kortney Kersten, Dr. Jake Boissonault, Dr. Rosalyn Kent, and Dr. Saona Seth – and those who will leave after I do – Michael Bellas, Taylor Bramlett, Derek Du Bois, Kristen Kelsall, John Robinson, Keenan Wright, Dr. Kuthuru Suresh, Dr. Shalini, and Dr. Karabi Nath. I am also grateful for guidance and support from the amazing research scientists in the lab: Dr. Antek Wong-Foy, Dr. Tom Vaid, and Dr. Leila Foroughi. Finally, I had the immense privilege to work with three fantastic undergraduate students: Sasha Gill-Ljunghammer, Jeff Torano, and of course, Andy Kalenak. Each of them has made an enormous impact on me, and I am grateful for what they taught me about hard work and creative thinking, and for their friendship.

Outside of lab, I have been thankful for Michael Wade Wolfe, Ri Harris, Sibin Wang, Joe Meadows, and Takunda Chazovachii. I have appreciated their willingness to share late game nights, morning dim sum trips, brew days, and heartfelt conversations, and will sorely miss having them in such close proximity.

I would not have made it through the past 5 years without the love and support of my wife, Susan Nussbaum. She has been an inspiration for me on my hardest days, and continues to help me be a better person. I cannot imagine sharing life with anyone else. I have been fortunate to also have the support of her family, Bruce and Vicki Nussbaum, Lucy Nussbaum, Rebecca Nussbaum, Jake Schapiro, and Tyler Nussbaum, as well as that of my parents, Susan and Kurt Blachnik. My

parents are a continual inspiration for me, and I hope to one day match their generosity, compassion, and commitment to their community.

Table of Contents

Acknowledgements ii

List of Tables vi

List of Figures x

Abstract xxx

Chapter 1. Introduction 1

1.1 Metal–organic frameworks 1

1.2 MOF applications 3

1.3 MOF preparation 20

1.3.1 Synthesis 20

1.3.2 Activation 23

1.4 Challenges facing adoption of MOFs 26

1.5 Outline of thesis 28

1.6 References 29

Chapter 2. The Metal–Organic Framework Collapse Continuum: Insights from Two-Dimensional Powder X-ray Diffraction 36

2.1 Introduction 36

2.2 Experimental details 41

2.3 Results and Discussion 41

2.4 Conclusions 50

2.5 Supporting Information 51

2.5.1 Reagents 51
2.5.2 Syntheses 52
2.5.3 Experimental details 52
2.5.4 Particle size determination 53
2.5.5 Additional Figures 54
2.6 References 78

Chapter 3. Resolvation-Based Damage to Metal–Organic Frameworks and Approaches to Mitigation 81

3.1 Introduction 81

3.2 Results and discussion 84

3.2.1 UMCM-9 84
3.2.2 IRMOF-3 86
3.2.3 FJI-1 89
3.2.4 UiO-66 91
3.3 Conclusions 92

3.4 Methods 92

3.5 Supplemental Information 93

3.5.1 Reagents 93
3.5.2 Syntheses 94
3.5.3 Experimental details 95
3.5.4 Resolvation protocols 96
3.5.5. Additional figures 99
3.5.6. BET surface area values 103

3.6 References 106

Chapter 4. *N*, *N*-Diethyl-3-methylbenzamide (DEET) Acts as a Metal–Organic Framework Synthesis Solvent with Phase-Directing Capabilities 109

4.1 Introduction 109

4.2 Results and Discussion 111

4.3 Conclusions 115

4.4 Supporting Information 116

4.4.1 Reagents 116
4.4.2 Syntheses 117
4.4.3 Powder X-ray diffraction 119
4.4.4 Vapor pressure measurements 125
4.4.5 Surface area determination 128
4.4.6 Optical microscopy 131
4.4.7 Scanning electron microscopy 137
4.4.8 ^{1}H-NMR 140

4.5 References 141

Chapter 5. Solvent Choice in MOF Linker Exchange Permits Microstructural Control 143

5.1 Introduction 143

5.2 Results and Discussion 148

5.3 Conclusions 159

5.4 Supporting Information 160

5.4.1 Reagents 160
5.4.2 Syntheses 161
5.4.3 Linker exchange 162

5.4.4 MOF activation and Raman mapping 164
5.4.5 Data processing 165
5.4.6 Linker solution concentration calculations 166
5.4.7 MOF-5 → IRMOF-3 linker exchange data 169
5.4.8 Mixed solvent data 171
5.5 References 171

Chapter 6. Conclusions and Future Directions 174

6.1 Summary of Work 174

6.2 Future Directions 175

APPENDIX A 178

Raw isotherm data from Chapter 3 178

List of Tables

Table 2.1. Surface area measurements of products from each MOF activation (all in m^2 g^{-1}). 45

Table 3.1. UMCM-9 resolvation washing steps. 96

Table 3.2. UMCM-9 RSE washing steps. 97

Table 3.3. IRMOF-3 resolvation washing steps. 97

Table 3.4. IRMOF-3 RSE washing steps. 97

Table 3.5. FJI-1 resolvation washing steps. 97

Table 3.6. FJI-1 RSE washing steps. 98

Table 3.7. UiO-66 resolvation washing steps. 98

Table 3.8. UiO-66 RSE washing steps. 98

Table 3.9. UMCM-9 BET surface area values. Pristine values associated with each sample are given in parentheses. 104

Table 3.10. IRMOF-3 BET surface area values. Pristine values associated with each sample are given in parentheses. 104

Table 3.11. FJI-1 BET surface area values. Pristine values associated with each sample are given in parentheses. 104

Table 3.12. UiO-66 BET surface area values. Pristine values associated with each sample are given in parentheses. 104

Table 4.1. Evaporation rate data, calculated vapor pressure, and 1/T and ln(P) values used for bulk DEET vapor pressure characterization. 127

Table 4.2. Evaporation rate data, calculated vapor pressure, and 1/T and ln(P) values used for DEET in MOF-5 vapor pressure characterization. 128

Table 4.3. Chemical shifts, integral boundaries, integrals, and assignments for peaks in Figure S22, normalized to 100 bdc linkers (thus 400 bdc (H_a) protons).....141

Table 5.1. Measured shell parameters for individual solvents. Values are given as the average ± the standard error of the mean ($\sigma/\sqrt{n}$). Degree of shell exchange indicates the maximum degree of exchange measured in the shell. Thickness is given as shell full-width at half-max. 151

Table 5.2. Measured shell parameters for mixed solvents. Degree of shell exchange indicates the maximum degree of exchange measured in the shell. Thickness is given as shell full-width at half-max. Values are given as the average ± the standard error of the mean ($\sigma/\sqrt{n}$). 171

Table A.1. N_2 isotherm data for pristine UMCM-9 samples used. Samples are labelled with their BET surface areas, given in parentheses. 178

Table A.2. N_2 isotherm data for hexane resolvated UMCM-9 samples used.....181

Table A.3. N_2 isotherm data for CH_2Cl_2 resolvated UMCM-9 samples used. 183

Table A.4. N_2 isotherm data for THF resolvated UMCM-9 samples used. 185

Table A.5. N_2 isotherm data for DMF resolvated UMCM-9 samples used. 186

Table A.6. N_2 isotherm data for DMSO resolvated UMCM-9 samples used. 188

Table A.7. N_2 isotherm data for CH_2Cl_2 RSE UMCM-9 samples used. 190

Table A.8. N_2 isotherm data for THF RSE UMCM-9 samples used. 191

Table A.9. N_2 isotherm data for DMF RSE UMCM-9 samples used. 193

Table A.10. N_2 isotherm data for DMSO RSE UMCM-9 samples used. 195

Table A.11. N_2 isotherm data for pristine IRMOF-3 samples used. Samples are labelled with their BET surface areas, given in parentheses. 196

Table A.12. N_2 isotherm data for CH_2Cl_2 resolvated IRMOF-3 samples used. 198

Table A.13. N_2 isotherm data for THF resolvated IRMOF-3 samples used. 200

Table A.14. N_2 isotherm data for DMF resolvated IRMOF-3 samples used. 201

Table A.15. N_2 isotherm data for DMSO resolvated IRMOF-3 samples used. 203

Table A.16. N_2 isotherm data for THF RSE IRMOF-3 samples used. 205

Table A.17. N_2 isotherm data for DMF RSE IRMOF-3 samples used. 206

Table A.18. N_2 isotherm data for DMSO RSE IRMOF-3 samples used. 208

Table A.19. N_2 isotherm data for pristine FJI-1 samples used. Samples are labelled with their BET surface areas, given in parentheses. 210

Table A.20. N_2 isotherm data for hexane resolvated FJI-1 samples used. 213

Table A.21. N_2 isotherm data for CH_2Cl_2 resolvated FJI-1 samples used. 215

Table A.22. N_2 isotherm data for THF resolvated FJI-1 samples used. 216

Table A.23. N_2 isotherm data for DMF resolvated FJI-1 samples used. 218

Table A.24. N_2 isotherm data for DMSO resolvated FJI-1 samples used. 220

Table A.25. N_2 isotherm data for CH_2Cl_2 RSE FJI-1 samples used. 221

Table A.26. N_2 isotherm data for THF RSE FJI-1 samples used. 223

Table A.27. N_2 isotherm data for DMF RSE FJI-1 samples used. 225

Table A.28. N_2 isotherm data for DMSO RSE FJI-1 samples used. 226

Table A.29. N_2 isotherm data for pristine UiO-66 samples used. Samples are labelled with their BET surface areas, given in parentheses. 228

Table A.30. N_2 isotherm data for EtOH resolvated UiO-66 samples used. 230

Table A.31. N_2 isotherm data for DMF resolvated UiO-66 samples used. 231

Table A.32. N_2 isotherm data for DMSO resolvated UiO-66 samples used. 233

Table A.33. N_2 isotherm data for H_2O resolvated UiO-66 samples used. 235

Table A.34. N_2 isotherm data for DMF RSE UiO-66 samples used.....236

Table A.35. N_2 isotherm data for DMSO RSE UiO-66 samples used. 238

Table A.36. N_2 isotherm data for H_2O RSE UiO-66 samples used. 240

List of Figures

Figure 1.1. Four different MOF synthesis based on the same zinc nitrate starting material. Conditions appropriate for generating each MOF phase (time, temperature, solvent, molar equivalents of linker) are given. 2

Figure 1.2. Linkers for the MOFs (a) SNU-70, (b) UMCM-9, (c) PCN-610/NU-1000, and (d) NPF-200. 4

Figure 1.3. Linkers for the MOFs (a) MOF-177 and (b) NU-111. 5

Figure 1.4. Metal clusters for (a) HKUST-1 and (b) MIL-101. Coordination sites that can be made accessible in these clusters are denoted as X. F^- in the MIL-101 Cr_3O cluster is tightly bound for charge-balance reasons, and may be replaced by NO_3^- depending on the synthesis conditions used. 6

Figure 1.5. (a) 2,5-Dioxyterephthalate, the linker for MOF-74, (b) ethanolamine, (c) terephthalate, the linker for MOF-5, (d) 2-aminoterephthalate, the linker for IRMOF-3, and (e) 2'-(aminomethyl)-3,3"-dioxy-[1,1':4',1"-terphenyl]-4,4"-dicarboxylate, the linker for IRMOF-74-III-CH_2NH_2. 7

Figure 1.6. (a) γ-Cyclodextrin, used to make CD-MOF-2, (b) biphenyl-3,4',5-tricarboxlate, the linker in UMCM-150. 8

Figure 1.7. Several chromophore-containing MOF linkers: (a) {M[4,4′-$(CO_2)_2$-bpy]$_2$bpy} (M = Ru^{2+} or Os^{2+}), (b) {M[4,4′-$(CO_2)_2$-bpy]$_2(CN)_2$} (M = Ru^{2+} or Os^{2+}), (c) DA-ZnP, (d) F-ZnP, (e) ZnTCPP, and (f) bodipy. 10

Figure 1.8. (a) 5-(bis(4-carboxybenzyl)amino)-isophthalate, (b) Coumarin 343, (c) Coumarin 6, (d) $Ru(bpy)_3^{2+}$. 11

Figure 1.9. 2-Sulfoterephthalate, the linker in MIL-101-SO_3H.....12

Figure 1.10. Two reactions catalyzed by MIL-101-SO_3H. (a) Reduction of cellulose to cellobiose, D-xylose, and glucose. (b) Ring opening of styrene oxide with methanol.....13

Figure 1.11. The $Zr_6(R\text{-}CO_2)_8$ cluster found in MOF-545. Eight μ_3-O^{2-} ligands (one located in each face of the Zr_6 octahedron) are omitted for clarity. Coordination sites marked with X are coordinated by H_2O in the as-synthesized material. 14

Figure 1.12. Substrates oxidized by MOF-545. (a) 1,2,3-Trihydroxybenzene, (b) 3,3,5,5-tetramethylbenzidine, (c) *o*-phenylenediamine, and (d) 2,2′-azinodi(3-ethylbenzothiazoline)-6-sulfonate. 14

Figure 1.13. Several Mn-salen linkers used for creation of CMOFs. (a) (*R*,*R*)-(-)-*N*,*N*'-Bis(3-carboxyl-5-tert-butylsalicylidene)-1,2-cyclohexanediamino manganese(III) chloride, (b) (2*E*,2'*E*)-3,3'-(5,5'-(1*E*,1'*E*)-(1*R*,2*R*)-cyclohexane-1,2-diylbis(azan-1-yl-1-ylidene) bis(methan-1-yl-1-ylidene)bis(3-tert-butyl-4-hydroxy-5,1-phenylene))diacrylate manganese(III) chloride, and (c) 5',5''-(1*E*,1'*E*)-(1*R*,2*R*)-cyclohexane-1,2-diylbis(azan-1-yl-1-ylidene)bis(methan-1-yl-1-ylidene)bis(3'-tert-butyl-4'-hydroxybiphenyl-4-carboxylate) manganese(III) chloride.....15

Figure 1.14. (a) Trimesate, linker for MIL-100, and (b) 2-methylimidazolate, linker for ZIF-8..16

Figure 1.15. Several drugs and other molecules studied for MIL-100- and MIL-100(Fe)-mediated controlled release. (a) Ibuprofen, (b) azidothymidine triphosphate, (c) busulfan, (d) cidofovir, (e) doxorubicin, (f) benzophenone-3, (g) benzophenone-4, (h) caffeine, and (i) urea.....18

Figure 1.16. The biopolymer heparin.....18

Figure 1.17. Drugs and drug analogs loaded into ZIF-8 for controlled release studies. (a) 5-Fluorouracil, (b) camptothecin, (c) fluorescein, (d) rhodamine B, (e) methyl orange, and (f) methylene blue. 20

Figure 1.18. Schematic representation of the synthesis of MOF-5. Terephthalic acid and zinc nitrate tetrahydrate are dissolved in DEF and incubated in a 100 °C oven for 24 hours, yielding colorless cubic crystals. 21

Figure 1.19. Several species that have been used as modulators in the synthesis of UiO-66. (a) Formic acid, (b) acetic acid, (c) dichloroacetic acid, (d) trifluoroacetic acid, and (e) benzoic acid. 22

Figure 1.20. Schematic representation of the activation of MOF-5. First, the as-synthesized crystals are washed 3× with DMF, then 3× with CH_2Cl_2, followed by removal of CH_2Cl_2 under vacuum. 24

Figure 1.21. Two linkers. (a) Dihydro-1,2,4,5-tetrazine-3,6-dicarboxylate, linker in UiO-66(dhtz) and (b) 5,5′,5″-(4,4′,4″-(benzene-1,3,5-triyl)tris(1H-1,2,3-triazole-4,1-diyl))-triisophthalate, linker in NU-125. 28

Figure 2.1. Generalized procedure for MOF activation involving solvent exchange and evacuation. 37

Figure 2.2. Possible outcomes of solvated MOF activation (center). Clockwise, starting from top: successful activation, incomplete removal of guests, formation of mixed amorphous/crystalline phase, formation of amorphous shell with retention of internal crystallinity, formation of a fully amorphous phase. 39

Figure 2.3. Schematic depiction of two-dimensional powder X-ray diffraction (2D-PXRD) and example 2D powder X-ray diffractogram. β- and 2Θ-axes are shown in the bottom left. 41

Figure 2.4. MOF structures and the corresponding dicarboxylic acids from which they are derived. Top: MOF-5, benzenedicarboxylic acid. Center: UMCM-9, 2,6-napthalenedicarboxylic acid and 4,4'-biphenyldicarboxylic acid. Bottom: SNU-70, 4-(2-carboxyvinyl)benzoic acid. Each framework also contains Zn_4O nodes. 43

Figure 2.5. 2D-PXRD images collected from MOF-5 during the course of activation from hexane. Changes in spot positions between frames are mainly consistent with sample reorientation during solvent removal rather than with changes in crystallinity. 45

Figure 2.6. 2D-PXRD images collected from SNU-70 during the course of activation from THF. The disappearance of X-ray signal after complete application of vacuum indicates complete loss of crystallinity. 46

Figure 2.7. 2D-PXRD images collected from UMCM-9 during the course of activation from CH_2Cl_2. No signal is discernable in the first frame (760 Torr) due to attenuation of X-rays by CH_2Cl_2. The presence of spotty X-ray signal in the 250-190 Torr scan indicates that crystallinity is maintained in the sample until solvent is evacuated. 47

Figure 2.8. 2D-PXRD images collected from SNU-70 during the course of activation from hexane. Broadening in both the 2Θ- and β-axes is observed, but the sample maintains some crystallite orientation after the activation. 48

Figure 2.9. Ranked MOF activation efficacies with illustrations of each product. 50

Figure 2.10. 2D-PXRD images collected from MOF-5 during the course of activation from CH_2Cl_2. Sample evacuation progress as monitored by pressure in Torr is given in the upper left of each diffractogram. The intersection of each 2Θ arc with the edge of the diffractogram is displayed in the bottom right axis. These intersections are identical in every 2D pattern shown. Lack of appreciable signal in the first two diffractograms is attributed to X-ray attenuation by

CH_2Cl_2, rather than lack of sample crystallinity. After evacuation of the majority of CH_2Cl_2, small diffraction spots are observed, consistent with high retention of sample crystallinity. The flat cutoffs in X-ray intensity seen in each diffractogram are due to interference by the house-made capillary holder apparatus rather than the sample itself.....54
Figure 2.11. 2D-PXRD images collected from MOF-5 during the course of activation from hexane. Sample evacuation progress as monitored by pressure in Torr is given in the upper left of each diffractogram. The intersection of each 2Θ arc with the edge of the diffractogram is displayed in the bottom right axis. These intersections are identical in every 2D pattern shown. Changes in spot positions between frames are mainly consistent with sample reorientation during solvent removal rather than with changes in crystallinity. 55
Figure 2.12. 2D-PXRD images collected from UMCM-9 during the course of activation from THF. Sample evacuation progress as monitored by pressure in Torr is given in the upper left of each diffractogram. The intersection of each 2Θ arc with the edge of the diffractogram is displayed in the bottom right axis. These intersections are identical in every 2D pattern shown. While distinct spots are observed while the sample is solvated, complete loss of distinct spots is observed after evacuation is complete. This further demonstrates that evacuation, rather than solvent exchange, is responsible for collapse in this system. 56
Figure 2.13. 2D-PXRD images collected from UMCM-9 during the course of activation from hexane. Sample evacuation progress as monitored by pressure in Torr is given in the upper left of each diffractogram. The intersection of each 2Θ arc with the edge of the diffractogram is displayed in the bottom right axis. These intersections are identical in every 2D pattern shown. Very few changes are observed during this evacuation, other than a slight increase in spot intensities after evacuation due to the removal of (albeit weakly) X-ray attenuating hexane. 57

Figure 2.14. 2D-PXRD images collected from SNU-70 during the course of activation from CH_2Cl_2. Sample evacuation progress as monitored by pressure in Torr is given in the upper left of each diffractogram. The intersection of each 2Θ arc with the edge of the diffractogram is displayed in the bottom right axis. These intersections are identical in every 2D pattern shown. Very little diffracted X-ray intensity is observed before the removal of the highly attenuating CH_2Cl_2, and the final diffractogram is consistent with an amorphous product.....58
Figure 2.15. Relationship between sample orientation and β-axis broadness/distribution of diffraction spots. In a single crystalline sample, single spots with narrow β-axis width are observed. In a polycrystalline sample with a high degree of preferred orientation, these spots would broaden along the β-axis. In a polycrystalline sample with no preferred orientation, X-ray spots would be observed distributed across the β-axis ring with narrow β-axis widths. 59
Figure 2.16. Diffracted X-ray intensity as a function of 2Θ during the activation of MOF-5 from CH_2Cl_2. Very little diffracted X-ray intensity is observed before the removal of the highly attenuating CH_2Cl_2. Despite the apparent broad peak-width seen in this projection of the data, individual spots (Figure 2.10) have narrow 2Θ-axis broadness, highlighting the importance of considering the 2D X-ray diffractograms in understanding the data. 60
Figure 2.17. Diffracted X-ray intensity for the 6.9 °2Θ peak as a function of β during the activation of MOF-5 from CH_2Cl_2. 2D diffractograms were integrated between 6.2 and 7.3 °2Θ. Very little diffracted X-ray intensity is observed before the removal of the highly attenuating CH_2Cl_2. Sharp peaks are observed after removal of solvent, consistent with no changes to the sample crystallinity. 60
Figure 2.18. Diffracted X-ray intensity for the 9.7 °2Θ peak as a function of β during the activation of MOF-5 from CH_2Cl_2. 2D diffractograms were integrated between 9.0 and 10.2 °2Θ.

Very little diffracted X-ray intensity is observed before the removal of the highly attenuating CH_2Cl_2. Sharp peaks are observed after removal of solvent, consistent with no changes to the sample crystallinity. 61
Figure 2.19. Diffracted X-ray intensity as a function of 2Θ during the activation of MOF-5 from hexane. While this integrated diffractogram shows very narrow 2Θ-axis broadness, the 2Θ-axis broadness of individual spots in the 2D diffractogram are similar to those seen in the activation of MOF-5 from both CH_2Cl_2 and THF. Changes in peak intensity over time are attributed to sample reorientation during solvent removal, as the integrated intensity is dominated by several crystallites (Figures 2.20 and 2.21). 61
Figure 2.20. Diffracted X-ray intensity for the 6.9 °2Θ peak as a function of β during the activation of MOF-5 from hexane. 2D diffractograms were integrated between 6.2 and 7.3 °2Θ. Sharp peaks are observed throughout the course of the activation, consistent with no changes to the sample crystallinity.....62
Figure 2.21. Diffracted X-ray intensity for the 9.7 °2Θ peak as a function of β during the activation of MOF-5 from hexane. 2D diffractograms were integrated between 9.0 and 10.2 °2Θ. Sharp peaks are observed throughout the course of the activation, consistent with no changes to the sample crystallinity.....62
Figure 2.22. Diffracted X-ray intensity as a function of 2Θ during the activation of MOF-5 from THF. Very few changes are observed, indicative of a successful activation. 63
Figure 2.23. Diffracted X-ray intensity for the 6.9 °2Θ peak as a function of β during the activation of MOF-5 from THF. 2D diffractograms were integrated between 6.2 and 7.3 °2Θ. Sharp peaks are observed throughout the course of the activation, consistent with no changes to the sample crystallinity.....63

Figure 2.24. Diffracted X-ray intensity for the 9.7 °2Θ peak as a function of β during the activation of MOF-5 from THF. 2D diffractograms were integrated between 9.0 and 10.2 °2Θ. Sharp peaks are observed throughout the course of the activation, consistent with no changes to the sample crystallinity.....64
Figure 2.25. Diffracted X-ray intensity as a function of 2Θ during the activation of UMCM-9 from CH_2Cl_2. Very little diffracted X-ray intensity is observed before the removal of the highly attenuating CH_2Cl_2. Peak broadening is observed between the 250-200 Torr scan and the 0 Torr scan, indicating that the change to the sample crystallinity occur only after complete removal of solvent, and that solvent exchange was not responsible for the collapse event. 64
Figure 2.26. Diffracted X-ray intensity for the 5.5 °2Θ peak as a function of β during the activation of UMCM-9 from CH_2Cl_2. 2D diffractograms were integrated between 5.0 and 6.0 °2Θ. Very little diffracted X-ray intensity is observed before the removal of the highly attenuating CH_2Cl_2. Sharp peaks are observed in the 250-200 Torr scan, while a single broad peak is observed after complete solvent removal. This β-axis broadening indicates an increase in sample polycrystallinity (Figure 2.15). 65
Figure 2.27. Diffracted X-ray intensity for the 7.8 °2Θ peak as a function of β during the activation of UMCM-9 from CH_2Cl_2. 2D diffractograms were integrated between 7.3 and 8.3 °2Θ. Very little diffracted X-ray intensity is observed before the removal of the highly attenuating CH_2Cl_2. Sharp peaks are observed in the 250-200 Torr scan, while no peaks are observed after complete solvent removal. 65
Figure 2.28. Diffracted X-ray intensity for the 11.0 °2Θ peak as a function of β during the activation of UMCM-9 from CH_2Cl_2. 2D diffractograms were integrated between 10.1 and 11.3 °2Θ. Very little diffracted X-ray intensity is observed before the removal of the highly

attenuating CH_2Cl_2. Sharp peaks are observed in the 250-200 Torr scan, while only broad peaks are observed after complete solvent removal. 66
Figure 2.29. Diffracted X-ray intensity as a function of 2Θ during the activation of UMCM-9 from hexane. No substantial changes are observed over the course of the activation. 67
Figure 2.30. Diffracted X-ray intensity for the 5.5 °2Θ peak as a function of β during the activation of UMCM-9 from hexane. 2D diffractograms were integrated between 5.0 and 6.0 °2Θ. No substantial changes to the β-axis peak broadness are observed. 67
Figure 2.31. Diffracted X-ray intensity for the 7.8 °2Θ peak as a function of β during the activation of UMCM-9 from hexane. 2D diffractograms were integrated between 7.3 and 8.3 °2Θ. No substantial changes to the β-axis peak broadness are observed. 68
Figure 2.32. Diffracted X-ray intensity for the 11.0 °2Θ peak as a function of β during the activation of UMCM-9 from hexane. 2D diffractograms were integrated between 10.1 and 11.3 °2Θ. No substantial changes to the β-axis peak broadness are observed. 68
Figure 2.33. Diffracted X-ray intensity as a function of 2Θ during the activation of UMCM-9 from THF. While peaks are observed prior to solvent removal, the final product shows no appreciable crystallinity. 69
Figure 2.34. Diffracted X-ray intensity for the 5.5 °2Θ peak as a function of β during the activation of UMCM-9 from THF. 2D diffractograms were integrated between 5.0 and 6.0 °2Θ. While peaks are observed prior to solvent removal, the final product shows no appreciable crystallinity. 69
Figure 2.35. Diffracted X-ray intensity for the 7.8 °2Θ peak as a function of β during the activation of UMCM-9 from THF. 2D diffractograms were integrated between 7.3 and 8.3 °2Θ.

While peaks are observed prior to solvent removal, the final product shows no appreciable crystallinity. 70
Figure 2.36. Diffracted X-ray intensity for the 11.0 °2Θ peak as a function of β during the activation of UMCM-9 from THF. 2D diffractograms were integrated between 10.1 and 11.3 °2Θ. While peaks are observed prior to solvent removal, the final product shows no appreciable crystallinity. 70
Figure 2.37. Diffracted X-ray intensity as a function of 2Θ during the activation of SNU-70 from CH_2Cl_2. No peaks other than a small signal at 5.9 °2Θ are visible prior to solvent evacuation. After evacuation, the observed signal consists of broad peaks consistent with an amorphous product. The peaks of this final diffractograms appear artificially large due to X-ray attenuation in earlier scans. 71
Figure 2.38. Diffracted X-ray intensity for the 5.9 °2Θ peak as a function of β during the activation of SNU-70 from CH_2Cl_2. 2D diffractograms were integrated between 5.4 and 6.6 °2Θ. No appreciable β-resolved signal is apparent during this activation. 72
Figure 2.39. Diffracted X-ray intensity for the 8.3 °2Θ peak as a function of β during the activation of SNU-70 from CH_2Cl_2. 2D diffractograms were integrated between 7.7 and 9.0 °2Θ. No appreciable β-resolved signal is apparent during this activation. 72
Figure 2.40. Diffracted X-ray intensity for the 11.7 °2Θ peak as a function of β during the activation of SNU-70 from CH_2Cl_2. 2D diffractograms were integrated between 11.2 and 12.2 °2Θ. No appreciable β-resolved signal is apparent during this activation. 73
Figure 2.41. Diffracted X-ray intensity as a function of 2Θ during the activation of SNU-70 from hexane. Slight broadening is observed, particularly for the 8.3 °2Θ peak, but instrumental broadening generally dominates in this presentation of the data; the 2Θ broadening of individual

spots is more apparent in the 2D diffractograms (Figure 8). The loss of the 10.1 °2Θ peak is attributed to sample orientation changes during the experiment, as only 1-2 spots at this position are apparent prior to solvent removal.....73
Figure 2.42. Diffracted X-ray intensity for the 5.9 °2Θ peak as a function of β during the activation of SNU-70 from hexane. 2D diffractograms were integrated between 5.4 and 6.6 °2Θ. Peak broadening is observed upon removal of solvent, consistent with an increase in sample polycrystallinity and a slight decrease in crystallite preferred orientation, as discussed in Chapters 2.1-2.4. 74
Figure 2.43. Diffracted X-ray intensity for the 8.3 °2Θ peak as a function of β during the activation of SNU-70 from hexane. 2D diffractograms were integrated between 7.7 and 9.0 °2Θ. Peak broadening is observed upon removal of solvent, consistent with an increase in sample polycrystallinity and a slight decrease in crystallite preferred orientation, as discussed in the main text.....74
Figure 2.44. Diffracted X-ray intensity for the 11.7 °2Θ peak as a function of β during the activation of SNU-70 from hexane. 2D diffractograms were integrated between 11.2 and 12.2 °2Θ. Peak broadening is observed upon removal of solvent, consistent with an increase in sample polycrystallinity and a slight decrease in crystallite preferred orientation, as discussed in the main text.....75
Figure 2.45. Diffracted X-ray intensity as a function of 2Θ during the activation of SNU-70 from THF. Retention of sample crystallinity is observed until complete removal of solvent.....76
Figure 2.46. Diffracted X-ray intensity for the 5.9 °2Θ peak as a function of β during the activation of SNU-70 from THF. 2D diffractograms were integrated between 5.4 and 6.6 °2Θ. Retention of sample crystallinity is observed until complete removal of solvent.....76

Figure 2.47. Diffracted X-ray intensity for the 8.3 °2Θ peak as a function of β during the activation of SNU-70 from THF. 2D diffractograms were integrated between 7.7 and 9.0 °2Θ. Retention of sample crystallinity is observed until complete removal of solvent. 77
Figure 2.48. Diffracted X-ray intensity for the 11.7 °2Θ peak as a function of β during the activation of SNU-70 from THF. 2D diffractograms were integrated between 11.2 and 12.2 °2Θ. Retention of sample crystallinity is observed until complete removal of solvent. 77
Figure 3.1. Possible effects of activated MOF resolvation. 82
Figure 3.2. Structures (top) and linkers (bottom) of MOFs studied. Left to right: UMCM-9 (2,6-naphthalenedicarboxylate and 4,4'-biphenyldicarboxylate), IRMOF-3 (2-aminoterephthalate), FJI-1 (1,3,5-tris(4-carboxyphenyl)benzene and 4,4'-bipyridine), and UiO-66 (terephthalate).....84
Figure 3.3. Percent residual surface area versus resolvation solvent for UMCM-9. Blue: direct resolvation. Yellow: resolvation via RSE from hexane. 85
Figure 3.4. 2D-PXRD patterns for UMCM-9 samples subjected to either direct resolvation or RSE treatment. Top left: pristine UMCM-9 activated from hexane. Top right: pristine UMCM-9 activated from hexane, resolvated with hexane, and re-activated from hexane. Left: UMCM-9 resolvated with listed solvents, re-activated from hexane. Right: UMCM-9 resolvated with hexane, exchanged into listed solvents, and re-activated from hexane.....86
Figure 3.5. Percent residual surface area versus resolvation solvent for IRMOF-3. Blue: direct resolvation. Yellow: resolvation via RSE from hexane. 88
Figure 3.6. 2D-PXRD patterns for IRMOF-3 samples subjected to either direct resolvation or RSE treatment. Top left: pristine IRMOF-3 activated from hexane. Top right: pristine IRMOF-3 activated from CH_2Cl_2, resolvated with CH_2Cl_2, and re-activated from CH_2Cl_2. Left: IRMOF-3

resolvated with listed solvents, re-activated from CH_2Cl_2. Right: IRMOF-3 resolvated with CH_2Cl_2, exchanged into listed solvents, and re-activated from CH_2Cl_2. 88
Figure 3.7. Percent residual surface area versus resolvation solvent for FJI-1. Blue: direct resolvation. Yellow: resolvation via RSE from hexane. 90
Figure 3.8. 2D-PXRD patterns for FJI-1 samples subjected to either direct resolvation or RSE treatment. Top left: pristine FJI-1 activated from $scCO_2$. Top right: pristine FJI-1 activated via $scCO_2$ from DMF, resolvated with hexane, and re-activated via $scCO_2$ from hexane. Left: FJI-1 resolvated with listed solvents, re-activated via $scCO_2$. Right: FJI-1 resolvated with hexane, exchanged into listed solvents, and re-activated via $scCO_2$. 90
Figure 3.9. Percent residual surface area versus resolvation solvent for UiO-66. Blue: direct resolvation. Yellow: resolvation via RSE from hexane. 99
Figure 3.10. 2D-PXRD patterns for UiO-66 samples subjected to either direct resolvation or RSE treatment. Top left: pristine UiO-66 activated from EtOH. Top right: pristine UiO-66 activated from EtOH, resolvated with EtOH, and re-activated from EtOH. Left: UiO-66 resolvated with listed solvents, re-activated from EtOH. Right: UiO-66 resolvated with EtOH, exchanged into listed solvents, and re-activated from EtOH. UiO-66 was synthesized according to a common protocol which yields a microcrystalline powder; this synthesis was chosen with the goal of studying the behavior of a material that is most relevant to the field. However, the small crystallite size of this material makes it impossible to distinguish β-axis changes in the 2D-PXRD patterns of the material.....99
Figure 3.11. Diffracted X-ray intensity as a function of 2Θ for the UMCM-9 resolvation and RSE samples studied. Greater retention of 10-15 °2Θ peaks can be observed for high surface

tension solvent (DMF, DMSO) RSE samples relative to the direct resolvation samples, consistent with better retention of sample crystallinity. 100
Figure 3.12. Diffracted X-ray intensity as a function of 2Θ for the IRMOF-3 resolvation and RSE samples studied. Greater retention of 20-25 °2Θ peaks can be observed for high surface tension solvent (DMF, DMSO) RSE samples relative to the direct resolvation samples, consistent with better retention of sample crystallinity. 101
Figure 3.13. Diffracted X-ray intensity as a function of 2Θ for the FJI-1 resolvation and RSE samples studied. Differences between peak intensities in samples which maintained near full surface area (e.g. pristine vs. CH_2Cl_2 RSE) are partially attributed to relatively high sample preferred orientation in prepared FJI-1 capillaries due to incomplete sample grinding, a requisite for determining changes in sample polycrystallinity via 2D-PXRD, as well as much larger initial crystal sizes (~5 mm). 101
Figure 3.14. Diffracted X-ray intensity as a function of 2Θ for the UiO-66 resolvation and RSE samples studied. Diffraction patterns are overlaid to demonstrate their strong similarity. The only observed changes in intensity are attributed to small differences in the quantity of sample packed into the capillaries. 102
Figure 3.15. 2D-PXRD pattern for a DMF-solvated UMCM-9 sample subjected to direct DMF resolvation. 102
Figure 3.16. 2D-PXRD pattern for a DMF-solvated UMCM-9 sample subjected to DMF resolvation via RSE. 102
Figure 3.17. 2D-PXRD pattern for a DMF-solvated IRMOF-3 sample subjected to direct DMF resolvation. 103

Figure 3.18. 2D-PXRD pattern for a DMF-solvated IRMOF-3 sample subjected to DMF resolvation via RSE. 103
Figure 3.19. 2D-PXRD pattern for a DMF-solvated FJI-1 sample subjected to direct DMF resolvation. 103
Figure 3.20. 2D-PXRD pattern for a DMF-solvated FJI-1 sample subjected to DMF resolvation via RSE. 103
Figure 4.1. Chemical structures of *N*,*N*-diethyl-3-methylbenzamide and *N*,*N*-diethylformamide. 110
Figure 4.2. PXRD patterns of DEET-synthesized MOF-5 (above) and calculated PXRD pattern for MOF-5 (below). 112
Figure 4.3. Metal-organic frameworks successfully synthesized in DEET along with their precursor metal salts and linker acids. 112
Figure 4.4. Crystal structure of the novel Zn/btc phase with coordinated solvent omitted for clarity. Viewed along the a-axis. 113
Figure 4.5. Mass loss versus time for bulk liquid DEET (above) and for DEET loaded in MOF-5 (below) in a Knudsen effusion cell. 115
Figure 4.6. PXRD pattern of DEET-synthesized UMCM-1 (above) and calculated PXRD pattern for UMCM-1 (below). 120
Figure 4.7. PXRD pattern of DEET-synthesized UMCM-9 (above) and calculated PXRD pattern for UMCM-9 (below). The broader peaks in the experimental pattern are consistent with previously reported UMCM-9 patterns, and can be attributed to the inherent structural disorder in the MOF system.[4] 120

Figure 4.8. PXRD pattern of DEET-synthesized MOF-177 (above) and calculated PXRD pattern for MOF-177 (below).....121
Figure 4.9. PXRD pattern of DEET-synthesized HKUST-1 (above) and calculated PXRD pattern for HKUST-1 (below).....121
Figure 4.10. PXRD pattern of DEET-synthesized MIL-53(Al) (above), DMF-synthesized MIL-53(Al) (middle), and calculated PXRD pattern for MIL-53(Al) (below). The broad peaks and high background in both experimental patterns suggest that this synthesis (regardless of solvent) yields relatively small crystalline domains and/or a substantial fraction of amorphous material. 122
Figure 4.11. PXRD pattern of DEET-synthesized MOF-519 (above), DMF-synthesized MOF-519 (middle), and calculated PXRD pattern for MOF-519 (below).....123
Figure 4.12. PXRD pattern of DEET-synthesized Zn/NH_2-bdc (above) and calculated PXRD pattern for IRMOF-3 (below).....123
Figure 4.13. PXRD pattern of DEET-synthesized Zn/btc (above), calculated PXRD pattern for that phase (middle), and calculated PXRD pattern for Zn-HKUST-1 (below).....124
Figure 4.14. PXRD pattern of DEET-synthesized Cu/bdc (above) and calculated PXRD pattern for Cu-MOF-2 (below).....124
Figure 4.15. Clausius–Clapeyron plot for bulk DEET.....126
Figure 4.16. Clausius–Clapeyron plot for DEET in MOF-5.....127
Figure 4.17. N_2 sorption isotherm for MOF-5 synthesized in DEET. 130
Figure 4.18. BET fit of isotherm data taken from MOF-5 synthesized in DEET. 130

Figure 4.19. Optical micrographs of DEET-synthesized MOF-5 (a, b). The product shows the characteristic cubic morphology of the standard MOF-5 synthesis. Crystal sizes vary, but most are 200 – 600 μm in diameter. 131
Figure 4.20. Optical micrographs of DEET-synthesized UMCM-1 (a, b). The product shows the characteristic needle morphology of the standard UMCM-1 synthesis. Crystals are as long as 1 mm, and range from 20 – 50 μm in diameter. 132
Figure 4.21. Optical micrographs of DEET-synthesized UMCM-9 (a, b). The product shows the characteristic cubic morphology of the standard UMCM-9 synthesis. Crystals are as large as ~250 μm in diameter, but most are closer to 100 μm.....133
Figure 4.22. Optical micrographs of DEET-synthesized MOF-177 (a, b). Crystals appear blocky and occasionally octahedral, as the DMF-synthesis characteristically yields. Crystals are as large as ~200 μm in diameter, but most are closer to 10 – 50 μm range. 134
Figure 4.23. Optical micrographs of DEET-synthesized Zn/btc (a, b). The observed crystals have irregular/blocky morphologies. Crystals are 100 – 300 μm in diameter.....135
Figure 4.24. Optical micrographs of DEET-synthesized MOF-519 (a) and DMF-synthesized MOF-519 (b). Both syntheses yield crystals which appear to be elongated octahedra (approximately 5 × 5 × 10 μm).....136
Figure 4.25. Scanning electron micrographs of DEET-synthesized HKUST-1 (a, b). Intergrown blocky crystals with sharp corners and flat faces are observed, with diameters generally ranging between 50 – 100 nm 138
Figure 4.26. Scanning electron micrographs of DEET-synthesized Cu/bdc (a) and DMF-synthesized MOF-2 (b). Both appear to be stacked, intergrown plates. 139

Figure 4.27. ^{1}H NMR spectrum of digested DEET-synthesized MOF-5 after solvent exchange and activation. Translucent colored overlays are for labelling only, the actual integration boundaries are given in Table 4.3. No DEET is observed in the solution. 140
Figure 5.1. Schematic representation of the MOF-5 → MOF-5-d_4 linker exchange. Center: a partially exchanged core–shell MOF structure with a cubic region removed from the corner, with the two constituent linkers shown below. Right: an example (flattened) slice of a partially bdc-d_4 exchanged section of MOF-5. Linkers aligned perpendicular to the page have been omitted for clarity. Left: percent incorporation versus crystal depth plot for bdc and bdc-d_4 in the model system shown. Shell width, in the form of full-width at half-max, and maximum extent of exchange are both shown.....146
Figure 5.2. Solvents studied for their behavior in the MOF-5 → MOF-5-d4 linker exchange...148
Figure 5.3. Venn diagram summarizing solvent overall performance in the MOF-5 → MOF-5-d_4 linker exchange. Solvents are separated depending on their ability to dissolve 10 mM H_2bdc-d_4, maintain the phase stability of MOF-5 for 24 hours, and facilitate the MOF-5 → MOF-5-d_4 linker exchange. 149
Figure 5.4. Maximum extent of exchange versus shell full-width at half-max for shells resulting from several PSE solvents. Extent of exchange and shell FWHM refer to the bdc-d_4 shells resulting from the MOF-5 → MOF-5-d_4 linker exchange after 24 hours in the presence of 10 mM H_2bdc-d_4. Error bars indicate the standard error of the mean. Solvents in red (dioxane, butyl acetate, and propylene carbonate) did not fully dissolve 10 mM H_2bdc-d_4. 151
Figure 5.5. Measured shell parameters for binary mixtures of DMF and *N*,*N*-diethyl-3-methylbenzamide. Solvent composition is given as % DMF, with *N*,*N*-diethyl-3-methylbenzamide constituting the remainder of the solvent mixture. Extent of exchange indicates

the maximum degree of exchange (%) measured in the shell. Thickness is given in μm as shell full-width at half-max. Values are given as the average ± the standard error of the mean ($\sigma/\sqrt{n}$). 159

Figure 5.6. Relationship between laser position on sample and observed linker incorporation for a model core-shell system. A) Model MOF-5 → MOF-5-d_4 core-shell system (higher bdc-d_4 density shown in red) with five example laser spot locations indicated. B) Idealized percent incorporation versus depth in the crystal for the model in (A). Each of the five sample laser spot locations are shown on the plot.....166

Figure 5.7. Comparison of *N*,*N*-diethylformamide and *N*-methyl-2-pyrrolidone in facilitating the MOF-5 → IRMOF-3 linker exchange. Left, above: Raman spectra of cross-sectioned MOF resulting from the MOF-5 → IRMOF-3 linker exchange in *N*,*N*-diethylformamide. Spectra taken at the far edge of the shell, 5.9 μm deep in the crystal, and 60.0 μm deep in the crystal are shown. Left, middle: Raman spectra of cross-sectioned MOF resulting from the MOF-5 → IRMOF-3 linker exchange in *N*-methyl-2-pyrrolidone. Spectra taken at the far edge of the shell and 6.1 μm deep in the crystal are shown. Left, below: Raman spectra of pure phase MOF-5 and IRMOF-3. Right, above: locations of Raman spectra collected of the sample resulting from the MOF-5 → IRMOF-3 linker exchange in *N*,*N*-diethylformamide. Visual artifacts in the image (discontinuities in image brightness) result from the automated image stitching process in WiRE 5.3 rather than from the sample itself. Right, below: locations of Raman spectra collected of the sample resulting from the MOF-5 → IRMOF-3 linker exchange in *N*-methyl-2-pyrrolidone. ..169

Figure 5.8. Magnified regions of interest from Raman spectra given in Figure S2 of the MOF-5 → IRMOF-3 linker exchange. Left: 780 – 840 cm^{-1} region. Right: 1230 – 1310 cm^{-1} region. Above: Raman spectra of cross-sectioned MOF resulting from the MOF-5 → IRMOF-3 linker

exchange in *N*,*N*-diethylformamide. Spectra taken at the far edge of the shell, 5.9 μm deep in the crystal, and 60.0 μm deep in the crystal are shown. Exchange at least as deep as 60 μm is observed. Middle: Raman spectra of cross-sectioned MOF resulting from the MOF-5 → IRMOF-3 linker exchange in *N*-methyl-2-pyrrolidone. Spectra taken at the far edge of the shell and 6.1 μm deep in the crystal are shown. Exchange is observed at the surface, but is minimal 6.1 μm deep in the crystal. Below: Raman spectra of phase pure MOF-5 and IRMOF-3.....170

Abstract

Metal-organic frameworks (MOFs) are the largest, highest performing class of porous materials, with applications including gas storage, catalysis, separations, and controlled release, but their widespread application has been hindered by a number of factors. Several challenges in the field are 1) structural degradation during relevant conditions or processing steps, 2) an overreliance on expensive, toxic precursor chemicals and synthesis solvents, and 3) difficulty achieving desired MOF phases and microstructures. This dissertation focuses on addressing all three of these challenges. In Chapter 2, MOF degradation during the process of activation (solvent removal), a major barrier to the preparation of many potentially useful frameworks, is explored. The process is demonstrated to have potential to generate a range of products along the crystalline-amorphous continuum, including materials that have increased polycrystallinity with no decrease in accessible surface area. In addition to revealing new insights into the scope of outcomes possible from activation-induced damage, these findings highlight the importance of proper sample characterization during optimization of MOF activation conditions, an important consideration as MOFs move towards large-scale production. In Chapter 3, the same characterization techniques are applied to probe the reverse of activation: resolvation of activated MOFs. MOF resolvation is commonly performed when characterizing catalytically active frameworks, and the utility of high-performing MOF systems may be masked if resolvation can beget MOF collapse. This work reveals that this process indeed has destructive potential, which can be mitigated by stepwise resolvation starting with low surface tension solvents. These findings inform best practices for treatment of MOFs intended for liquid-phase catalysis as well as in other solvated applications,

such as molecular sensing and pollutant capture. In Chapter 4, the problem of (alkyl formamide) MOF synthesis solvent toxicity is addressed. In particular, a greener, safer route to the creation of MOFs is explored through the use of *N*,*N*-diethyl-3-methylbenzamide (DEET), the most common and effective insect repellant, as a MOF synthesis solvent. MOFs synthesized in DEET are demonstrated to have potential as a component of controlled-release DEET formulations which operate via vapor pressure suppression. This work to make MOF syntheses safer is vital as MOF syntheses are translated from the research scale (grams) to the industrial scale (kilograms-tons). Finally, in Chapter 5, the process of MOF linker exchange, a technique useful for generation of otherwise inaccessible MOFs and MOF microstructures, is studied. Specifically, the role of solvent in the process of MOF linker exchange is examined, and the possibility of modulating linker distributions within MOFs (microstructural control) by careful choice of solvent is demonstrated. This work lays the foundation for efficient generation of core–shell MOFs, and provides valuable chemical insight into the process of MOF linker exchange, increasing the potential widespread utility of these materials.

Chapter 1. Introduction

1.1 Metal–organic frameworks

Metal–organic frameworks, or MOFs, are a class of materials pioneered in 1989 by Robson and Hoskins.[1–4] MOFs are characterized by several qualities: they comprise organic linker molecules which coordinatively bridge inorganic nodes, they have crystalline network structures, and they span 2-3 dimensions.[5] The properties of MOFs can be controlled by judicious choice of metal, linker, and synthesis conditions, making these materials highly tunable and modular. (Figure 1.1) Furthermore, MOFs often possess extremely high specific surface areas: ~5000 m^2 g^{-1} for several MOFs[6,7] constructed from commercially available linker molecules, >7000 m^2 g^{-1} for the highest performing synthesized examples[8], and a theoretical upper limit[8] of ~14600 m^2 g^{-1}.* These values greatly exceed the highest reported surface areas of established porous materials (~3000 m^2 g^{-1} for activated carbon,[11] ~1000 m^2 g^{-1} for zeolites[12,13]), prompting numerous investigations into the feasibility of replacing these sorbents with MOFs. In the three decades following the genesis of MOF chemistry as a subfield of materials chemistry, MOFs have undergone extensive development, characterization, and optimization, and have begun transitioning into the industrial space, as did organic polymers in the 1940s and 1950s. This introduction will discuss applications of these materials, standard methods for their preparation, and barriers to their widespread use.

---

* "Surface area" in this work refers exclusively to Brunauer-Emmett-Teller (BET) surface area.[9,10]

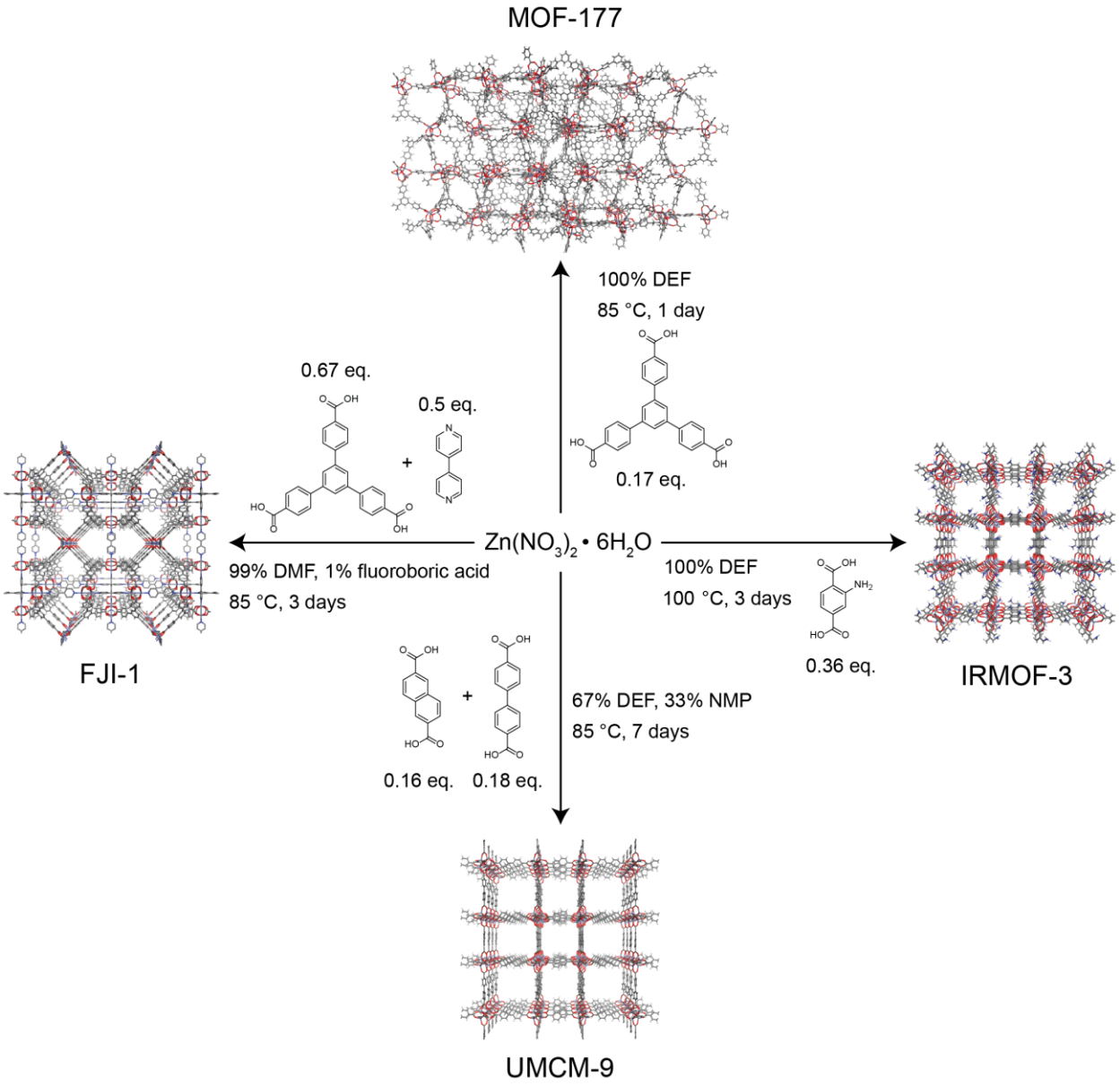

Figure 1.1. Four different MOF synthesis based on the same zinc nitrate starting material. Conditions appropriate for generating each MOF phase (time, temperature, solvent, molar equivalents of linker) are given.

1.2 MOF applications

Myriad applications for MOFs have been proposed and explored. Three major areas of MOF research are in the fields of energy, catalysis, and medicine. A variety of representative systems studied for applications in these areas are discussed here, and their relevant chemical and structural features are highlighted.

Energy applications

While MOFs have been extensively investigated for use in many energy applications, their remarkable surface areas make them particularly attractive for fuel gas storage applications (H_2,[14,15] CH_4[16]), where favorable gas-framework interactions allow gas cylinders loaded with MOF to take up more gas at a given loading pressure than empty cylinders. Usable gravimetric H_2 capacity has been correlated with gravimetric surface area and porosity, and has been found to be generally higher in MOFs with spherical pores than in MOFs with cylindrical pores due to spherical pores offering a greater number of favorable framework–guest interactions. MOFs with excellent H_2 uptake have been constructed from a variety of metals: four of the highest performing MOFs for H_2 storage include the Zn-based SNU-70[17] (surface area: 4944 $m^2\ g^{-1}$, pore volume: 2.14 $cm^3\ g^{-1}$) and UMCM-9[18] (surface area: 5039 $m^2\ g^{-1}$, pore volume: 2.31 $cm^3\ g^{-1}$), the Cu-based PCN-610/NU-100[19,20] (surface area: 6050 $m^2\ g^{-1}$, pore volume: 3.17 $cm^3\ g^{-1}$), and the Zr-based NPF-200[21] (surface area: 5463 $m^2\ g^{-1}$, pore volume: 2.17 $cm^3\ g^{-1}$).[14,15] (Figure 1.2) CH_4 working capacity, like H_2 capacity, is strongly correlated with MOF pore volume and surface area, with high performing MOFs for this application including the Zn-based MOF-177[22] (surface area: 4740 $m^2\ g^{-1}$, pore volume: 1.89 $cm^3\ g^{-1}$) and the Cu-based NU-111[23] (surface area: 4930 $m^2\ g^{-1}$, pore volume: 2.09 $cm^3\ g^{-1}$). (Figure 1.3)

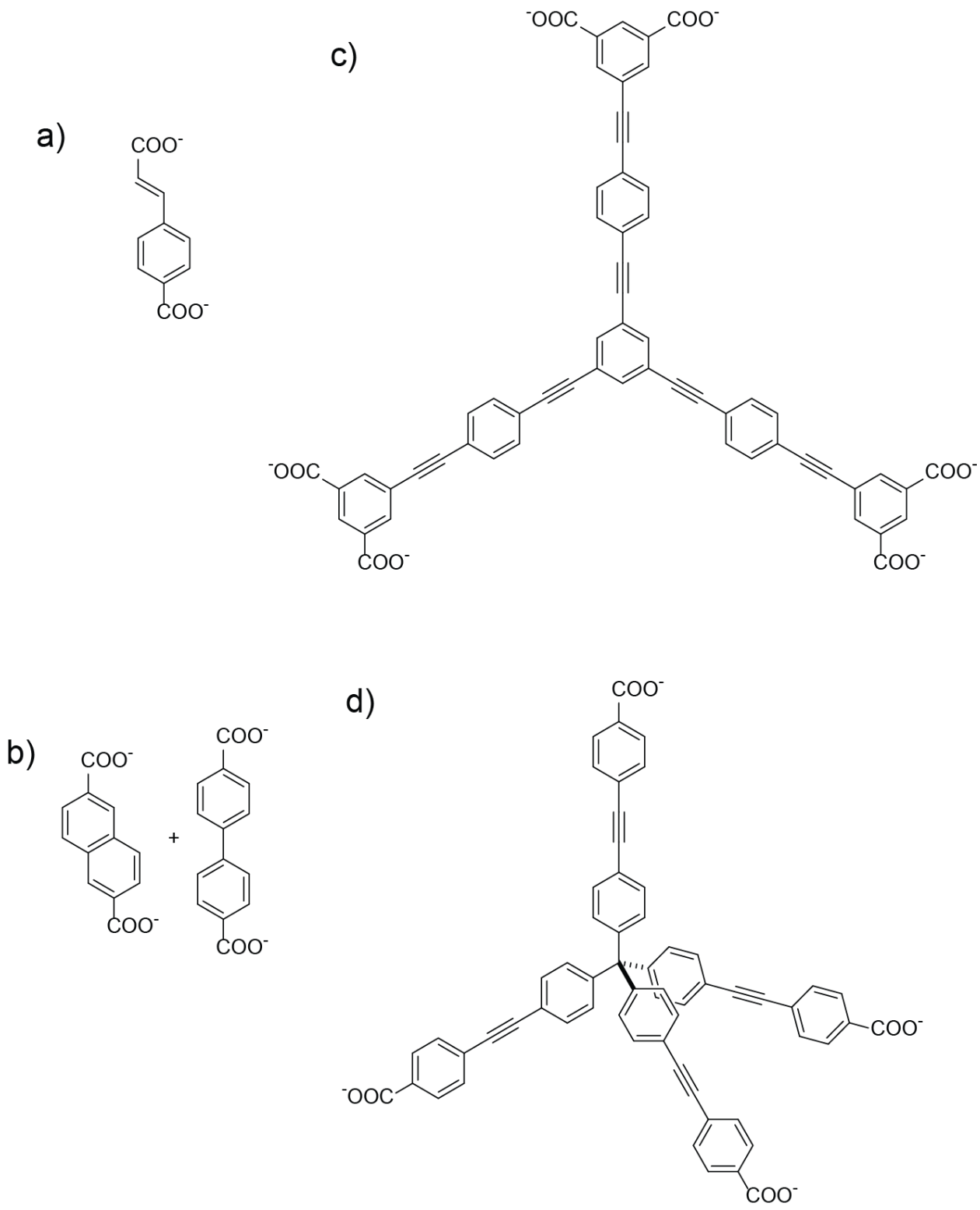

Figure 1.2. Linkers for the MOFs (a) SNU-70, (b) UMCM-9, (c) PCN-610/NU-1000, and (d) NPF-200.

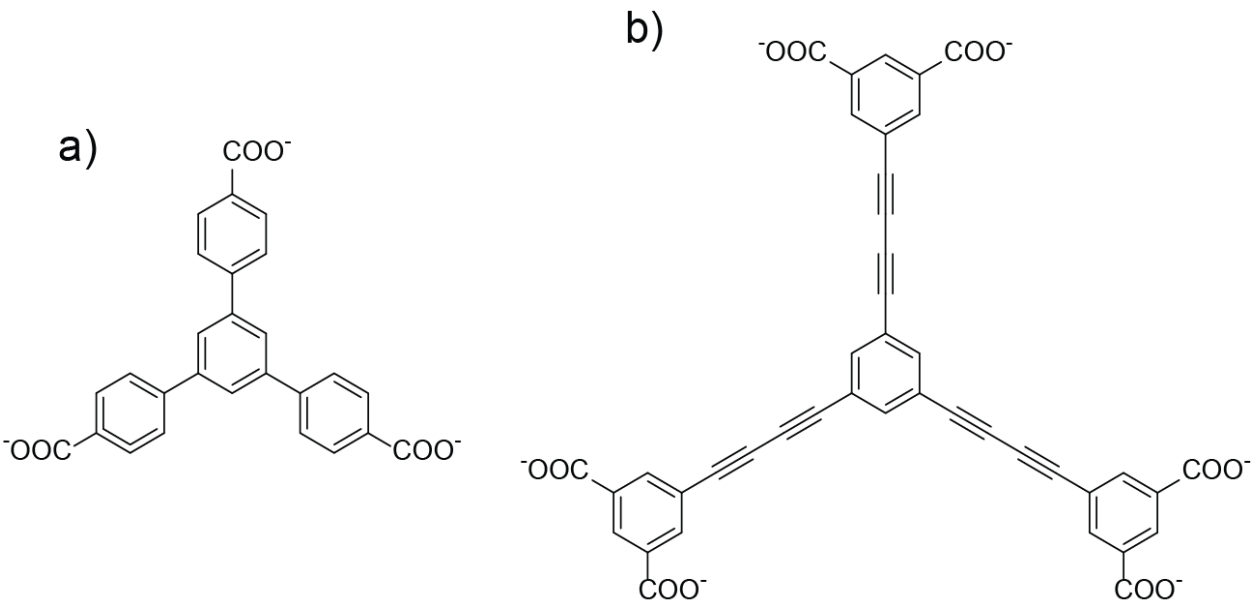

Figure 1.3. Linkers for the MOFs (a) MOF-177 and (b) NU-111.

MOFs have also been studied for CO_2 capture,[24] an energetically-costly process vital to reducing overall greenhouse gas emissions. Unlike H_2 and CH_4 uptake, which mainly benefit from improvements to surface area and pore volume, CO_2 affinity of MOFs is strongly determined by the presence of chemical features of the framework with which the molecule can interact. Such moieties include open metal sites, Lewis basic sites, and polar linker functional groups.

Open metal sites are created in MOFs by removing terminal (non-bridging) coordinating species – such as water, methanol, or *N*,*N*-dimethylformamide (DMF) – using heat and/or vacuum, freeing Lewis-acidic metal sites which can then coordinate CO_2. Two highly studied MOFs which show enhanced CO_2 uptake as a consequence of open metal sites are HKUST-1[25] and MIL-101.[26] These MOFs are based on the metal clusters $Cu_2(R\text{-}CO_2)_4$ and $Cr_3O(R\text{-}CO_2)_6$, respectively, which can each coordinate 2 species per cluster. (Figure 1.4)

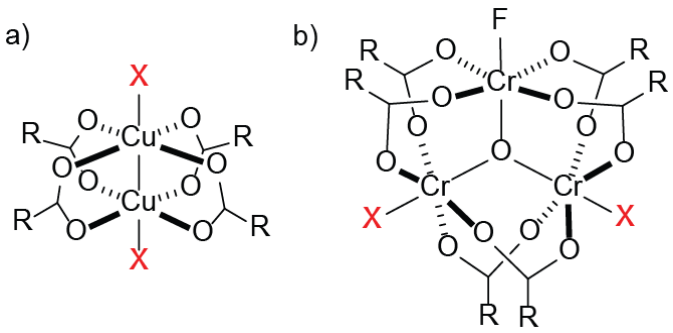

Figure 1.4. Metal clusters for (a) HKUST-1 and (b) MIL-101. Coordination sites that can be made accessible in these clusters are denoted as X. F^- in the MIL-101 Cr_3O cluster is tightly bound for charge-balance reasons, and may be replaced by NO_3^- depending on the synthesis conditions used.

Metal choice has a strong impact on CO_2 uptake in MOFs containing open metal sites, as was shown using the model system MOF-74.[27] MOF-74 is based on one-dimensional metal oxide chains with each metal atom coordinated octahedrally by 5 oxygen atoms associated with linker molecules (2,5-dioxidoterephthalate), leaving one potential open site per metal atom. (Figure 1.5a) Mg-MOF-74 was found to outperform the Zn, Ni, and Co variants of the MOF, a result attributed to the greater ionic character of the Mg–O bond, resulting in stronger metal ion–CO_2 quadrupole interactions with this framework. Another approach to improving MOF CO_2 affinity is installation of Lewis basic sites into the framework, generally in the form of amines. These can allow MOFs to chemisorb CO_2 in a similar fashion to ethanolamine in industrial CO_2 scrubbing.[28,29] (Figure 1.5b) This concept has been demonstrated by comparison of MOF-5 and the isoreticular (same network topology) analog IRMOF-3, which differs from MOF-5 by the presence of a pendant amino group on its linker,[25] (Figure 1.5c,d) as well as in other isoreticular pairs based on these two linkers, including MIL-53,[30] UiO-66,[31] and MIL-125.[32] However, amino groups vary in their efficacy at this task: in a series of IRMOF-74-III derivatives, the aminomethyl derivative was most effective due to its greater alkylamine character.[33] (Figure 1.5e)

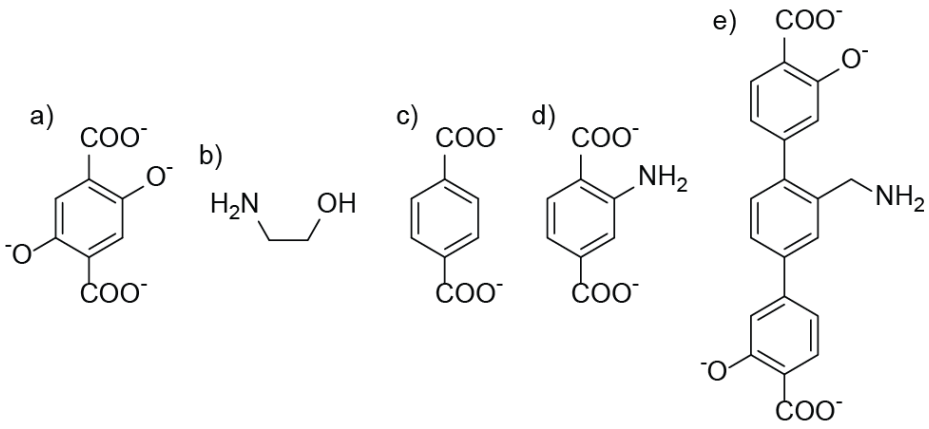

Figure 1.5. (a) 2,5-Dioxyterephthalate, the linker for MOF-74, (b) ethanolamine, (c) terephthalate, the linker for MOF-5, (d) 2-aminoterephthalate, the linker for IRMOF-3, and (e) 2'-(aminomethyl)-3,3"-dioxy-[1,1':4',1"-terphenyl]-4,4"-dicarboxylate, the linker for IRMOF-74-III-CH_2NH_2.

Other functional groups that can increase CO_2 affinity include polar groups such as -F, -Cl, -Br, -OH, -COOH, $-NO_2$, and $-SO_3$, which participate in dipole-quadrupole interactions with CO_2.[34] An example of a MOF with higher CO_2 capacity as a result of these interactions is CD-MOF-2, a Rb-based MOF with γ-cyclodextrin as its linker.[35,36] (Figure 1.6a) This MOF shows two distinct types of CO_2 uptake: at low coverage, chemisorption associated with the most reactive hydroxyl groups (forming carbonates) is observed, and at higher coverage, physisorption to less-reactive sugar alcohol groups dominates. While the strongly chemisorbed CO_2 cannot be removed under vacuum even after 12 hours, the physisorbed species (which make up the bulk of sorbed CO_2 at full coverage) are readily desorbed, demonstrating the difference in binding strength arising from these two sorption modes.

MOFs have been examined for removal of organosulfur compounds from fuel,[37,38] which is a necessary process for reducing SO_x emissions by the transportation sector. Two frameworks that have been found to perform well for this application include UMCM-150, based on Cu and biphenyl-3,4',5-tricarboxlate (Figure 1.6b), and the Ni variety of MOF-74. Both of these frameworks contain solvent-bound coordination sites which can be made coordinatively

undersaturated, which may explain their organosulfur affinity. This can be seen in Ni-MOF-74, where the Ni-S bond between *S*-heterocycles and Ni was found to be partially covalent in nature.

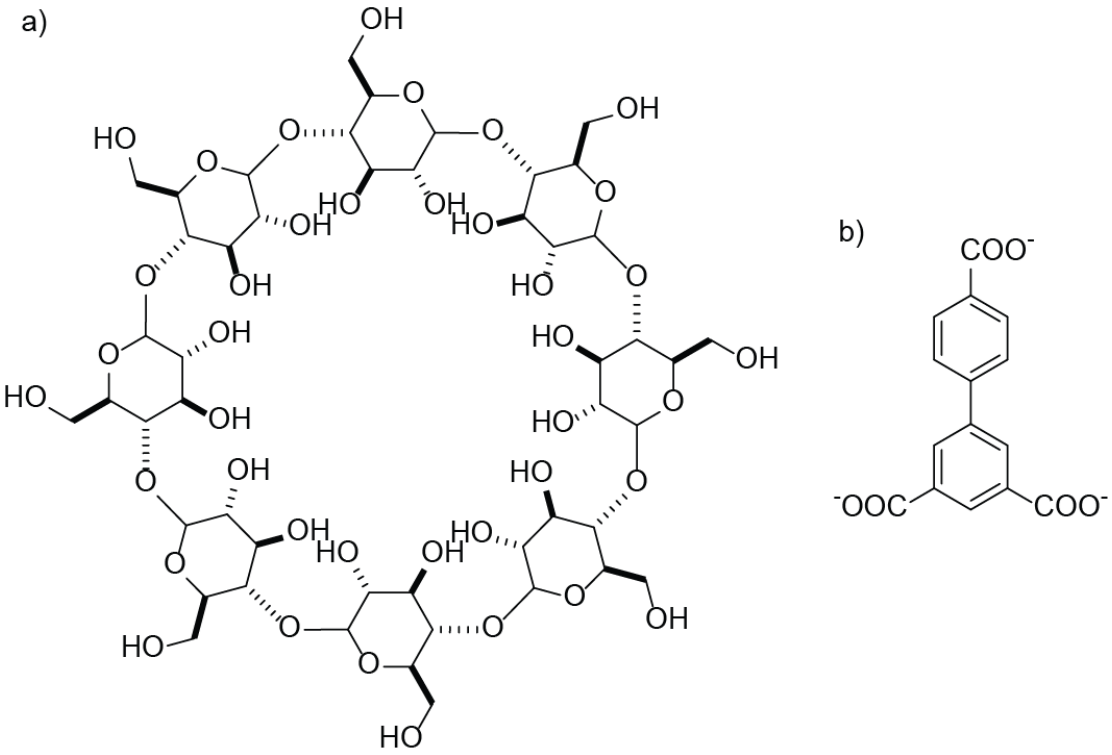

Figure 1.6. (a) γ-Cyclodextrin, used to make CD-MOF-2, (b) biphenyl-3,4',5-tricarboxlate, the linker in UMCM-150.

A final energy application of MOFs is in the area of light harvesting/solar energy conversion.[39-41] Generally, MOFs for light harvesting utilize chromophores within the framework to absorb visible light, then relay that energy to generate redox-separated states which can be harnessed (e.g. for chemical transformations). Several linkers with absorption in the solar spectrum are shown in Figure 1.7. MOFs made from Ru- or Os-based linkers containing 4,4′-$(CO_2)_2$-bpy ligands (Figure 1.7a,b) show phosphorescent behavior characterized by strong absorption in the visible region and are readily excited to a long-lived triplet metal-to-ligand charge transfer state.[42] Quenching studies showed that the MOFs were efficient at both light harvesting and excited-state

electron transfer. Another common strategy for creating light-harvesting MOFs is to utilize linkers based on porphyrin cores.[43-45] (Figure 1.7c,d) MOFs containing these linkers have been shown to have excellent energy transfer behavior, but their absorption bands often do not cover the full usable solar spectrum. To deal with this imperfect overlap between the linker absorption spectrum and the solar spectrum, secondary chromophores can be introduced into the framework to act as sensitizers. This can be accomplished by including multiple types of linkers in the same framework that absorb complementary regions of the solar spectrum. An example of this approach is the creation of a MOF based on bodipy and ZnTCPP.[43] (Figure 1.7e,f) In this framework, bodipy acts as an antenna chromophore which absorbs and transfers energy to the porphyrin struts, allowing the MOF to harvest a greater portion of the visible spectrum than either linker alone would permit.

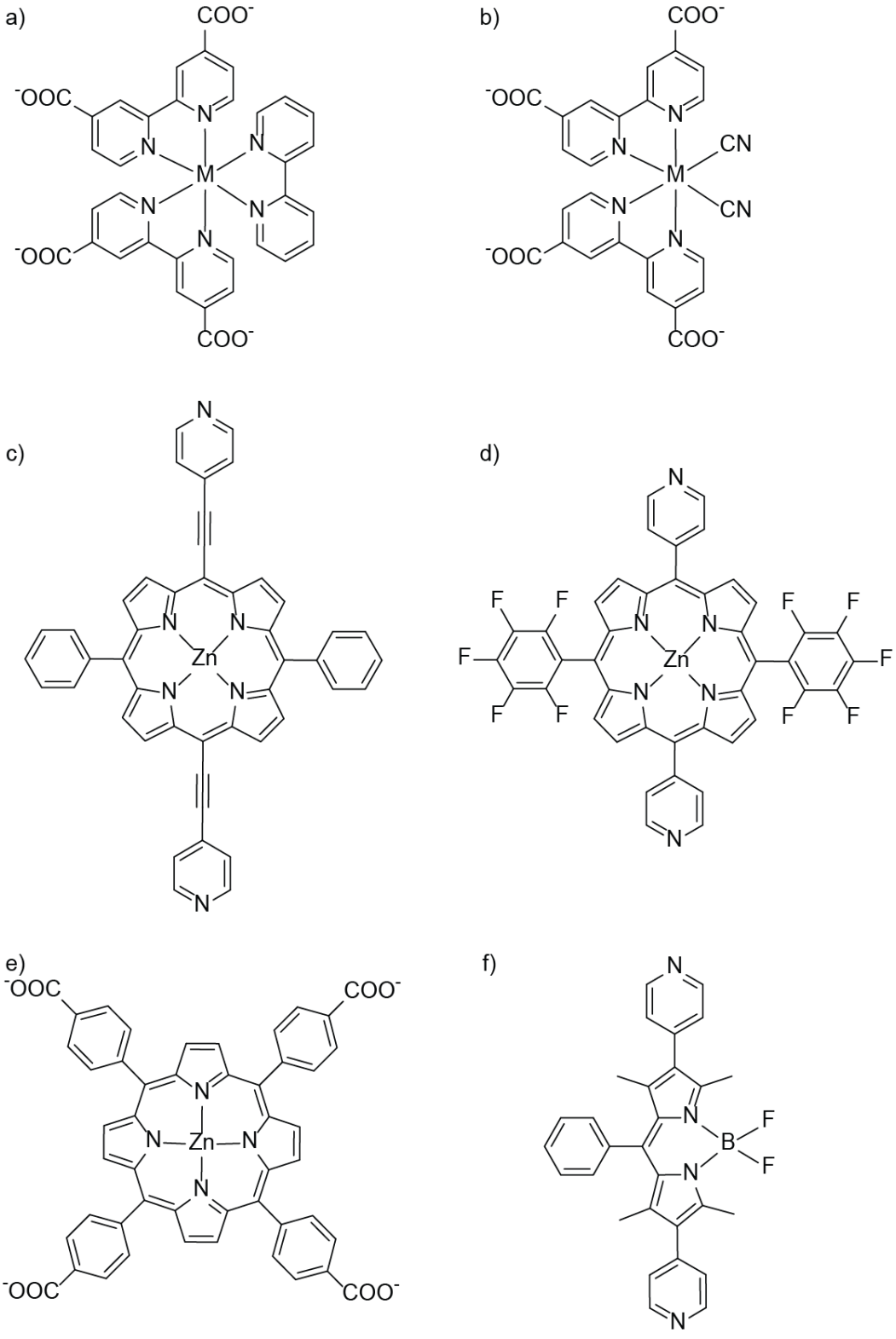

Figure 1.7. Several chromophore-containing MOF linkers: (a) {M[4,4′-$(CO_2)_2$-bpy]$_2$bpy} (M = Ru^{2+} or Os^{2+}), (b) {M[4,4′-$(CO_2)_2$-bpy]$_2(CN)_2$} (M = Ru^{2+} or Os^{2+}), (c) DA-ZnP, (d) F-ZnP, (e) ZnTCPP, and (f) bodipy.

Another approach to sensitizing MOFs for light harvesting is the introduction of dyes into the framework, which are adsorbed rather than covalently bound to the MOF. An example of this approach is the absorption of organic dyes into the zeolitic MOF (Et_2NH_2)-[In(BCBAIP)]·4DEF·4EtOH (H_4BCBAIP: 5-(bis(4-carboxybenzyl)amino)-isophthalic acid).[46] (Figure 1.8a) In this system, Coumarin 343 and Coumarin 6 (Figure 1.8b,c) are able to accept excitation energy from the framework particularly efficiently due to excellent overlap between the emission spectrum of the MOF and the absorption spectra of the dyes. Taken to its extreme, this approach can be used to imbue otherwise inert frameworks with light harvesting behavior, such as in the case of doping the cationic dye $Ru(bpy)_3^{2+}$ (Figure 1.8d) into the non-photoactive UiO-67.[47,48] In this situation, the MOF acts as an inert scaffold for the dye, rather than a framework to be sensitized.

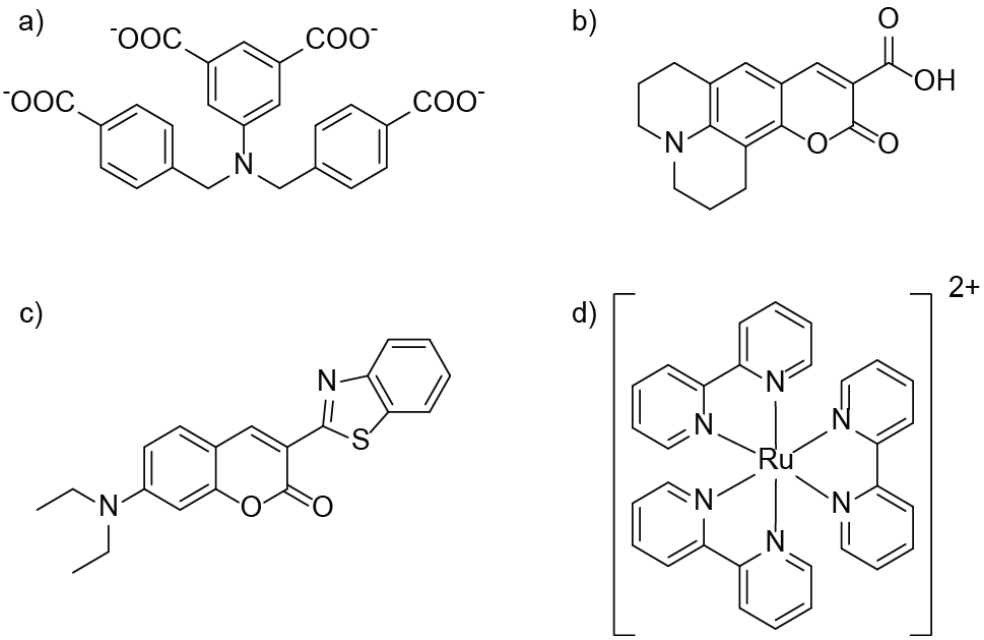

Figure 1.8. (a) 5-(bis(4-carboxybenzyl)amino)-isophthalate, (b) Coumarin 343, (c) Coumarin 6, (d) $Ru(bpy)_3^{2+}$.

Catalysis

MOFs have been heavily studied in the area of catalysis. These materials offer the tunability, well-defined structures, and (ideally) fully accessible active sites of homogeneous, soluble catalysts, while offering the recoverability of heterogeneous, insoluble catalysts.[49] Several representative catalytically active MOFs include MIL-101-SO_3H, MOF-525, and the CMOF series. These systems, their benefits over traditional catalysts, and reactions they have been used to catalyze will be discussed presently.

MIL-101-SO_3H is based on the same $Cr_3O(R\text{-}CO_2)_6$ cluster as MIL-101 (Figure 1.4b), but its linker is the sulfonic acid derivative of the terephthalate linker in MIL-101.[50] (Figure 1.9) This acid functionality gives the MOF the ability to catalyze cellulose reduction (Figure 1.10a), and the high chemical stability of the carboxylate-Cr_3O cluster coordination bond allows the MOF to withstand boiling water. Relative to other solid acid catalysts, MIL-101-SO_3H was found to be highly reusable, maintaining its level of catalytic activity after 13 cycles. MIL-101-SO_3H has also been used for catalyzing epoxide ring opening reactions, e.g. styrene oxide ring opening.[51] (Figure 1.10b) The MOF outperformed all other catalysts tested for that reaction, and was particularly effective when methanol was used as the nucleophile due to its small size and rapid diffusion through the MOF pores. The high crystallinity of the MOF and its correspondingly highly uniform active sites allow the MOF to impart a high degree of regioselectivity, predictably giving products attributable to an acid-catalyzed S_N1 ring-opening mechanism.

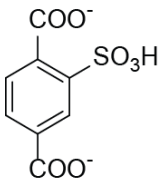

Figure 1.9. 2-Sulfoterephthalate, the linker in MIL-101-SO_3H.

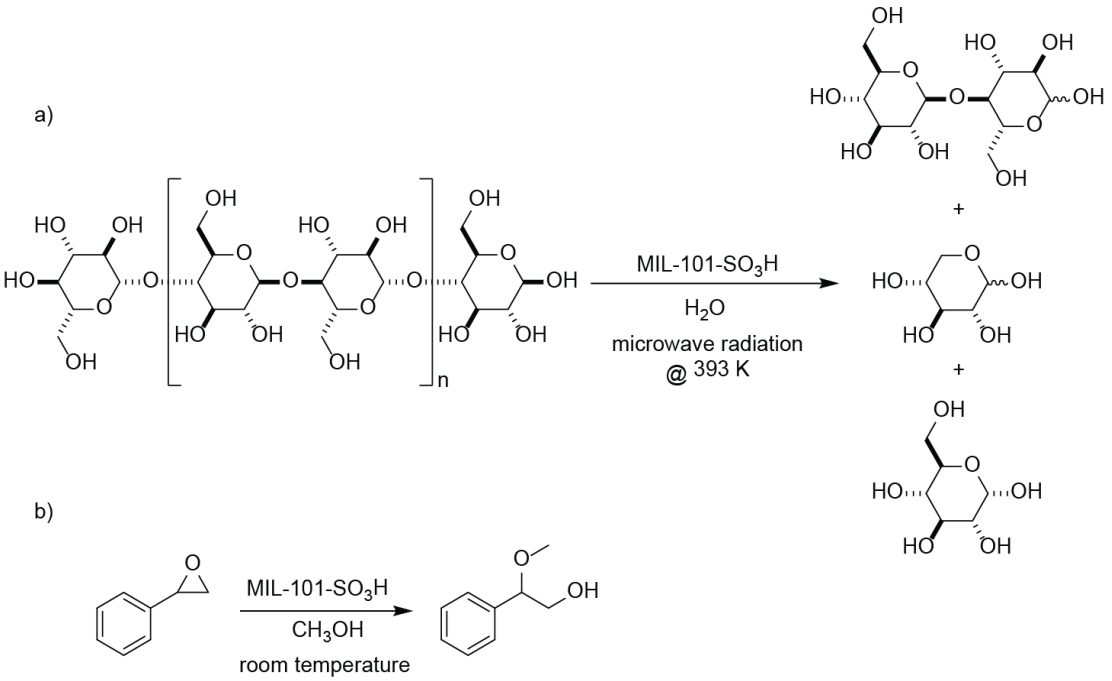

Figure 1.10. Two reactions catalyzed by MIL-101-SO_3H. (a) Reduction of cellulose to cellobiose, D-xylose, and glucose. (b) Ring opening of styrene oxide with methanol.

Another MOF with well-characterized catalytic activity is MOF-545.[52] MOF-545 is based on the $Zr_6O_8(H_2O)_8(R\text{-}CO_2)_8$ cluster (Figure 1.11), which, like the Cr_3O cluster, is associated with high stability frameworks. This cluster can accommodate 8 carboxylates associated with the porphyrin-based, heme-type linker TCPP-FeCl. (Figure 1.7e, but with Zn^{2+} replaced with $[FeCl]^{2+}$) This cluster is distinct from the $Zr_6O_4(OH)_4(R\text{-}CO_2)_{12}$ cluster, which coordinates an additional 4 carboxylate ligands in its open equatorial positions and is most-commonly associated with the UiO-66/-67/-68 series of MOFs. MOF-545 has been used for oxidation of a number of different substrates, including 1,2,3-trihydroxybenzene, 3,3,5,5-tetramethylbenzidine, *o*-phenylenediamine, and 2,2′-azinodi(3-ethylbenzothiazoline)-6-sulfonate.[53,54] (Figure 1.12) The MOF was found to have comparable peroxidase activity to the heme protein myoglobin, with the benefit of retained activity in organic solvents such as ethanol, in which myoglobin agglomerates and loses enzymatic efficacy. This stability, combined with a high density of catalytic centers and exceptionally large channels, makes MOF-545 a particularly useful system.

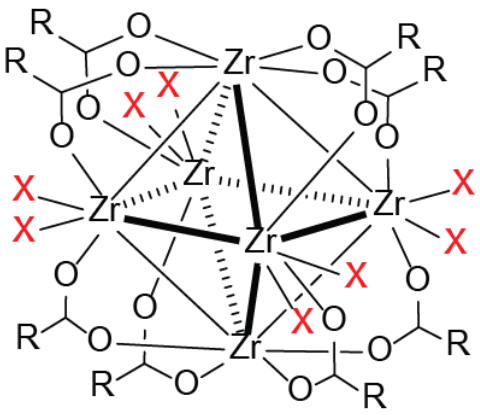

Figure 1.11. The $Zr_6(R\text{-}CO_2)_8$ cluster found in MOF-545. Eight $\mu_3\text{-}O^{2-}$ ligands (one located in each face of the Zr_6 octahedron) are omitted for clarity. Coordination sites marked with X are coordinated by H_2O in the as-synthesized material.

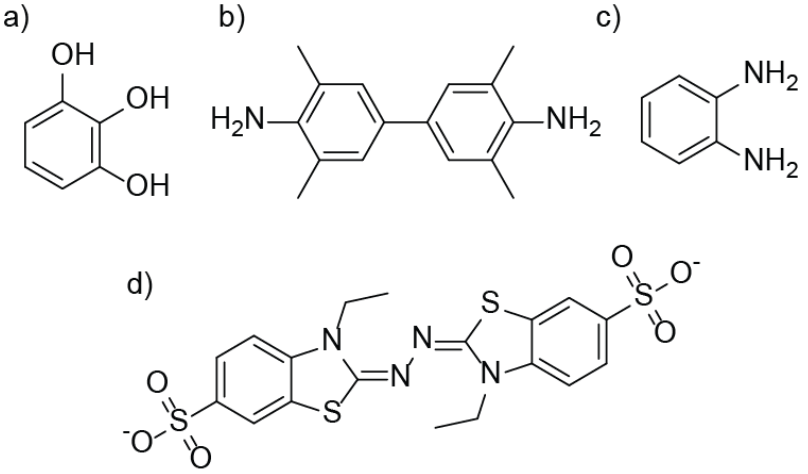

Figure 1.12. Substrates oxidized by MOF-545. (a) 1,2,3-Trihydroxybenzene, (b) 3,3,5,5-tetramethylbenzidine, (c) *o*-phenylenediamine, and (d) 2,2′-azinodi(3-ethylbenzothiazoline)-6-sulfonate.

Relative to MIL-101-SO_3H and MOF-545, the CMOF series (abbreviated from chiral MOF) is based on a less-stable linker-metal cluster coordination bond.[55,56] In particular, this series contains $Zn_4O(R\text{-}CO_2)_6$ clusters coordinated by 6 carboxylate ligands in an octahedral geometry, which are associated with poor water and mechanical stability.[57] The linkers in this series are based on salen ligands (Figure 1.13) metallated with transition metals (e.g. Mn,[55] Ru[56]). These MOFs have been used for alkene epoxidation and asymmetric cyclopropanation of substituted alkenes, both with high enantioselectivity. Varying the channel size, either by modulating linker length or

degree of framework interpenetration, was found to have a significant impact on MOF catalytic activity due to changes in the rate of reagent/product diffusion in/out of the MOF. When the channels became large enough, the reaction rate was found to rival that of analogous homogeneous catalysts, i.e. the limiting factor was the intrinsic reactivity of the catalytic centers. Despite their less robust metal cluster, MOFs in the CMOF series are also recyclable, showing retention of structure and activity upon reuse. This chemical stability also allows for oxidation state modification of materials post-synthesis: in the case of CMOFs comprising Ru-based linkers, it was found that Ru^{3+} could be reduced *in situ* to Ru^{2+} in a reversible single-crystal to single-crystal fashion, the first report of such a transformation.

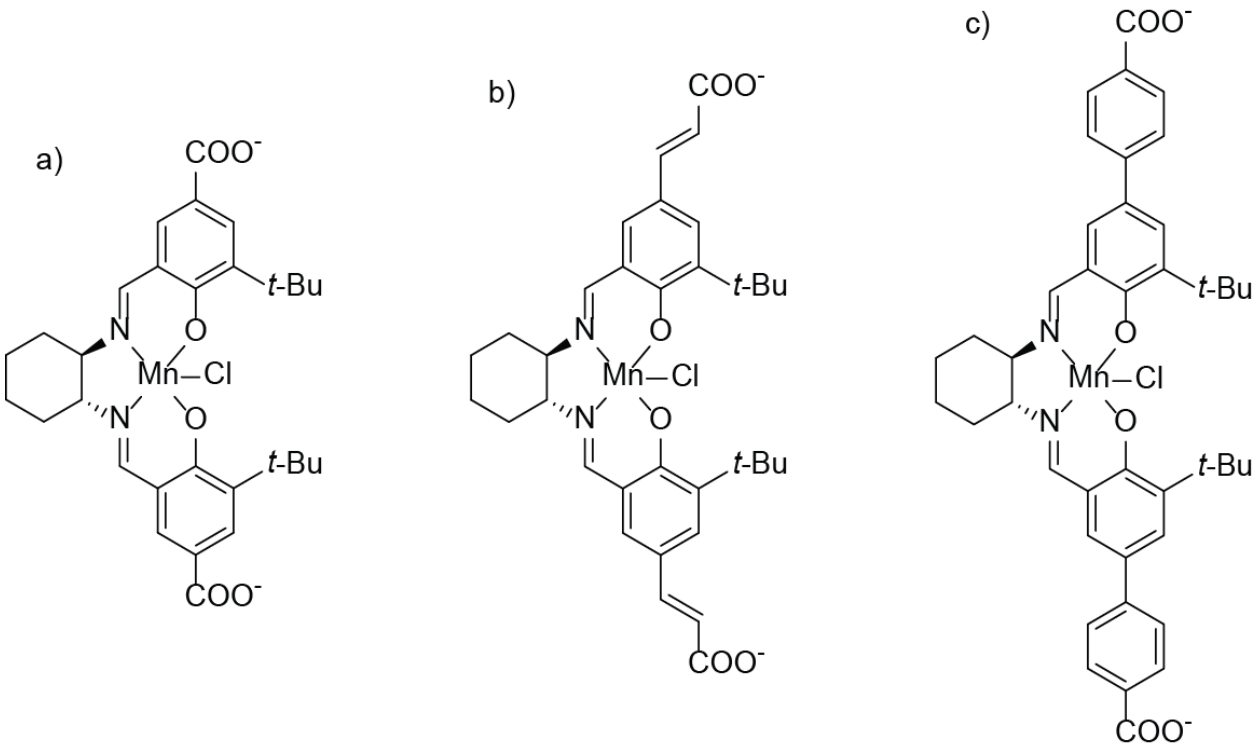

Figure 1.13. Several Mn-salen linkers used for creation of CMOFs. (a) (*R*,*R*)-(-)-*N*,*N*'-Bis(3-carboxyl-5-tert-butylsalicylidene)-1,2-cyclohexanediamino manganese(III) chloride, (b) (2*E*,2'*E*)-3,3'-(5,5'-(1*E*,1'*E*)-(1*R*,2*R*)-cyclohexane-1,2-diylbis(azan-1-yl-1-ylidene) bis(methan-1-yl-1-ylidene)bis(3-tert-butyl-4-hydroxy-5,1-phenylene))diacrylate manganese(III) chloride, and (c) 5',5''-(1*E*,1'*E*)-(1*R*,2*R*)-cyclohexane-1,2-diylbis(azan-1-yl-1-ylidene)bis(methan-1-yl-1-ylidene)bis(3'-tert-butyl-4'-hydroxybiphenyl-4-carboxylate) manganese(III) chloride.

Human health applications

In the area of health and medicine, there are several avenues for utilizing MOFs. Controlled and targeted release of drugs[57-60] is one major application that utilizes the high void volume of these materials, as well as their hydrolytic (in)stability to modulate drug release rate. Several systems that have been studied for this application include MIL-100[61] (based on the $Cr_3O(R\text{-}CO_2)_6$ cluster, Figure 1.4b, and trimesate, Figure 1.14a), MIL-100(Fe)[62] (constructed using the same trimesate linker, but with Fe^{3+} replacing Cr^{3+} in the metal cluster), and ZIF-8[63] (Zn^{2+} ions and 2-methylimidazolate linker, Figure 1.14b).

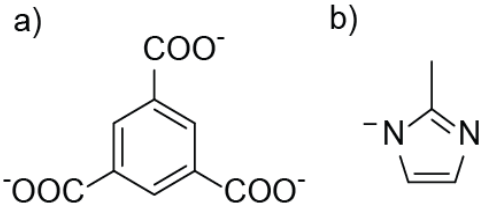

Figure 1.14. (a) Trimesate, linker for MIL-100, and (b) 2-methylimidazolate, linker for ZIF-8.

MIL-100 was used in early studies on MOF controlled drug release due to its large pores, which allow the framework to accommodate a significant quantity of drug, combined with its chemical inertness and highly crystalline structure.[61] When solution-loaded with ibuprofen (Figure 1.15a) in hexane, MIL-100 achieved loadings of 0.35 g ibuprofen/g MOF, which took 3 days to fully remove in constantly stirring simulated body fluid. Solid-state NMR of the drug-loaded MOF shows a distribution of ibuprofen conformations, indicating that a variety of different interactions exist between the drug and the framework. While these fundamental studies on MIL-100 were useful for establishing the basis for MOF-mediated controlled drug release, the high toxicity of chromium precludes its use in pharmaceutical formulations. This prompted research into MOFs based on less-toxic metals such as iron, which is utilized in the iron(III) analog MIL-100(Fe).

MIL-100(Fe) (as one of several iron(III) carboxylate MOFs) was studied for its drug delivery efficacy due to its greater biocompatibility, which was probed along with its degradability and imaging properties.[62] The MOF was found to have minimal toxicity: female rats dosed up to 220 mg kg^{-1} MIL-100(Fe) showed no significant or irreversible differences relative to the control group. Once the low toxicity of the MOF was established, it was loaded with a range of different guests, including the anticancer or antiviral drugs busulfan, azidothymidine triphosphate, cidofovir, and doxorubicin, and cosmetic molecules including caffeine, urea, benzophenone-3, and benzophenone-4. (Figure 1.15b-i) MIL-100(Fe) was found to have exceptional capacity for all of these species, even when loading from relatively dilute solutions, a sign of the framework affinity for these molecules. Drug release was chiefly limited by the rate of drug diffusion out of the pores and the strength of drug–matrix interactions rather than by the rate of MOF degradation: for instance, azidothymidine triphosphate was wholly released after 3 days, at which time the MOF was only ~10 % degraded. The MOF was also found to act as a contrast agent *in vivo*, making it a candidate material for combined therapeutic/diagnostic applications. The properties of MIL-100(Fe) can be improved by external surface modification, as was demonstrated using the biocompatible polymer heparin.[64] (Figure 1.16) Heparin associates to MIL-100(Fe) via strong sulfate-iron interactions and decreases cell recognition and uptake of the MOF, offering a route to provide MOF-drug composites with stealth properties. This and similar coatings may allow for reduced inflammation responses and tighter control of *in vivo* fate, an approach which broadens the utility of MOFs in biomedicine.

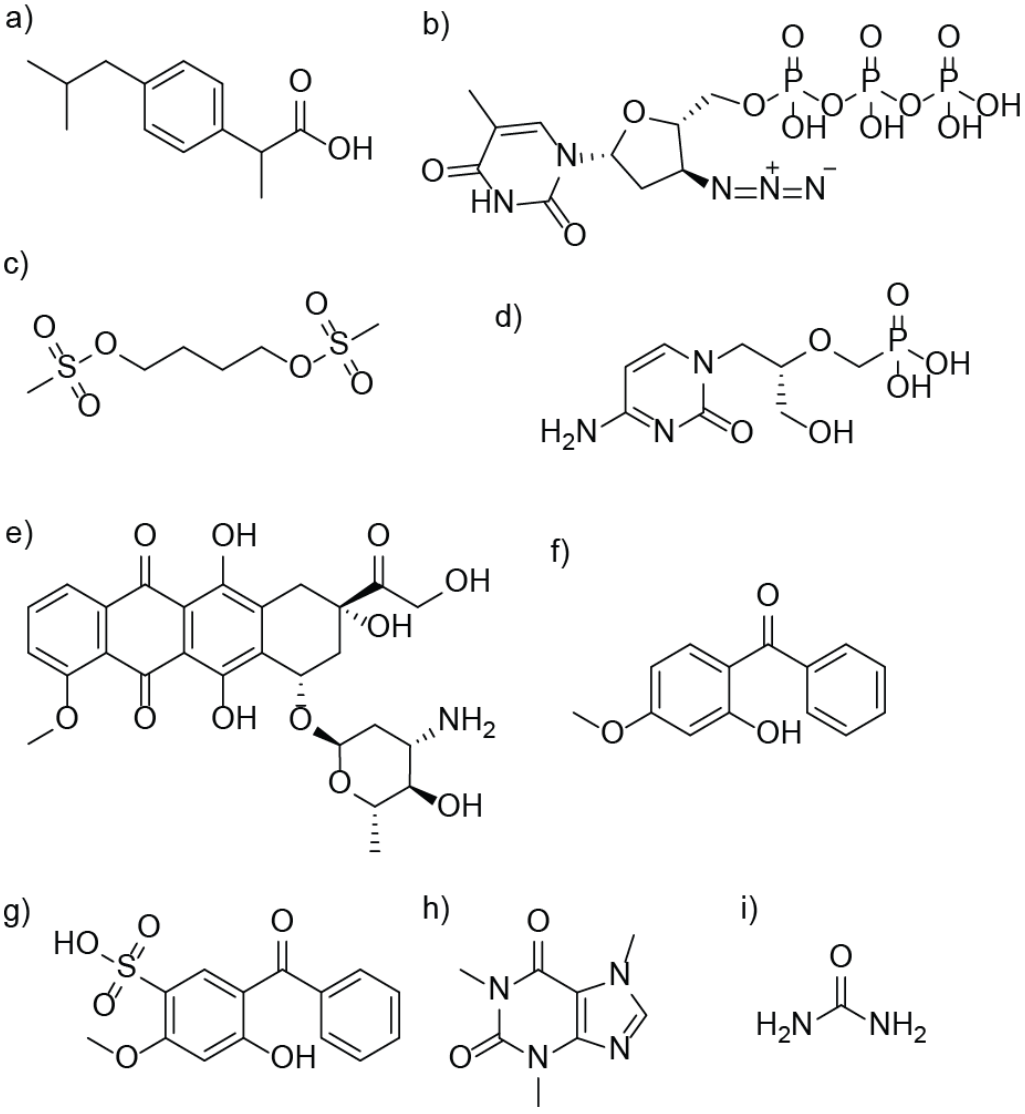

Figure 1.15. Several drugs and other molecules studied for MIL-100- and MIL-100(Fe)-mediated controlled release. (a) Ibuprofen, (b) azidothymidine triphosphate, (c) busulfan, (d) cidofovir, (e) doxorubicin, (f) benzophenone-3, (g) benzophenone-4, (h) caffeine, and (i) urea.

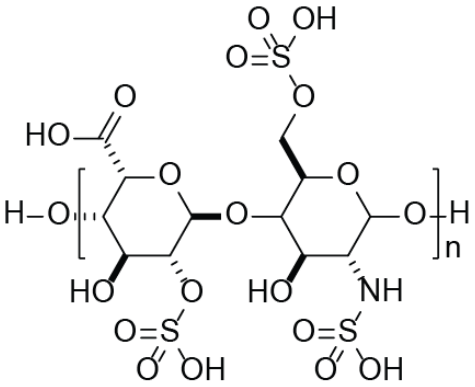

Figure 1.16. The biopolymer heparin.

While MIL-100 and MIL-100(Fe) release drug primarily through simple diffusion of the drug out of the intact framework, targeted release is an important mode of drug delivery which may allow for administration of chemotherapeutic drugs with diminished side effects. In particular, while blood and normal tissue is ~pH 7.4, tumor tissue is generally acidic, in the range of pH 5.5 – 6.0. Thus, pH responsive MOF drug delivery systems which can selectively target cancer cells and reduce adverse effects associated with nonselective drug release have seen extensive study. ZIF-8 has highly pH-dependent stability, making it useful for pH-responsive drug release in acidic target regions.[65] In particular, it is stable after 7 days in phosphate-buffered saline solution, but loses crystallinity and dissolves within minutes in an acetate buffer solution. ZIF-8 has been tested for pH-responsive release of several different drugs and drug analogs, including 5-fluorouracil, camptothecin, fluorescein, rhodamine B, methyl orange, methylene blue, (Figure 1.17) and doxorubicin (Figure 1.15e).[63,65-67] When synthesized as particles with appropriate dimensions, the MOF has been found to be suitable for cell internalization with minimal cytotoxicity. Its small window sizes disfavor diffusion-related release of drug, suppressing premature drug release, demonstrating the importance of such macromolecular considerations when designing and choosing MOF drug delivery systems.

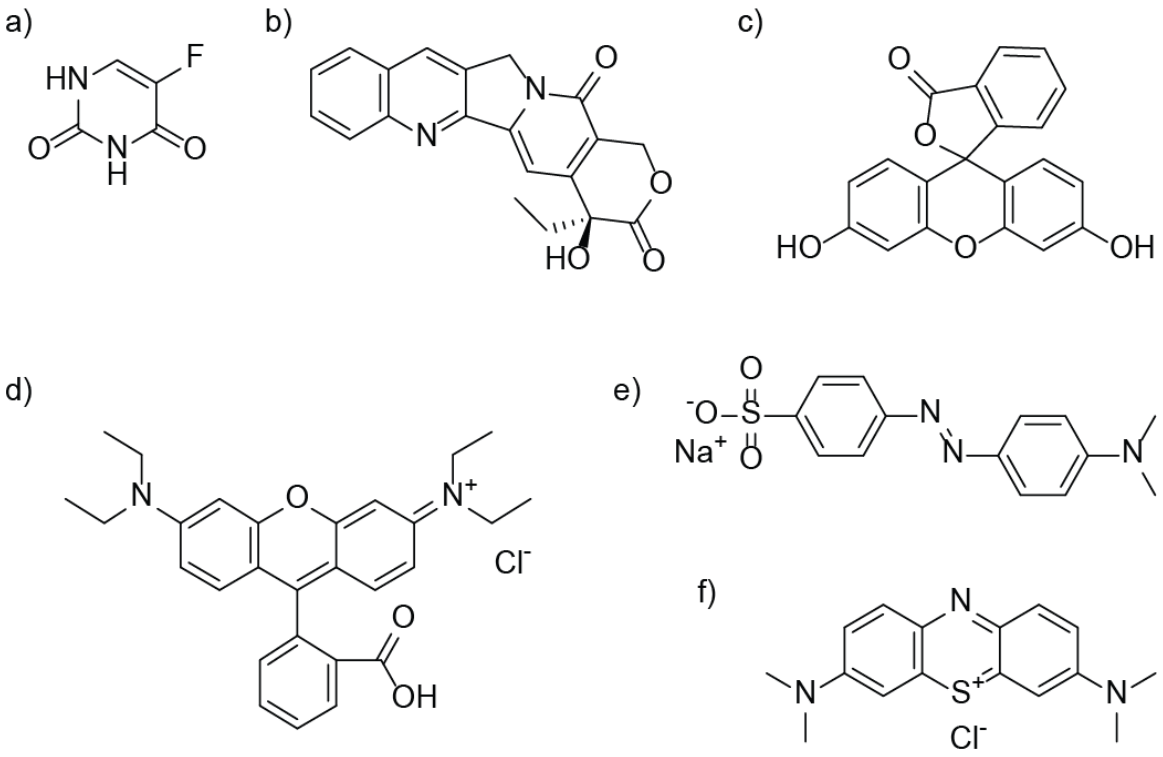

Figure 1.17. Drugs and drug analogs loaded into ZIF-8 for controlled release studies. (a) 5-Fluorouracil, (b) camptothecin, (c) fluorescein, (d) rhodamine B, (e) methyl orange, and (f) methylene blue.

1.3 MOF preparation

1.3.1 Synthesis

MOFs are generally prepared under solvothermal synthesis conditions. A typical MOF synthesis may involve dissolving the MOF constituents (linker, metal salt) in a formamide solvent (DMF and *N*,*N*-diethylformamide (DEF) are most common), sealing the resulting solution in a glass vial or jar, and placing it in an oven or heat block in the range of 70 °C – 120 °C for 16 hours – 7 days. Conditions suitable for synthesis of four different MOFs – MOF-5, UiO-66, HKUST-1, and UMCM-9 – are described below.

MOF-5[68]

Terephthalic acid (100 mg, 0.6 mmol) and zinc(II) nitrate tetrahydrate (500 mg, 1.9 mmol) are dissolved in 15 mL DEF in a 20 mL scintillation vial, which is then sealed with a Teflon-lined

cap. The vial is then placed in a 100 °C oven for 24 hours to generate 0.7 – 1.0 mm colorless cubic crystals. (Figure 1.18) DEF is chosen for this synthesis for two main reasons. First, as a formamide solvent, DEF decomposes at elevated temperatures, leading to slow generation of carbon monoxide and basic alkylamine species, which can deprotonate linker molecules and give rise to slow, controlled crystal growth.[69,70] This slow growth is important for creation of highly crystalline materials: quick, room temperature syntheses of MOF-5 exist wherein base is added directly to the reaction medium, but materials from such syntheses are generally characterized by low surface areas. Second, DEF is chosen over other formamide solvents due to its templating behavior during the synthesis. When DMF is instead used in the synthesis, a phase-impure product results: the combination of Zn^{2+} and bdc^{2-} can give rise to a number of other (crystalline and noncrystalline) materials.[71] DEF is thought to favor MOF-5 formation by reversibly coordinating metal clusters during crystal growth, and as a function of its larger size, preventing the formation of phases with more condensed structures than MOF-5.[72-74] The formamide alkyl chain size, then, influences the pore size of the resulting material.

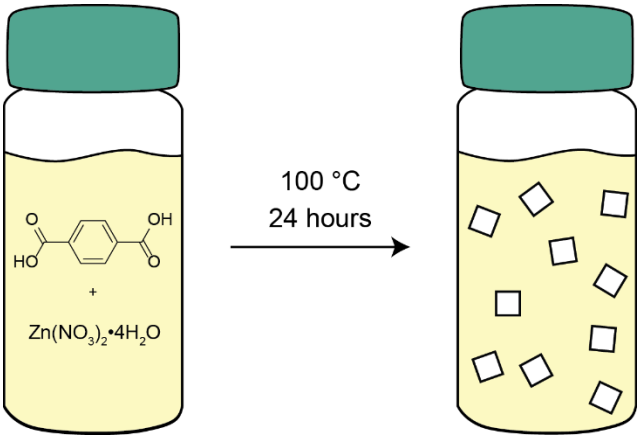

Figure 1.18. Schematic representation of the synthesis of MOF-5. Terephthalic acid and zinc nitrate tetrahydrate are dissolved in DEF and incubated in a 100 °C oven for 24 hours, yielding colorless cubic crystals.

UiO-66[75]

Terephthalic acid (123 mg, 0.75 mmol) is combined with zirconium(IV) chloride (125 mg, 0.54 mmol) and dissolved in a mixture of 15 mL DMF and 1 mL HCl. The reaction mixture is sealed in a 20 mL scintillation vial and incubated in an 85 °C oven for 16 hours to yield a white, microcrystalline powder. HCl serves to speed up the reaction: its presence lowers the barrier for linker–node dissociation, accelerating structural rearrangement and MOF growth. As an additive that acts to alter the process of MOF formation, HCl is referred to as a modulator in this synthesis. Other modulators can be used in the synthesis of UiO-66 (e.g. formic acid, acetic acid, dichloroacetic acid, trifluoroacetic acid, benzoic acid; Figure 1.19) to control MOF properties such as defect concentration, surface area, and pore size.[76-79]

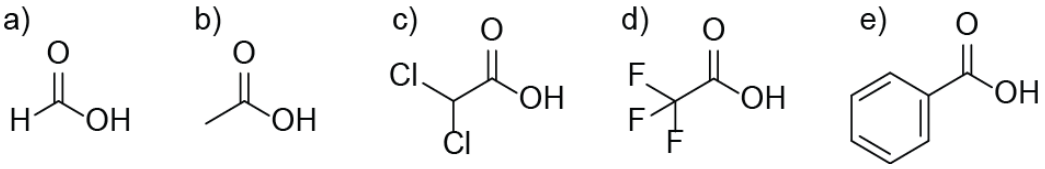

Figure 1.19. Several species that have been used as modulators in the synthesis of UiO-66. (a) Formic acid, (b) acetic acid, (c) dichloroacetic acid, (d) trifluoroacetic acid, and (e) benzoic acid.

HKUST-1[80]

Trimesic acid (300 mg, 1.44 mmol) and copper(II) nitrate hemipentahydrate (600.0 mg, 2.58 mmol) are dissolved in a solvent mixture comprising 5 mL each of DMF, EtOH, and H_2O. The reaction mixture is kept in a 20 mL vial in an 85 °C oven for 20 hours. It is relatively uncommon to include water in MOF syntheses, which highlights the stability of HKUST-1 to such nucleophilic species.[81] This mixed solvent approach is useful for decreasing the quantity of relatively expensive organic solvents needed to make MOFs. The use of mixed solvents also allows for control over many relevant properties (e.g. solubilizing power, viscosity, boiling point) of the solvent mixture, which can be useful for tuning MOF syntheses. An alternative synthesis of

HKUST-1 utilizes only MeOH as a solvent,[82] which has the benefit of limiting strongly-bound water and DMF in the framework, making later solvent removal much more facile.

UMCM-9[18]

Zinc(II) nitrate tetrahydrate (238.0 mg, 0.800 mmol), 2,6-naphthalenedicarboxylic acid (28.7 mg, 0.132 mmol), and 4,4'-biphenyldicarboxylic acid (35.6 mg, 0.147 mmol) are dissolved in a mixture of 6.7 mL DEF and 13.3 mL *N*-methylpyrrolidone (NMP), and incubated in an 85 °C oven for 4-7 days. NMP is an amide, which is expected to degrade at a much slower rate than formamides such as DEF. In this synthesis, by diluting DEF, NMP may limit the rate of base formation, slowing crystal growth. This slow crystallization is particularly important for construction of MOFs capable of interpenetration: the MOFs composed of Zn_4O^{6-} and either of the two linkers in UMCM-9 (2,6-naphthalenedicarboxylate: IRMOF-8, 4,4'-biphenyldicarboxylate: IRMOF-9) are known to interpenetrate in standard solvothermal synthetic conditions.[83,84] The relatively long synthesis time of up to a week aids in generating a highly crystalline, non-interpenetrated material for this system.

1.3.2 Activation

Before MOFs can be used for most applications, guests must be removed from the pores of the material. This process is referred to as *activation,* a term borrowed from its use to describe the process of improving the absorptive properties of carbon or alumina. MOF activation involves two equally important steps: solvent exchange and solvent removal. Solvent exchange accomplishes removal of reaction byproducts and unreacted starting materials from the MOF pores as well as replacement of low-volatility synthesis solvent with high-volatility activation solvent, which can be more easily removed. Solvent removal is generally accomplished with vacuum and/or heat.

MOF-5

After synthesis, the MOF crystals are washed 3× with DMF, then 3× with methylene chloride (CH_2Cl_2). (Figure 1.20) DMF is used to remove metal ions, unreacted linker molecules, and other polar/charged species which have lower solubility in the less-polar CH_2Cl_2. CH_2Cl_2 is then used to displace DMF from the framework. CH_2Cl_2 is a preferable activation solvent to DMF as it has a lower boiling point (~40 °C versus ~153 °C), making it easier and quicker to evaporatively remove, as well as lower surface tension (26.5 mN m^{-1} versus 37.1 mN m^{-1}), which is associated with less destructive potential upon removal from the framework. After solvent exchange is completed, excess solvent is removed, and the MOF is placed under room temperature dynamic vacuum for ~16 hours. This process is generally sufficient to remove all activation solvent, and the MOF can then be removed from vacuum and stored under an inert atmosphere until needed.

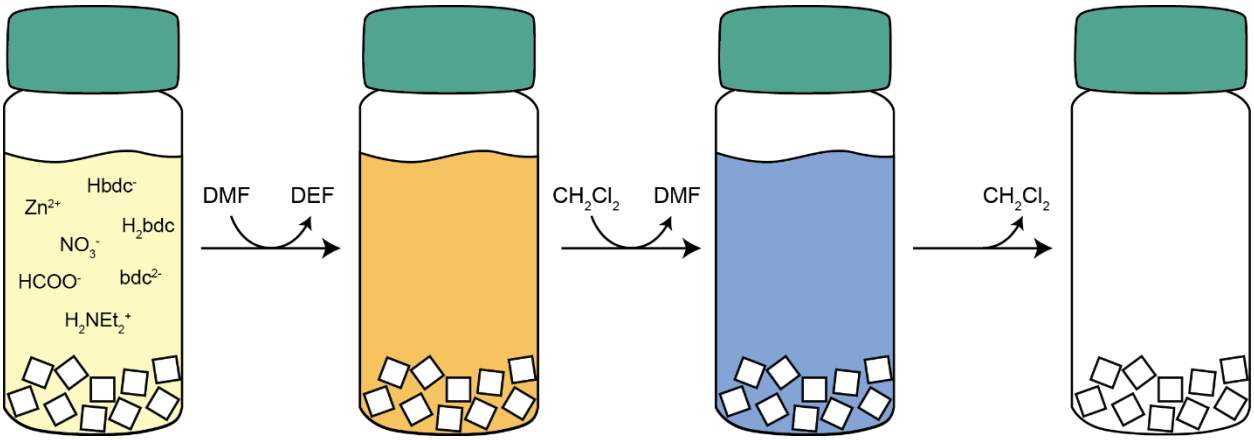

Figure 1.20. Schematic representation of the activation of MOF-5. First, the as-synthesized crystals are washed 3× with DMF, then 3× with CH_2Cl_2, followed by removal of CH_2Cl_2 under vacuum.

UiO-66

Unlike MOF-5, UiO-66 (as synthesized by most reported preparations) takes the form of a fine, microcrystalline powder. In this and similar cases, MOF can remain suspended in solvent for hours-days, preventing easy decanting of solvent during MOF washes. In such cases, filtration or

centrifugation is necessary to aggregate the MOF during solvent exchange. While filtration is sufficient for robust MOFs like UiO-66 which are highly moisture insensitive, centrifugation is a safer choice to minimize atmospheric exposure of MOFs which are less stable; centrifugation also mitigates sample loss associated with material becoming lodged in filter paper/frits. To activate UiO-66, one approach is to wash the material 3× with DMF, then 3× with EtOH, prior to overnight vacuum treatment at 150 °C.

HKUST-1

As with UiO-66, typical syntheses of HKUST-1 also yield a microcrystalline MOF, necessitating centrifugation or filtration to perform solvent exchange. Triplicate washes with DMF followed by CH_2Cl_2 are commonly performed for activation of HKUST-1, followed by overnight solvent removal under vacuum at 170 °C. For HKUST-1 synthesized in MeOH, the MOF can instead by washed using methanol alone, and activated under vacuum at 150 °C overnight.[82]

UMCM-9

UMCM-9 is similar to MOF-5 in its structure (ditopic linkers octahedrally bridging Zn_4O^{6-} clusters) but its longer linkers make the MOF more sensitive to activation. The standard MOF-5 treatment of 3× DMF washes followed by 3× with CH_2Cl_2 and overnight room temperature vacuum evacuation gives a product with roughly a quarter of the maximum surface area when applied to this MOF. Thus, even gentler methods must be used for activation of UMCM-9. One approach is to utilize supercritical CO_2 for solvent removal,[18] the best-in-class method for activation of sensitive MOFs. This activation method can be performed directly after the DMF washes. If the (relatively costly) equipment to perform supercritical CO_2 activation is not available, an alternative approach is to perform one additional solvent exchange: this time from CH_2Cl_2 to the even lower surface tension solvent hexane, from which UMCM-9 can be successfully

activated.[85] For MOFs even more sensitive than UMCM-9 (e.g. FJI-1), ultralow surface tension solvents such as perfluoropentane can be utilized.

1.4 Challenges facing adoption of MOFs

MOFs face several barriers to their widespread adoption. These include issues with stability during activation and handling, an overreliance on toxic synthesis solvents, and a lack of established protocols for generation of desirable MOF topologies and microstructures.

MOF structural damage arising during activation or handling is generally termed "MOF collapse." This phenomenon is distinct from hydrolysis (or other types of solvolysis) as it is believed to result chiefly from physical rather than chemical factors. Particularly, for activation-induced MOF collapse, the root cause is generally attributed to capillary forces imposed on the framework during solvent removal, which leads to bond breakage at the molecular scale, and loss of accessible porosity and decreased net crystallinity on the macroscopic scale.

While approaches for mitigating the damage associated with MOF activation-induced collapse have been developed and improved in recent years,[85] the process is relatively understudied, limiting further development of such methods. Furthermore, MOF collapse can also occur due to processes and procedures other than activation, for instance via application of pressure, ball milling, heating, or electrical discharge,[86] or from exposure to water,[57] but relatively little work has been done on characterizing the stability landscape for these materials.

Synthesis solvents used to create MOFs are often highly toxic and thus undesirable from a health and safety perspective. Two major approaches exist to address this problem: the use of less-harmful solvents during synthesis, and the use of no (or nearly no) solvents at all. Less-harmful solvents include alcohols (methanol, ethanol, etc.) and water, but many systems (e.g. most Zn-based MOFs) are poorly suited to synthesis in these solvents and will either generate undesired

byproducts or no products under such synthesis conditions. MOF synthesis in the absence of (or in minimal) solvent (e.g. mechanochemical syntheses, liquid-assisted grinding) is another approach to limiting the use of toxic synthesis solvents, but commonly results in lower crystallinity, lower surface area, and much smaller crystalline domains than standard solvothermal syntheses.

Many desirable MOFs cannot be directly synthesized, either because their linkers are unstable under the conditions necessary for MOF synthesis or because other phases are preferentially formed when their synthesis is attempted. An example of the former was reported by Nickerl et al. regarding their attempt to synthesize a UiO-66 derivative – UiO-66(dhtz) – based on dihydrotetrazine dicarboxylate.[87] (Figure 1.21a) In this synthetic attempt, the MOF was not formed, presumably both because the linker has poor thermal stability, and because the linker is unstable in low pH conditions (as discussed in Section 1.3.1, UiO-66 syntheses generally utilize acidic modulator species). An example of a situation where an undesired phase was generated that precluded direct synthesis of a MOF was reported by Karagiaridi et al.[88] Free carboxylate groups in MOFs have utility for catalysis, proton conductivity, and ammonia capture. In attempting to synthesize a particular MOF containing free carboxylate groups, the authors observed that the resulting phase differed in powder X-ray diffractogram peak intensity, crystal morphology, and most importantly, surface area (470 $m^2 g^{-1}$ vs. ~3000 $m^2 g^{-1}$) from what would be expected if the material possessed the desired topology. The desired phase, NU-125-HBTC, was NU-125 with a percentage of its structural linker (5,5′,5″-(4,4′,4″-(benzene-1,3,5-triyl)tris(1H-1,2,3-triazole-4,1-diyl))-triisophthalate, Figure 1.21b) replaced with trimesate linkers (Figure 1.14a) coordinating MOF metal clusters using only two of their three caboxylates. However, this phase is either not kinetically accessible during this synthesis, or it is not the thermodynamically favorable product.

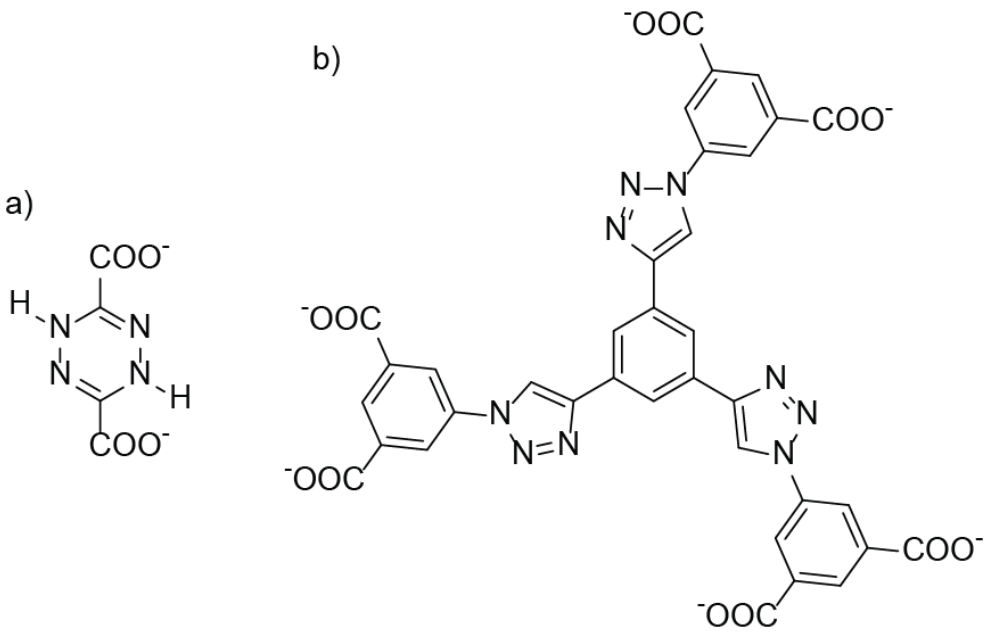

Figure 1.21. Two linkers. (a) Dihydro-1,2,4,5-tetrazine-3,6-dicarboxylate, linker in UiO-66(dhtz) and (b) 5,5′,5″-(4,4′,4″-(benzene-1,3,5-triyl)tris(1H-1,2,3-triazole-4,1-diyl))-triisophthalate, linker in NU-125.

The elusiveness of MOFs like UiO-66(dhtz) and NU-125-HBTC has prompted the development of several techniques for alteration of MOFs post-synthesis – these include chemical reactions on linkers in the MOF (post-synthetic modification) and exchange of metals and/or linkers in the MOF (post-synthetic exchange). These techniques involve incubation of a parent MOF in a solution including either the desired reagent or the species to be exchanged into the MOF. While UiO-66(dhtz) and NU-125-HBTC both resist direct synthesis, they were achieved using post-synthetic linker exchange. Depending on the relative diffusion/reaction rates of linkers during post-synthetic linker exchange, this process can also generate core–shell microstructures. This type of MOF microstructure has myriad applications (see Chapter 5), but robust methods for controlling shell thickness and extent of exchange/modification remain to be established.

1.5 Outline of thesis

This thesis concerns understanding and mitigating challenges with the wider application of MOFs. Chapter 2 describes the characterization of activation-induced MOF collapse in a series of

Zn-MOFs. Chapter 3 involves the characterization of the reverse of activation, resolvation, and the destructive potential of this process in MOF handling. Chapter 4 comprises a synthetic study demonstrating the potential of *N*,*N*-diethyl-3-methylbenzamide (DEET, the most commonly used and most effective known insect repellant) to replace toxic formamide species as a greener, safer MOF synthesis solvent. Chapter 5 contains a study regarding solvent effects on the process of MOF linker exchange. Finally, Chapter 6 summarizes the implications and connecting themes of the aforementioned Chapters, and posits future directions resulting from this research.

1.6 References

(1) Hoskins, B. F.; Robson, R. Infinite Polymeric Frameworks Consisting of Three Dimensionally Linked Rod-like Segments. *J. Am. Chem. Soc.* **1989**, 111, 5962–5964.

(2) Hoskins, B. F.; Robson, R. Design and Construction of a New Class of Scaffolding-like Materials Comprising Infinite Polymeric Frameworks of 3-D-Linked Molecular Rods - A Reappraisal of the $Zn(CN)_2$ And $Cd(CN)_2$ Structures and the Synthesis and Structure of the Diamond-Related Frameworks $N(CH_3)_4$ $Cu^{I}Zn^{II}(CN)_4$ And Cu^{I} 4,4',4'',4'''-Tetracyanotetraphenylmethane $BF_{4-x}C_6H_5NO_2$. *J. Am. Chem. Soc.* **1990**, 112, 1546–1554.

(3) Abrahams, B. F.; Hoskins, B. F.; Robson, R. A New Type of Infinite 3D Polymeric Network Containing 4-Connected, Peripherally-Linked Metalloporphyrin Building Blocks. *J. Am. Chem. Soc.* **1991**, 113, 3606–3607.

(4) Abrahams, B. F.; Hoskins, B. F.; Liu, J.; Robson, R. The Archetype for a New Class of Simple Extended 3D Honeycomb Frameworks. The Synthesis and x-Ray Crystal Structures of $Cd(CN)_{5/3}(OH)_{1/3}\cdot 1/3(C_6H_{12}N_4)$, $Cd(CN)_2\cdot 1/3(C_6H_{12}N_4)$, and $Cd(CN)_2\cdot 2/3H_2O\cdot TBuOH$ ($C_6H_{12}N_4$ = Hexamethylenetetramine) Revealing Two Topologically Equivalent but Geometrically Different Frameworks. *J. Am. Chem. Soc.* **1991**, 113, 3045–3051.

(5) Seth, S.; Matzger, A. J. Metal–Organic Frameworks: Examples, Counterexamples, and an Actionable Definition. *Cryst. Growth Des.* **2017**, 17, 4043–4048.

(6) Park, H. J.; Suh, M. P. Mixed-Ligand Metal-Organic Frameworks with Large Pores: Gas Sorption Properties and Single-Crystal-to-Single-Crystal Transformation on Guest Exchange. *Chem. Eur. J.* **2008**, 14, 8812–8821.

(7) Koh, K.; Van Oosterhout, J. D.; Roy, S.; Wong-Foy, A. G.; Matzger, A. J. Exceptional Surface Area from Coordination Copolymers Derived from Two Linear Linkers of Differing Lengths. *Chem. Sci.* **2012**, 3, 2429–2432.

(8) Farha, O. K.; Eryazici, I.; Jeong, N. C.; Hauser, B. G.; Wilmer, C. E.; Sarjeant, A. A.; Snurr, R. Q.; Nguyen, S. T.; Yazaydın, A. Ö.; Hupp, J. T. Metal–Organic Framework Materials with Ultrahigh Surface Areas: Is the Sky the Limit? *J. Am. Chem. Soc.* **2012**, 134, 15016–15021.

(9) Brunauer, S.; Emmett, P. H.; Teller, E. Adsorption of Gases in Multimolecular Layers. *J. Am. Chem. Soc.* **1938**, 60, 309–319.

(10) Walton, K. S.; Snurr, R. Q. Applicability of the BET Method for Determining Surface Areas of Microporous Metal−Organic Frameworks. *J. Am. Chem. Soc.* **2007**, 129, 8552–8556.
(11) Alslaibi, T. M.; Abustan, I.; Ahmad, M. A.; Foul, A. A. A Review: Production of Activated Carbon from Agricultural Byproducts via Conventional and Microwave Heating: Activated Carbon from Agricultural Byproducts by Conventional and Microwave Heating. *J. Chem. Technol. Biotechnol.* **2013**, 88, 1183–1190.
(12) Bae, Y.-S.; Yazaydın, A. Ö.; Snurr, R. Q. Evaluation of the BET Method for Determining Surface Areas of MOFs and Zeolites That Contain Ultra-Micropores. *Langmuir* **2010**, 26, 5475–5483.
(13) Galarneau, A.; Mehlhorn, D.; Guenneau, F.; Coasne, B.; Villemot, F.; Minoux, D.; Aquino, C.; Dath, J.-P. Specific Surface Area Determination for Microporous/Mesoporous Materials: The Case of Mesoporous FAU-Y Zeolites. *Langmuir* **2018**, 34, 14134–14142.
(14) Ahmed, A.; Seth, S.; Purewal, J.; Wong-Foy, A. G.; Veenstra, M.; Matzger, A. J.; Siegel, D. J. Exceptional Hydrogen Storage Achieved by Screening Nearly Half a Million Metal-Organic Frameworks. *Nat. Commun.* **2019**, 10, 1–9.
(15) Zhang, X.; Lin, R.; Wang, J.; Wang, B.; Liang, B.; Yildirim, T.; Zhang, J.; Zhou, W.; Chen, B. Optimization of the Pore Structures of MOFs for Record High Hydrogen Volumetric Working Capacity. *Adv. Mater.* **2020**, 32, 1907995.
(16) Li, B.; Wen, H.-M.; Zhou, W.; Xu, J. Q.; Chen, B. Porous Metal-Organic Frameworks: Promising Materials for Methane Storage. *Chem* **2016**, 1, 557–580.
(17) Prasad, T. K.; Suh, M. P. Control of Interpenetration and Gas-Sorption Properties of Metal-Organic Frameworks by a Simple Change in Ligand Design. *Chem. Eur. J.* **2012**, 18, 8673–8680.
(18) Koh, K.; Van Oosterhout, J. D.; Roy, S.; Wong-Foy, A. G.; Matzger, A. J. Exceptional Surface Area from Coordination Copolymers Derived from Two Linear Linkers of Differing Lengths. *Chem. Sci.* **2012**, 3, 2429–2432.
(19) Farha, O. K.; Yazaydın, A. Ö.; Eryazici, I.; Malliakas, C. D.; Hauser, B. G.; Kanatzidis, M. G.; Nguyen, S. T.; Snurr, R. Q.; Hupp, J. T. De Novo Synthesis of a Metal−Organic Framework Material Featuring Ultrahigh Surface Area and Gas Storage Capacities. *Nat. Chem.* **2010**, 2, 944−948.
(20) Yuan, D.; Zhao, D.; Sun, D.; Zhou, H. -C. An Isoreticular Series of Metal−Organic Frameworks with Dendritic Hexacarboxylate Ligands and Exceptionally High Gas-Uptake Capacity. *Angew. Chem. Int. Ed.* **2010**, 49, 5357−5361.
(21) Zhang, X.; Zhang, X.; Johnson, J. A.; Chen, Y. -S.; Zhang, J. Highly Porous Zirconium Metal–Organic Frameworks with β-UH_3-like Topology Based on Elongated Tetrahedral Linkers. *J. Am. Chem. Soc.* **2016**, 138, 8380−8383.
(22) Zacharia, R.; Cossement, D.; Lafi, L.; Chahine, R. Volumetric hydrogen sorption capacity of monoliths prepared by mechanical densification of MOF-177. *J. Mater. Chem.* **2010**, 20, 2145–2151.
(23) Peng, Y.; Srinivas, G.; Wilmer, C. E.; Eryazici, I.; Snurr, R. Q.; Hupp, J. T.; Yildirim, T.; Farha, O. K. Simultaneously high gravimetric and volumetric methane uptake characteristics of the metal–organic framework NU-111. *Chem. Commun.* **2013**, 49, 2992–2994.

(24) Ding, M.; Flaig, R. W.; Jiang, H.-L.; Yaghi, O. M. Carbon Capture and Conversion Using Metal–Organic Frameworks and MOF-Based Materials. *Chem. Soc. Rev.* **2019**, 48, 2783–2828.
(25) Millward, A. R.; Yaghi, O. M. Metal−Organic Frameworks with Exceptionally High Capacity for Storage of Carbon Dioxide at Room Temperature. *J. Am. Chem. Soc.* **2005**, 127, 17998–17999.
(26) Llewellyn, P. L.; Bourrelly, S.; Serre, C.; Vimont, A.; Daturi, M.; Hamon, L.; De Weireld, G.; Chang, J. S.; Hong, D. Y.; Hwang, Y. K.; Jhung, S. H. High uptakes of CO_2 and CH_4 in Mesoporous Metal–Organic Frameworks MIL-100 and MIL-101. *Langmuir* **2008**, 24, 7245–7250.
(27) Caskey, S. R.; Wong-Foy A. G.; Matzger, A. J. Dramatic Tuning of Carbon Dioxide Uptake via Metal Substitution in a Coordination Polymer with Cylindrical Pores. *J. Am. Chem. Soc.* **2008**, 130, 10870–10871.
(28) Rochelle, G. T. Amine Scrubbing for CO_2 Capture. *Science*, **2009**, 325, 1652–1654.
(29) MacDowell, N.; Florin, N.; Buchard, A.; Hallett, J.; Galindo, A.; Jackson, G.; Adjiman, C. S.; Williams, C. K.; Shah, N.; Fennell, P. An overview of CO_2 capture technologies. *Energy Environ. Sci.* **2010**, 3, 1645–1669.
(30) Couck, S.; Denayer, J. F. M.; Baron, G. V.; Rémy, T.; Gascon, J., Kapteijn, F. An Amine-Functionalized MIL-53 Metal−Organic Framework with Large Separation Power for CO_2 and CH_4. *J. Am. Chem. Soc.* **2009**, 131, 6326–6327.
(31) Yang, Q.; Wiersum, A. D.; Llewellyn, P. L.; Guillerm, V.; Serre, C.; Maurin, G. Functionalizing porous zirconium terephthalate UiO-66 (Zr) for natural gas upgrading: a computational exploration. *Chem. Commun.* **2011**, 47, 9603–9605.
(32) Kim, S. -N.; Kim, J.; Kim, H. -Y.; Cho, H. -Y.; Ahn, W. -S. Adsorption/catalytic properties of MIL-125 and NH_2-MIL-125. *Catal. Today* **2013**, 204, 85–93.
(33) Fracaroli, A. M.; Furukawa, H.; Suzuki, M.; Dodd, M.; Okajima, S.; Gándara, F.; Reimer, J. A.; Yaghi, O. M. Metal–organic frameworks with precisely designed interior for carbon dioxide capture in the presence of water. *J. Am. Chem. Soc.* **2014**, 136, 8863–8866.
(34) Gassensmith, J. J.; Furukawa, H.; Smaldone, R. A.; Forgan, R. S.; Botros, Y. Y.; Yaghi, O. M.; Stoddart, J. F. Strong and reversible binding of carbon dioxide in a green metal–organic framework. *J. Am. Chem. Soc.* **2011**, 133, 15312–15315.
(35) Smaldone, R. A.; Forgan, R. S.; Furukawa, H.; Gassensmith, J. J.; Slawin, A. M. Z.; Yaghi, O. M.; Stoddart, J. F. *Angew. Chem. Int. Ed.* **2010**, 49, 8630–8634.
(36) Wu, D.; Gassensmith, J.J.; Gouvêa, D.; Ushakov, S.; Stoddart, J.F.; Navrotsky, A. Direct Calorimetric Measurement of Enthalpy of Adsorption of Carbon Dioxide on CD-MOF-2, a Green Metal–Organic Framework. *J. Am. Chem. Soc.* **2013**, 135, 6790–6793.
(37) Cychosz, K. A.; Wong-Foy, A. G.; Matzger, A. J. Enabling Cleaner Fuels: Desulfurization by Adsorption to Microporous Coordination Polymers. *J. Am. Chem. Soc.* **2009**, 131, 14538–14543.
(38) Van de Voorde, B.; Hezinová, M.; Lannoeye, J.; Vandekerkhove, A.; Marszalek, B.; Gil, B.; Beurroies, I.; Nachtigall, P.; De Vos, D. Adsorptive Desulfurization with CPO-27/MOF-74: An Experimental and Computational Investigation. *Phys. Chem. Chem. Phys.* **2015**, 17, 10759–10766.
(39) Wang, J. -L.; Wang, C.; Lin, W. Metal–Organic Frameworks for Light Harvesting and Photocatalysis. *ACS Catal.* **2012**, 2, 2630–2640.

(40) So, M. C.; Wiederrecht, G. P.; Mondloch, J. E.; Hupp, J. T.; Farha, O. K. Metal–Organic Framework Materials for Light-Harvesting and Energy Transfer. *Chem. Commun.* **2015**, 51, 3501–3510.
(41) Foster, M. E.; Azoulay, J. D.; Wong, B. M.; Allendorf, M. D. Novel Metal–Organic Framework Linkers for Light Harvesting Applications. *Chem. Sci.* **2014**, 5, 2081–2090.
(42) Kent, C. A.; Mehl, B. P.; Ma, L.; Papanikolas, J. M.; Meyer, T. J.; Lin, W. Energy Transfer Dynamics in Metal−Organic Frameworks. *J. Am. Chem. Soc*. **2010**, 132, 12767–12769.
(43) Lee, C. Y.; Farha, O. K.; Hong, B. J.; Sarjeant, A. A.; Nguyen, S. T.; Hupp, J. T. Light-Harvesting Metal–Organic Frameworks (MOFs): Efficient Strut-to-Strut Energy Transfer in Bodipy and Porphyrin-Based MOFs. *J. Am. Chem. Soc.* **2011**, 133, 15858–15861.
(44) Jin, S.; Son, H. J.; Farha, O. K.; Wiederrecht, G. P.; Hupp, J. T. Energy Transfer from Quantum Dots to Metal–Organic Frameworks for Enhanced Light Harvesting. *J. Am. Chem. Soc*. **2013**, 135, 955–958.
(45) So, M. C.; Jin, S.; Son, H. J.; Wiederrecht, G. P.; Farha, O. K.; Hupp, J. T. Layer-by-Layer Fabrication of Oriented Porous Thin Films Based on Porphyrin-Containing Metal–Organic Frameworks. *J. Am. Chem. Soc.* **2013**, 135, 15698–15701.
(46) Sun, L.; Xing, H.; Liang, Z.; Yu, J.; Xu, R. A 4 + 4 strategy for synthesis of zeolitic metal–organic frameworks: an indium-MOF with SOD topology as a light-harvesting antenna. *Chem. Commun.* **2013**, 49, 11155–11157.
(47) Maza, W. A.; Morris, A. J. Photophysical Characterization of a Ruthenium(II) Tris(2,2′-bipyridine)-Doped Zirconium UiO-67 Metal–Organic Framework. *J. Phys. Chem. C* **2014**, 118, 8803–8817.
(48) Maza, W. A.; Ahrenholtz, S. R.; Epley, C. C.; Day, C. S.; Morris, A. J. Solvothermal Growth and Photophysical Characterization of a Ruthenium(II) Tris(2,2′-Bipyridine)-Doped Zirconium UiO-67 Metal Organic Framework Thin Film. *J. Phys. Chem. C* **2014**, 118, 14200–14210.
(49) Jiao, L.; Wang, Y.; Jiang, H.-L.; Xu, Q. Metal-Organic Frameworks as Platforms for Catalytic Applications. *Adv. Mater.* **2018**, 30, 1703663.
(50) Akiyama, G.; Matsuda, R.; Sato, H.; Takata, M.; Kitagawa, S. Cellulose Hydrolysis by a New Porous Coordination Polymer Decorated with Sulfonic Acid Functional Groups. *Adv. Mater.* **2011**, 23, 3294–3297.
(51) Zhou, Y. -X.; Chen, Y. -Z.; Hu, Y.; Huang, G.; Yu, S. -H.; Jiang, H. -L. MIL-101-SO_3H: A Highly Efficient Brønsted Acid Catalyst for Heterogeneous Alcoholysis of Epoxides under Ambient Conditions. *Chem. Eur. J.* **2014**, 20, 14976–14980.
(52) Morris, W.; Volosskiy, B.; Demir, S.; Gándara, F.; McGrier, P. L.; Furukawa, H.; Cascio, D.; Stoddart, J. F.; Yaghi, O. M. Synthesis, Structure, and Metalation of Two New Highly Porous Zirconium Metal–Organic Frameworks. *Inorg. Chem.* **2012**, 51, 6443–6445.
(53) Feng, D.; Gu, Z. -Y.; Li, J. -R.; Jiang, H. -L.; Wei, Z.; Zhou, H. -C. Zirconium-Metalloporphyrin PCN-222: Mesoporous Metal-Organic Frameworks with Ultrahigh Stability as Biomimetic Catalysts. *Angew. Chem., Int. Ed.* **2012**, 51, 10307–10310.
(54) Chen, Y.; Hoang, T.; Ma, S. Biomimetic Catalysis of a Porous Iron-Based Metal–Metalloporphyrin Framework. *Inorg. Chem.* **2012**, 51, 12600–12602.
(55) Song, F.; Wang, C.; Falkowski, J. M.; Ma, L.; Lin, W. Isoreticular Chiral Metal−Organic Frameworks for Asymmetric Alkene Epoxidation: Tuning Catalytic Activity by

Controlling Framework Catenation and Varying Open Channel Sizes. *J. Am. Chem. Soc.* **2010**, 132, 15390–15398.
(56) Falkowski, J. M.; Wang, C.; Liu, S.; Lin, W. Actuation of Asymmetric Cyclopropanation Catalysts: Reversible Single-Crystal to Single-Crystal Reduction of Metal-Organic Frameworks. *Angew. Chem. Int. Ed.* **2011**, 50, 8674–8678.
(57) Cychosz, K. A.; Matzger, A. J. Water Stability of Microporous Coordination Polymers and the Adsorption of Pharmaceuticals from Water. *Langmuir* **2010**, 26, 17198–17202.
(58) Wu, M.-X.; Yang, Y.-W. Metal-Organic Framework (MOF)-Based Drug/Cargo Delivery and Cancer Therapy. *Adv. Mater.* **2017**, 29, 1606134.
(59) Suresh, K.; Matzger, A. J. Enhanced Drug Delivery by Dissolution of Amorphous Drug Encapsulated in a Water Unstable Metal-Organic Framework (MOF). *Angew. Chem. Int. Ed.* **2019**, 58, 16790–16794.
(60) Yang, J.; Yang, Y. Metal–Organic Frameworks for Biomedical Applications. *Small* **2020**, 16, 1906846.
(61) Horcajada, P.; Serre, C.; Vallet-Regí, M.; Sebban, M.; Taulelle, F.; Férey, G. Metal–Organic Frameworks as Efficient Materials for Drug Delivery. *Angew. Chem.* **2006**, 118, 6120–6124.
(62) Horcajada, P.; Chalati, T.; Serre, C.; Gillet, B.; Sebrie, C.; Baati, T.; Eubank, J. F.; Heurtaux, D.; Clayette, P.; Kreuz, C.; Chang, J. S.; Hwang, Y. K.; Marsaud, V.; Bories, P. N.; Cynober, L.; Gil, S.; Férey, G.; Couvreur, P.; Gref, R. Porous metal-organic-framework nanoscale carriers as a potential platform for drug delivery and imaging. *Nature Mater.* **2010**, 9, 172–178.
(63) Sun, C.-Y.; Qin, C.; Wang, X. -L.; Yang, G. -S.; Shao, K. -Z.; Lan, Y. -Q.; Su, Z. -M.; Huang, P.; Wang, C. -G.; Wang, E. -B. Zeolitic imidazolate framework-8 as efficient pH-sensitive drug delivery vehicle. *Dalton Trans.* **2012**, 41, 6906–6909.
(64) Bellido, E.; Hidalgo, T.; Lozano, M.V.; Guillevic, M.; Simón-Vázquez, R.; Santander-Ortega, M.J.; González-Fernández, Á.; Serre, C.; Alonso, M.J.; Horcajada, P. Heparin-Engineered Mesoporous Iron Metal-Organic Framework Nanoparticles: Toward Stealth Drug Nanocarriers. *Adv. Healthcare Mater.* **2015**, *4*, 1246–1257.
(65) Luzuriaga, M. A.; Benjamin, C. E.; Gaertner, M. W.; Lee, H.; Herbert, F. C.; Mallick, S.; Gassensmith, J. J. ZIF-8 degrades in cell media, serum, and some—but not all—common laboratory buffers. *Supramol. Chem.* **2019**, 31, 485–490.
(66) Zhuang, J.; Kuo, C. H.; Chou, L.Y.; Liu, D. Y.; Weerapana, E.; Tsung, C. K. Optimized Metal–Organic-Framework Nanospheres for Drug Delivery: Evaluation of Small-Molecule Encapsulation. *ACS Nano* **2014**, 8, 3, 2812–2819.
(67) Zheng, H.; Zhang, Y.; Liu, L.; Wan, W.; Guo, P.; Nyström, A. M.; Zou, X. One-pot Synthesis of Metal–Organic Frameworks with Encapsulated Target Molecules and Their Applications for Controlled Drug Delivery. *J. Am. Chem. Soc.* **2016**, 138, 962–968.
(68) Eddaoudi, M.; Li, H.; Yaghi, O. M. Highly Porous and Stable Metal−Organic Frameworks: Structure Design and Sorption Properties. *J. Am. Chem. Soc.* **2000**, 122, 1391–1397.
(69) Tranchemontagne, D. J.; Mendoza-Cortes, J. L.; O'Keeffe, M.; Yaghi, O. M. Secondary building units, nets and bonding in the chemistry of metal–organic frameworks. *Chem. Soc. Rev.* **2009**, 38, 1257–1283.
(70) Long, J. R.; Yaghi, O. M. The pervasive chemistry of metal–organic frameworks. *Chem. Soc. Rev.* **2009**, 38, 1213–1214.

(71) Kaye, S. S.; Dailly, A.; Yaghi, O. M.; Long, J. R. Impact of Preparation and Handling on the Hydrogen Storage Properties of Zn_4O(1,4-benzenedicarboxylate)$_3$ (MOF-5). *J. Am. Chem. Soc.* **2007**, 129, 14176–14177.
(72) Zhang, Z.; Zaworotko, M. J. Template-directed synthesis of metal–organic materials. *Chem. Soc. Rev*. **2014**, 43, 5444–5455.
(73) Chen, B.; Wang, X.; Zhang, Q.; Xi, X.; Cai, J.; Qi, H.; Shiand S.; Wang, J. Synthesis and characterization of the interpenetrated MOF-5. *J. Mater. Chem*. **2010**, 20, 3758–3767.
(74) Kim, H.; Das, S.; Kim, M. G.; Dybtsev, D. N.; Kim, Y.; Kim, K. Synthesis of Phase-Pure Interpenetrated MOF-5 and Its Gas Sorption Properties. *Inorg. Chem*. **2011**, 50, 3691–3696.
(75) Katz, M. J.; Brown, Z. J.; Colon, Y. J.; Siu, P. W.; Scheidt, K. A.; Snurr, R. Q.; Hupp, J. T.; Farha, O. K. A facile synthesis of UiO-66, UiO-67 and their derivatives. *Chem. Commun.* **2013**, 49, 9449–9451.
(76) Hu, Z.; Castano, I.; Wang, S.; Wang, Y.; Peng, Y.; Qian, Y.; Chi, C.; Wang, X.; Zhao, D. Modulator Effects on the Water-Based Synthesis of Zr/Hf Metal-Organic Frameworks: Quantitative Relationship Studies between Modulator, Synthetic Condition, and Performance. *Cryst. Growth Des*. **2016**, 16, 2295–2301.
(77) Atzori, C.; Shearer, G.C.; Maschio, L.; Civalleri, B.; Bonino, F.; Lamberti, C.; Svelle, S.; Lillerud, K.P.; Bordiga, S. Effect of Benzoic Acid as a Modulator in the Structure of UiO-66: An Experimental and Computational Study. *J. Phys. Chem. C* **2017**, 121, 9312–9324.
(78) Morris, W.; Wang, S.; Cho, D.; Auyeung, E.; Li, P.; Farha, O.K.; Mirkin, C.A. Role of Modulators in Controlling the Colloidal Stability and Polydispersity of the UiO-66 Metal–Organic Framework. *ACS Appl. Mater. Interfaces* **2017**, 9, 33413–33418.
(79) Vermoortele, F.; Bueken, B.; Le Bars, G.; Van de Voorde, B.; Vandichel, M.; Houthoofd, K.; Vimont, A.; Daturi, M.; Waroquier, M.; Van Speybroeck, V.; Kirschhock, C. Synthesis Modulation as a Tool to Increase the Catalytic Activity of Metal–Organic Frameworks: The Unique Case of UiO-66(Zr). *J. Am. Chem. Soc.* **2013**, 135, 11465–11468.
(80) Rowsell, J. L. C.; Yaghi, O. M. Effects of Functionalization, Catenation, and Variation of the Metal Oxide and Organic Linking Units on the Low-Pressure Hydrogen Adsorption Properties of Metal−Organic Frameworks. *J. Am. Chem. Soc.* **2006**, 128, 1304–1315
(81) Bhunia, M. K.; Hughes, J. T.; Fettinger, J. C.; Navrotsky, A. Thermochemistry of paddle wheel MOFs: Cu-HKUST-1 and Zn-HKUST-1. *Langmuir* **2013**, 29, 8140–8145.
(82) Elsaidi, S. K.; Ongari, D.; Xu, W.; Mohamed, M. H.; Haranczyk, M.; Thallapally, P. K. Xenon recovery at room temperature using metal-organic frameworks. *Chem. Eur. J.* **2017**, 23, 10758–10762.
(83) Eddaoudi, M.; Kim, J.; Rosi, N.; Vodak, D.; Wachter, J.; O'Keeffe, M.; Yaghi, O.M. Systematic design of pore size and functionality in isoreticular MOFs and their application in methane storage. *Science* **2002**, 295, 469–472.
(84) Feldblyum, J. I.; Wong-Foy, A. G.; Matzger, A. J. Non-interpenetrated IRMOF-8: synthesis, activation, and gas sorption. *Chem. Commun.* **2012**, 48, 9828–9830.
(85) Ma, J.; Kalenak, A. P.; Wong-Foy, A. G.; Matzger, A. J. Rapid Guest Exchange and Ultra-Low Surface Tension Solvents Optimize Metal-Organic Framework Activation. *Angew. Chem. Int. Ed.* **2017**, 56, 14618–14621.
(86) Bennett, T. D.; Cheetham, A. K. Amorphous Metal−Organic Frameworks. *Acc. Chem. Res*. **2014**, 47, 1555–1562.

(87) Nickerl, G.; Senkovska, I.; Kaskel, S. Tetrazine functionalized zirconium MOF as an optical sensor for oxidizing gases. *Chem. Commun.* **2015**, 51, 2280–2282.
(88) Karagiaridi, O.; Vermeulen, N. A.; Klet, R. C.; Wang, T. C.; Moghadam, P. Z.; Al-Juaid, S. S.; Stoddart, J. F.; Hupp, J. T.; Farha, O. K. Functionalized Defects through Solvent-Assisted Linker Exchange: Synthesis, Characterization, and Partial Postsynthesis Elaboration of a Metal-Organic Framework Containing Free Carboxylic Acid Moieties. *Inorg. Chem.* **2015,** 54, 1785–1790.

Chapter 2. The Metal–Organic Framework Collapse Continuum: Insights from Two-Dimensional Powder X-ray Diffraction*

2.1 Introduction

Metal-organic frameworks (MOFs) are a class of crystalline polymers comprising metal ions or clusters bridged by organic linkers.[1] These materials often boast high specific surface areas and exceptional modularity, allowing tuning of their properties by choice of metal and linker. MOFs have demonstrated potential for use in areas including gas storage,[2–4] separations,[5] catalysis,[6] sensing,[7] drug delivery,[8] light harvesting,[9] and energetic materials.[10] One complication in bringing these materials to market is that many MOFs that have been produced experimentally, and are projected to have excellent properties, do not achieve their full potential due to the phenomenon of framework collapse.[11]

MOFs are generally synthesized solvothermally in polar, high boiling point solvents such as *N*,*N*-diethylformamide or *N*,*N*-dimethylformamide. To access the high porosity and internal surface area of MOFs, it is necessary to remove solvent and other guests from their pores through a process referred to as activation. To facilitate this process, synthesis solvent is generally exchanged with easily removed, low polarity solvents such as CH_2Cl_2 or $CHCl_3$ prior to evacuation (Figure 2.1).[12] For certain types of MOFs, this activation approach yields products with lower-than-predicted surface areas and relatively broadened powder X-ray diffraction (PXRD) peaks.

* Adapted from Dodson, R.A.; Wong-Foy, A.G.; Matzger, A.J. *Chem. Mater.* **2018**, *30*, 6559-6565.

This peak broadening indicates decreased framework crystallinity, and the phenomenon is generally referred to as MOF/pore collapse.[13]

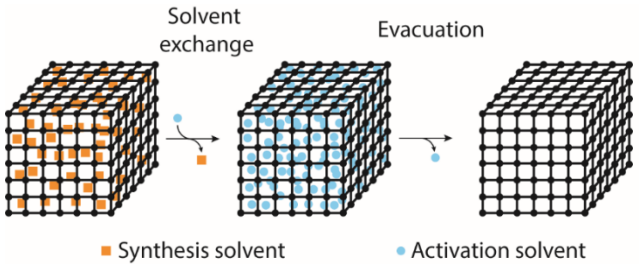

Figure 2.1. Generalized procedure for MOF activation involving solvent exchange and evacuation.

MOF collapse during activation is poorly understood, and is generally visualized as complete or partial loss of crystallinity due to forces imposed on the framework during solvent removal.[13] The structural damage may occur at any stage during the removal of activation solvent, or it may happen during the process of solvent exchange. Because the majority of applications for MOFs rely on their high internal surface areas, it is vital to understand the factors that lead to MOF collapse as well as the structures of the resulting products. It is generally observed that MOFs with longer,[14] flexible[15] linkers are more prone to collapse than are MOFs with shorter rigid linkers. In addition to this structural factor, MOF collapse has been correlated with higher surface tension activation solvents.[13] One route for solvent removal from difficult-to-activate MOFs is treatment with supercritical CO_2 ($scCO_2$) in batch[16,17] or flowing modes;[18] however, this technique requires specialized equipment and can be problematic for large-scale syntheses. Recent work has shown that ultralow surface tension solvents such as hexane and perfluoropentane can match the performance of the $scCO_2$ method for activation of fragile MOFs.[19] While techniques for MOF activation are still being developed and optimized, little is known regarding the process of MOF pore collapse during activation.

There are several possible physical explanations that could account for broadened PXRD peaks and low surface areas in MOFs post-activation (Figure 2.2). One commonly cited cause for low MOF product surface areas is incomplete removal of solvent or other guests from MOF pores. This would be sufficient to explain low surface area, but would be expected to have no effect on MOF crystallinity. Another common explanation for the symptoms of MOF collapse is capillary forces leading to full or partial loss of structural integrity, accompanied by formation of a new, often amorphous, phase. In this scenario, PXRD peaks should show 2θ-axis broadening, along with a decrease of measurable surface area. A final scenario for MOF collapse is the loss of surface porosity with retention of bulk crystallinity during solvent removal, as with the activations of zinc paddlewheel-based MOFs such as Zn-HKUST-1[20,21] and SDU-1,[22] as well as other systems such as the Cd-based MOF IFP-6.[23] This would cause no substantial change in the PXRD pattern but would lead to a loss of measurable surface area. Of course, these mechanisms need not act in isolation, and so, for a given material, all three mechanisms may contribute, resulting in suboptimal activation.

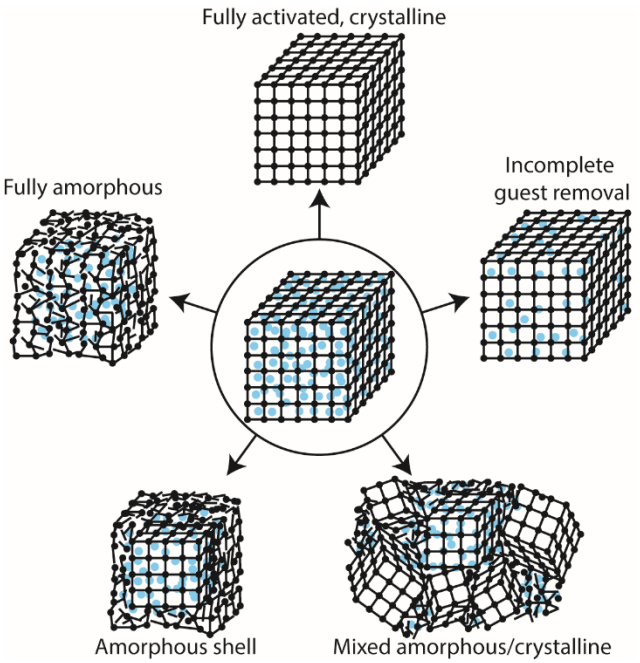

Figure 2.2. Possible outcomes of solvated MOF activation (center). Clockwise, starting from top: successful activation, incomplete removal of guests, formation of mixed amorphous/crystalline phase, formation of amorphous shell with retention of internal crystallinity, formation of a fully amorphous phase.

PXRD has been used previously to monitor structural changes in MOFs. Specifically, *in-situ* PXRD has been used to study MOF syntheses in both solvothermal[24,25] and mechanochemical[26–28] conditions, to characterize structural changes arising from high pressures,[29,30] and to determine mechanisms of guest adsorption.[31,32] These studies have generally focused on PXRD peak changes with respect to the 2Θ-axis. Herein, we have utilized *in-situ* two-dimensional powder X-ray diffraction (2D-PXRD) to probe the nature of MOF collapse by monitoring the activation of a series of MOFs based on the well-studied Zn_4O cluster. 2D-PXRD was chosen to study MOF collapse because the technique offers complementary information about both sample crystallinity and sample orientation. Specifically, in addition to the standard 2Θ-axis, which relates to lattice plane spacing, 2D-PXRD data is also separated along a second axis, herein referred to as the β-axis (γ-axis in some publications) (Figure 2.3). A sample composed primarily of single crystals with minimal internal strain and relatively few defects diffracts X-rays to give

2D-PXRD spots with narrow widths in both the 2Θ- and β-axes. Crystalline samples with more disorder, in the form of higher strain or a greater number of defects, give rise to PXRD peaks which are broader along the 2Θ-axis, as do samples with decreased long-ranged order due to extremely small particle sizes (i.e. Scherrer broadening). For an amorphous sample lacking long-range order, 2Θ-axis peak broadening occurs such that characteristic lattice spacings in the material are obscured. If a single-crystalline sample is broken up into smaller crystallites that retain their original orientation, no changes would be observed along the β-axis. However, if some portion of the crystallites moved or were deflected from their original orientation during this process, the 2D-PXRD peaks would broaden along the β-axis to cover a wider arc along the diffraction cone. In the extreme case, the entire arc would be evenly covered, indicating a complete loss of sample preferred orientation. Thus, while the 2Θ-axis gives information about crystallite size, strain, and defect character, the β-axis gives information about crystallite orientation.

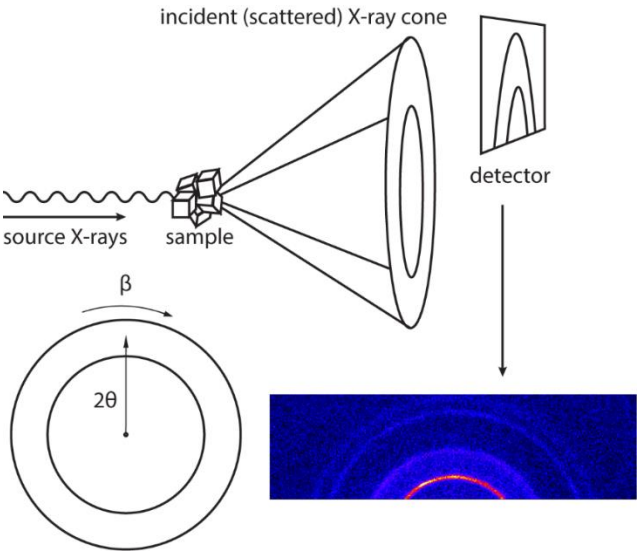

Figure 2.3. Schematic depiction of two-dimensional powder X-ray diffraction (2D-PXRD) and example 2D powder X-ray diffractogram. β- and 2Θ-axes are shown in the bottom left.

2.2 Experimental details

MOFs were synthesized using previously reported procedures.[33–35] MOF samples were loaded into 1 mm diameter Kapton capillaries and crushed to ensure an adequate particle sampling population, giving an average apparent particle diameter of ~25 μm (3.77 to 92.05 μm, see SI for more detailed discussion). Once loaded, capillaries were mounted inside a Rigaku SmartLab X-ray diffractometer operating in point focus mode outfitted with a Pilatus 2D detector. The samples were evacuated from atmospheric to full vacuum (<0.1 Torr) at a constant ramp rate of 750 Torr h^{-1} using a JKEM Digital Vacuum Regulator (Model 200). PXRD patterns were monitored *in-situ* over the course of the activation in transmission geometry using Cu K_α radiation between 3-12° 2Θ, with 5-minute exposure times.

2.3 Results and Discussion

Three activation solvents and three MOF systems were examined. The solvents used were CH_2Cl_2, tetrahydrofuran (THF), and hexane. CH_2Cl_2 (dipole moment: 1.6 D, surface tension: 28.2

mN m^{-1} at 25 °C)[36] is a common solvent for MOF activation due to its low boiling point and high vapor pressure; it is unsuitable for the activation of some MOFs but succeeds often. THF is not commonly used for MOF activation, but it has a similar dipole moment (1.75 D) and surface tension (26.4 mN m^{-1} at 25 °C) to CH_2Cl_2, which may cause it to behave similarly in the activation of MOFs. However, as an ether, THF may have stronger coordinating interactions with the MOF metal nodes than CH_2Cl_2, potentially causing more damage to the framework upon removal. THF is also much less electron-dense than CH_2Cl_2, making it more transparent to X-rays and facilitating its use in *in-situ* MOF activation PXRD studies. Hexane (dipole moment: 0 D, surface tension: 17.9 mN m^{-1} at 25 °C) has recently shown promise as an activation solvent for MOFs not amenable to activation from CH_2Cl_2.[19] The MOFs chosen for study were MOF-5, UMCM-9, and SNU-70 (Figure 2.4). Each of these MOFs contain Zn_4O metal clusters that bind linear linkers in an octahedral fashion to form cubic frameworks. As the metal clusters and resultant coordination geometries are consistent throughout this series of MOFs, any observed disparities in activation behavior can be attributed to the choice of linker. MOF-5 contains 1,4-benzenedicarboxylate as its linker and gives full surface area upon activation from commonly used activation solvents. UMCM-9 is a mixed-linker MOF composed of 2,6-napthalenedicarboxylate and 4,4'-biphenyldicarboxylate, and it requires the use of solvents with very low surface tension for activation.[35] SNU-70 is formed from 4-(2-carboxyvinyl)benzoic acid, which can adopt different relative orientation angles of its coordinating carboxylates, imposing more stringent restrictions still on its activation conditions; the only successful reported procedure for activation of SNU-70 to date is $scCO_2$ treatment.[34]

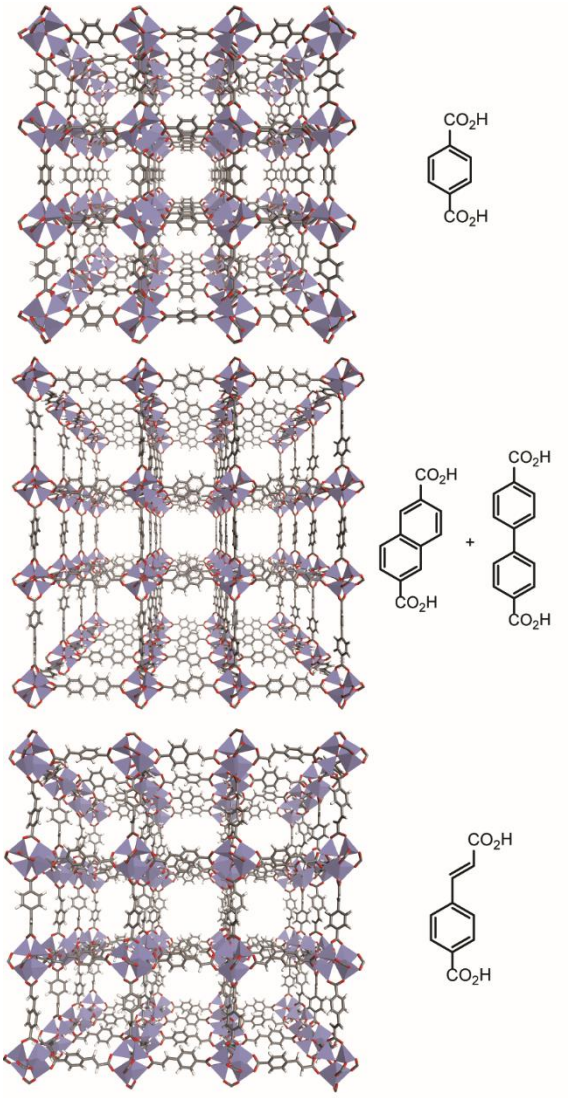

Figure 2.4. MOF structures and the corresponding dicarboxylic acids from which they are derived. Top: MOF-5, benzenedicarboxylic acid. Center: UMCM-9, 2,6-napthalenedicarboxylic acid and 4,4'-biphenyldicarboxylic acid. Bottom: SNU-70, 4-(2-carboxyvinyl)benzoic acid. Each framework also contains Zn_4O nodes.

Based on the 2D-PXRD studies, MOF activations can be divided into three broad categories: entirely successful activations which preserved sample monocrystallinity, entirely unsuccessful activations which resulted in fully amorphous products, and partially successful activations which imposed structural damage without full loss of sample crystallinity. Of the MOF/solvent combinations studied here, MOF-5/CH_2Cl_2, MOF-5/hexane, MOF-5/THF, and

UMCM-9/hexane were deemed successful, with 2D powder X-ray diffractograms for a representative experiment (MOF-5 activation from hexane) shown in Figure 2.5. Sample evacuation progress as monitored by pressure in Torr is given in the upper left of each diffractogram. The intersection of each 2Θ arc with the edge of the diffractogram is displayed in the bottom right axis. These intersections are identical in every 2D pattern shown. Successful activations are characterized by retention of distinct spots in the 2D powder X-ray diffractograms, indicating that monocrystalline domains in the sample are preserved during the solvent removal process. These activation conditions also result in MOF samples achieving their predicted BET surface areas (Table 2.1). This retention of full surface area confirms that the crystalline framework is empty and accessible to guest molecules.

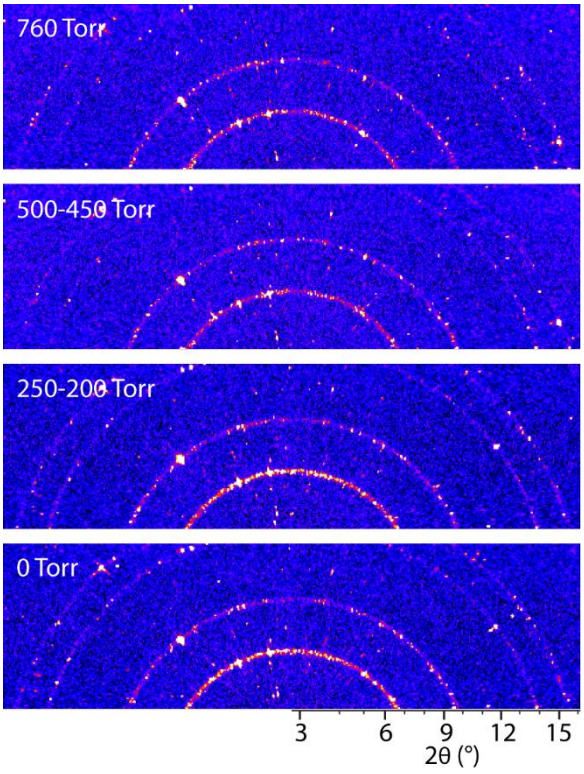

Figure 2.5. 2D-PXRD images collected from MOF-5 during the course of activation from hexane. Changes in spot positions between frames are mainly consistent with sample reorientation during solvent removal rather than with changes in crystallinity.*

Table 2.1. Surface area measurements of products from each MOF activation (all in $m^2\ g^{-1}$).

solvent	MOF-5	UMCM-9	SNU-70
CH_2Cl_2	3191	1383	113.1
THF	3256	21.33	37.87
Hexane	3682	5170	5306

Three MOF-solvent pairs gave unsuccessful activations: UMCM-9/THF, SNU-70/THF, and SNU-70/CH_2Cl_2. A representative set of diffractograms for this category (activation of SNU-70 from THF) is presented in Figure 2.6. These activation procedures result in complete loss of

* Throughout this chapter, "0 Torr" refers to the vacuum regulator setpoint rather than the physical pressure. Actual pressure at this setpoint corresponds to <0.1 Torr.

crystallinity as measured by 2D-PXRD; spots visible prior to the solvent removal, which prove that extensive structural collapse does not occur upon solvent exchange, were found to disappear entirely after removal of the solvent. To the extent that arcs are visible in the 2D diffractograms, they are extremely broadened along the 2Θ-axis with very low intensity, consistent with an amorphous product. In addition to this loss of crystallinity, the resulting products are characterized by very low (~20-100 m^2/g) surface area values. These observations, together, indicate that the sample is no longer crystalline, and that the resulting amorphous product either has diminished porosity or that it contains pores that are restricted so as to prohibit gas entry.

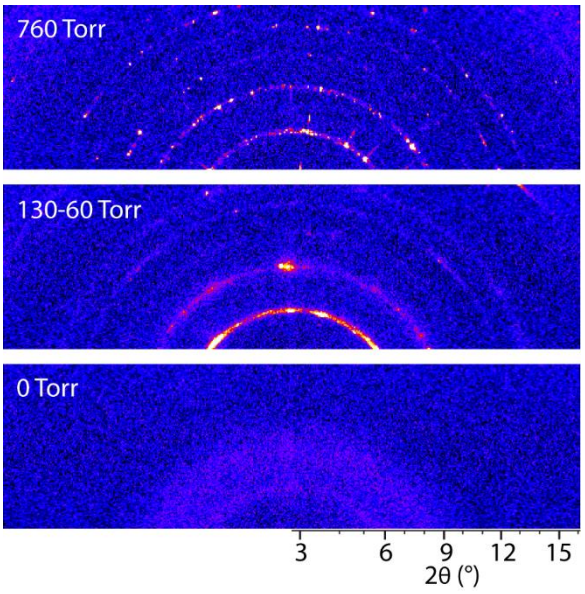

Figure 2.6. 2D-PXRD images collected from SNU-70 during the course of activation from THF. The disappearance of X-ray signal after complete application of vacuum indicates complete loss of crystallinity.

While fully successful and unsuccessful activations are useful for determining best- and worst-case scenarios for solvent removal, the "moderately successful" category offers the most insight into the process of MOF collapse. The two MOF/solvent pairs with moderate activation success are UMCM-9/ CH_2Cl_2 and SNU-70/hexane. 2D powder X-ray diffractograms taken of UMCM-9 activated from CH_2Cl_2 show significant peak broadening along both the 2Θ- and β-axes

(Figure 2.7). At the start of the UMCM-9/CH_2Cl_2 activation, no PXRD spots are observed, due to X-ray attenuation by CH_2Cl_2; however, spots are visible after the majority of bulk CH_2Cl_2 has evaporated (~250-190 Torr), again indicating that sample crystallinity is maintained while the MOF is solvated. Streaks are observed after complete evacuation, indicating that the collapse event occurs while solvent within the MOF pores is removed. These streaks are not uniform across the visible β-axis arc, which shows that crystallites in the resulting MOF product retain some degree of their orientation.

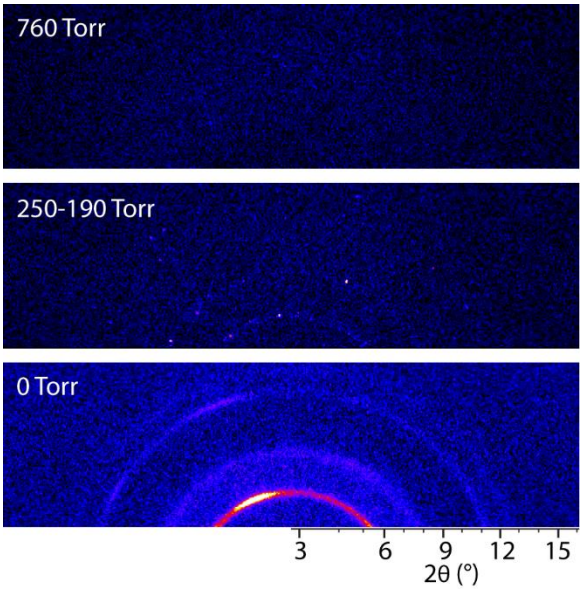

Figure 2.7. 2D-PXRD images collected from UMCM-9 during the course of activation from CH_2Cl_2. No signal is discernable in the first frame (760 Torr) due to attenuation of X-rays by CH_2Cl_2. The presence of spotty X-ray signal in the 250-190 Torr scan indicates that crystallinity is maintained in the sample until solvent is evacuated.

SNU-70 activated from hexane was also found to retain some crystallite orientation: while the spots in its 2D-PXRD pattern broaden along the β-axis, they do not become rings with homogeneous intensities (Figure 2.8). The SNU-70/hexane activation product undergoes less β-axis broadening than does the UMCM-9/CH_2Cl_2 product, indicating that the crystallites are more similarly oriented relative to the starting material. In addition, SNU-70/hexane shows better

retention of higher 2Θ-axis peaks, which significantly decrease in intensity and increase in width in UMCM-9/CH_2Cl_2. This suggests that short-range order is better maintained in SNU-70/hexane, consistent with a more successful activation (vide infra).

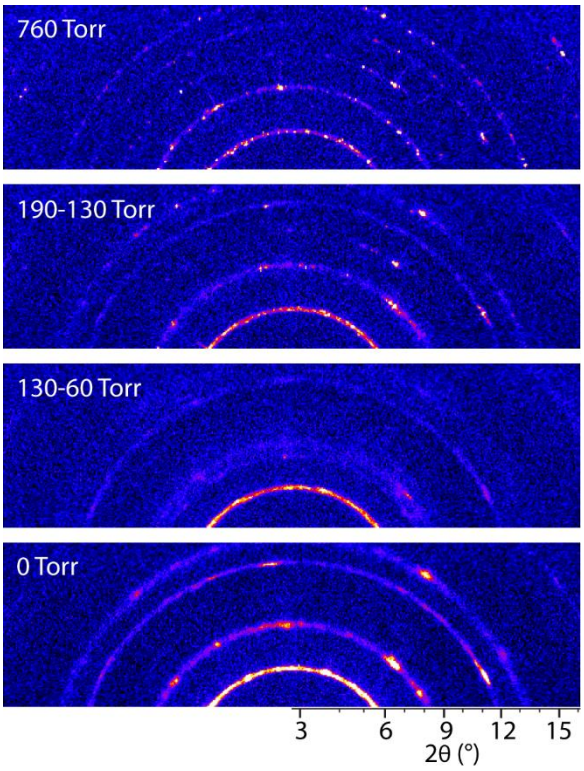

Figure 2.8. 2D-PXRD images collected from SNU-70 during the course of activation from hexane. Broadening in both the 2Θ- and β-axes is observed, but the sample maintains some crystallite orientation after the activation.

While each of the fully successful activations gives products with full calculated surface area, and each of the unsuccessful activations gives products with negligible surface area, the two "moderately successful" activations differ in their ability to achieve full surface area. The product of the activation of UMCM-9 from CH_2Cl_2 was measured to have approximately 25% of the expected surface area, as reported previously.[19] However, the SNU-70/hexane activation yields a product with surface area on-par with that resulting from $scCO_2$ activation. These surface area

values combined with 2D-PXRD data yield insight into the products of each of these activations. The relatively greater loss of surface area in UMCM-9/CH_2Cl_2 combined with the almost-complete loss of texture in the PXRD pattern suggests that some degree of amorphization occurs, as in the unsuccessful activations, but that distinct crystalline regions exist in sufficient quantities to afford a product with accessible porosity. The increasing peak spread along the β-axis indicates reorientation of the remaining crystallites, demonstrating that crystalline domains are no longer oriented and are likely separated by amorphous regions. By contrast, in the case of SNU-70/hexane, retention of the full surface area suggests no loss in total sample crystallinity; however, the 2Θ- and β-axis broadening indicate that the single-crystalline domains originally present in the sample are disrupted. In particular, it is likely that cracks form within the MOF crystals causing only slight deflection of adjacent domains. This process appears to be disruptive on the molecular level, as evidenced by 2Θ-axis peak broadening, consistent with strain and/or extremely small crystallite domains. In addition, these cracks would effectively increase the number of crystallite orientations in the sample, causing some degree of β-axis broadening while retaining the net orientation of the original sample.

With knowledge of the accessible surface areas, crystallinities, and mosaicities of each MOF activation product, their respective final structures and activation efficacies can be assigned (Figure 2.9). Each of the unsuccessful activations (SNU-70/THF, SNU-70/CH_2Cl_2, UMCM-9/THF) gives an amorphous product, and each of the successful activations (MOF-5/CH_2Cl_2, MOF-5/THF, MOF-5/hexane, UMCM-9/hexane) gives a product which retains its monocrystallinity. Activation of UMCM-9 from CH_2Cl_2 gives a polycrystalline product with partial amorphous character, which retains some preferred orientation from the original crystalline

sample. Activation of SNU-70 from hexane gives a polycrystalline product with no observable amorphous character and high retention of crystallite orientation.

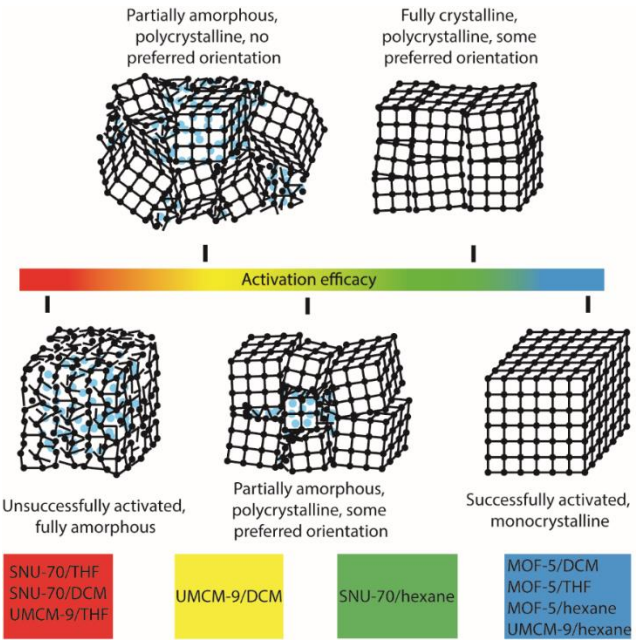

Figure 2.9. Ranked MOF activation efficacies with illustrations of each product.

2.4 Conclusions

By monitoring the activation of a series of Zn_4O-based MOFs using *in-situ* 2D-PXRD, a number of insights into the MOF activation process were made. It was found that when collapse occurred during activation, it always took place during solvent evacuation rather than during solvent exchange. It was also shown that it is possible to drastically decrease the crystallite size of MOFs during solvent removal with no detriment to the bulk surface area of the sample. This phenomenon is expected to enhance the rate of guest transport throughout MOFs and warrants further exploration. Another notable finding is that 2Θ-axis broadening of MOF PXRD peaks can be uncorrelated with amorphization and collapse; SNU-70/hexane retains full surface area, but shows broadened PXRD peaks. Without considering the effect of crystallite size on 2Θ-axis peak broadness, PXRD data in the absence of surface area measurements might have been taken to

imply that the activated MOF was of poor quality. Finally, in this set of samples, it is observed that preservation of crystallite orientation, as judged by modest broadening along the β-axis, is correlated with retention of surface area. From this observation, we have developed a scale to describe possible outcomes for MOF activation and collapse, depending on success of activation, onto which additional MOF/solvent pairs can be placed depending on changes seen using 2D-PXRD. The generality of these conclusions is now being probed across a broader class of structural types.

2.5 Supporting Information

2.5.1 Reagents

Zinc nitrate hexahydrate (Fisher Scientific, ACS grade), 1,4-benzenedicarboxylic acid (H_2BDC, Fisher Scientific, 98%), 2,6-naphthalenedicarboxylic acid (H_2NDC, TCI America, 98%), 4,4'-biphenyldicarboxylic acid (H_2BPDC, Acros Organics, 98%), 4-(2-carboxyvinyl)benzoic acid (Ark Pharm, Inc, 95+%), *N*-methyl-2-pyrrolidone (NMP, Fisher Scientific, Laboratory grade) were used as received. *N*,*N*-Dimethylformamide (DMF, Fisher Scientific, 99.5%), dichloromethane (CH_2Cl_2, Fisher scientific, HPLC grade), tetrahydrofuran (THF, Fisher Scientific, HPLC grade), hexane (Fisher Scientific, Anhydrous) were stored over activated 4 Å molecular sieves to minimize water content. The dryness of these solvents was verified by Karl Fischer titration (0.5-2 ppm H_2O). *N*,*N*-Diethylformamide (DEF, TCI America, >99.0%) was purified by storage on activated charcoal for ~1 month followed by removal of impurities via silica gel column.

2.5.2 Syntheses

Each MOF synthesis was preceded by dissolution of reagents by sonication and was carried out in a 20 mL scintillation vial sealed with a PTFE-lined cap, and the washing procedures for each MOF were identical. The as-synthesized crystals were removed from the reaction vial and washed with DMF (3 × 10 mL) and then washed (3 × 10 mL) with the desired activation solvent. In the case of hexane, the crystals were first exchanged into CH_2Cl_2 due to the immiscibility of hexane and DMF. Procedures specific to individual MOFs are included below:

Synthesis of MOF-5. H_2BDC (66.7 mg, 0.401 mmol) and $Zn(NO_2)_3 \cdot 6H_2O$ (357 mg, 1.20 mmol) were dissolved in DEF (10 mL). The reaction was performed at 100 °C for 24 hours.

Synthesis of UMCM-9. H_2NDC (28.7 mg, 0.132 mmol), H_2BPDC (35.6 mg, 0.147 mmol), and $Zn(NO_2)_3 \cdot 6H_2O$ (238 mg, 0.798 mmol) were dissolved in DEF (6.7 mL) and NMP (13.3 mL). The reaction was performed at 85 °C for 7 days.

Synthesis of SNU-70. 4-(2-carboxyvinyl)benzoic acid (14.4 mg, 0.075 mmol) and $Zn(NO_2)_3 \cdot 6H_2O$ (29.7 mg, 0.10 mmol) were dissolved in DEF (5 mL). The reaction was performed at 105 °C for 12 hours.

2.5.3 Experimental details

Due to the height error associated with sample-filled 1 mm capillaries, data were refined prior to analysis by adjusting the beam center position such that the primary peak (corresponding to the 200 reflection) aligned with the known value for each MOF. This correction was applied uniformly across each experiment to ensure that any peak shifts would be apparent. The samples were evacuated from atmospheric to full vacuum (<0.1 Torr) at a constant ramp rate of 750 Torr $hour^{-1}$ using a JKEM Digital Vacuum Regulator (Model 200). PXRD patterns were monitored *in-situ* over the course of the activation in transmission geometry using Cu K_α radiation between 3-

12° 2Θ, with 5-minute exposure times. Sample surface area was calculated using the BET method from N_2 sorption isotherms measured on a Quantachrome Autosorb iQ2 gas sorption analyzer.

2.5.4 Particle size determination

To obtain an estimate for the limit of the particle sizes observed in these studies, mapping microscopy was utilized. A capillary of the same type used for the PXRD studies was filled with SNU-70 (which contains the smallest apparent crystallites of the three MOFs studied here) in hexane, crushed in the same fashion as performed prior to each PXRD study, evacuated, then emptied onto a glass slide. Using a Leica DM2500 optical microscope outfitted with a QImaging QIClick CCD camera, a sample of the particles were imaged. Particles statistics were subsequently measured using Image Pro Premier 3D 9.3. A total of 295 particles were considered, with mean diameters ranging from 3.77 to 92.05 μm, an average mean diameter of 25.11 μm, and a standard deviation of 19.52 μm. These particle sizes should not be taken to be representative of crystallite or coherent domain sizes, but instead provide a limit on the scale of these values.

2.5.5 Additional Figures

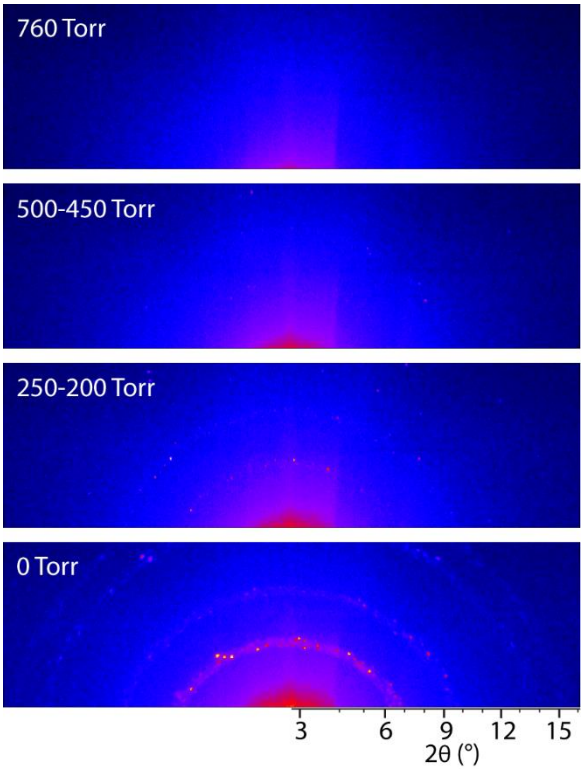

Figure 2.10. 2D-PXRD images collected from MOF-5 during the course of activation from CH_2Cl_2. Sample evacuation progress as monitored by pressure in Torr is given in the upper left of each diffractogram. The intersection of each 2Θ arc with the edge of the diffractogram is displayed in the bottom right axis. These intersections are identical in every 2D pattern shown. Lack of appreciable signal in the first two diffractograms is attributed to X-ray attenuation by CH_2Cl_2, rather than lack of sample crystallinity. After evacuation of the majority of CH_2Cl_2, small diffraction spots are observed, consistent with high retention

of sample crystallinity. The flat cutoffs in X-ray intensity seen in each diffractogram are due to interference by the house-made capillary holder apparatus rather than the sample itself.

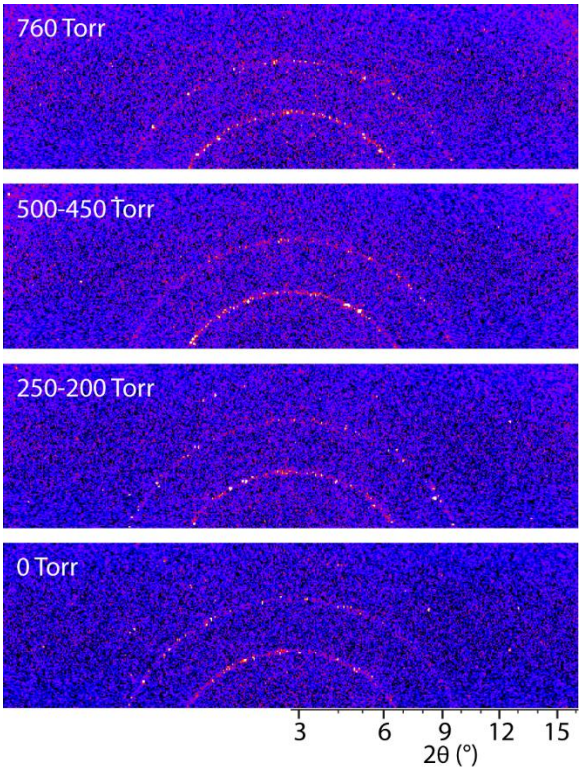

Figure 2.11. 2D-PXRD images collected from MOF-5 during the course of activation from hexane. Sample evacuation progress as monitored by pressure in Torr is given in the upper left of each diffractogram. The intersection of each 2Θ arc with the edge of the diffractogram is displayed in the bottom right axis. These

intersections are identical in every 2D pattern shown. Changes in spot positions between frames are mainly consistent with sample reorientation during solvent removal rather than with changes in crystallinity.

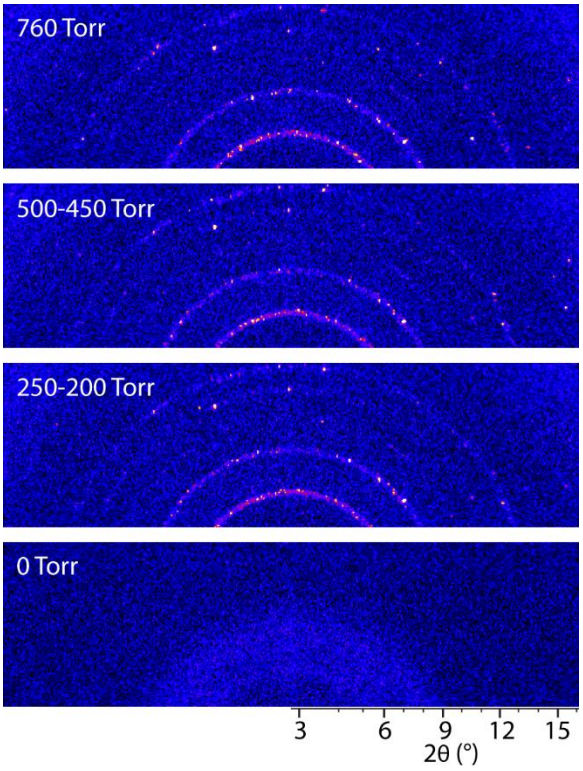

Figure 2.12. 2D-PXRD images collected from UMCM-9 during the course of activation from THF. Sample evacuation progress as monitored by pressure in Torr is given in the upper left of each diffractogram. The intersection of each 2Θ arc with the edge of the diffractogram is displayed in the bottom right axis. These intersections are identical in every 2D pattern shown. While distinct spots are observed while the sample is

solvated, complete loss of distinct spots is observed after evacuation is complete. This further demonstrates that evacuation, rather than solvent exchange, is responsible for collapse in this system.

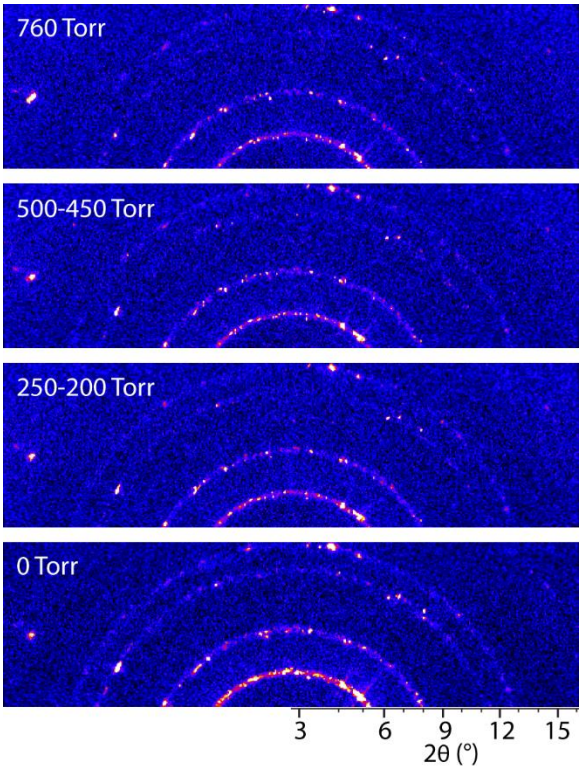

Figure 2.13. 2D-PXRD images collected from UMCM-9 during the course of activation from hexane. Sample evacuation progress as monitored by pressure in Torr is given in the upper left of each diffractogram. The intersection of each 2Θ arc with the edge of the diffractogram is displayed in the bottom right axis. These intersections are identical in every 2D pattern shown. Very few changes are observed

during this evacuation, other than a slight increase in spot intensities after evacuation due to the removal of (albeit weakly) X-ray attenuating hexane.

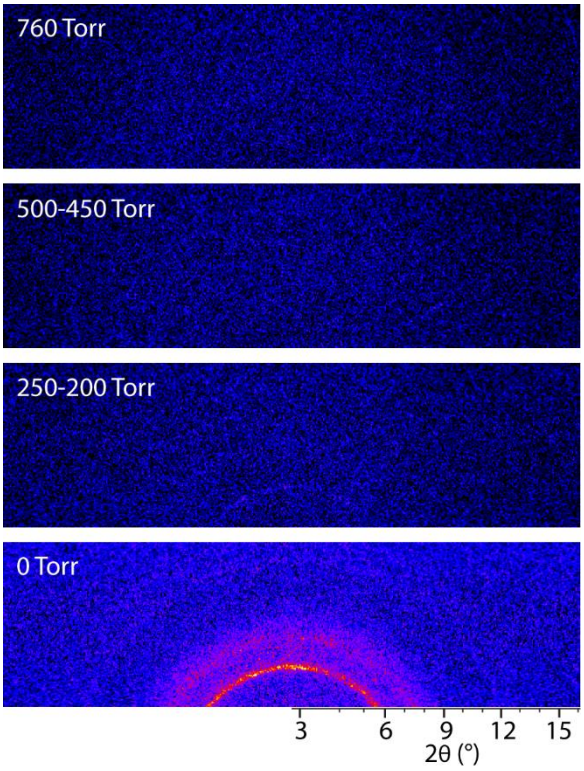

Figure 2.14. 2D-PXRD images collected from SNU-70 during the course of activation from CH_2Cl_2. Sample evacuation progress as monitored by pressure in Torr is given in the upper left of each diffractogram. The intersection of each 2Θ arc with the edge of the diffractogram is displayed in the bottom right axis. These intersections are identical in every 2D pattern shown. Very little diffracted X-ray intensity

is observed before the removal of the highly attenuating CH_2Cl_2, and the final diffractogram is consistent with an amorphous product.

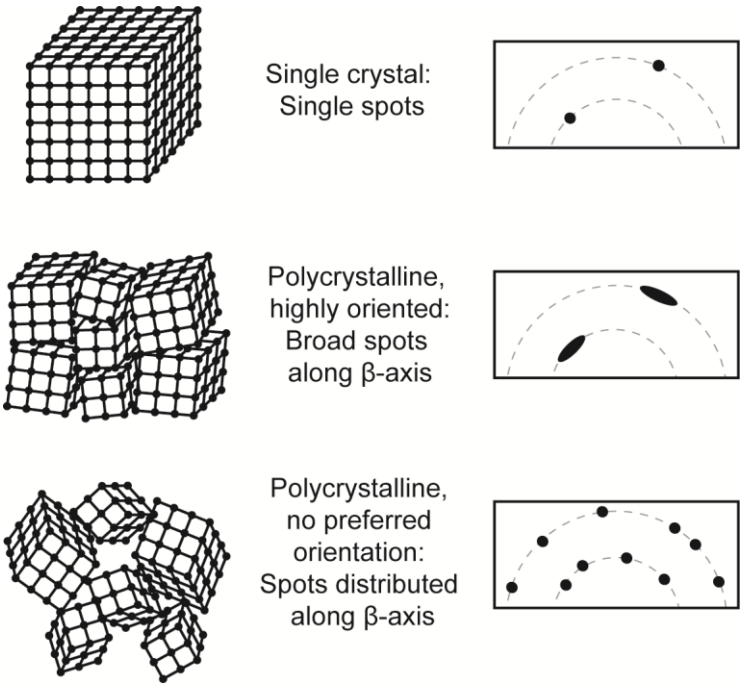

Figure 2.15. Relationship between sample orientation and β-axis broadness/distribution of diffraction spots. In a single crystalline sample, single spots with narrow β-axis width are observed. In a polycrystalline sample with a high degree of preferred orientation, these spots would broaden along the β-axis. In a

polycrystalline sample with no preferred orientation, X-ray spots would be observed distributed across the β-axis ring with narrow β-axis widths.

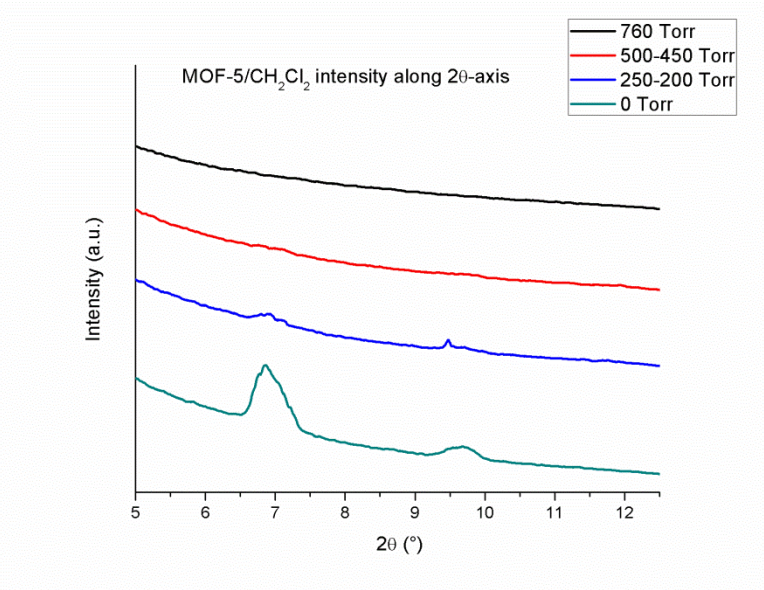

Figure 2.16. Diffracted X-ray intensity as a function of 2Θ during the activation of MOF-5 from CH_2Cl_2. Very little diffracted X-ray intensity is observed before the removal of the highly attenuating CH_2Cl_2. Despite the apparent broad peak-width seen in this projection of the data, individual spots (Figure 2.10) have narrow 2Θ-axis broadness, highlighting the importance of considering the 2D X-ray diffractograms in understanding the data.

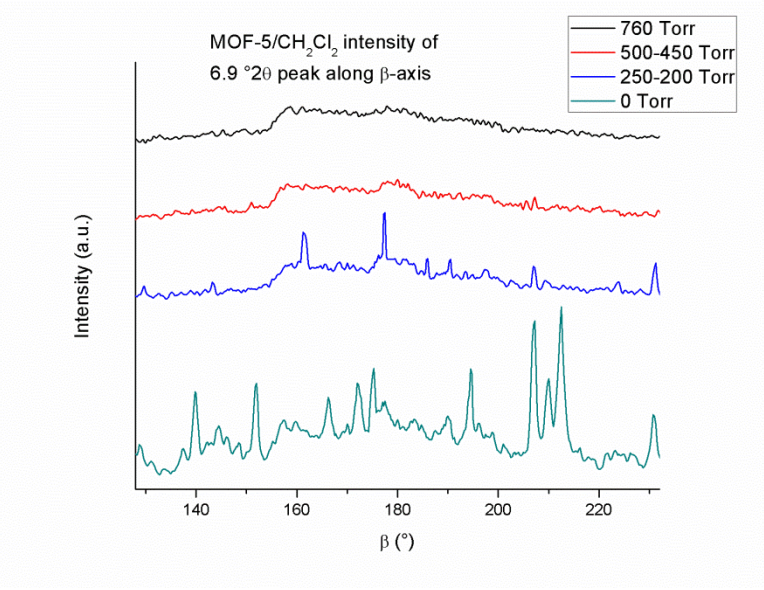

Figure 2.17. Diffracted X-ray intensity for the 6.9 °2Θ peak as a function of β during the activation of MOF-5 from CH_2Cl_2. 2D diffractograms were integrated between 6.2 and 7.3 °2Θ. Very little diffracted X-ray

intensity is observed before the removal of the highly attenuating CH_2Cl_2. Sharp peaks are observed after removal of solvent, consistent with no changes to the sample crystallinity.

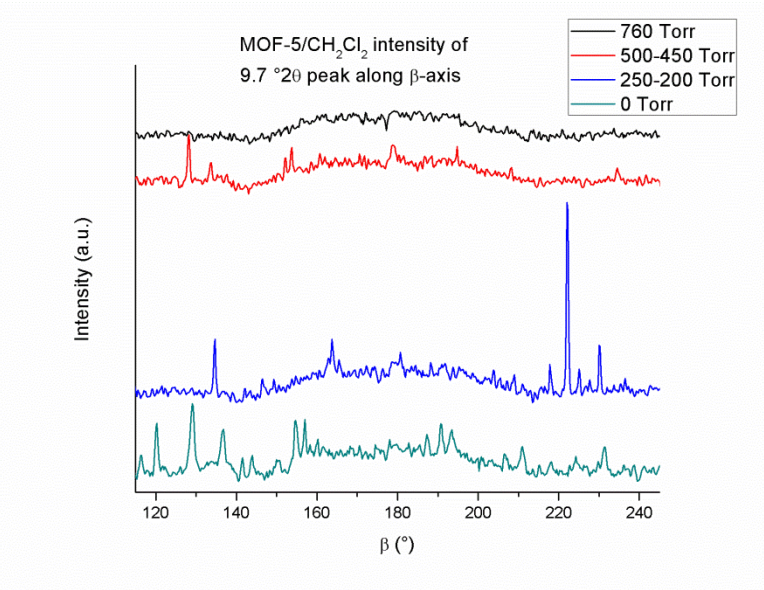

Figure 2.18. Diffracted X-ray intensity for the 9.7 °2Θ peak as a function of β during the activation of MOF-5 from CH_2Cl_2. 2D diffractograms were integrated between 9.0 and 10.2 °2Θ. Very little diffracted X-ray intensity is observed before the removal of the highly attenuating CH_2Cl_2. Sharp peaks are observed after removal of solvent, consistent with no changes to the sample crystallinity.

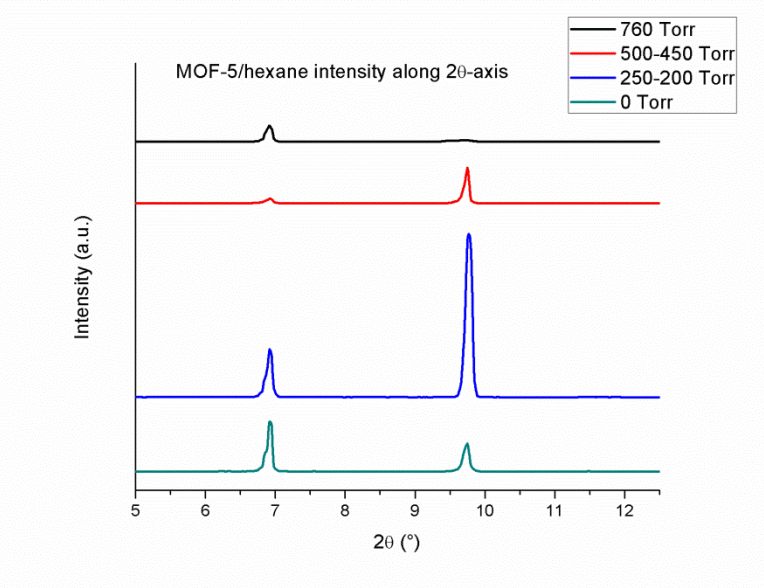

Figure 2.19. Diffracted X-ray intensity as a function of 2Θ during the activation of MOF-5 from hexane. While this integrated diffractogram shows very narrow 2Θ-axis broadness, the 2Θ-axis broadness of individual spots in the 2D diffractogram are similar to those seen in the activation of MOF-5 from both

CH_2Cl_2 and THF. Changes in peak intensity over time are attributed to sample reorientation during solvent removal, as the integrated intensity is dominated by several crystallites (Figures 2.20 and 2.21).

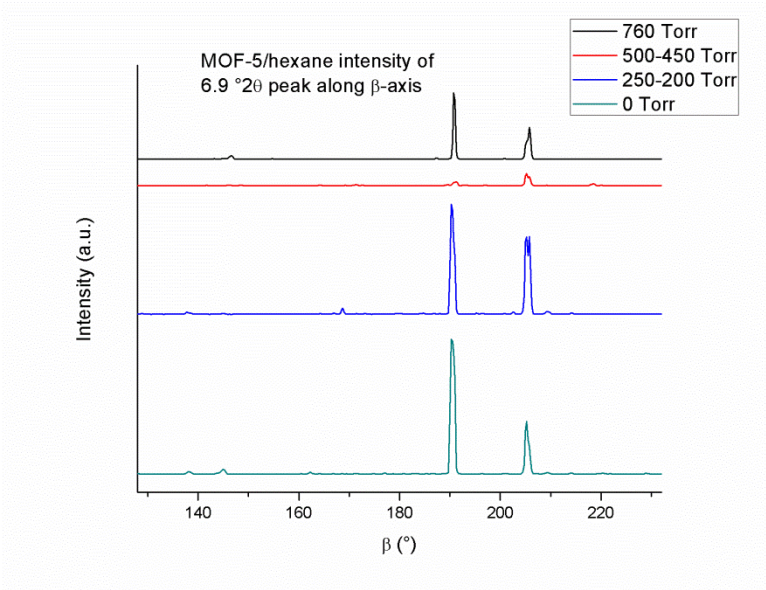

Figure 2.20. Diffracted X-ray intensity for the 6.9 °2Θ peak as a function of β during the activation of MOF-5 from hexane. 2D diffractograms were integrated between 6.2 and 7.3 °2Θ. Sharp peaks are observed throughout the course of the activation, consistent with no changes to the sample crystallinity.

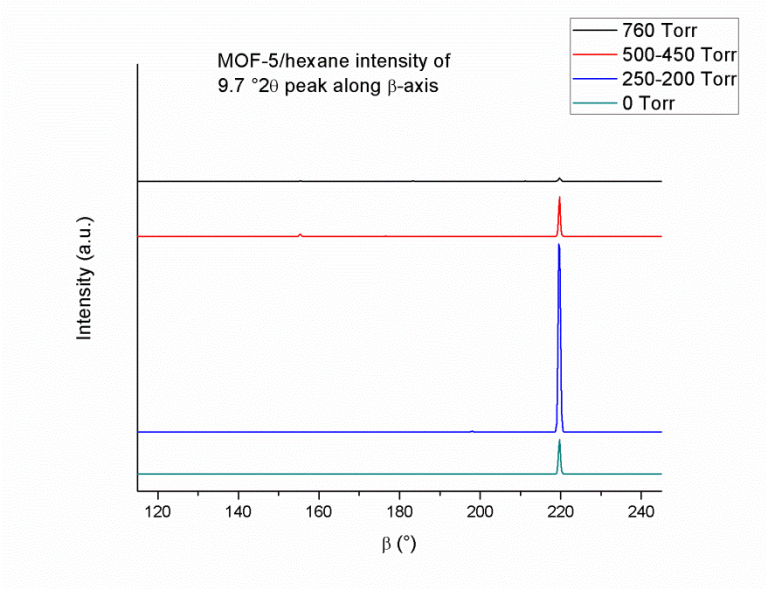

Figure 2.21. Diffracted X-ray intensity for the 9.7 °2Θ peak as a function of β during the activation of MOF-5 from hexane. 2D diffractograms were integrated between 9.0 and 10.2 °2Θ. Sharp peaks are observed throughout the course of the activation, consistent with no changes to the sample crystallinity.

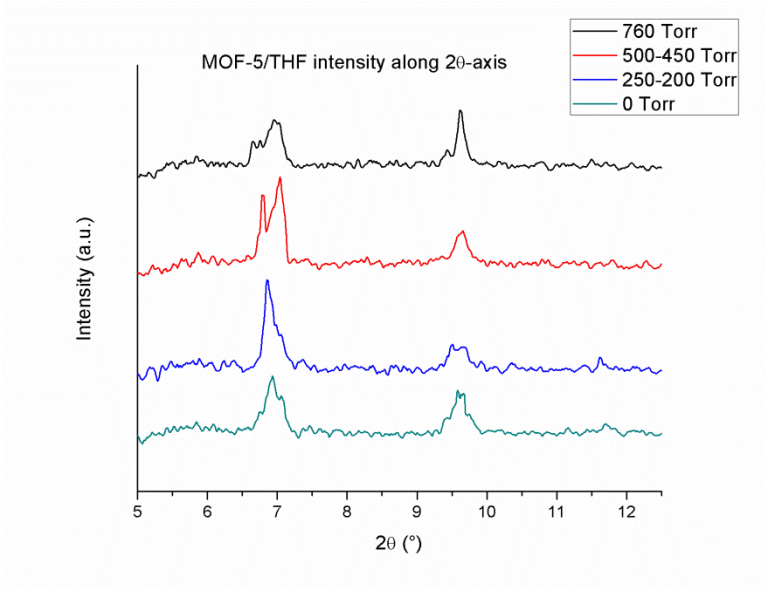

Figure 2.22. Diffracted X-ray intensity as a function of 2Θ during the activation of MOF-5 from THF. Very few changes are observed, indicative of a successful activation.

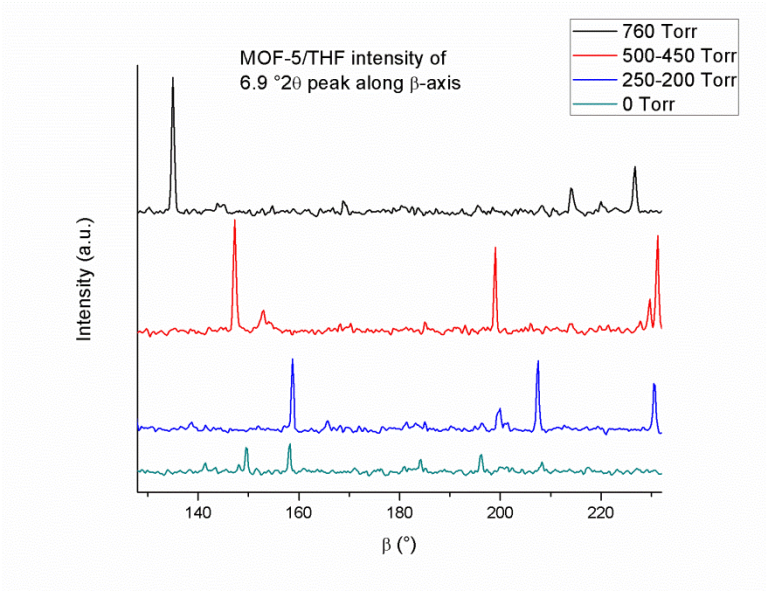

Figure 2.23. Diffracted X-ray intensity for the 6.9 °2Θ peak as a function of β during the activation of MOF-5 from THF. 2D diffractograms were integrated between 6.2 and 7.3 °2Θ. Sharp peaks are observed throughout the course of the activation, consistent with no changes to the sample crystallinity.

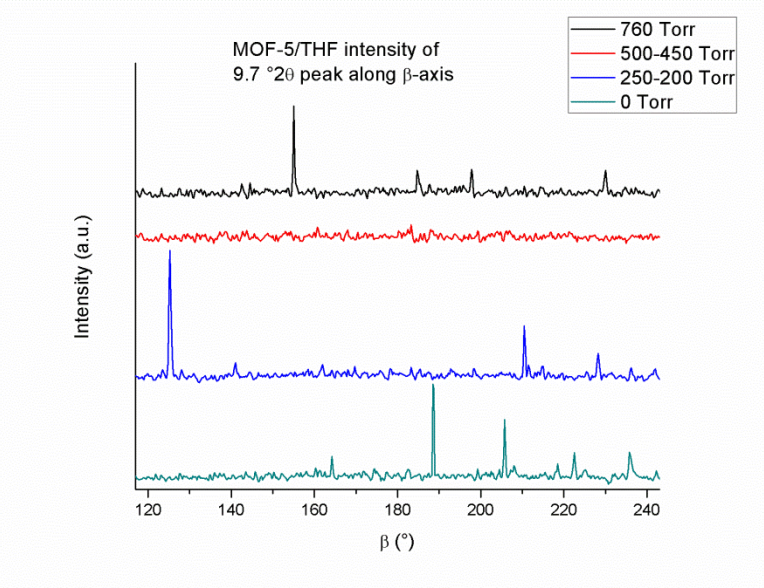

Figure 2.24. Diffracted X-ray intensity for the 9.7 °2Θ peak as a function of β during the activation of MOF-5 from THF. 2D diffractograms were integrated between 9.0 and 10.2 °2Θ. Sharp peaks are observed throughout the course of the activation, consistent with no changes to the sample crystallinity.

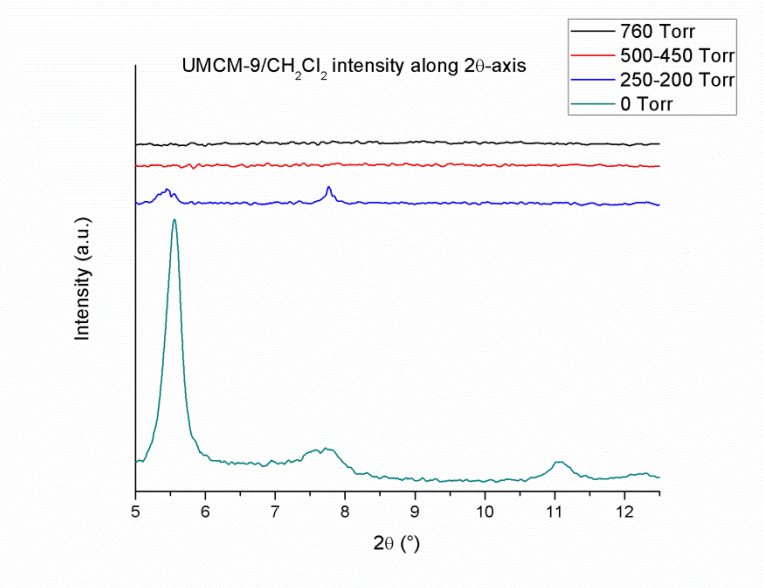

Figure 2.25. Diffracted X-ray intensity as a function of 2Θ during the activation of UMCM-9 from CH_2Cl_2. Very little diffracted X-ray intensity is observed before the removal of the highly attenuating CH_2Cl_2. Peak broadening is observed between the 250-200 Torr scan and the 0 Torr scan, indicating that the change to

the sample crystallinity occur only after complete removal of solvent, and that solvent exchange was not responsible for the collapse event.

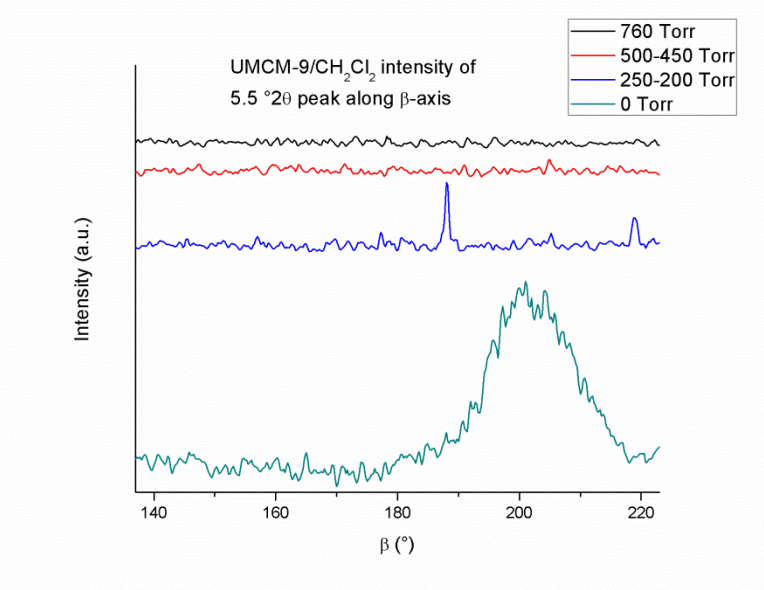

Figure 2.26. Diffracted X-ray intensity for the 5.5 °2Θ peak as a function of β during the activation of UMCM-9 from CH_2Cl_2. 2D diffractograms were integrated between 5.0 and 6.0 °2Θ. Very little diffracted X-ray intensity is observed before the removal of the highly attenuating CH_2Cl_2. Sharp peaks are observed in the 250-200 Torr scan, while a single broad peak is observed after complete solvent removal. This β-axis broadening indicates an increase in sample polycrystallinity (Figure 2.15).

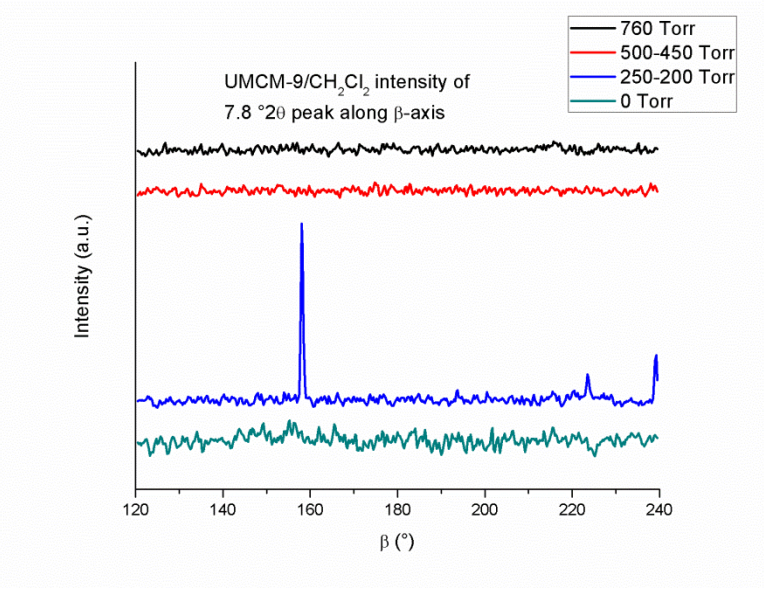

Figure 2.27. Diffracted X-ray intensity for the 7.8 °2Θ peak as a function of β during the activation of UMCM-9 from CH_2Cl_2. 2D diffractograms were integrated between 7.3 and 8.3 °2Θ. Very little diffracted

X-ray intensity is observed before the removal of the highly attenuating CH_2Cl_2. Sharp peaks are observed in the 250-200 Torr scan, while no peaks are observed after complete solvent removal.

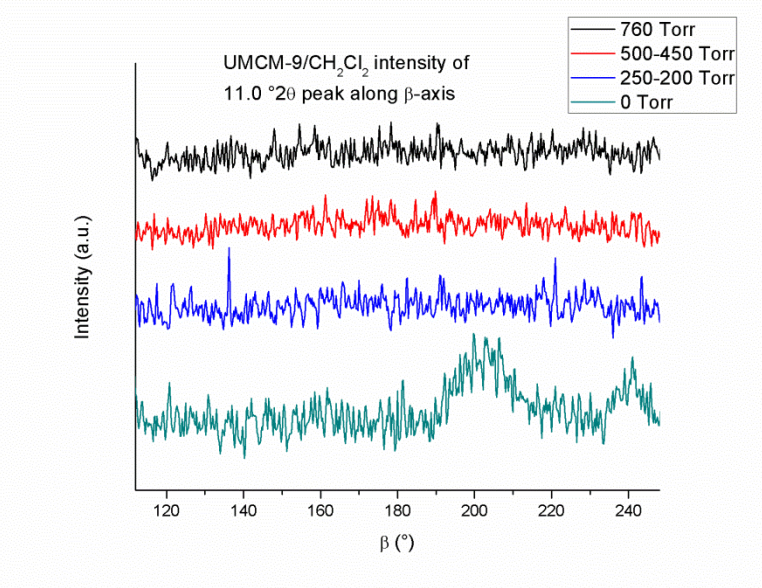

Figure 2.28. Diffracted X-ray intensity for the 11.0 °2Θ peak as a function of β during the activation of UMCM-9 from CH_2Cl_2. 2D diffractograms were integrated between 10.1 and 11.3 °2Θ. Very little

diffracted X-ray intensity is observed before the removal of the highly attenuating CH_2Cl_2. Sharp peaks are observed in the 250-200 Torr scan, while only broad peaks are observed after complete solvent removal.

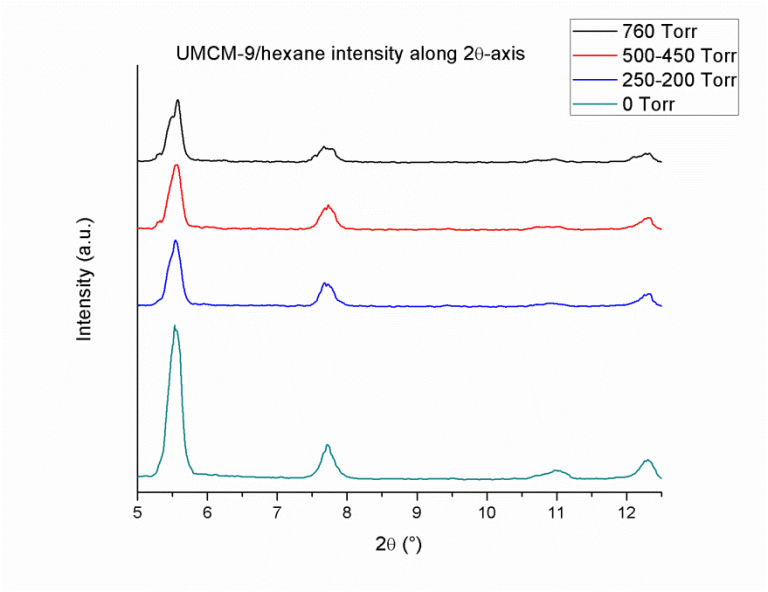

Figure 2.29. Diffracted X-ray intensity as a function of 2Θ during the activation of UMCM-9 from hexane. No substantial changes are observed over the course of the activation.

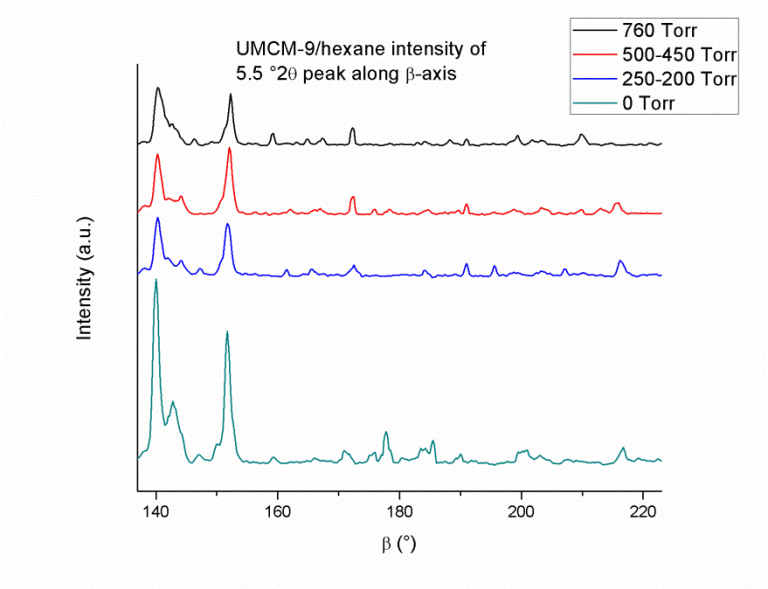

Figure 2.30. Diffracted X-ray intensity for the 5.5 °2Θ peak as a function of β during the activation of UMCM-9 from hexane. 2D diffractograms were integrated between 5.0 and 6.0 °2Θ. No substantial changes to the β-axis peak broadness are observed.

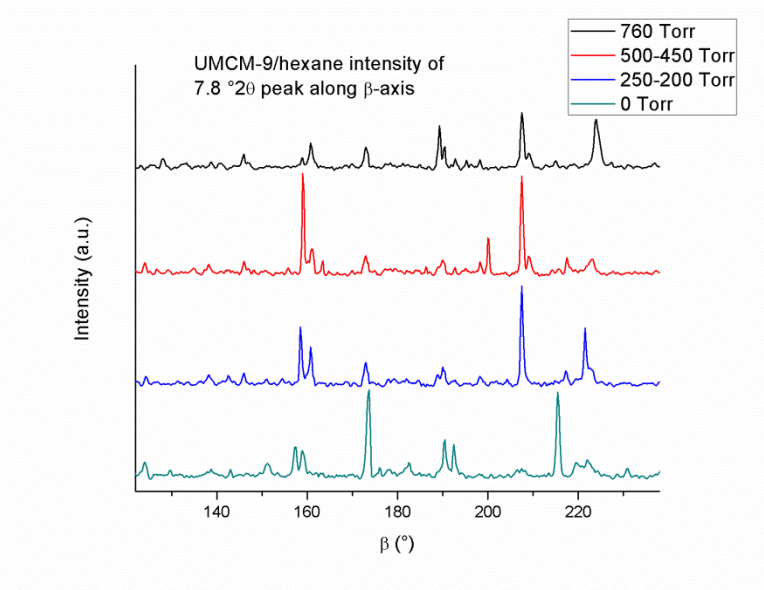

Figure 2.31. Diffracted X-ray intensity for the 7.8 °2Θ peak as a function of β during the activation of UMCM-9 from hexane. 2D diffractograms were integrated between 7.3 and 8.3 °2Θ. No substantial changes to the β-axis peak broadness are observed.

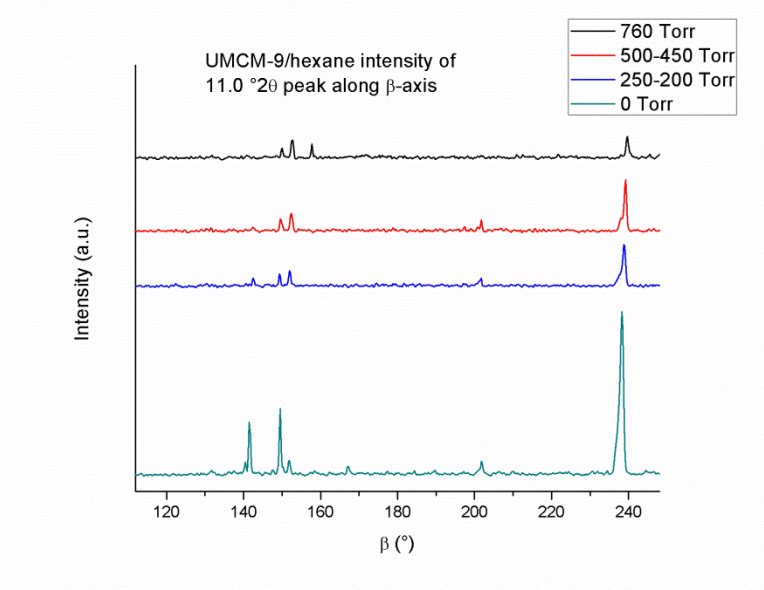

Figure 2.32. Diffracted X-ray intensity for the 11.0 °2Θ peak as a function of β during the activation of UMCM-9 from hexane. 2D diffractograms were integrated between 10.1 and 11.3 °2Θ. No substantial changes to the β-axis peak broadness are observed.

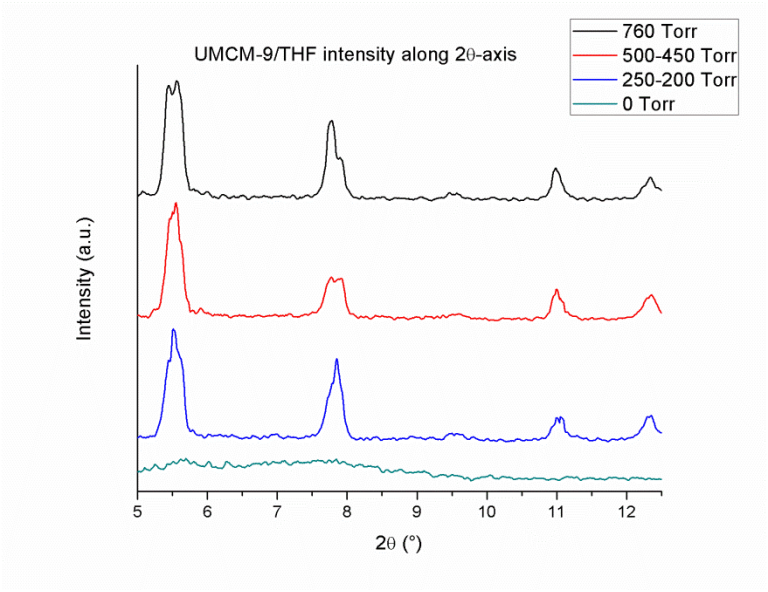

Figure 2.33. Diffracted X-ray intensity as a function of 2Θ during the activation of UMCM-9 from THF. While peaks are observed prior to solvent removal, the final product shows no appreciable crystallinity.

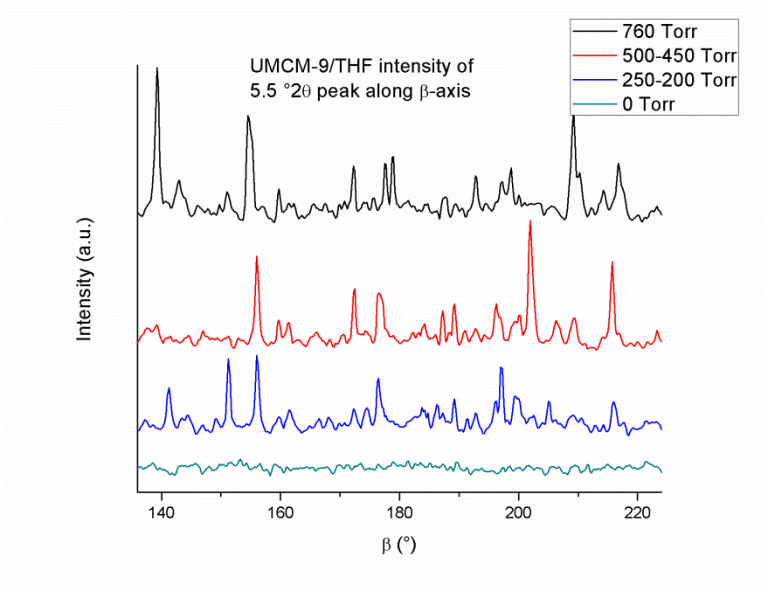

Figure 2.34. Diffracted X-ray intensity for the 5.5 °2Θ peak as a function of β during the activation of UMCM-9 from THF. 2D diffractograms were integrated between 5.0 and 6.0 °2Θ. While peaks are observed prior to solvent removal, the final product shows no appreciable crystallinity.

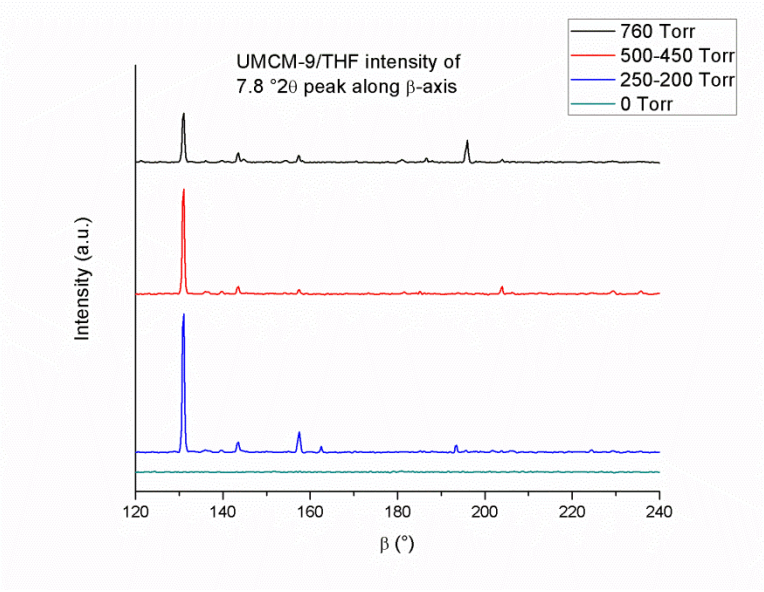

Figure 2.35. Diffracted X-ray intensity for the 7.8 °2Θ peak as a function of β during the activation of UMCM-9 from THF. 2D diffractograms were integrated between 7.3 and 8.3 °2Θ. While peaks are observed prior to solvent removal, the final product shows no appreciable crystallinity.

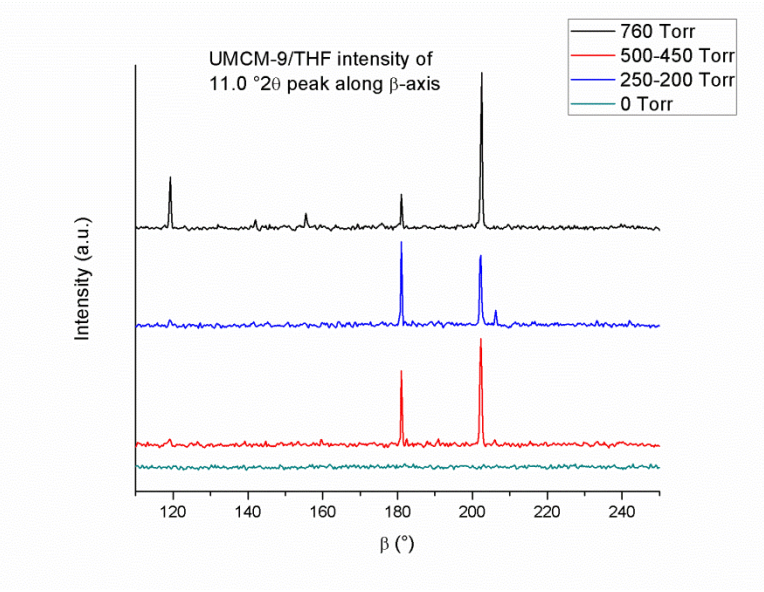

Figure 2.36. Diffracted X-ray intensity for the 11.0 °2Θ peak as a function of β during the activation of UMCM-9 from THF. 2D diffractograms were integrated between 10.1 and 11.3 °2Θ. While peaks are observed prior to solvent removal, the final product shows no appreciable crystallinity.

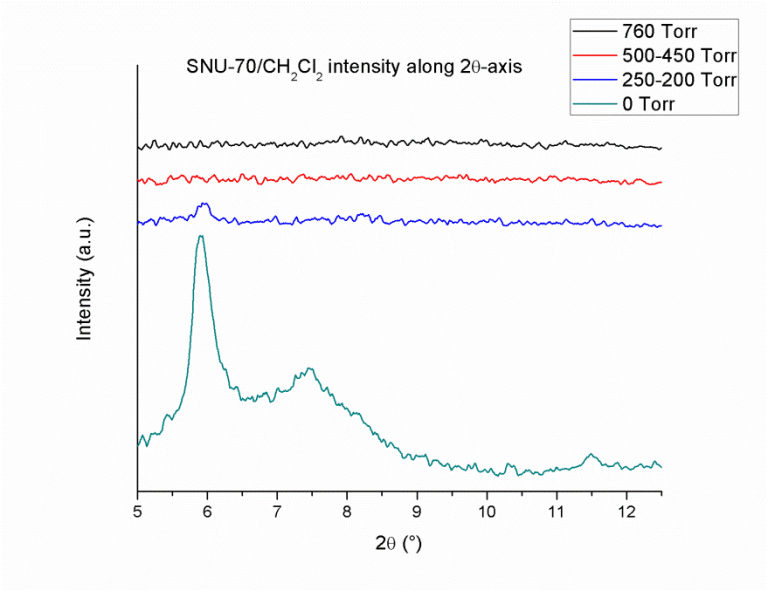

Figure 2.37. Diffracted X-ray intensity as a function of 2Θ during the activation of SNU-70 from CH_2Cl_2. No peaks other than a small signal at 5.9 °2Θ are visible prior to solvent evacuation. After evacuation, the

observed signal consists of broad peaks consistent with an amorphous product. The peaks of this final diffractograms appear artificially large due to X-ray attenuation in earlier scans.

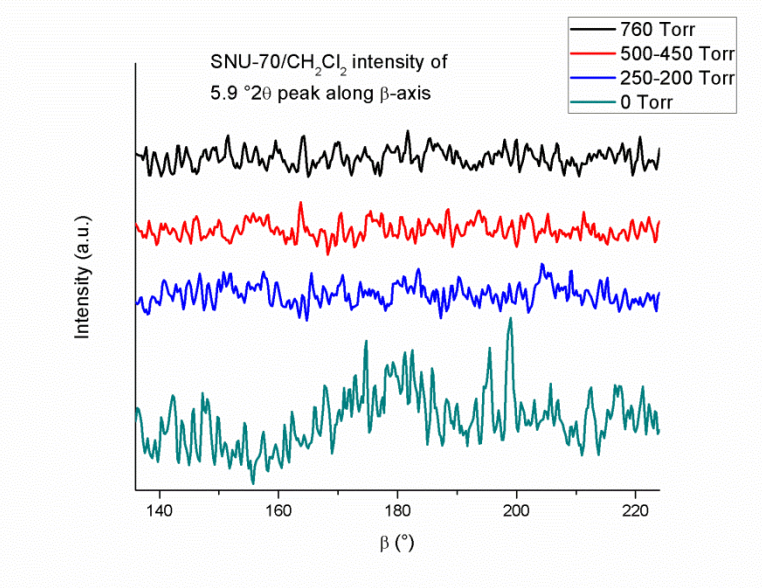

Figure 2.38. Diffracted X-ray intensity for the 5.9 °2Θ peak as a function of β during the activation of SNU-70 from CH_2Cl_2. 2D diffractograms were integrated between 5.4 and 6.6 °2Θ. No appreciable β-resolved signal is apparent during this activation.

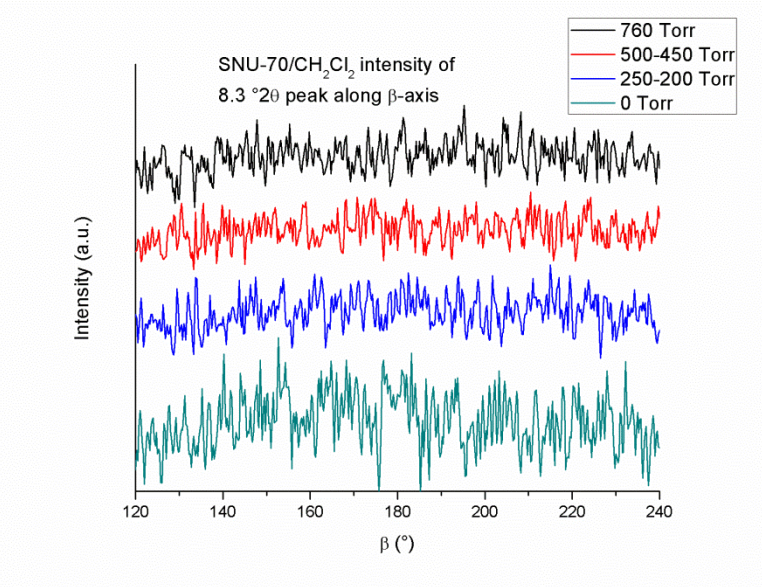

Figure 2.39. Diffracted X-ray intensity for the 8.3 °2Θ peak as a function of β during the activation of SNU-70 from CH_2Cl_2. 2D diffractograms were integrated between 7.7 and 9.0 °2Θ. No appreciable β-resolved signal is apparent during this activation.

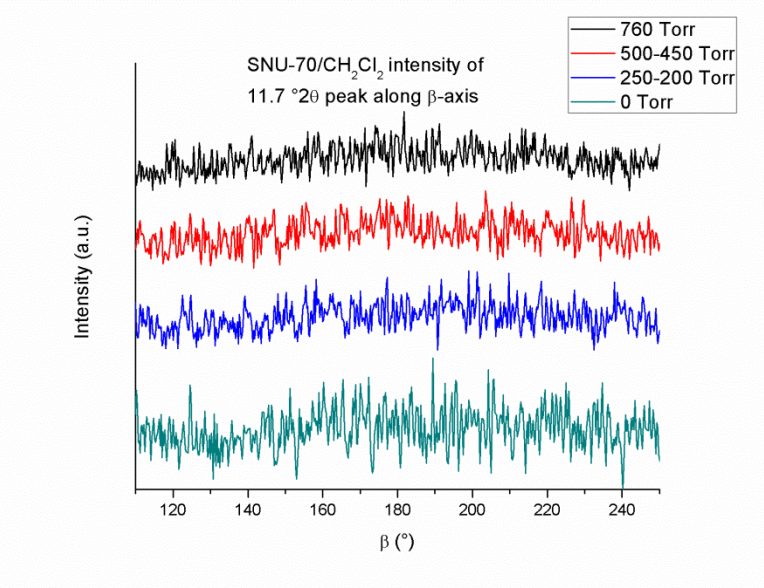

Figure 2.40. Diffracted X-ray intensity for the 11.7 °2Θ peak as a function of β during the activation of SNU-70 from CH_2Cl_2. 2D diffractograms were integrated between 11.2 and 12.2 °2Θ. No appreciable β-resolved signal is apparent during this activation.

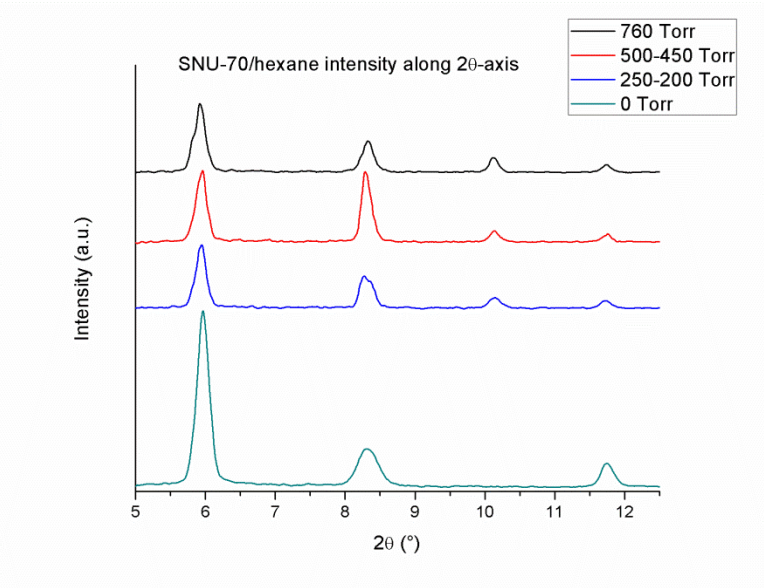

Figure 2.41. Diffracted X-ray intensity as a function of 2Θ during the activation of SNU-70 from hexane. Slight broadening is observed, particularly for the 8.3 °2Θ peak, but instrumental broadening generally dominates in this presentation of the data; the 2Θ broadening of individual spots is more apparent in the 2D

diffractograms (Figure 8). The loss of the 10.1 °2Θ peak is attributed to sample orientation changes during the experiment, as only 1-2 spots at this position are apparent prior to solvent removal.

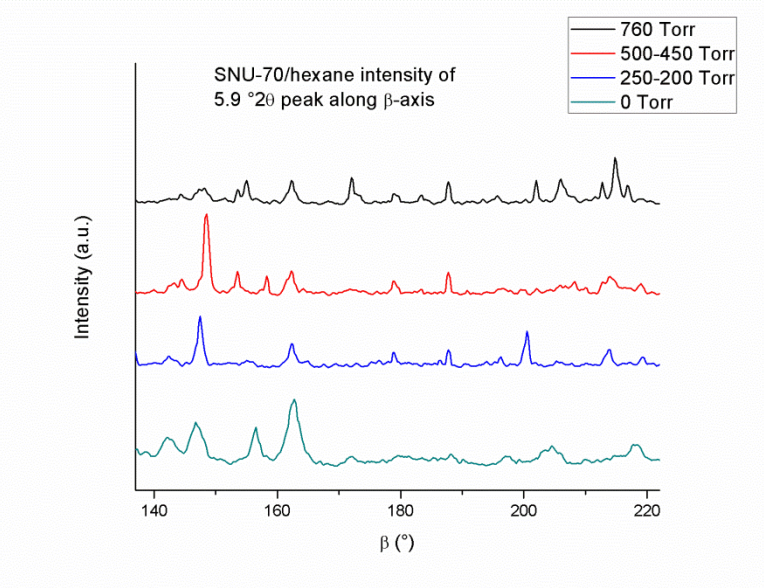

Figure 2.42. Diffracted X-ray intensity for the 5.9 °2Θ peak as a function of β during the activation of SNU-70 from hexane. 2D diffractograms were integrated between 5.4 and 6.6 °2Θ. Peak broadening is observed upon removal of solvent, consistent with an increase in sample polycrystallinity and a slight decrease in crystallite preferred orientation, as discussed in Chapters 2.1-2.4.

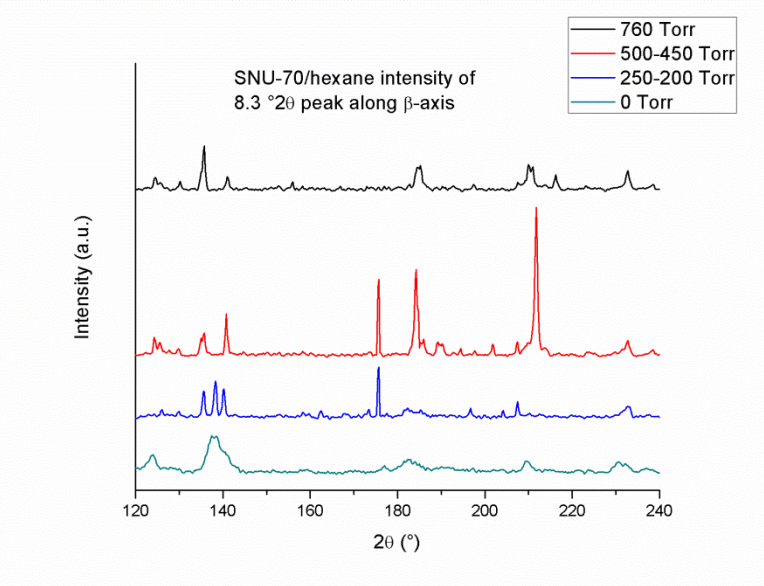

Figure 2.43. Diffracted X-ray intensity for the 8.3 °2Θ peak as a function of β during the activation of SNU-70 from hexane. 2D diffractograms were integrated between 7.7 and 9.0 °2Θ. Peak broadening is observed

upon removal of solvent, consistent with an increase in sample polycrystallinity and a slight decrease in crystallite preferred orientation, as discussed in the main text.

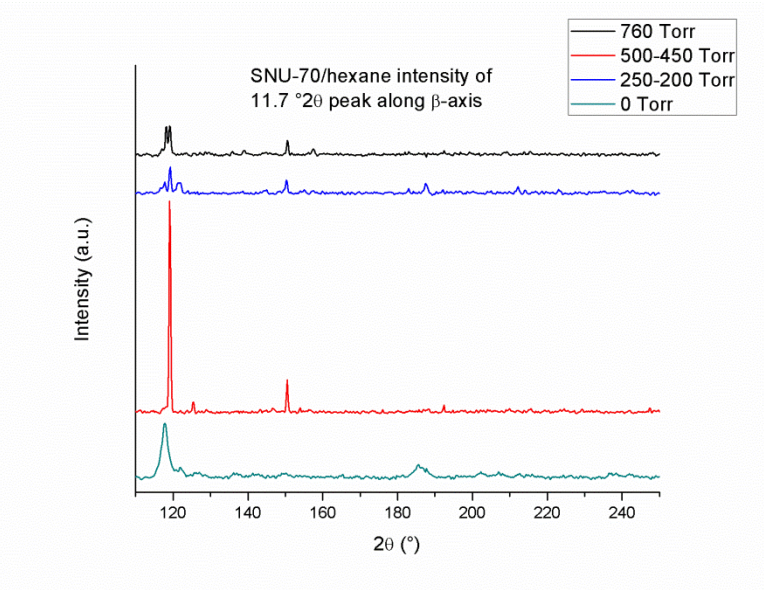

Figure 2.44. Diffracted X-ray intensity for the 11.7 °2Θ peak as a function of β during the activation of SNU-70 from hexane. 2D diffractograms were integrated between 11.2 and 12.2 °2Θ. Peak broadening is

observed upon removal of solvent, consistent with an increase in sample polycrystallinity and a slight decrease in crystallite preferred orientation, as discussed in the main text.

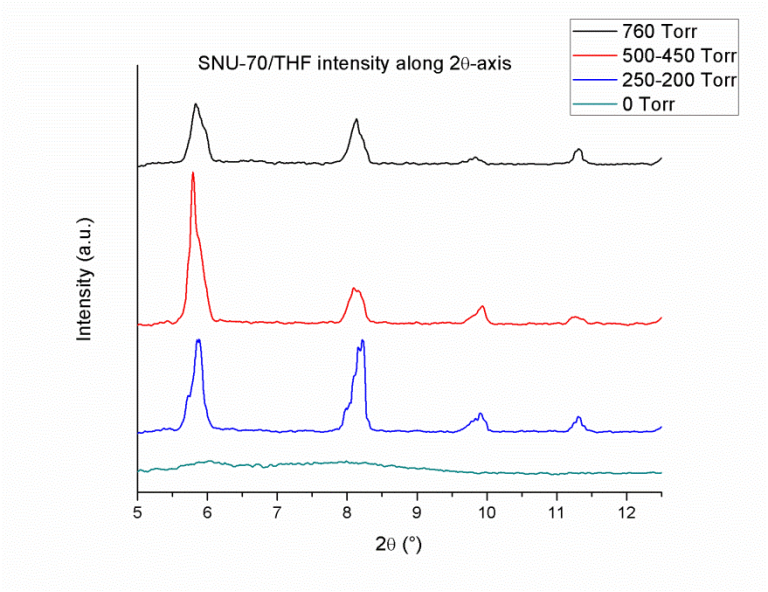

Figure 2.45. Diffracted X-ray intensity as a function of 2Θ during the activation of SNU-70 from THF. Retention of sample crystallinity is observed until complete removal of solvent.

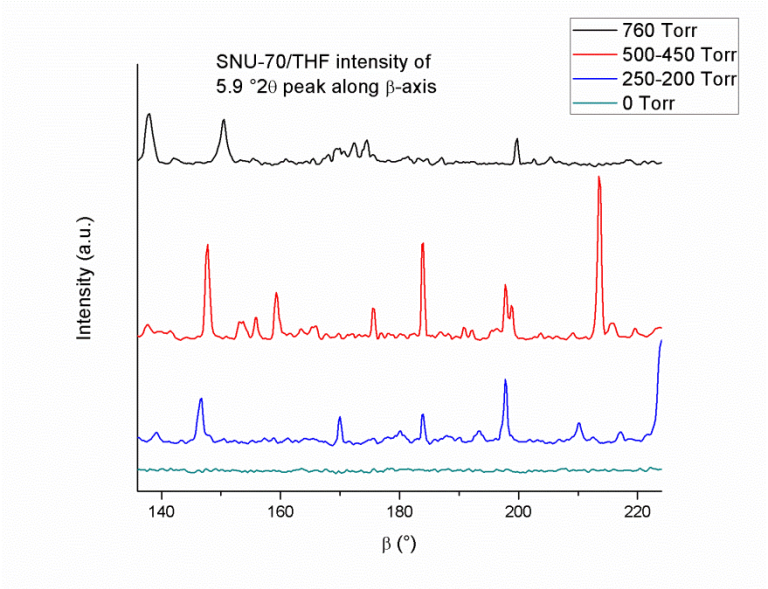

Figure 2.46. Diffracted X-ray intensity for the 5.9 °2Θ peak as a function of β during the activation of SNU-70 from THF. 2D diffractograms were integrated between 5.4 and 6.6 °2Θ. Retention of sample crystallinity is observed until complete removal of solvent.

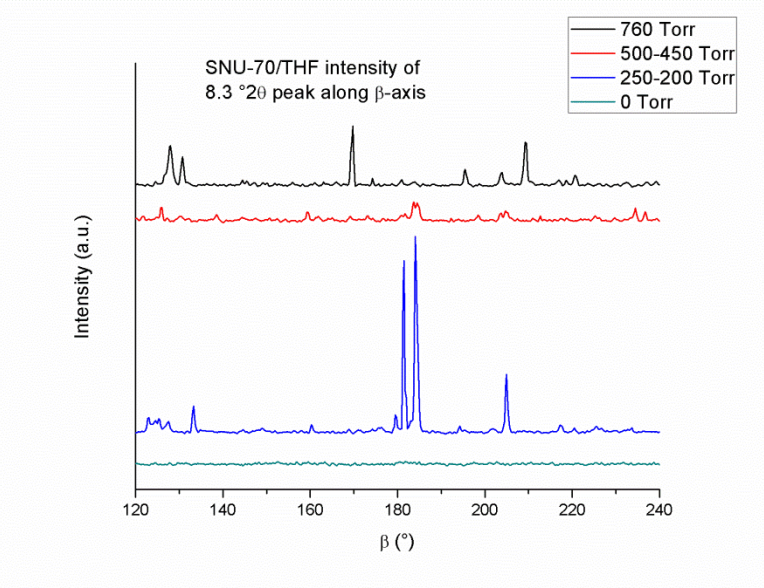

Figure 2.47. Diffracted X-ray intensity for the 8.3 °2Θ peak as a function of β during the activation of SNU-70 from THF. 2D diffractograms were integrated between 7.7 and 9.0 °2Θ. Retention of sample crystallinity is observed until complete removal of solvent.

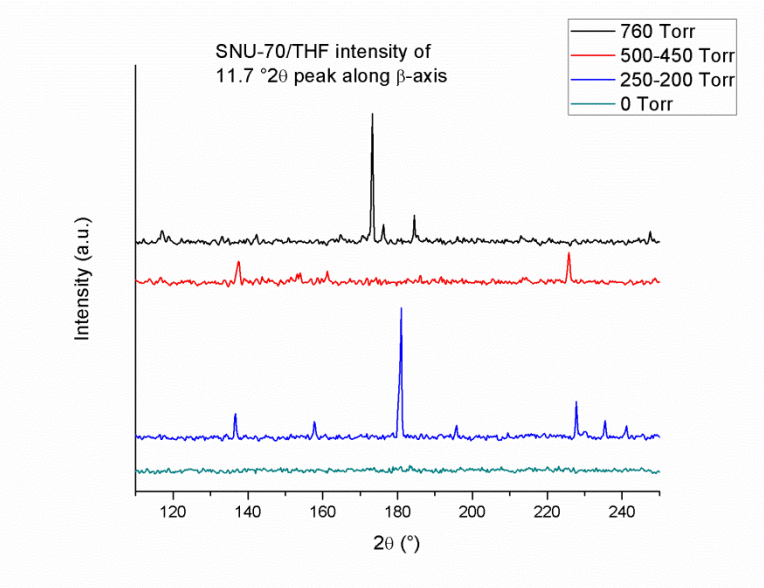

Figure 2.48. Diffracted X-ray intensity for the 11.7 °2Θ peak as a function of β during the activation of SNU-70 from THF. 2D diffractograms were integrated between 11.2 and 12.2 °2Θ. Retention of sample crystallinity is observed until complete removal of solvent.

2.6 References

(1) Seth, S.; Matzger, A. J. Metal–Organic Frameworks: Examples, Counterexamples, and an Actionable Definition. *Cryst. Growth Des.* **2017**, *17* (8), 4043–4048.
(2) Suh, M. P.; Park, H. J.; Prasad, T. K.; Lim, D.-W. Hydrogen Storage in Metal–Organic Frameworks. *Chem. Rev.* **2012**, *112* (2), 782–835.
(3) Li, B.; Wen, H.-M.; Zhou, W.; Xu, J. Q.; Chen, B. Porous Metal-Organic Frameworks: Promising Materials for Methane Storage. *Chem* **2016**, *1* (4), 557–580.
(4) Sumida, K.; Rogow, D. L.; Mason, J. A.; McDonald, T. M.; Bloch, E. D.; Herm, Z. R.; Bae, T.-H.; Long, J. R. Carbon Dioxide Capture in Metal–Organic Frameworks. *Chem. Rev.* **2012**, *112* (2), 724–781.
(5) Qiu, S.; Xue, M.; Zhu, G. Metal–Organic Framework Membranes: From Synthesis to Separation Application. *Chem Soc Rev* **2014**, *43* (16), 6116–6140.
(6) Lee, J.; Farha, O. K.; Roberts, J.; Scheidt, K. A.; Nguyen, S. T.; Hupp, J. T. Metal–Organic Framework Materials as Catalysts. *Chem. Soc. Rev.* **2009**, *38* (5), 1450.
(7) Kreno, L. E.; Leong, K.; Farha, O. K.; Allendorf, M.; Van Duyne, R. P.; Hupp, J. T. Metal–Organic Framework Materials as Chemical Sensors. *Chem. Rev.* **2012**, *112* (2), 1105–1125.
(8) Wuttke, S.; Lismont, M.; Escudero, A.; Rungtaweevoranit, B.; Parak, W. J. Positioning Metal-Organic Framework Nanoparticles within the Context of Drug Delivery – A Comparison with Mesoporous Silica Nanoparticles and Dendrimers. *Biomaterials* **2017**, *123*, 172–183.
(9) Zhang, X.; Wang, W.; Hu, Z.; Wang, G.; Uvdal, K. Coordination Polymers for Energy Transfer: Preparations, Properties, Sensing Applications, and Perspectives. *Coord. Chem. Rev.* **2015**, *284*, 206–235.
(10) McDonald, K. A.; Seth, S.; Matzger, A. J. Coordination Polymers with High Energy Density: An Emerging Class of Explosives. *Cryst. Growth Des.* **2015**, *15* (12), 5963–5972.
(11) Ahmed, A.; Liu, Y.; Purewal, J.; Tran, L. D.; Veenstra, M.; Wong-Foy, A.; Matzger, A.; Siegel, D. Balancing Gravimetric and Volumetric Hydrogen Density in MOFs. *Energy Env. Sci* **2017**.
(12) Eddaoudi, M.; Li, H.; Yaghi, O. M. Highly Porous and Stable Metal−Organic Frameworks: Structure Design and Sorption Properties. *J. Am. Chem. Soc.* **2000**, *122* (7), 1391–1397.
(13) Mondloch, J. E.; Karagiaridi, O.; Farha, O. K.; Hupp, J. T. Activation of Metal–Organic Framework Materials. *CrystEngComm* **2013**, *15* (45), 9258.
(14) An, J.; Farha, O. K.; Hupp, J. T.; Pohl, E.; Yeh, J. I.; Rosi, N. L. Metal-Adeninate Vertices for the Construction of an Exceptionally Porous Metal-Organic Framework. *Nat. Commun.* **2012**, *3* (1).
(15) Dutta, A.; Wong-Foy, A. G.; Matzger, A. J. Coordination Copolymerization of Three Carboxylate Linkers into a Pillared Layer Framework. *Chem. Sci.* **2014**, *5* (10), 3729.
(16) Nelson, A. P.; Farha, O. K.; Mulfort, K. L.; Hupp, J. T. Supercritical Processing as a Route to High Internal Surface Areas and Permanent Microporosity in Metal−Organic Framework Materials. *J. Am. Chem. Soc.* **2009**, *131* (2), 458–460.
(17) Farha, O. K.; Hupp, J. T. Rational Design, Synthesis, Purification, and Activation of Metal−Organic Framework Materials. *Acc. Chem. Res.* **2010**, *43* (8), 1166–1175.
(18) Liu, B.; Wong-Foy, A. G.; Matzger, A. J. Rapid and Enhanced Activation of Microporous Coordination Polymers by Flowing Supercritical CO2. *Chem. Commun.* **2013**, *49* (14), 1419.

(19) Ma, J.; Kalenak, A. P.; Wong-Foy, A. G.; Matzger, A. J. Rapid Guest Exchange and Ultra-Low Surface Tension Solvents Optimize Metal-Organic Framework Activation. *Angew. Chem. Int. Ed.* **2017**, *56* (46), 14618–14621.
(20) Feldblyum, J. I.; Liu, M.; Gidley, D. W.; Matzger, A. J. Reconciling the Discrepancies between Crystallographic Porosity and Guest Access As Exemplified by Zn-HKUST-1. *J. Am. Chem. Soc.* **2011**, *133* (45), 18257–18263.
(21) Bhunia, M. K.; Hughes, J. T.; Fettinger, J. C.; Navrotsky, A. Thermochemistry of Paddle Wheel MOFs: Cu-HKUST-1 and Zn-HKUST-1. *Langmuir* **2013**, *29* (25), 8140–8145.
(22) Yang, J.; Wang, X.; Dai, F.; Zhang, L.; Wang, R.; Sun, D. Improving the Porosity and Catalytic Capacity of a Zinc Paddlewheel Metal-Organic Framework (MOF) through Metal-Ion Metathesis in a Single-Crystal-to-Single-Crystal Fashion. *Inorg. Chem.* **2014**, *53* (19), 10649–10653.
(23) Mondal, S. S.; Bhunia, A.; Attallah, A. G.; Matthes, P. R.; Kelling, A.; Schilde, U.; Müller-Buschbaum, K.; Krause-Rehberg, R.; Janiak, C.; Holdt, H.-J. Study of the Discrepancies between Crystallographic Porosity and Guest Access into Cadmium-Imidazolate Frameworks and Tunable Luminescence Properties by Incorporation of Lanthanides. *Chem. - Eur. J.* **2016**, *22* (20), 6905–6913.
(24) Wu, Y.; Breeze, M. I.; O'Hare, D.; Walton, R. I. High Energy X-Rays for Following Metal-Organic Framework Formation: Identifying Intermediates in Interpenetrated MOF-5 Crystallisation. *Microporous Mesoporous Mater.* **2017**, *254*, 178–183.
(25) Wu, Y.; Breeze, M. I.; Clarkson, G. J.; Millange, F.; O'Hare, D.; Walton, R. I. Exchange of Coordinated Solvent During Crystallization of a Metal-Organic Framework Observed by In Situ High-Energy X-Ray Diffraction. *Angew. Chem. Int. Ed.* **2016**, *55* (16), 4992–4996.
(26) Friščić, T.; Halasz, I.; Beldon, P. J.; Belenguer, A. M.; Adams, F.; Kimber, S. A. J.; Honkimäki, V.; Dinnebier, R. E. Real-Time and in Situ Monitoring of Mechanochemical Milling Reactions. *Nat. Chem.* **2013**, *5* (1), 66–73.
(27) Julien, P. A.; Užarević, K.; Katsenis, A. D.; Kimber, S. A. J.; Wang, T.; Farha, O. K.; Zhang, Y.; Casaban, J.; Germann, L. S.; Etter, M.; et al. In Situ Monitoring and Mechanism of the Mechanochemical Formation of a Microporous MOF-74 Framework. *J. Am. Chem. Soc.* **2016**, *138* (9), 2929–2932.
(28) Stolar, T.; Batzdorf, L.; Lukin, S.; Zilic, D.; Motillo, C.; Friscic, T.; Emmerling, F.; Halasz, I.; Uzarevic, K. In Situ Monitoring of the Mechanosynthesis of the Archetypal Metal-Organic Framework HKUST-1: Effect of Liquid Additives on the Milling Reactivity. *Inorg. Chem.* **2017**, *56*, 6599–6608.
(29) Dong, Z.; Mi, Z.; Shi, W.; Jiang, H.; Zheng, Y.; Yang, K. High Pressure Effects on Hydrate Cu-BTC Investigated by Vibrational Spectroscopy and Synchrotron X-Ray Diffraction. *RSC Adv.* **2017**, *7*, 55504–55512.
(30) Gagnon, K. J.; Beavers, C. M.; Clearfield, A. MOFs Under Pressure: The Reversible Compression of a Single Crystal. *J. Am. Chem. Soc.* **2013**, *135*, 1252–1255.
(31) Nevjestic, I.; Depauw, H.; Gast, P.; Tack, P.; Deduytsche, D.; Leus, K.; Van Landeghem, M.; Goovaerts, E.; Vincze, L.; Detavernier, C.; et al. Sensing the Framework State and Guest Molecules in MIL-53(Al) via the Electron Paramagnetic Resonance Spectrum of VIV Dopant Ions. *Phys. Chem. Chem. Phys.* **2017**, *19*, 24545–24554.
(32) Giacobbe, C.; Lavigna, E.; Maspero, A.; Galli, S. Elucidating the CO2 Adsorption Mechanisms in the Triangular Channels of the Bis(Pyrazolate) MOF Fe2(BPEB)3 by in Situ

Synchrotron X-Ray Diffraction and Molecular Dynamics Simulations. *J. Mater. Chem. Mater. Energy Sustain.* **2017**, *5*, 16964–16975.
(33) Li, H.; Eddaoudi, M.; O'Keeffe, M.; Yaghi, O. M. Design and Synthesis of an Exceptionally Stable and Highly Porous Metal-Organic Framework. *Nature* **1999**, *402* (6759), 276–279.
(34) Prasad, T. K.; Suh, M. P. Control of Interpenetration and Gas-Sorption Properties of Metal-Organic Frameworks by a Simple Change in Ligand Design. *Chem. Eur. J.* **2012**, *18* (28), 8673–8680.
(35) Koh, K.; Van Oosterhout, J. D.; Roy, S.; Wong-Foy, A. G.; Matzger, A. J. Exceptional Surface Area from Coordination Copolymers Derived from Two Linear Linkers of Differing Lengths. *Chem. Sci.* **2012**, *3* (8), 2429.
(36) Lides, D., R. *CRC Handbook of Chemistry and Physics*, 83rd ed.; CRC Press LLC: Boca Raton, FL, 2002.

Chapter 3. Resolvation-Based Damage to Metal–Organic Frameworks and Approaches to Mitigation*

3.1 Introduction

Metal-organic frameworks, or MOFs, represent a promising class of materials for a wide variety of applications. Many potential MOF applications, including catalysis,[1,2] environmental remediation/pollutant capture,[3] separations,[4] and chemical sensing,[5] rely on the material interacting with species in the liquid phase. In such cases, and particularly in the area of MOF catalysis, it is the general practice for MOFs to be synthesized solvothermally, activated via solvent removal, and then resolvated via direct immersion in the relevant solvent.[6–15] We have recently outlined best practices for avoiding framework collapse during MOF activation – low-surface tension activation solvents such as hexane, perfluoropentane, and supercritical CO_2 ($scCO_2$) have been found to be the least harmful to fragile MOFs.[16,17] However, the reverse of this process, resolvation, has received little, if any, attention. From a practical standpoint, it is important to understand the limits of these materials in liquid-phase applications. As an example, if structural reorganization were to occur during resolvation, it could compromise the access of reactants to the catalytic centers leading to lower apparent activity than would be observed with pristine materials. A reasonable question to ask is if solvation of a dry MOF is any different than solvent exchange for an already-solvated MOF. Solvent exchange is extensively used as a step in MOF activation, and generally occurs from a higher surface tension solvent to a lower surface tension solvent.

*Adapted from Dodson, R.A.; Matzger, A.J. *ACS Mater. Lett.* **2019**, 1, 344-349.

Exchanging to low surface tension solvents is a necessary step for many MOFs as the high surface tension formamide solvents typically used in MOF synthesis have low volatility and cannot be removed without material degradation. It is unknown if increasing solvent surface tension has the potential to cause structural collapse, with the logical extreme being solvation of a dry MOF directly by the solvent of synthesis. Clearly chemical incompatibility is not present here, but there is, for example, the potential for capillary-force induced damage (Figure 3.1).

Herein, the structural impacts of MOF resolvation and best practices for doing so are outlined. The effect of transferring MOFs into solvents with increasing surface tensions via stepwise solvent exchange is also explored.

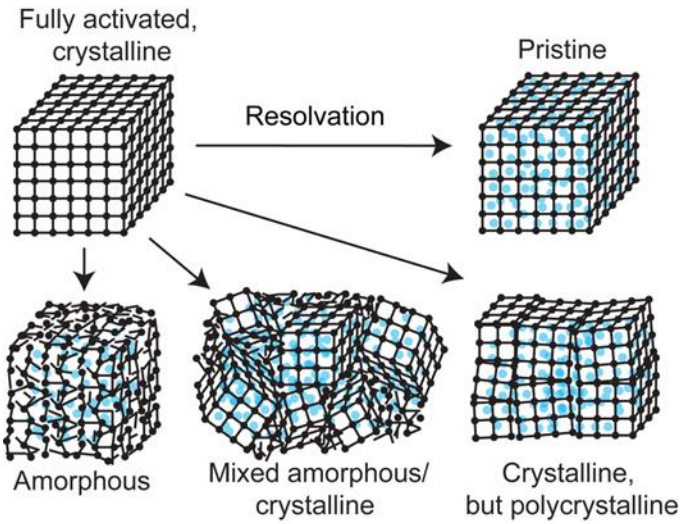

Figure 3.1. Possible effects of activated MOF resolvation.

A total of four MOF systems were examined: UMCM-9, IRMOF-3, FJI-1, and UiO-66 (Figure 3.2). UMCM-9[18] is a Zn_4O-based MOF known to exhibit moderate sensitivity to its activation solvent.[16] In addition to being based on Zn, which is a common structural metal in catalytically active MOFs,[19–25] UMCM-9 was chosen on the basis of this sensitivity, as it was expected that if the process of resolvation was destructive, it would be possible to access MOF products with varying degrees of structural degradation by choice of solvent. IRMOF-3[26] is also

based on the Zn_4O cluster, and was chosen for the catalytic activity imparted by its pendant amino group. IRMOF-3 has been used to catalyze reactions including Hantzsch couplings[27,28] and Claisen-Schmidt condensations,[29] and a modified version of the framework was used for *N*-arylation of heterocycles with aryl bromides.[30] While IRMOF-3 is topologically equivalent to UMCM-9, it contains shorter linkers and smaller pores, which are generally associated with greater structural stability. This is reflected in its standard activation protocol, which takes place from CH_2Cl_2. However, the highest surface area reported for this MOF resulted from $scCO_2$ activation,[17] indicating that the material may display sensitivity to its activation solvent and thus may also be sensitive to resolvation. FJI-1[31] was chosen as a system representative of very sensitive MOFs. Until recently, no effective activation protocol existed for this MOF other than $scCO_2$ treatment, characteristic of a very fragile material.[16] The final system, UiO-66,[32] was chosen as an example of a MOF with best-in-class stability. UiO-66 is highly thermally and chemically resistant,[32–34] making it useful as a reference by which to judge the other systems in

this study.

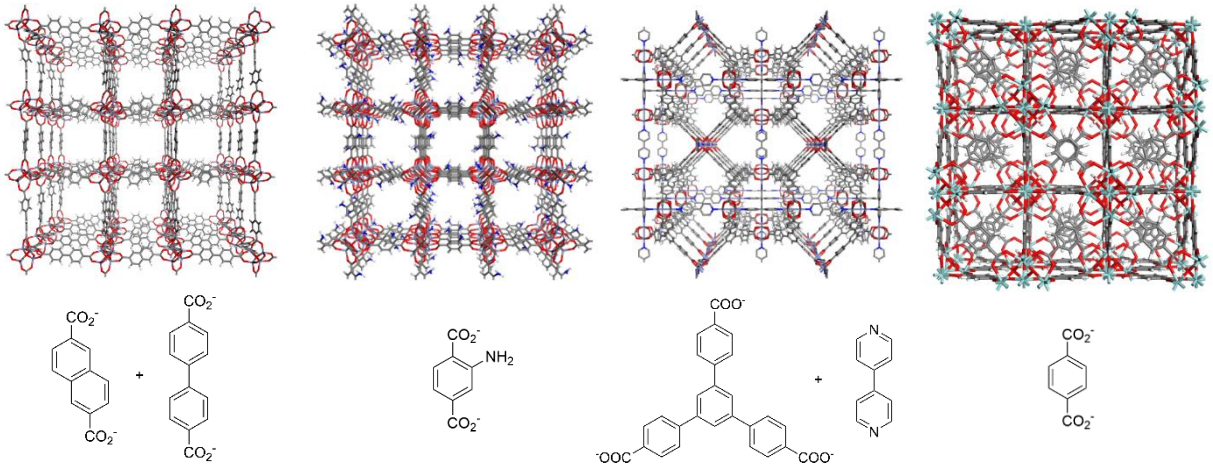

Figure 3.2. Structures (top) and linkers (bottom) of MOFs studied. Left to right: UMCM-9 (2,6-naphthalenedicarboxylate and 4,4'-biphenyldicarboxylate), IRMOF-3 (2-aminoterephthalate), FJI-1 (1,3,5-tris(4-carboxyphenyl)benzene and 4,4'-bipyridine), and UiO-66 (terephthalate).

3.2 Results and discussion

3.2.1 UMCM-9

UMCM-9 showed high sensitivity to choice of resolvation solvent. In particular, while resolvation with hexane and CH_2Cl_2 did not lead to significant changes in sample surface area, resolvation with THF, DMF, and DMSO all led to substantial surface area loss (Figure 3.3, see Appendix A for all isotherm data associated with this chapter). The fact that UMCM-9 did not show a surface area decrease upon resolvation with CH_2Cl_2 is surprising – when CH_2Cl_2 is used as an activation solvent for the MOF, the framework undergoes a surface area decrease of roughly 75%.[16] This suggests that while resolvation has destructive potential, it is to a much lesser degree than MOF activation. When considering the trends within THF, DMF, and DMSO, their damage induced tracks with surface tension values (THF: 26.40 mN m^{-1}, DMF: 37.10 mN m^{-1}, DMSO: 43.54 mN m^{-1}) as it does in the case of resolvation-induced collapse.[35]

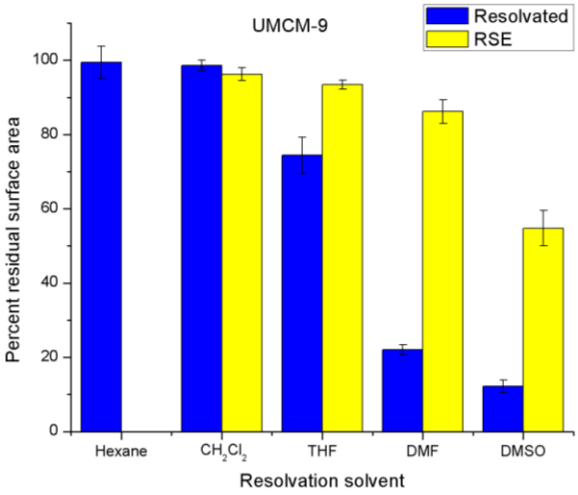

Figure 3.3. Percent residual surface area versus resolvation solvent for UMCM-9. Blue: direct resolvation. Yellow: resolvation via RSE from hexane.

The utility of the RSE method of resolvation is apparent when comparing the surface area values of UMCM-9 samples exposed to this treatment with that of those subjected to direct resolvation. While resolvation with THF led to a 26% decrease in surface area, resolvation with hexane followed by exchange into THF caused only a 7% decrease. This advantage was even more striking for the higher surface tension solvents DMF and DMSO, wherein the RSE protocol decreased surface area loss from 78% to 14%, and 88% to 45%, respectively. This structural degradation is reflected in the 2D-PXRD patterns obtained for each of the samples (Figure 3.4). While sharp spots indicative of retention of monocrystalline domains are apparent in the hexane resolvated sample, both CH_2Cl_2 samples, and the THF RSE sample, moderate broadening along the 2θ- and β-axes is visible in the diffractograms of the THF resolvated, DMF RSE, and DMSO RSE samples, consistent with decreased sample monocrystallinity and increased amorphous character. To ensure that resolvation rather than re-activation was responsible for the observed crystallographic changes, representative DMF resolvation and DMF RSE samples were also subjected to 2D-PXRD in their DMF-solvated state. (see Chapter 3.5 for full experimental details) In the case of the DMF and DMSO resolvated samples, complete broadening of spots to arcs along

the β-axis is observed, indicating that the crystalline domains within the samples have lost all orientational coherence, and that the samples have drastically increased in polycrystallinity. This observation combined with the decreased surface area and significant 2θ-axis peak broadening (see Chapter 3.5.5 for supplemental figures) indicates that the amorphous character of these samples has also increased.

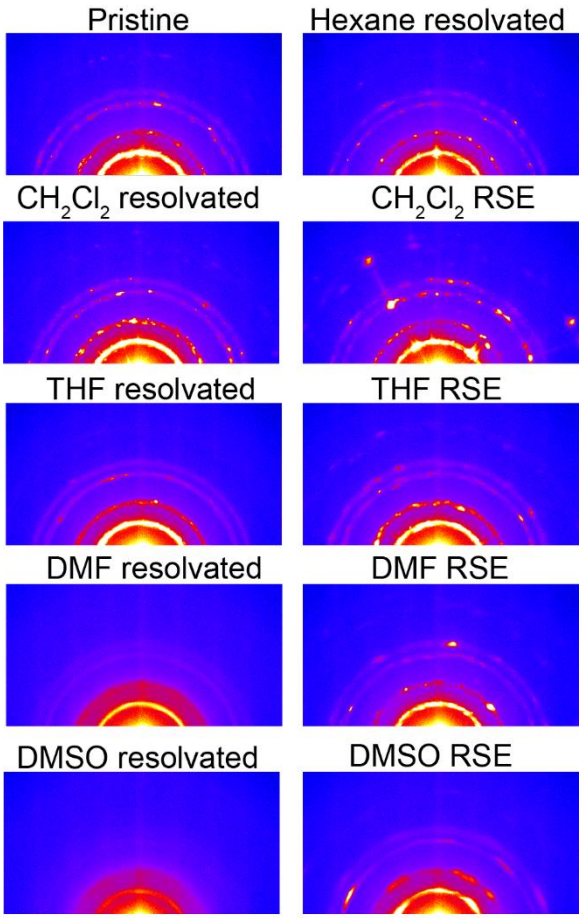

Figure 3.4. 2D-PXRD patterns for UMCM-9 samples subjected to either direct resolvation or RSE treatment. Top left: pristine UMCM-9 activated from hexane. Top right: pristine UMCM-9 activated from hexane, resolvated with hexane, and re-activated from hexane. Left: UMCM-9 resolvated with listed solvents, re-activated from hexane. Right: UMCM-9 resolvated with hexane, exchanged into listed solvents, and re-activated from hexane.

3.2.2 IRMOF-3

While less sensitive to resolvation-induced damage than UMCM-9, IRMOF-3 also undergoes degradation upon resolvation with high surface tension solvents; direct resolvation with

DMF and DMSO incurred surface area losses of 43% and 62%, respectively (Figure 3.5). This structural damage is reflected in the 2D-PXRD patterns of each of these products, which both show extensive streaking along the β-axis, indicating an almost complete loss of crystallite orientational coherence (Figure 3.6). While there is apparent damage incurred to the MOF upon resolvation by these high surface tension solvents, this damage is to a much lesser degree than was observed in UMCM-9, as neither sample showed full peak broadening to homogeneous arcs along the β-axis. The MOF was more resistant to THF resolvation, which only caused an 8% loss in surface area. This is comparable to resolvation with its activation solvent (CH_2Cl_2), which caused a 6% decrease in surface area. 2D-PXRD patterns for both of these samples showed slight peak broadening along the 2θ- and β-axes indicating a low amount of structural degradation, consistent with this low degree of surface area decrease.

As in the case of UMCM-9, the RSE protocol for resolvation was found to substantially decrease the damage done to the MOF compared to direct resolvation. In particular, RSE into DMF and DMSO led to surface area losses of only 15% and 21%, roughly a factor of 3 lower than the decrease induced by direct resolvation with these solvents. The RSE protocol also gave markedly less β-axis streaking in the 2D-PXRD patterns of both samples, indicating higher orientational coherence and thus a lower degree of structural degradation.

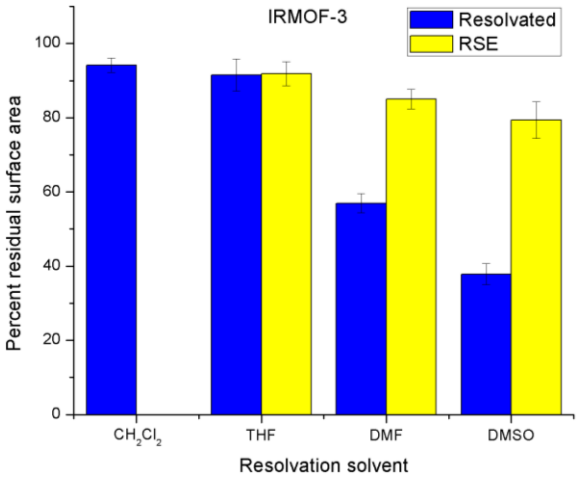

Figure 3.5. Percent residual surface area versus resolvation solvent for IRMOF-3. Blue: direct resolvation. Yellow: resolvation via RSE from hexane.

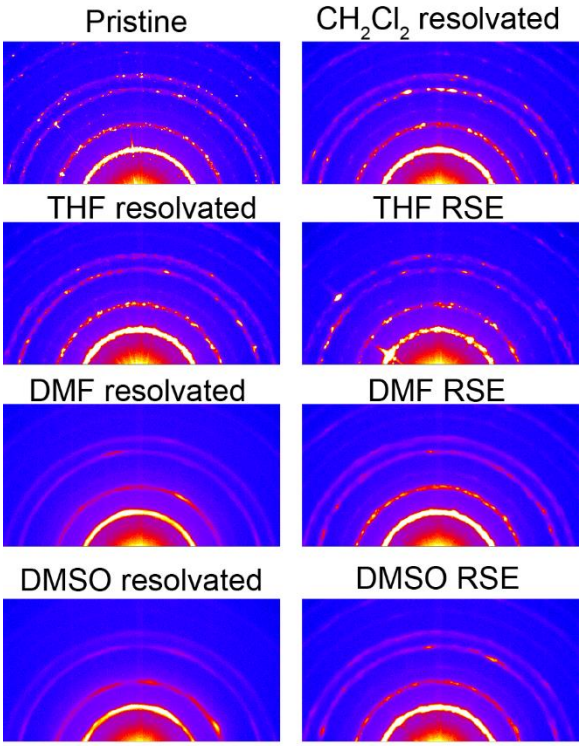

Figure 3.6. 2D-PXRD patterns for IRMOF-3 samples subjected to either direct resolvation or RSE treatment. Top left: pristine IRMOF-3 activated from hexane. Top right: pristine IRMOF-3 activated from CH_2Cl_2, resolvated with CH_2Cl_2, and re-activated from CH_2Cl_2. Left: IRMOF-3 resolvated with listed

solvents, re-activated from CH_2Cl_2. Right: IRMOF-3 resolvated with CH_2Cl_2, exchanged into listed solvents, and re-activated from CH_2Cl_2.

3.2.3 FJI-1

As discussed above, FJI-1 is a highly sensitive MOF, for which the most advanced activation techniques must be utilized. On this basis, it was expected that the framework would be entirely intolerant to resolvation by standard solvents. Indeed, resolvation with the majority of solvents tested led to major losses in surface area and changes in product 2D-PXRD patterns indicative of structural damage (Figures 3.7, 3.8). In particular, direct resolvation with THF, DMF, and DMSO led to surface area decreases of 57%, 66%, and 41%, as well as full β-axis peak broadening in the 2D-PXRD patterns, suggesting a complete loss of sample orientational coherence. Resolvation with CH_2Cl_2 caused a 31% loss in sample surface area, but relatively smaller changes in the 2D-PXRD pattern of the sample, which still showed distinct spots characteristic of retained monocrystalline domains. Remarkably, resolvation with hexane followed by $scCO_2$ activation caused less than 1% surface area loss – activation of the MOF from the same solvent causes a nearly complete loss in sample surface area.[16]

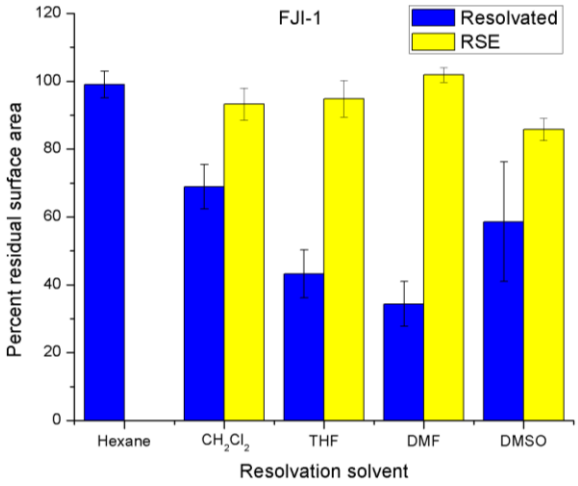

Figure 3.7. Percent residual surface area versus resolvation solvent for FJI-1. Blue: direct resolvation. Yellow: resolvation via RSE from hexane.

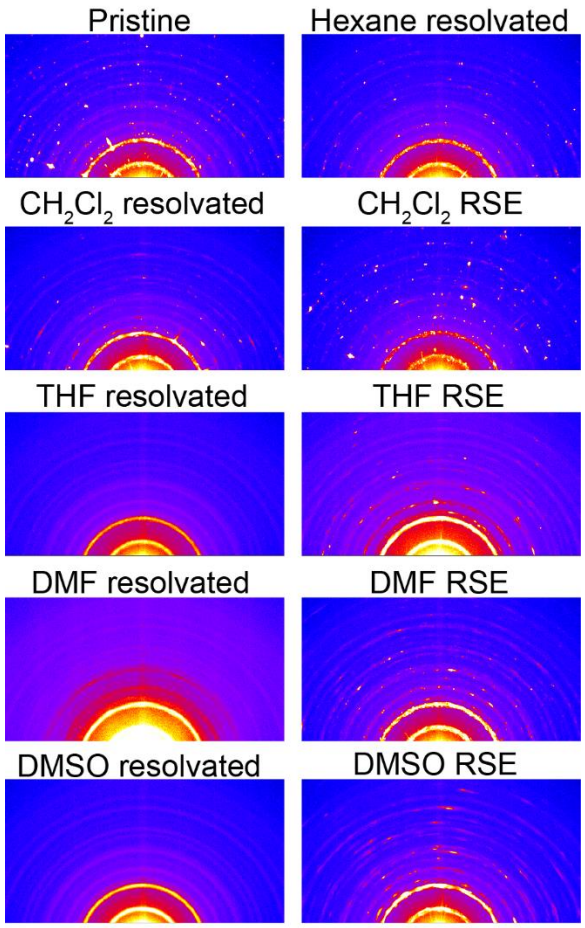

Figure 3.8. 2D-PXRD patterns for FJI-1 samples subjected to either direct resolvation or RSE treatment. Top left: pristine FJI-1 activated from $scCO_2$. Top right: pristine FJI-1 activated via $scCO_2$ from DMF, resolvated with hexane, and re-activated via $scCO_2$ from hexane. Left: FJI-1 resolvated with listed solvents,

re-activated via $scCO_2$. Right: FJI-1 resolvated with hexane, exchanged into listed solvents, and re-activated via $scCO_2$.

FJI-1 was found to be extraordinarily amenable to RSE as an alternative to direct resolvation. When subjected to RSE into CH_2Cl_2, THF, DMF, and DMSO, the MOF showed surface area losses of only 7%, 5%, 0%, and 14%, respectively. This hugely improved sample surface area retention was accompanied by correspondingly improved 2D-PXRD patterns, which showed only mild peak broadening along both axes, highlighting the preservation of MOF structural integrity after RSE. This result indicates that solvent exchange to higher surface tension solvents can be relatively benign, even in the case of highly unstable frameworks.

Of the three Zn-based MOFs studied, despite being the most sensitive to activation-induced collapse, FJI-1 was the least damaged by direct resolvation with DMSO, and showed comparable sensitivity to UMCM-9 when resolvated with DMF. FJI-1 was also the least impacted by RSE into DMF and DMSO. Despite this, FJI-1 was the most affected by resolvation with the lower surface tension solvents CH_2Cl_2 and THF. This break from established stability trends demonstrates the necessity of characterizing individual resolvation protocols for each system, as a resolvation method optimized for a one system may be suboptimal for another.

3.2.4 UiO-66

Due to the much higher stability of UiO-66, several changes were made to the solvents chosen for resolvation. Specifically, EtOH was chosen as the RSE solvent, and only high surface tension solvents were used (DMF, DMSO, H_2O). UiO-66 was tolerant of both RSE and direct resolvation with all solvents examined. This resolvation insensitivity is reflected both in the full retention of surface area and in the lack of visible changes in sample PXRD patterns. (See Chapter 3.5.5 for

associated figures) While consistent with the high stability of this MOF, this observation highlights that resolvation-induced damage is not a problem for all systems.

3.3 Conclusions

Resolvation-induced damage must be considered when utilizing MOFs in liquid phase applications. In addition to drawing attention to this fact, it was demonstrated that in cases where fragile MOFs are to be used, resolvation with low surface tension solvents followed by exchange into higher surface tension solvents is the least destructive route to resolvation. The utility of this method is highlighted by the case of FJI-1, an extremely fragile MOF, which could be nearly non-destructively resolvated via stepwise exchange starting from hexane. While optimized procedures should be developed on a system-by-system basis, this work provides a rationally implementable protocol from which to begin this optimization. Future studies should examine the same phenomenon in other important classes of MOFs, such as those containing coordinatively unsaturated metal sites. Paying attention to the role of resolvation offers the distinct benefit of ensuring MOF function is maximized for a given material in a particular solvent system and that performance results are not convoluted by solvation-induced framework damage.

3.4 Methods

To test the structural impact of MOF resolvation, samples were activated according to standard practices for each system and then submerged in a variety of solvents. UMCM-9 was activated from hexane, IRMOF-3 was activated from CH_2Cl_2, FJI-1 was activated from DMF via flowing $scCO_2$, and UiO-66 was activated from EtOH (additional details regarding MOF activation are given in Chapter 3.5). After resolvation, samples were allowed to equilibrate for ~20 minutes and were then exchanged into their activation solvent. In cases where the resolvation solvent and

the activation solvent were immiscible (i.e. DMF and hexane), CH_2Cl_2 was used as an intermediate solvent. Samples were then re-activated in an identical fashion to their initial activation, and subjected to surface area analysis (via N_2 sorption) and two-dimensional powder X-ray diffraction (2D-PXRD). The exception to this general protocol is FJI-1, which was instead activated via flowing $scCO_2$ directly from the resolvation solvent. To determine the efficacy of achieving resolvation with high surface tension solvents via stepwise exchange from lower surface tension solvents, a similar procedure was utilized; activated MOFs were resolvated with their activation solvent, then transferred to higher surface tension solvents via stepwise exchange. As this method represents the reverse of standard solvent exchange methods for MOFs, with the use of subsequently higher surface tension solvents rather than lower, this protocol is termed "reverse solvent exchange" and will be denoted as RSE throughout this text. After being subjected to RSE, samples were then treated in the same fashion as above, with identical washing steps and subsequent re-activation.

3.5 Supplemental Information

3.5.1 Reagents

Zinc perchlorate hexahydrate (Alfa Aesar, reagent grade), zirconium(IV) chloride (Strem, sublimed grade), 1,4-benzenedicarboxylic acid (H_2bdc, Fisher Scientific, 98%), 2-aminoterephthalic acid (H_2bdc-NH_2, Sigma-Aldrich, 99%), 2,6-naphthalenedicarboxylic acid (H_2ndc, TCI America, 98%), 4,4'-biphenyldicarboxylic acid (H_2bpdc, Acros Organics, 98%), 1,3,5-tri(4-carboxyphenyl)benzene (H_3btb, Alfa Aesar, 97%), 4,4'-bipyridine (4,4'-bpy, Acros Organics, 98%), ethanol (Decon Laboratories, anhydrous), hydrochloric acid (Fisher Scientific, certified ACS plus), and fluoroboric acid (Acros Organics, 50 wt% solution in water) were used as received. Zinc nitrate hexahydrate (Fisher Scientific, ACS grade) was partially dehydrated by

room temperature evacuation (~16 hr, <0.01 Torr) to yield zinc nitrate tetrahydrate (verified by thermogravimetric analysis). Hexane (Fisher Scientific, anhydrous), dichloromethane (CH_2Cl_2, Fisher scientific, HPLC grade), tetrahydrofuran (THF, Fisher Scientific, HPLC grade), *N*,*N*-dimethylformamide (DMF, Fisher Scientific, 99.5%), and dimethyl sulfoxide (DMSO, Fisher Scientific, HPLC grade) were stored over activated 4 Å molecular sieves to minimize water content. The dryness of these solvents was monitored by Karl Fischer titration (<10 ppm H_2O). *N*,*N*-Diethylformamide (DEF, TCI America, >99.0%) was purified by storage on activated charcoal for ~1 month followed by removal of impurities via silica gel column. Deionized water was used without further purification.

3.5.2 Syntheses

Each MOF synthesis was preceded by dissolution of reagents by sonication and was carried out in a 20 mL scintillation vial sealed with a PTFE-lined cap, and the washing procedures for each MOF were identical. The as-synthesized crystals were removed from the reaction vial and washed with DMF (3 × 10 mL) and then washed (3 × 10 mL) with the desired activation solvent as described below. Procedures specific to individual MOFs are included below:

Synthesis of UMCM-9. H_2ndc (29.1 mg, 0.135 mmol), H_2bpdc (36.8 mg, 0.152 mmol), and $Zn(NO_2)_3 \cdot 4H_2O$ (216.0 mg, 0.826 mmol) were dissolved in DEF (6.7 mL) and NMP (13.3 mL). The reaction was performed at 85 °C for 7 days. Prior to activation, UMCM-9 was washed 3× with DMF, 3× with CH_2Cl_2, then 3× with hexane. Activation was performed by room temperature evacuation of hexane from the MOF (~0.001 Torr) for 16 hrs.

Synthesis of IRMOF-3. H_2bdc-NH_2 (75.0 mg, 0.414 mmol) and $Zn(NO_2)_3 \cdot 4H_2O$ (300.0 mg, 1.147 mmol) were dissolved in DMF (10 mL). The reaction was performed at 100 °C for 16 hours. Prior

to activation, IRMOF-3 was washed 3× with DMF, then 3× with CH_2Cl_2. Activation was performed by room temperature evacuation of CH_2Cl_2 from the MOF (~0.001 Torr) for 16 hrs.

Synthesis of FJI-1. H_3btb (175.0 mg, 0.399 mmol), 4,4'-bpy (47.0 mg, 0.301 mmol) and $Zn(ClO_4)_2 \cdot 6H_2O$ (223.0 mg, 0.599 mmol) were dissolved in DMF (10 mL) with fluoroboric acid (0.1 mL). The reaction was performed at 85 °C for 72 hours. Prior to activation, FJI-1 was washed 3× with DMF. Activation was performed by flowing $scCO_2$ treatment for 4 hrs (backpressure regulator set at 100 bar; 1 hr at 2 mL min^{-1} at ambient temperature, 1 hr at 2 mL min^{-1} at 55 °C, 2 hrs at 1 mL min^{-1} at 55 °C).

Synthesis of UiO-66. H_2bdc (123.0 mg, 0.740 mmol) and $ZrCl_4$ (125.0 mg, 0.536 mmol) were dissolved in DMF (15 mL) with hydrochloric acid (1 mL). The reaction was performed at 85 °C for 16 hours. Prior to activation, UiO-66 was washed 3× with DMF, then 3× with EtOH. Activation was performed by evacuation of EtOH from the MOF (~0.001 Torr) for 16 hrs at 120 °C.

3.5.3 Experimental details

PXRD patterns were collected in 1 mm diameter Kapton capillaries using a Rigaku SmartLab X-ray diffractometer (Cu K_α radiation) operating in point focus mode outfitted with a Pilatus 2D detector. Patterns were collected between 3-40 °2Θ, with 8-minute exposure times. Due to the height error associated with sample-filled 1 mm capillaries, data were refined prior to analysis by adjusting the beam center position such that the primary peak of the pristine sample aligned with the known value for each MOF. This correction was applied uniformly across each set of MOFs to ensure that any peak shifts would be apparent. Sample surface areas were calculated using the BET method from N_2 sorption isotherms measured on a Quantachrome NOVA 4200 gas sorption analyzer.

3.5.4 Resolvation protocols

Generally, resolvation was performed by direct submersion of activated, pristine MOF samples (~30 mg) in the solvent under examination (2 mL). Following a 20-minute equilibration period (after which samples sank to the bottom of the vial and bubbles were no longer observed to emerge from the MOFs), the solvent was decanted and replaced with activation solvent appropriate for the MOF (3× washes/4 mL/20 min). After equilibration with the third wash of the activation solvent, MOFs were re-activated as described above. Deviations were made from this protocol in two cases:

1. UMCM-9 was activated from hexane, which is immiscible with DMF and DMSO. When UMCM-9 was resolvated with these two solvents, the samples were washed 3× with CH_2Cl_2 prior to the 3× washes with hexane.
2. FJI-1 was re-activated via flowing $scCO_2$ directly from the resolvation solvent.

Reverse solvent exchange (RSE) was performed in a similar fashion to resolvation. Rather than direct submersion in the solvent to be studied, the MOFs were first resolvated with their activation solvent (or hexane, in the case of FJI-1). For UMCM-9 RSE into DMF or DMSO, this therefore required 6 washing steps with CH_2Cl_2, in order to facilitate the hexane → DMF/DMSO exchange as well as the DMF/DMSO → hexane exchange. Similarly, FJI-1 RSE into DMF or DMSO required 3 washing steps with CH_2Cl_2, in order to facilitate the hexane → DMF/DMSO exchange. The exact steps for each resolvation/RSE treatment are given in Tables 3.1-3.8.

Table 3.1. UMCM-9 resolvation washing steps.

Wash #	Hexane resolvation	CH_2Cl_2 resolvation	THF resolvation	DMF resolvation	DMSO resolvation
1	Hexane	CH_2Cl_2	THF	DMF	DMSO
2		Hexane	Hexane	CH_2Cl_2	CH_2Cl_2
3		Hexane	Hexane	CH_2Cl_2	CH_2Cl_2
4		Hexane	Hexane	CH_2Cl_2	CH_2Cl_2
5				Hexane	Hexane
6				Hexane	Hexane

7				Hexane	Hexane

Table 3.2. UMCM-9 RSE washing steps.

Wash #	CH_2Cl_2 RSE	THF RSE	DMF RSE	DMSO RSE
1	Hexane	Hexane	Hexane	Hexane
2	CH_2Cl_2	THF	CH_2Cl_2	CH_2Cl_2
3	CH_2Cl_2	THF	CH_2Cl_2	CH_2Cl_2
4	CH_2Cl_2	THF	CH_2Cl_2	CH_2Cl_2
5	Hexane	Hexane	DMF	DMSO
6	Hexane	Hexane	DMF	DMSO
7	Hexane	Hexane	DMF	DMSO
8			CH_2Cl_2	CH_2Cl_2
9			CH_2Cl_2	CH_2Cl_2
10			CH_2Cl_2	CH_2Cl_2
11			Hexane	Hexane
12			Hexane	Hexane
13			Hexane	Hexane

Table 3.3. IRMOF-3 resolvation washing steps.

Wash #	CH_2Cl_2 resolvation	THF resolvation	DMF resolvation	DMSO resolvation
1	CH_2Cl_2	THF	DMF	DMSO
2		CH_2Cl_2	CH_2Cl_2	CH_2Cl_2
3		CH_2Cl_2	CH_2Cl_2	CH_2Cl_2
4		CH_2Cl_2	CH_2Cl_2	CH_2Cl_2

Table 3.4. IRMOF-3 RSE washing steps.

Wash #	THF RSE	DMF RSE	DMSO RSE
1	CH_2Cl_2	CH_2Cl_2	CH_2Cl_2
2	THF	DMF	DMSO
3	THF	DMF	DMSO
4	THF	DMF	DMSO
5	CH_2Cl_2	CH_2Cl_2	CH_2Cl_2
6	CH_2Cl_2	CH_2Cl_2	CH_2Cl_2
7	CH_2Cl_2	CH_2Cl_2	CH_2Cl_2

Table 3.5. FJI-1 resolvation washing steps.

Wash #	Hexane resolvation	CH_2Cl_2 resolvation	THF resolvation	DMF resolvation	DMSO resolvation
1	Hexane	CH_2Cl_2	THF	DMF	DMSO

Table 3.6. FJI-1 RSE washing steps.

Wash #	CH_2Cl_2 RSE	THF RSE	DMF RSE	DMSO RSE
1	Hexane	Hexane	Hexane	Hexane
2	CH_2Cl_2	THF	CH_2Cl_2	CH_2Cl_2
3	CH_2Cl_2	THF	CH_2Cl_2	CH_2Cl_2
4	CH_2Cl_2	THF	CH_2Cl_2	CH_2Cl_2
5			DMF	DMSO
6			DMF	DMSO
7			DMF	DMSO

Table 3.7. UiO-66 resolvation washing steps.

Wash #	EtOH resolvation	DMF resolvation	DMSO resolvation	H_2O resolvation
1	EtOH	DMF	DMSO	H_2O
2		EtOH	EtOH	EtOH
3		EtOH	EtOH	EtOH
4		EtOH	EtOH	EtOH

Table 3.8. UiO-66 RSE washing steps.

Wash #	DMF RSE	DMSO RSE	H_2O RSE
1	EtOH	EtOH	EtOH
2	DMF	DMSO	H_2O
3	DMF	DMSO	H_2O
4	DMF	DMSO	H_2O
5	EtOH	EtOH	EtOH
6	EtOH	EtOH	EtOH
7	EtOH	EtOH	EtOH

3.5.5. Additional figures

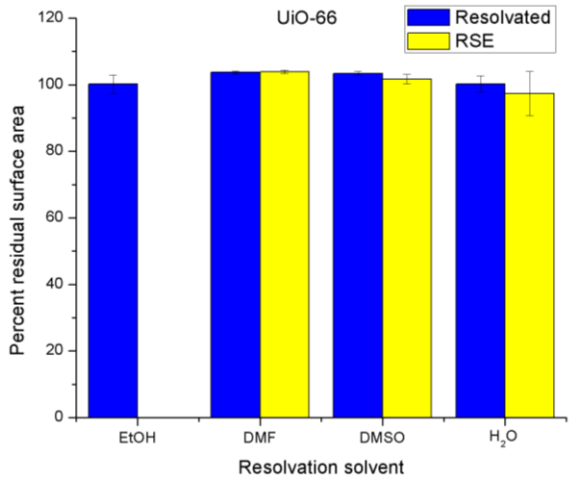

Figure 3.9. Percent residual surface area versus resolvation solvent for UiO-66. Blue: direct resolvation. Yellow: resolvation via RSE from hexane.

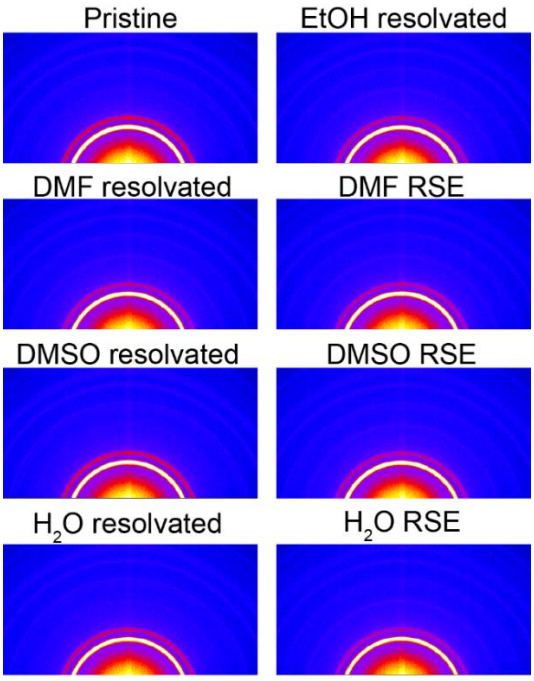

Figure 3.10. 2D-PXRD patterns for UiO-66 samples subjected to either direct resolvation or RSE treatment. Top left: pristine UiO-66 activated from EtOH. Top right: pristine UiO-66 activated from EtOH, resolvated with EtOH, and re-activated from EtOH. Left: UiO-66 resolvated with listed solvents, re-activated from EtOH. Right: UiO-66 resolvated with EtOH, exchanged into listed solvents, and re-activated from EtOH. UiO-66 was synthesized according to a common protocol which yields a microcrystalline powder; this synthesis was chosen with the goal of studying the behavior of a material that is most relevant to the field.

However, the small crystallite size of this material makes it impossible to distinguish β-axis changes in the 2D-PXRD patterns of the material

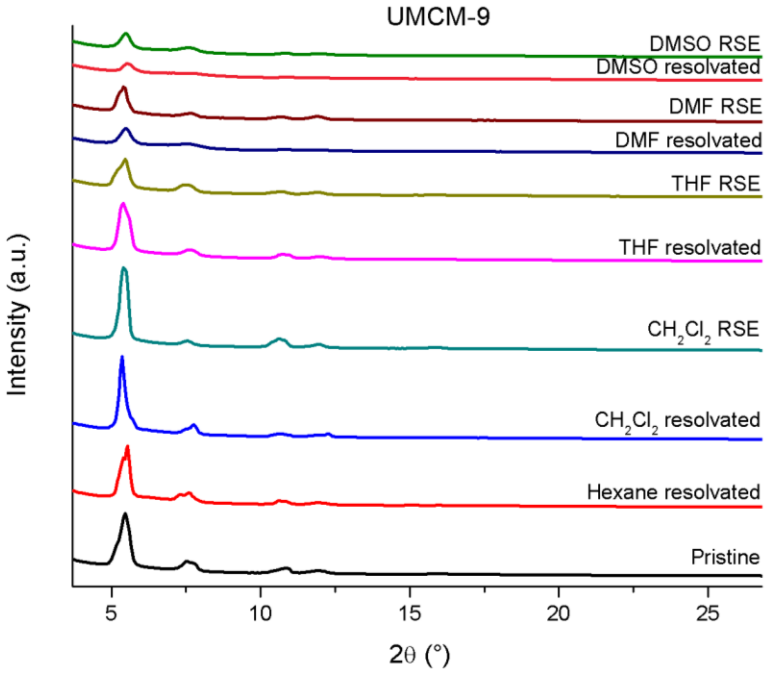

Figure 3.11. Diffracted X-ray intensity as a function of 2Θ for the UMCM-9 resolvation and RSE samples studied. Greater retention of 10-15 °2Θ peaks can be observed for high surface tension solvent (DMF, DMSO) RSE samples relative to the direct resolvation samples, consistent with better retention of sample crystallinity.

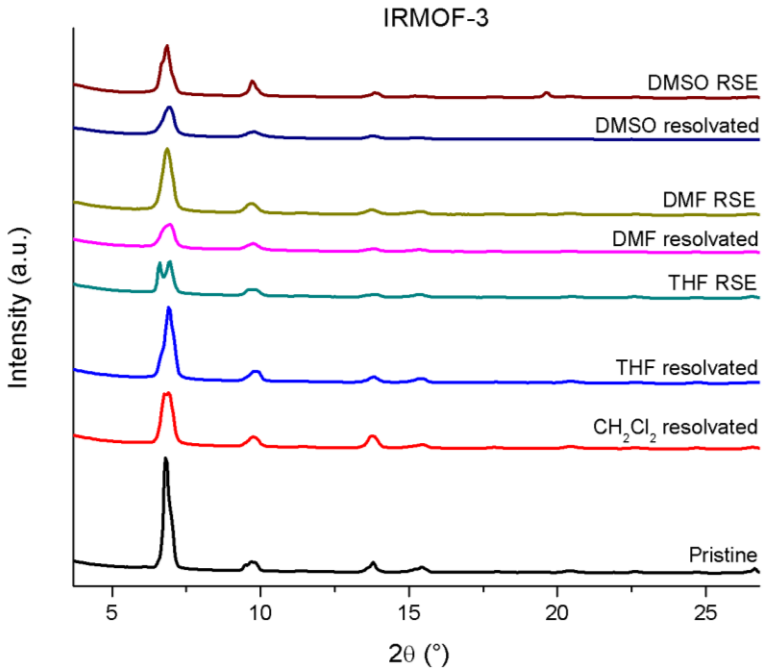

Figure 3.12. Diffracted X-ray intensity as a function of 2Θ for the IRMOF-3 resolvation and RSE samples studied. Greater retention of 20-25 °2Θ peaks can be observed for high surface tension solvent (DMF, DMSO) RSE samples relative to the direct resolvation samples, consistent with better retention of sample crystallinity.

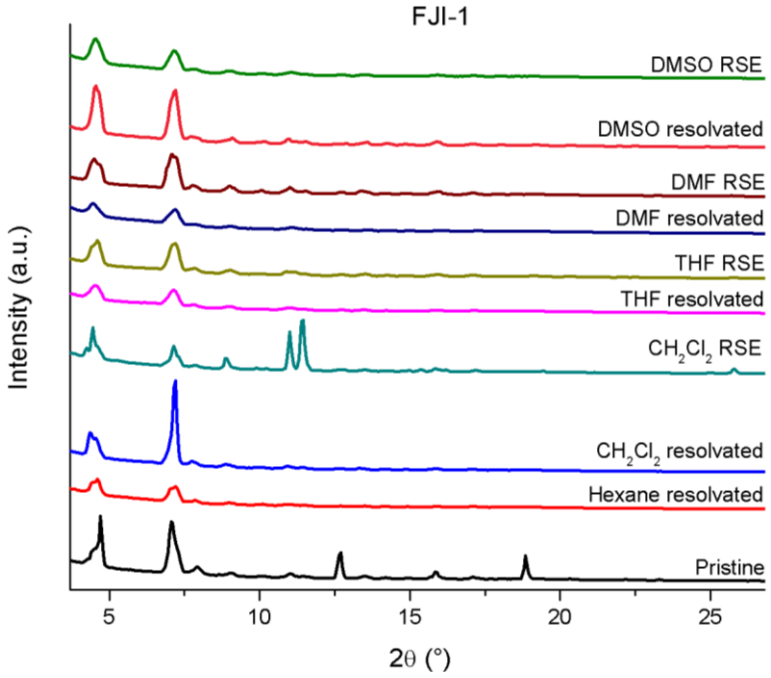

Figure 3.13. Diffracted X-ray intensity as a function of 2Θ for the FJI-1 resolvation and RSE samples studied. Differences between peak intensities in samples which maintained near full surface area (e.g. pristine vs. CH_2Cl_2 RSE) are partially attributed to relatively high sample preferred orientation in prepared

FJI-1 capillaries due to incomplete sample grinding, a requisite for determining changes in sample polycrystallinity via 2D-PXRD, as well as much larger initial crystal sizes (~5 mm).

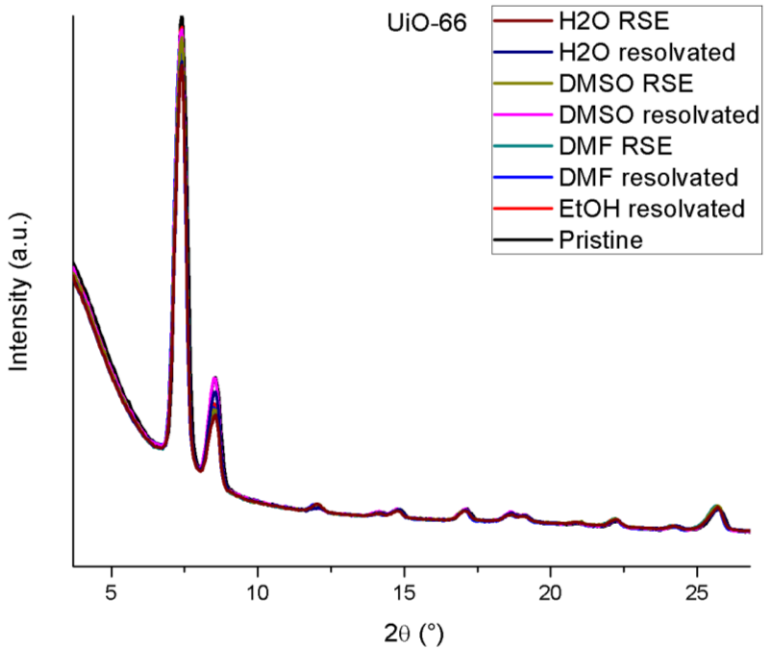

Figure 3.14. Diffracted X-ray intensity as a function of 2Θ for the UiO-66 resolvation and RSE samples studied. Diffraction patterns are overlaid to demonstrate their strong similarity. The only observed changes in intensity are attributed to small differences in the quantity of sample packed into the capillaries.

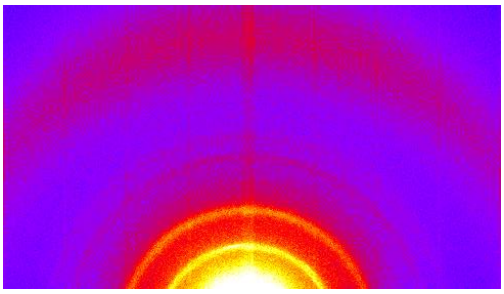

Figure 3.15. 2D-PXRD pattern for a DMF-solvated UMCM-9 sample subjected to direct DMF resolvation.

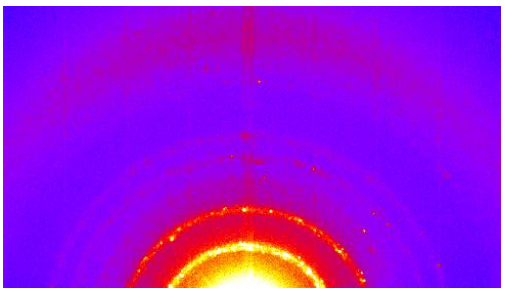

Figure 3.16. 2D-PXRD pattern for a DMF-solvated UMCM-9 sample subjected to DMF resolvation via RSE.

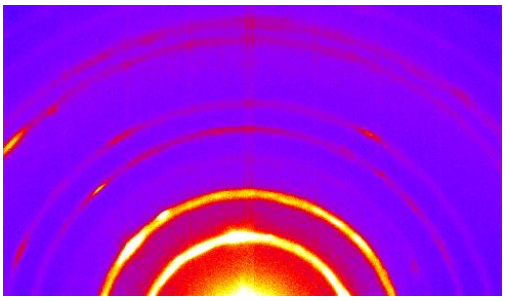

Figure 3.17. 2D-PXRD pattern for a DMF-solvated IRMOF-3 sample subjected to direct DMF resolvation.

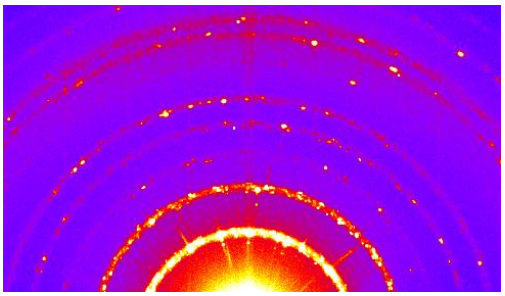

Figure 3.18. 2D-PXRD pattern for a DMF-solvated IRMOF-3 sample subjected to DMF resolvation via RSE.

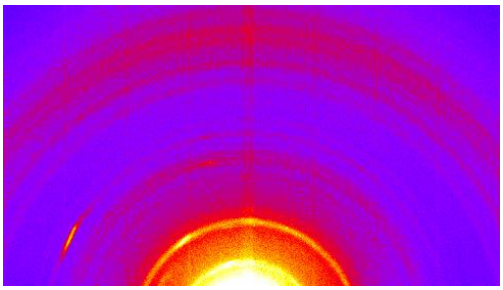

Figure 3.19. 2D-PXRD pattern for a DMF-solvated FJI-1 sample subjected to direct DMF resolvation.

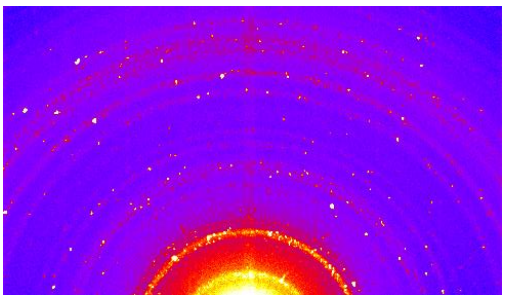

Figure 3.20. 2D-PXRD pattern for a DMF-solvated FJI-1 sample subjected to DMF resolvation via RSE.

3.5.6. BET surface area values

Table 3.9. UMCM-9 BET surface area values. Pristine values associated with each sample are given in parentheses.

Resolvation treatment	Trial 1	Trial 2	Trial 3
Hexane resolvated	4871.445 (4886.229)	4597.616 (4887.313)	4959.377 (4743.236)
CH_2Cl_2 resolvated	4839.069 (4886.229)	4723.449 (4887.313)	4748.670 (4743.236)
THF resolvated	3416.257 (4886.229)	3523.347 (4887.313)	3850.170 (4743.236)
DMF resolvated	1168.332 (4886.229)	1018.117 (4887.313)	1014.082 (4743.236)
DMSO resolvated	703.259 (4886.229)	582.618 (4887.313)	485.994 (4743.236)
CH_2Cl_2 RSE	4658.780 (4743.236)	4479.282 (4639.937)	4361.019 (4639.937)
THF RSE	4363.279 (4743.236)	4408.088 (4639.937)	4327.470 (4639.937)
DMF RSE	4282.618 (4743.236)	3982.966 (4639.937)	3823.027 (4639.937)
DMSO RSE	2744.301 (4743.236)	2710.679 (4639.937)	2230.496 (4639.937)

Table 3.10. IRMOF-3 BET surface area values. Pristine values associated with each sample are given in parentheses.

Resolvation treatment	Trial 1	Trial 2	Trial 3
CH_2Cl_2 resolvated	2736.511 (2846.728)	2612.838 (2758.320)	2493.790 (2723.582)
THF resolvated	2777.013 (2846.728)	2461.740 (2758.320)	2391.284 (2723.582)
DMF resolvated	1564.853 (2846.728)	1526.210 (2758.320)	1650.651 (2723.582)
DMSO resolvated	990.234 (2846.728)	1029.688 (2758.320)	1129.823 (2723.582)
THF RSE	2451.428 (2723.582)	2461.384 (2758.320)	2625.397 (2723.582)
DMF RSE	2220.588 (2723.582)	2358.293 (2758.320)	2395.788 (2723.582)
DMSO RSE	2112.042 (2723.582)	2055.453 (2758.320)	2345.879 (2723.582)

Table 3.11. FJI-1 BET surface area values. Pristine values associated with each sample are given in parentheses.

Resolvation treatment	Trial 1	Trial 2	Trial 3
Hexane resolvated	5141.839 (4922.309)	4309.985 (4512.863)	4617.747 (4756.530)
CH_2Cl_2 resolvated	3051.493 (4736.240)	3156.182 (4922.309)	3524.140 (4512.863)
THF resolvated	2167.888 (4736.240)	1646.980 (4922.309)	2474.469 (4922.309)
DMF resolvated	1403.073 (4736.240)	1461.875 (4922.309)	2080.085 (4756.530)
DMSO resolvated	3498.297 (4922.309)	1658.828 (4922.309)	3376.057 (4756.530)
CH_2Cl_2 RSE	4880.517 (4922.309)	4310.117 (4922.309)	4207.075 (4512.863)
THF RSE	4344.884 (4922.309)	4672.283 (4922.309)	4822.559 (4756.530)
DMF RSE	4690.209 (4736.240)	4624.500 (4512.863)	4954.712 (4756.530)
DMSO RSE	4447.164 (4922.309)	3726.097 (4512.863)	4023.650 (4756.530)

Table 3.12. UiO-66 BET surface area values. Pristine values associated with each sample are given in parentheses.

Resolvation treatment	Trial 1	Trial 2	Trial 3
EtOH resolvated	1535.346 (1544.766)	1504.327 (1544.766)	1604.913 (1544.766)
DMF resolvated	1594.223 (1544.766)	1600.819 (1544.766)	1612.196 (1544.766)
DMSO resolvated	1588.651 (1544.766)	1610.171 (1544.766)	1593.999 (1544.766)

H_2O resolvated	1505.456 (1544.766)	1543.641 (1544.766)	1597.201 (1544.766)
DMF RSE	1706.754 (1648.81)	1599.434 (1544.766)	1616.194 (1544.766)
DMSO RSE	1643.574 (1648.81)	1589.337 (1544.766)	1582.507 (1544.766)
H_2O RSE	1418.001 (1648.81)	1548.770 (1544.766)	1599.676 (1544.766)

3.6 References

(1) Jiao, L.; Wang, Y.; Jiang, H.-L.; Xu, Q. Metal-Organic Frameworks as Platforms for Catalytic Applications. *Adv. Mater.* **2018**, *30*, 1703663.

(2) Lee, J.; Farha, O. K.; Roberts, J.; Scheidt, K. A.; Nguyen, S. T.; Hupp, J. T. Metal–Organic Framework Materials as Catalysts. *Chem. Soc. Rev.* **2009**, *38*, 1450–1459.

(3) Cychosz, K. A.; Matzger, A. J. Water Stability of Microporous Coordination Polymers and the Adsorption of Pharmaceuticals from Water. *Langmuir* **2010**, *26*, 17198–17202.

(4) Cychosz, K. A.; Wong-Foy, A. G.; Matzger, A. J. Liquid Phase Adsorption by Microporous Coordination Polymers: Removal of Organosulfur Compounds. *J. Am. Chem. Soc.* **2008**, *130*, 6938–6939.

(5) Müller-Buschbaum, K.; Beuerle, F.; Feldmann, C. MOF Based Luminescence Tuning and Chemical/Physical Sensing. *Microporous Mesoporous Mater.* **2015**, *216*, 171–199.

(6) Deng, Q.; Wen, X.; Zhang, P. Pd/Cu-MOF as a Highly Efficient Catalyst for Synthesis of Cyclopentanone Compounds from Biomass-Derived Furanic Aldehydes. *Catal. Commun.* **2019**, *126*, 5–9.

(7) Gómez-Avilés, A.; Peñas-Garzón, M.; Bedia, J.; Dionysiou, D. D.; Rodríguez, J. J.; Belver, C. Mixed Ti-Zr Metal-Organic-Frameworks for the Photodegradation of Acetaminophen under Solar Irradiation. *Appl. Catal., B* **2019**, *253*, 253–262.

(8) Wang, Y.; Feng, L.; Pang, J.; Li, J.; Huang, N.; Day, G. S.; Cheng, L.; Drake, H. F.; Wang, Y.; Lollar, C.; et al. Photosensitizer-Anchored 2D MOF Nanosheets as Highly Stable and Accessible Catalysts toward Artemisinin Production. *Adv. Sci.* **2019**, *6*, 1802059.

(9) Valiente, A.; Carrasco, S.; Sanz-Marco, A.; Tai, C.-W.; Bermejo Gómez, A.; Martín-Matute, B. Aerobic Homocoupling of Arylboronic Acids Catalyzed by Regenerable Pd(II)@MIL-88B-NH2(Cr). *ChemCatChem* **2019,** *11*.

(10) Zhang, X.-L.; Zhang, D.-X.; Chang, G.-G.; Ma, X.-C.; Wu, J.; Wang, Y.; Yu, H.-Z.; Tian, G.; Chen, J.; Yang, X.-Y. Bimetallic (Zn/Co) MOFs-Derived Highly Dispersed Metallic Co/HPC for Completely Hydrolytic Dehydrogenation of Ammonia–Borane. *Ind. Eng. Chem. Res.* **2019,** 58, 7209–7216.

(11) Ju, S.; Yusuf, M.; Jang, S.; Kang, H.; Kim, S.; Park, K. H. Simple Transformation of Hierarchical Hollow Structures by Reduction of Metal-Organic Frameworks and Their Catalytic Activity in Oxidation of Benzyl Alcohol. *Chem. Eur. J.* **2019,** 25, 7852–7859.

(12) Hao, L.; Hurlock, M. J.; Li, X.; Ding, G.; Kriegsman, K. W.; Guo, X.; Zhang, Q. Efficient Oxidative Desulfurization Using a Mesoporous Zr-Based MOF. *Catal. Today*, https://doi.org/10.1016/j.cattod.2019.04.012.

(13) Doan, S. H.; Tran, C. B.; Cao, An. L. N.; Le, N. T. H.; Phan, N. T. S. A New Pathway to 2-Arylbenzoxazoles and 2-Arylbenzothiazoles Via One-Pot Oxidative Cyclization Reactions Under Iron-Organic Framework Catalysis. *Catal. Lett.* **2019,** 149, 2053–2063.

(14) Niu, Z.; Zhang, W.; Lan, P. C.; Aguila, B.; Ma, S. Promoting Frustrated Lewis Pairs for Heterogeneous Chemoselective Hydrogenation via the Tailored Pore Environment within Metal-Organic Frameworks. *Angew. Chem. Int. Ed.* **2019,** 58, 7420–7424.

(15) Li, B.; Ju, Z.; Zhou, M.; Su, K.; Yuan, D. A Reusable MOF Supported Single-Site Zinc(II) Catalyst for Efficient Intramolecular Hydroamination of *o*-Alkynylanilines. *Angew. Chem. Int. Ed.* **2019,** 58, 7687–7691.

(16) Ma, J.; Kalenak, A. P.; Wong-Foy, A. G.; Matzger, A. J. Rapid Guest Exchange and Ultra-Low Surface Tension Solvents Optimize Metal-Organic Framework Activation. *Angew. Chem. Int. Ed.* **2017**, *56* (46), 14618–14621.
(17) Liu, B.; Wong-Foy, A. G.; Matzger, A. J. Rapid and Enhanced Activation of Microporous Coordination Polymers by Flowing Supercritical CO_2. *Chem. Commun.* **2013**, *49*, 1419–1421.
(18) Koh, K.; Van Oosterhout, J. D.; Roy, S.; Wong-Foy, A. G.; Matzger, A. J. Exceptional Surface Area from Coordination Copolymers Derived from Two Linear Linkers of Differing Lengths. *Chem. Sci.* **2012**, *3*, 2429–2432.
(19) Sabo, M.; Henschel, A.; Fröde, H.; Klemm, E.; Kaskel, S. Solution Infiltration of Palladium into MOF-5: Synthesis, Physisorption and Catalytic Properties. *J. Mater. Chem.* **2007**, *17*, 3827–3832.
(20) Stubbs, A. W.; Braglia, L.; Borfecchia, E.; Meyer, R. J.; Román- Leshkov, Y.; Lamberti, C.; Dincă, M. Selective Catalytic Olefin Epoxidation with Mn^{II} -Exchanged MOF-5. *ACS Catal.* **2018**, *8*, 596–601.
(21) Opelt, S.; Türk, S.; Dietzsch, E.; Henschel, A.; Kaskel, S.; Klemm, E. Preparation of Palladium Supported on MOF-5 and Its Use as Hydrogenation Catalyst. *Catal. Commun.* **2008**, *9*, 1286–1290.
(22) Phan, N. T. S.; Le, K. K. A.; Phan, T. D. MOF-5 as an Efficient Heterogeneous Catalyst for Friedel–Crafts Alkylation Reactions. *Appl. Catal., A* **2010**, *382*, 246–253.
(23) Gao, S.; Zhao, N.; Shu, M.; Che, S. Palladium Nanoparticles Supported on MOF-5: A Highly Active Catalyst for a Ligand- and Copper-Free Sonogashira Coupling Reaction. *Appl. Catal., A* **2010**, *388*, 196–201.
(24) Vu, T. V.; Kosslick, H.; Schulz, A.; Harloff, J.; Paetzold, E.; Lund, H.; Kragl, U.; Schneider, M.; Fulda, G. Influence of the Textural Properties of Rh/MOF-5 on the Catalytic Properties in the Hydroformylation of Olefins. *Microporous Mesoporous Mater.* **2012**, *154*, 100–106.
(25) Song, F.; Wang, C.; Falkowski, J. M.; Ma, L.; Lin, W. Isoreticular Chiral Metal−Organic Frameworks for Asymmetric Alkene Epoxidation: Tuning Catalytic Activity by Controlling Framework Catenation and Varying Open Channel Sizes. *J. Am. Chem. Soc.* **2010**, *132*, 15390–15398.
(26) Eddaoudi, M.; Kim, J.; Rosi, N.; Vodak, D.; Wachter, J.; O'Keeffe, M.; Yaghi, O. M. Systematic Design of Pore Size and Functionality in Isoreticular MOFs and Their Application in Methane Storage. *Science* **2002**, *295*, 469–472.
(27) Rostamnia, S.; Xin, H. Basic Isoreticular Metal-Organic Framework (IRMOF-3) Porous Nanomaterial as a Suitable and Green Catalyst for Selective Unsymmetrical Hantzsch Coupling Reaction: Basic Metal-Organic Framework for Unsymmetrical Hantzsch Coupling. *Appl. Organomet. Chem.* **2014**, *28*, 359–363.
(28) Rostamnia, S.; Morsali, A. Basic Isoreticular Nanoporous Metal–Organic Framework for Biginelli and Hantzsch Coupling: IRMOF-3 as a Green and Recoverable Heterogeneous Catalyst in Solvent-Free Conditions. *RSC Adv.* **2014**, *4*, 10514.
(29) Wu, S.; Ma, X.; Ran, J.; Zhang, Y.; Qin, F.; Liu, Y. Application of Basic Isoreticular Nanoporous Metal–Organic Framework: IRMOF-3 as a Suitable and Efficient Catalyst for the Synthesis of Chalcone. *RSC Adv.* **2015**, *5*, 14221–14227.
(30) Maity, T.; Saha, D.; Koner, S. Aromatic N-Arylations Catalyzed by Copper-Anchored Porous Zinc-Based Metal-Organic Framework under Heterogeneous Conditions. *ChemCatChem* **2014**, *6*, 2373–2383.

(31) Han, D.; Jiang, F.-L.; Wu, M.-Y.; Chen, L.; Chen, Q.-H.; Hong, M.-C. A Non-Interpenetrated Porous Metal–Organic Framework with High Gas-Uptake Capacity. *Chem. Commun.* **2011**, *47*, 9861–9863.
(32) Cavka, J. H.; Jakobsen, S.; Olsbye, U.; Guillou, N.; Lamberti, C.; Bordiga, S.; Lillerud, K. P. A New Zirconium Inorganic Building Brick Forming Metal Organic Frameworks with Exceptional Stability. *J. Am. Chem. Soc.* **2008**, *130*, 13850–13851.
(33) DeCoste, J. B.; Peterson, G. W.; Schindler, B. J.; Killops, K. L.; Browe, M. A.; Mahle, J. J. The Effect of Water Adsorption on the Structure of the Carboxylate Containing Metal–Organic Frameworks Cu-BTC, Mg-MOF-74, and UiO-66. *J. Mater. Chem. A* **2013**, *1*, 11922.
(34) DeCoste, J. B.; Peterson, G. W.; Jasuja, H.; Glover, T. G.; Huang, Y.; Walton, K. S. Stability and Degradation Mechanisms of Metal–Organic Frameworks Containing the $Zr_6O_4(OH)_4$ Secondary Building Unit. *J. Mater. Chem. A* **2013**, *1*, 5642–5650.
(35) Dodson, R. A.; Wong-Foy, A. G.; Matzger, A. J. The Metal–Organic Framework Collapse Continuum: Insights from Two-Dimensional Powder X-Ray Diffraction. *Chem. Mater.* **2018**, *30*, 6559–6565.

Chapter 4. *N, N*-Diethyl-3-methylbenzamide (DEET) Acts as a Metal–Organic Framework Synthesis Solvent with Phase-Directing Capabilities[*]

4.1 Introduction

Metal-organic frameworks (MOFs) are a class of crystalline coordination polymers composed of metal ions or clusters bound by organic linker molecules. The often-high porosity and surface area of MOFs make these materials attractive for applications such as gas storage/separation, catalysis, and drug delivery. MOFs are generally synthesized solvothermally in formamide solvents such as *N*,*N*-dimethylformamide (DMF) and *N*,*N*-diethylformamide (DEF), or more rarely in water and/or alcohols. It is well-known in the field that choice of solvent is an important parameter for MOF synthesis, as two otherwise identical synthetic procedures, differentiated by synthesis solvent only, can yield unique materials with correspondingly disparate properties.

N,*N*-Diethyl-3-methylbenzamide, commonly known as DEET, is a potent insect repellent with an excellent history of efficacy and safety.[1] Notably, the structure of DEET is similar to DEF, except with the presence of a 3-methylbenzyl group rather than a hydrogen on its amide carbon (Figure 4.1). Despite its structural similarity to this widely used formamide solvent, few reports exist of researchers utilizing DEET for applications outside of its insect repellency.[†] Though

[*] Adapted from Dodson, R. A.; Kalenak, A. P.; Du Bois, D. R.; Matzger. A. J. *Chem. Commun.*, **2020,** 56, 9966-9969.

[†] DEET has also been reported or proposed as an additive to increase the skin permeability of drugs,[20] a polymer plasticizer,[21] and a carrier for dyes and flame retardants.[22]

comparable in cost to DMF, DEET has a much better safety record versus formamide solvents, which have well-documented hepatotoxicity.[2,3] This toxicity is important to consider because complete removal of synthesis solvents from MOFs can be difficult to achieve. This is especially concerning for MOFs intended to be used in applications involving food contact or drug delivery, where residual toxic solvents can pose a health risk to consumers. Use of DEET as a synthesis solvent (for either materials synthesis or chemical synthesis) is currently unexplored.[§]

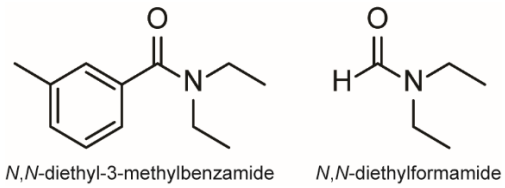

N,*N*-diethyl-3-methylbenzamide *N*,*N*-diethylformamide

Figure 4.1. Chemical structures of *N*,*N*-diethyl-3-methylbenzamide and *N*,*N*-diethylformamide.

The success of DEET as an insect repellent arises in part from its slow evaporation rate, which permits a longer duration of protection than more-volatile repellents. Because of the importance of volatility control, there have been many attempts to develop controlled-release formulations of DEET to further improve its longevity. Development of these formulations began in the 1980s, resulting in a polymer-based formulation commercialized by 3M.[4] Subsequently, a variety of other controlled-release formulations have been developed. Recently, a MOF-fabric composite, created by incubation of fabric in a DMF-based MOF synthesis solution, was developed and tested for DEET release.[5] This system achieved extended release by virtue of its higher DEET capacity, and showed quicker evaporation rates relative to the unmodified fabrics. In this study we a) demonstrate efficient MOF synthesis in DEET and b) show the potential of

[§] As of 22 January 2020, a SciFinder reaction substructure search with DEET Included as a reagent yielded two hits, both of which included DEET during reactions for the purpose of physically embedding it in the final product. A Reaxys search yielded no instances of DEET being used as a solvent in any reaction.

DEET-synthesized MOFs to extend the DEET release profile relative to the neat liquid via vapor pressure suppression.

4.2 Results and Discussion

The utility of DEET as a MOF synthesis solvent was critically assessed by screening a series of prototypical MOFs. Because of the large variety of systems attempted, synthetic conditions were not optimized, with representative synthetic parameters such as concentration, linker:metal ratio, and temperature left as described in previous synthetic protocols; therefore the results reported here represent a worst case scenario for the generality of DEET in MOF synthesis. Synthesis of MOF-5[6] was found to proceed when the synthesis solvent was changed from DEF to DEET, giving material with comparable cubic morphology (see Chapters 4.4.5-4.4.6 for morphological characterization data) and a powder X-ray diffraction (PXRD) pattern in excellent accord with that computed from the MOF-5 crystal structure (Figure 4.2). Furthermore, the BET surface area of the MOF-5 obtained from DEET was comparable to that of the DEF-synthesized material (~3300 m^2 g^{-1}), and no residual DEET was observed in the MOF post-activation via solution ^{1}H-NMR (see Chapter 4.4.8 for details). As in the case of MOF-5, the syntheses of the Zn_4O-based MOFs UMCM-1 (Zn, terephthalate (bdc), and 1,3,5-tris(4-carboxyphenyl)benzene (btb)),[7] UMCM-9 (Zn, 2,6-naphthalenedicarboxylate (ndc), and 4,4'-biphenyldicarboxylate (bpdc)),[8] and MOF-177 (Zn and btb)[9] were also successful in DEET. Three other prototypical MOF systems – HKUST-1 (Cu and trimesate (btc)),[10] MIL-53(Al) (Al and bdc),[11] and MOF-519 (Al and btb)[12] – were also successfully synthesized in DEET (Figure 4.3), all with no apparent decrease in bulk sample crystallinity relative to standard synthetic protocols.

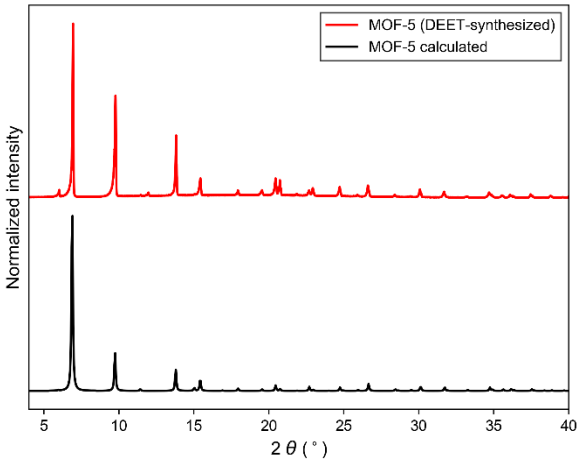

Figure 4.2. PXRD patterns of DEET-synthesized MOF-5 (above) and calculated PXRD pattern for MOF-5 (below).

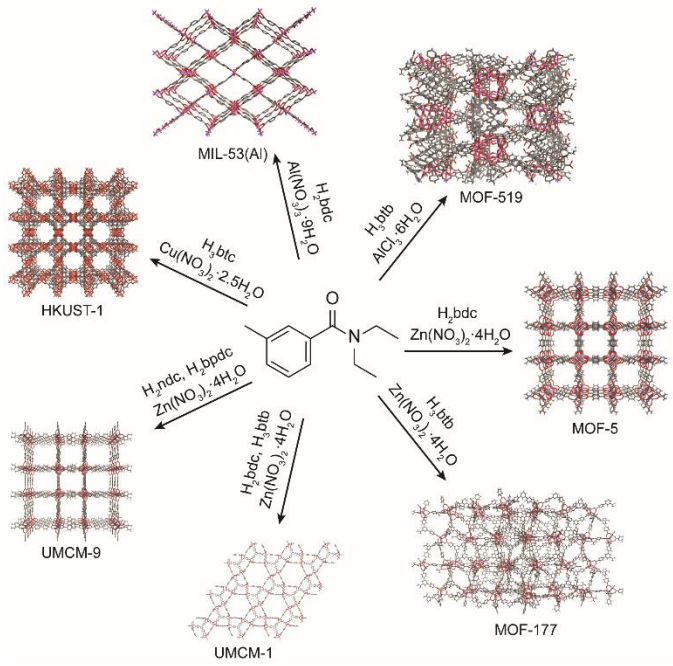

Figure 4.3. Metal-organic frameworks successfully synthesized in DEET along with their precursor metal salts and linker acids.

Attempted syntheses which were not observed to yield crystalline products with conditions that were successful when using DMF include the Zn-based MOFs FJI-1 and ZIF-8, and the Zr-based MOFs UiO-66, DUT-52, and UiO-67. It is likely that further optimization of synthetic conditions (temperature, concentration, cosolvent) will afford these materials in DEET. Several of the attempted MOF syntheses in DEET yielded new crystalline phases. In particular, this was

found when attempting to synthesize IRMOF-3 (Zn and 2-aminoterephthalate (NH_2bdc)), Zn-HKUST-1 (Zn and btc), and Cu-MOF-2 (Cu and bdc) (PXRD patterns of the resultant products as well as those of the targeted MOFs are given in Chapter 4.4.3). Zn/btc yields crystals large enough for single crystal X-ray diffraction. The structure of this phase is shown in Figure 4.4. Of particular note is its rare $Zn_2(RCO_2)_3$ cluster, distinct from the commonly seen $M_2(RCO_2)_4$ paddlewheel cluster. The $M_2(RCO_2)_3$ cluster in this structure achieves charge balance with one axial NO_3^- per cluster, while the opposite axial site on each cluster is bound by a DEET molecule. The ability of DEET to yield a novel MOF with such a seldom seen cluster demonstrates its phase-directing ability.

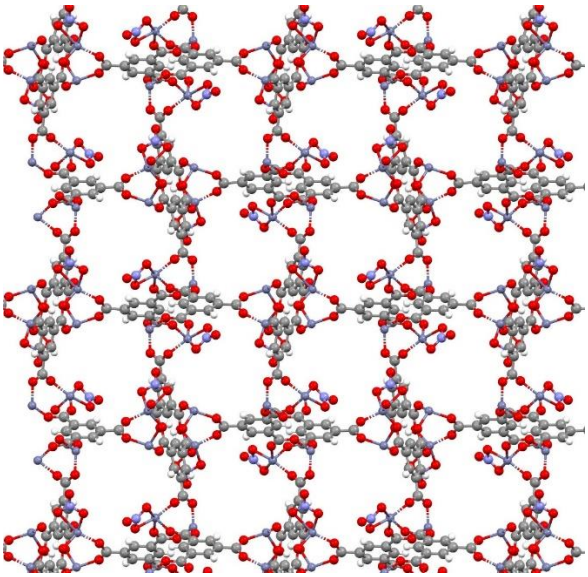

Figure 4.4. Crystal structure of the novel Zn/btc phase with coordinated solvent omitted for clarity. Viewed along the a-axis.

MOF syntheses generally utilize formamide solvents both because of their ability to solubilize a broad range of metal salts and carboxylic acid linkers and because formamide decomposition generates alkylamine species that increase the solution pH; this slowly increasing basicity facilitates controlled deprotonation of linker molecules and thus reversible MOF growth. Although DEET is an amide solvent, its decomposition pathways are expected to be distinct from

formamide solvents such as DMF and DEF.[13] The latter solvents can exude CO yielding alkylamine through a thermal decomposition pathway; no such path is evident in DEET, although hydrolysis might provide diethylamine and ultimately raise solution pH.[14]

In contrast with previously reported HKUST-1/fabric composite materials,[5] MOF-5 was found to behave exceptionally well at reducing the effective vapor pressure of DEET. In particular, relative to the extrapolated vapor pressure of DEET at 37 °C (1.2 mPa, this work), DEET loaded in MOF-5 has an equilibrium vapor pressure of 0.11 mPa at 37 °C, corresponding to 9.1% of the bulk vapor pressure as determined by measurements between 125 and 200 °C using the Knudsen effusion method (Figure 4.5, see Chapter 4.4.4 for full details on these measurements). This volatility suppression is substantial. Because the evaporation rate of a liquid empirically scales linearly with its vapor pressure,[15] we can project that this vapor pressure reduction would lead to a ~11× longer evaporation time. However, these calculations reflect the behavior of the DEET/MOF composite in a dry N_2 environment, which is not representative of climates in which mosquitoes represent a public health concern. In the presence of moisture and/or liquid water, MOF-5 is well-known to undergo structural degradation and eventual hydrolysis, which has been leveraged previously to increase drug release rates.[16] Thus, these evaporation rate estimates represent a lower limit scenario for DEET release, with real-world release rates likely falling between these results and those of the bulk liquid.

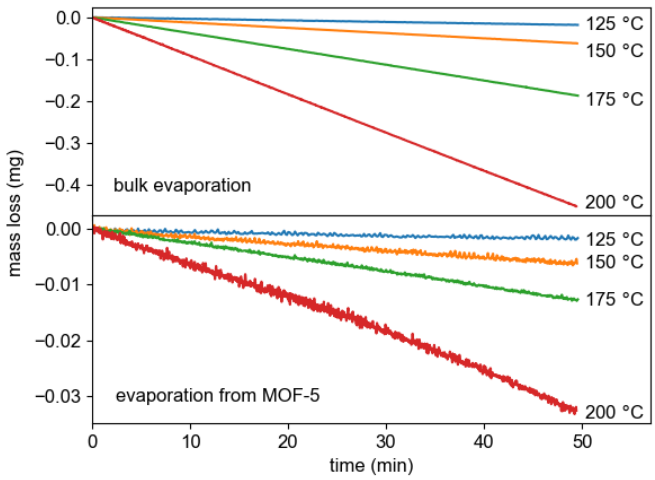

Figure 4.5. Mass loss versus time for bulk liquid DEET (above) and for DEET loaded in MOF-5 (below) in a Knudsen effusion cell.

Beyond its exceptional ability to lower the vapor pressure of guest molecules, there are several other properties of MOF-5 that could be valuable in a controlled-release formulation. One such property that could be exploited in topical formulations is UV absorption. For example, MOF-5 strongly absorbs UV radiation up to ~310 nm, with red-shifting of the absorption edge to ~325 nm upon exposure to water.[17] This would allow MOF-5-based topical formulations to block a significant portion of harmful UV-B radiation (290-320 nm). Another benefit of this MOF/DEET system is the simplicity of its creation: the controlled-release composite can be used directly after MOF synthesis. Choice of MOF will allow further tuning of release rate, moisture sensitivity, and UV-absorption profile offering a number of pathways for optimizing application of MOF-based topical formulations offering environment protection to the wearer.

4.3 Conclusions

DEET is an inexpensive, versatile, and low-toxicity MOF synthesis solvent. As MOFs find increasingly widespread use at the industrial scale,[18,19] it is imperative from an industrial health and safety perspective to have routes for synthesizing MOFs using the least toxic solvents possible. Because many MOF syntheses require amide solvents, DEET has the potential to fill this role as a

cheap, readily available, and safer synthesis solvent. Furthermore, the utility of MOFs to lower the effective vapor pressure in insect repellent formulations represents a promising new application for these materials.

4.4 Supporting Information

4.4.1 Reagents

Zinc perchlorate hexahydrate (Alfa Aesar, reagent grade), aluminum nitrate nonahydrate (Fisher, certified ACS grade), aluminum chloride hexahydrate (Sigma, 99%), cupric nitrate hemipentahydrate (Fisher, certified ACS grade), zirconium(IV) chloride (Strem, sublimed grade), 1,4-benzenedicarboxylic acid (H_2bdc, Fisher Scientific, 98%), 2-aminoterephthalic acid (H_2bdc-NH_2, Sigma-Aldrich, 99%), 2,6-naphthalenedicarboxylic acid (H_2ndc, TCI America, 98%), 4,4'-biphenyldicarboxylic acid (H_2bpdc, Acros Organics, 98%), 1,3,5-benzenetricarboxylic acid (H_3btc, TCI America, 98%), 1,3,5-tri(4-carboxyphenyl)benzene (H_3btb, Alfa Aesar, 97%), imidazole (Him, Aldrich, 99%), 2-methylimidazole (Hmim, Acros Organics, 99%), 2-nitroimidazole (Hnim, Oakwood Chemical, 98%), 4,4'-bipyridine (4,4'-bpy, Acros Organics, 98%), hydrochloric acid (Fisher Scientific, certified ACS plus), acetic acid (Fisher Scientific, glacial, certified ACS plus), nitric acid (Fisher Scientific, certified ACS plus), and fluoroboric acid (Acros Organics, 50 wt% solution in water) were used as received. Zinc nitrate hexahydrate (Fisher Scientific, ACS grade) was partially dehydrated by room temperature evacuation (~16 hr, <0.01 Torr) to yield zinc nitrate tetrahydrate (verified by thermogravimetric analysis). DCl in D_2O (Sigma Aldrich, 99+% atom D) and DMSO-d_6 (Acros Organics, 99.5+% atom D) were used for ^{1}H-NMR experiments. *N*,*N*-diethyl-3-methylbenzamide (DEET, Acros Organics, 98%), hexane (Fisher Scientific, anhydrous), methylene chloride (CH_2Cl_2, Fisher scientific, HPLC grade), *N*-methylpyrrolidone (Sigma Aldrich, 99.5%), and *N*,*N*-dimethylformamide (DMF, Fisher Scientific,

99.5%) were stored over activated 4 Å molecular sieves to minimize water content. The dryness of these solvents was monitored by Karl Fischer titration (<10 ppm H_2O). *N*,*N*-Diethylformamide (DEF, TCI America, >99.0%) was purified by storage on activated charcoal for ~1 month followed by removal of impurities via silica gel column.

4.4.2 Syntheses

MOF syntheses were generally performed with minimal modification relative to literature-reported protocols with the exception of solvent substitution. When syntheses called for zinc nitrate hexahydrate as a zinc source, the tetrahydrate was substituted. All MOF syntheses were also performed in the original formamide solvent to ensure the efficacy of these procedures. Unless otherwise stated, syntheses were performed in 20 mL vials with Teflon-lined caps. The specific syntheses performed were as follows attempting to make the named MOF:

Zn MOFs

MOF-5.[6] $Zn(NO_3)_2 \cdot 4H_2O$ (360.0 mg, 1.377 mmol) and H_2bdc (60.0 mg, 0.361 mmol) were dissolved in DEET (10 mL). The reaction was performed at 100 °C for 1 day.

IRMOF-3.[23] $Zn(NO_3)_2 \cdot 4H_2O$ (333.3 mg, 1.275 mmol) and $H_2bdc\text{-}NH_2$ (83.3 mg, 0.460 mmol) were dissolved in DEET (10 mL). The reaction was performed at 100 °C for 3 days.

UMCM-1.[7] $Zn(NO_3)_2 \cdot 4H_2O$ (566.6 mg, 2.167 mmol), H_2bdc (90.0 mg, 0.542 mmol), and H_3btb (213.4 mg, 0.487 mmol) were dissolved in 20 mL DEET. The reaction was performed at 85 °C for 2 days.

UMCM-9.[8] $Zn(NO_3)_2 \cdot 4H_2O$ (216.0 mg, 0.826 mmol), H_2ndc (29.1 mg, 0.135 mmol), and H_2bpdc (36.8 mg, 0.152 mmol) were dissolved in DEET (20 mL). The reaction was performed at 85 °C for 7 days.

MOF-177.[9] $Zn(NO_3)_2 \cdot 4H_2O$ (164.7 mg, 0.630 mmol) and H_3btb (39.5 mg, 0.090 mmol) were dissolved in DEET (10 mL). The reaction was performed at 85 °C for 4 days.

Zn-HKUST-1.[24] $Zn(NO_3)_2 \cdot 4H_2O$ (153.6 mg, 0.587 mmol) and H_3btc (35.6 mg, 0.169 mmol) were dissolved in DEET (10 mL). The reaction was performed at 85 °C for 16 hours.

ZIF-8.[25] $Zn(NO_3)_2 \cdot 4H_2O$ (210.0 mg, 0.803 mmol) and Hmim (60.0 mg, 0.731 mmol) were dissolved in DEET (18 mL). The reaction was performed at 140 °C for 1 day in a Teflon-lined stainless-steel autoclave.

ZIF-70.[26] $Zn(NO_3)_2 \cdot 4H_2O$ (209.2 mg, 0.800 mmol), Hnim (113.1 mg, 1.000 mmol), and Him (68.1 mg, 1.000 mmol) were dissolved in DEET (14 mL). The reaction was performed at 110 °C for 4 days.

FJI-1.[27] $Zn(ClO_4)_2 \cdot 6H_2O$ (223.0 mg, 0.599 mmol), H_3btb (175.0 mg, 0.399 mmol), and 4,4'-bpy (47.0 mg, 0.301 mmol) were dissolved in DEET (10 mL) along with 0.1 mL fluoroboric acid. The reaction was performed at 85 °C for 3 days.

Cu MOFs

HKUST-1.[10] $Cu(NO_3)_2 \cdot 2.5H_2O$ (400.0 mg, 1.720 mmol) and H_3btc (200 mg, 0.952 mmol) were dissolved in DEET (10 mL) along with a drop of concentrated HCl. The reaction was performed at 85 °C for 16 hours.

Cu-MOF-2.[28] $Cu(NO_3)_2 \cdot 2.5H_2O$ (121.0 mg, 0.520 mmol) and H_2bdc (83.2 mg, 0.501 mmol) were dissolved in DEET (10 mL). The reaction was performed at 110 °C for 36 hours.

Zr MOFs

UiO-66.[29] $ZrCl_4$ (83.3 mg, 0.358 mmol) and H_2bdc (82.0 mg, 0.494 mmol) were dissolved in DEET (10 mL) along with 0.67 mL HCl. The reaction was performed at 85 °C for 16 hours.

DUT-52.[30] $ZrCl_4$ (115.0 mg, 0.493 mmol) and H_2ndc (108.0 mg, 0.500 mmol) were dissolved in DEET (10 mL) along with 1.5 mL acetic acid. The reaction was performed at 85 °C for 16 hours.

UiO-67.[29] $ZrCl_4$ (44.7 mg, 0.192 mmol) and H_2bpdc (60.0 mg, 0.248 mmol) were dissolved in DEET (10 mL) along with 0.33 mL HCl. The reaction was performed at 85 °C for 16 hours.

Al MOFs

MIL-53(Al).[11] $Al(NO_3)_2 \cdot 9H_2O$ (96.3 mg, 0.257 mmol) and H_2bdc (96.0 mg, 0.578 mmol) were dissolved in DEET (10 mL). The reaction was performed at 120 °C for 3 days.

MOF-519.[12] $AlCl_3 \cdot 6H_2O$ (50.6 mg, 0.135 mmol) was dissolved in DEET (5 mL) and mixed with a 5 mL H_3btb (109.0 mg, 0.249 mmol) DEET solution along with 0.68 mL HNO_3. The reaction was performed at 150 °C for 3 days in a Teflon-lined stainless-steel autoclave.

4.4.3 Powder X-ray diffraction

Room-temperature powder X-ray diffraction was performed on a PANalytical Empyrean diffractometer in Bragg–Brentano geometry (Cu K_α radiation, 45 kV, and 40 mA). The incident beam was equipped with a Bragg–BrentanoHD X-ray optic using fixed slits/soller slits. X-ray detection was accomplished with a silicon-based linear position sensitive X'Celerator Scientific detector operating in 1D scanning mode. When necessary (MOF-5, UMCM-1, UMCM-9, MOF-177, Zn/btc), samples were finely ground to minimize preferred orientation and packed in the depression of a glass slide. Patterns were collected between 3 – 80 °2Θ, with a scan rate of 0.008 ° and 20 seconds per step. Powder X-ray diffractograms for DEET-synthesized MOFs along with diffraction patterns calculated from crystal structures are given in Figures 4.6-4.14. As needed, experimental patterns of materials created using the original synthesis solvent are given for comparison.

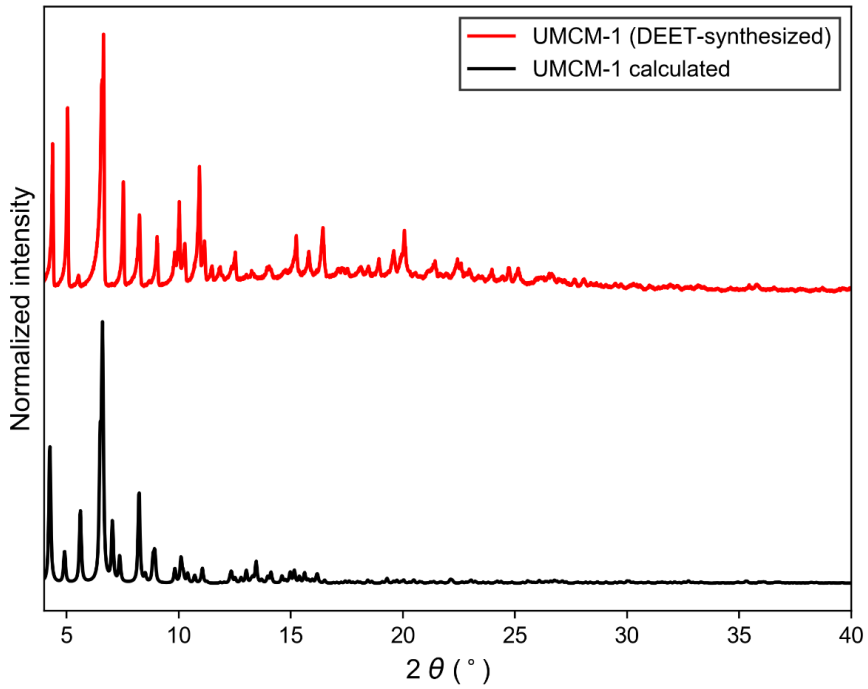

Figure 4.6. PXRD pattern of DEET-synthesized UMCM-1 (above) and calculated PXRD pattern for UMCM-1 (below).

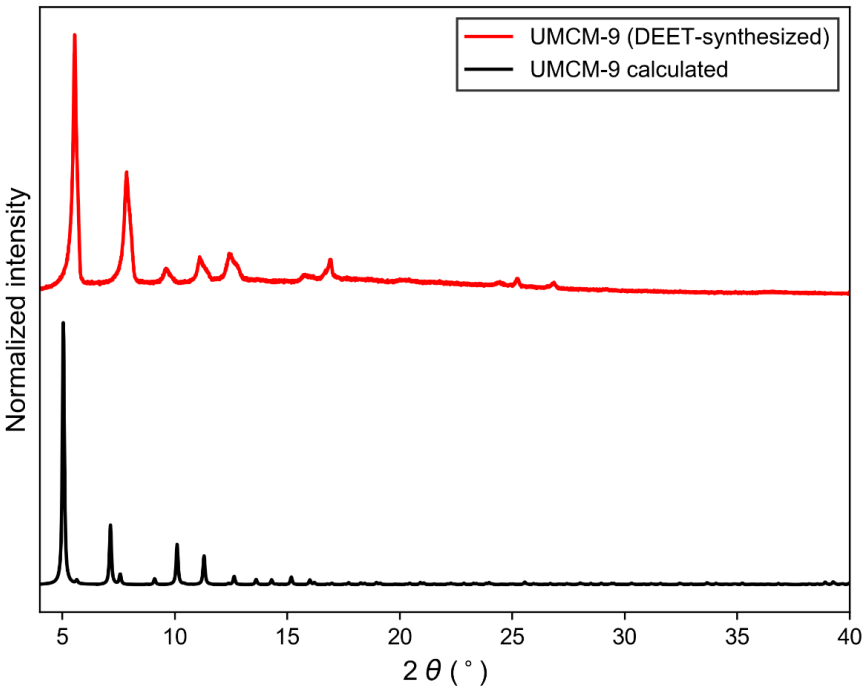

Figure 4.7. PXRD pattern of DEET-synthesized UMCM-9 (above) and calculated PXRD pattern for UMCM-9 (below). The broader peaks in the experimental pattern are consistent with previously reported UMCM-9 patterns, and can be attributed to the inherent structural disorder in the MOF system.[4]

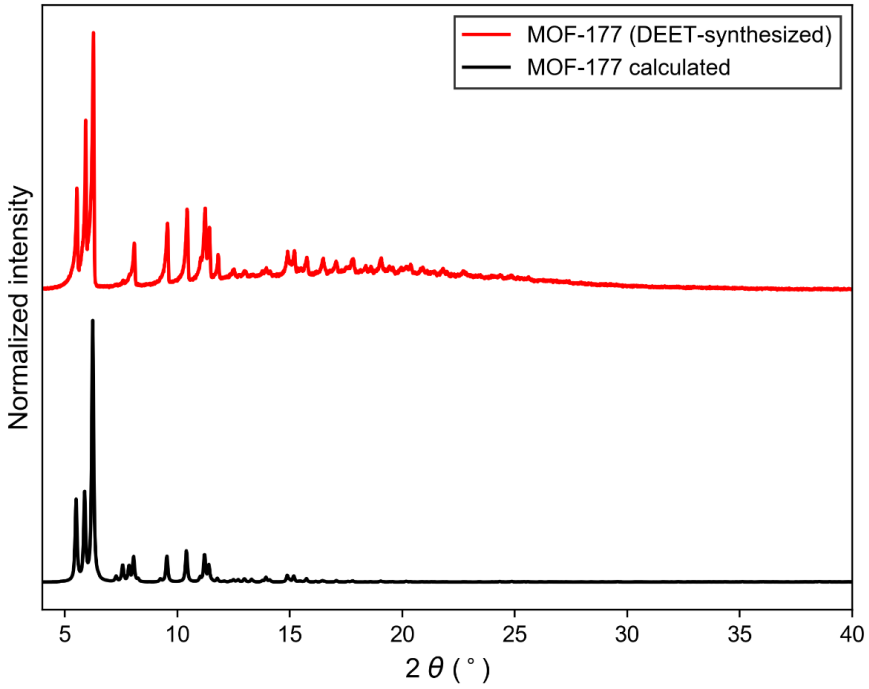

Figure 4.8. PXRD pattern of DEET-synthesized MOF-177 (above) and calculated PXRD pattern for MOF-177 (below).

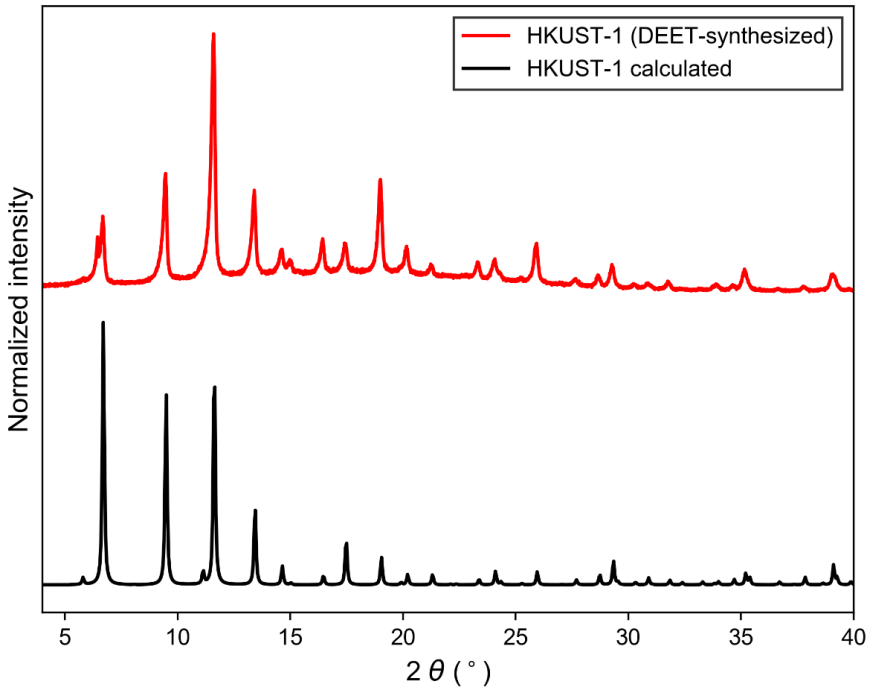

Figure 4.9. PXRD pattern of DEET-synthesized HKUST-1 (above) and calculated PXRD pattern for HKUST-1 (below).

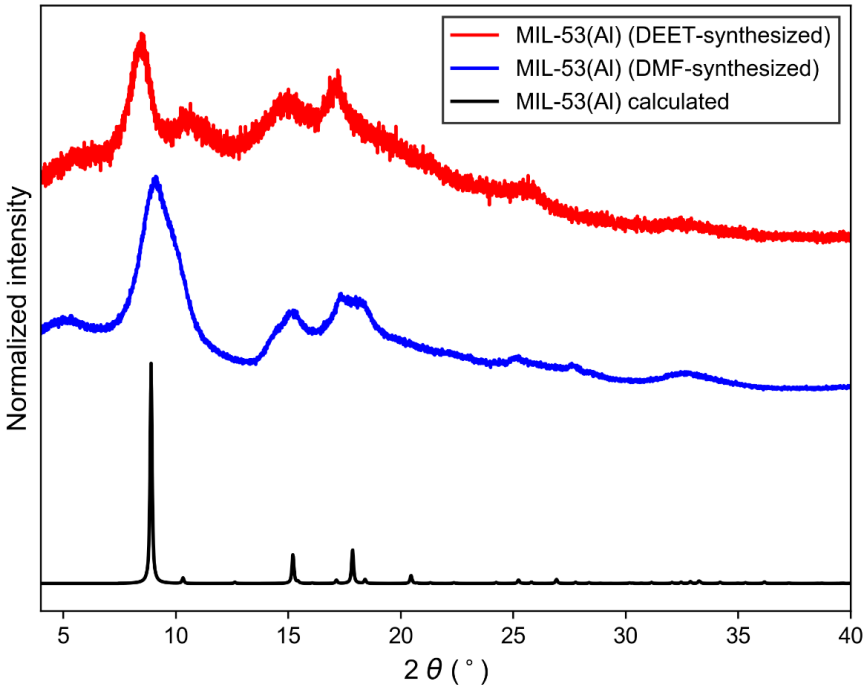

Figure 4.10. PXRD pattern of DEET-synthesized MIL-53(Al) (above), DMF-synthesized MIL-53(Al) (middle), and calculated PXRD pattern for MIL-53(Al) (below). The broad peaks and high background in both experimental patterns suggest that this synthesis (regardless of solvent) yields relatively small crystalline domains and/or a substantial fraction of amorphous material.

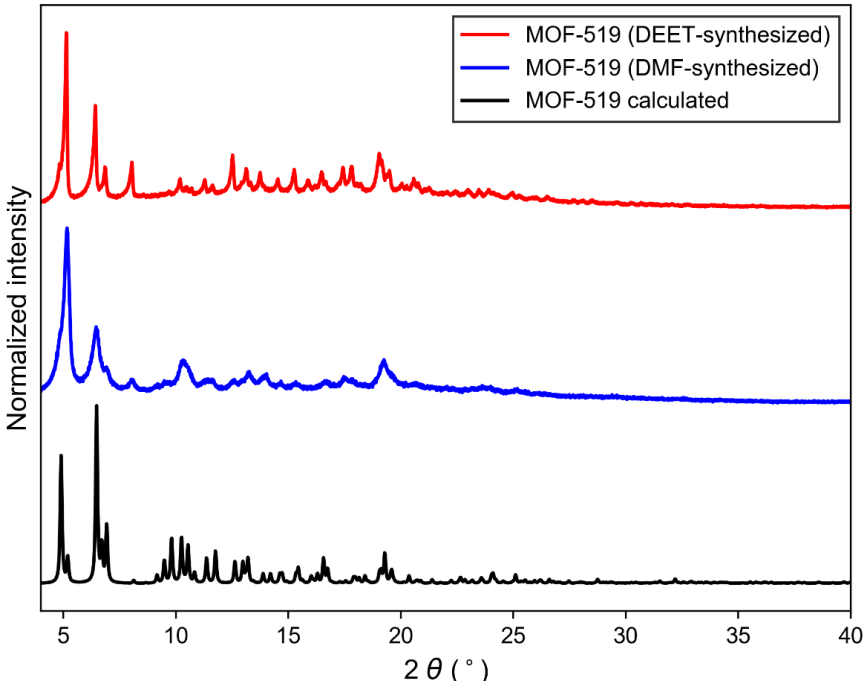

Figure 4.11. PXRD pattern of DEET-synthesized MOF-519 (above), DMF-synthesized MOF-519 (middle), and calculated PXRD pattern for MOF-519 (below).

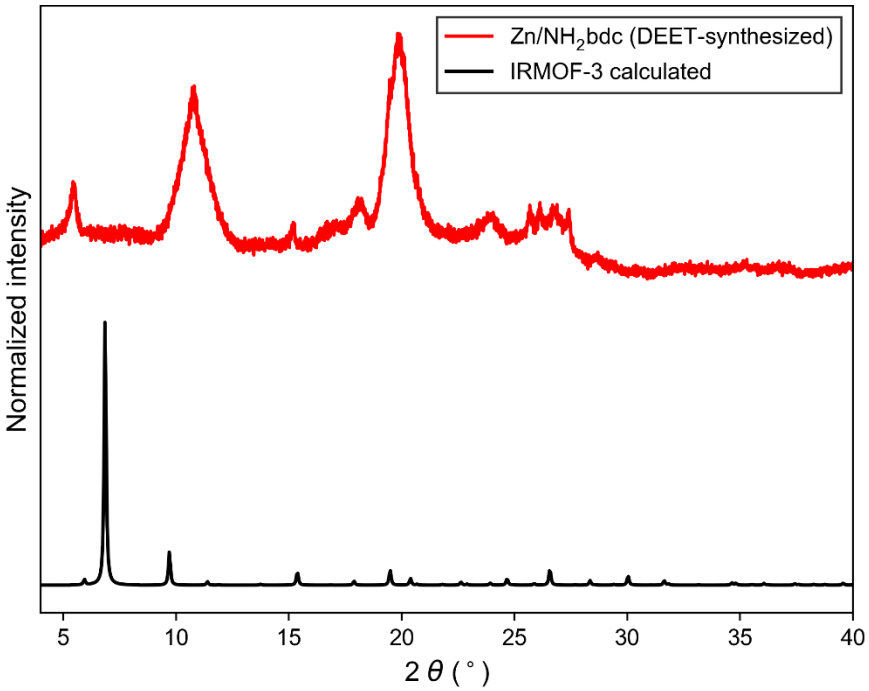

Figure 4.12. PXRD pattern of DEET-synthesized Zn/NH_2-bdc (above) and calculated PXRD pattern for IRMOF-3 (below).

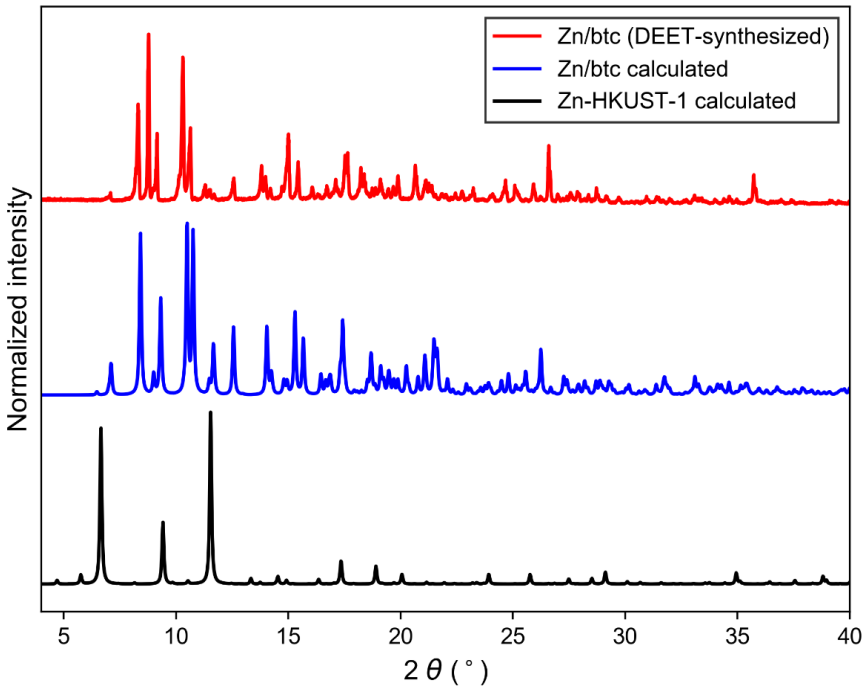

Figure 4.13. PXRD pattern of DEET-synthesized Zn/btc (above), calculated PXRD pattern for that phase (middle), and calculated PXRD pattern for Zn-HKUST-1 (below).

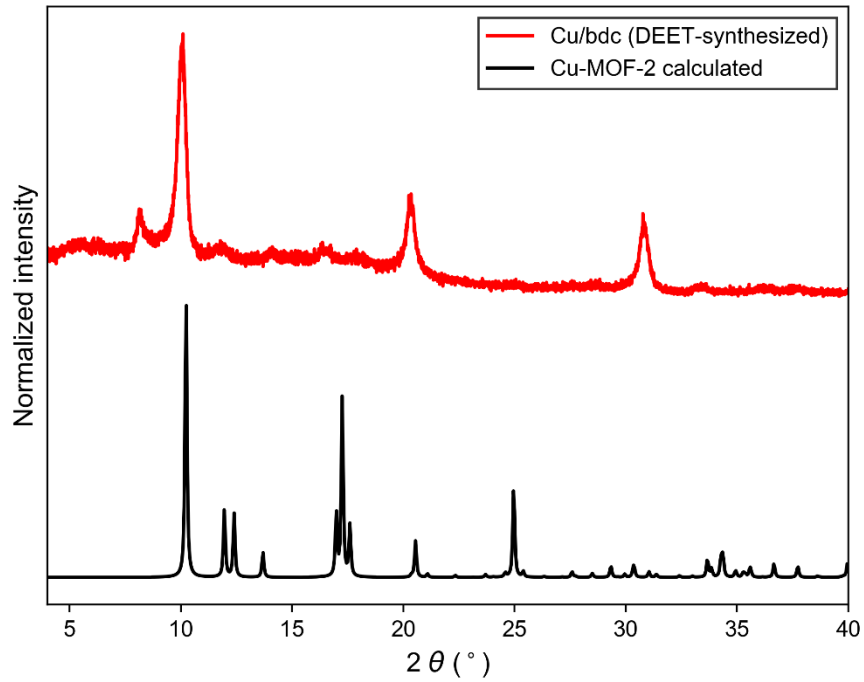

Figure 4.14. PXRD pattern of DEET-synthesized Cu/bdc (above) and calculated PXRD pattern for Cu-MOF-2 (below).

4.4.4 Vapor pressure measurements

Vapor pressures and heats of vaporization were determined using the Knudsen effusion method. Briefly, each sample was placed in an aluminum DSC pan which was then sealed with a hermetic lid containing a 75 μm-diameter laser-drilled hole (TA Instruments). This pan was then loaded into a TA Q50 thermogravimetric analyzer, and weight loss was recorded at constant temperature. Experiments were performed in triplicate. Temperature-dependent vapor pressures were calculated from measured mass loss rates using the Langmuir equation:[31]

$$p = \left(\frac{\Delta m}{\Delta t}\right)\left(\frac{1}{A}\right)\left(\frac{2\pi RT}{M}\right)^{1/2}$$

where p is the equilibrium vapor pressure (Pa), $\Delta m/\Delta t$ is mass loss rate (kg s^{-1}), A is the pinhole area (m^2), R is the ideal gas constant (8.314 m^3 Pa mol^{-1} K^{-1}), T is the temperature (K), and M is the molar molecular weight of the volatile species (kg mol^{-1}).

An example calculation is given below:

$\Delta m/\Delta t$ = 0.00356 mg min^{-1} = 5.93 × 10^{-11} kg s^{-1}

T = 175.00 °C = 448.15 K

A = π × (75 μm / 2)^2 = 4.42 × 10^{-9} m^2

M = 0.19127 kg mol^{-1}

$$p = (5.93 \times 10^{-11}\ \text{kg}\ s^{-1})\left(\frac{1}{4.42 \times 10^{-9} m^2}\right)\left(\frac{2\pi \times 8.314\ m^3\ Pa\ mol^{-1}K^{-1} \times 448.15\ K}{0.19127\ kg\ mol^{-1}}\right)^{1/2}$$

$$p = (1.34 \times 10^{-2}\ \text{kg}\ m^2\ s^{-1})(1.223 \times 10^5\ m^3\ Pa\ kg^{-1})^{1/2}$$

$$p = (1.34 \times 10^{-2}\ \text{kg}\ m^2\ s^{-1})(1.223 \times 10^5\ m^2\ s^{-2})^{1/2}$$

$$p = (1.34 \times 10^{-2}\ \text{kg}\ m^2\ s^{-1})(349.9\ m\ s^{-1})$$

$$p = 4.70\ \text{Pa}$$

Vapor pressures were then used along with the Clausius–Clapeyron relation to extrapolate the 37 °C vapor pressure of DEET in bulk as well as in MOF-5:

$$ln(P) = \frac{-\Delta H_{vap}}{R}\left(\frac{1}{T}\right) + C$$

The Clausius–Clapeyron plot for bulk DEET is given in Figure 4.15.

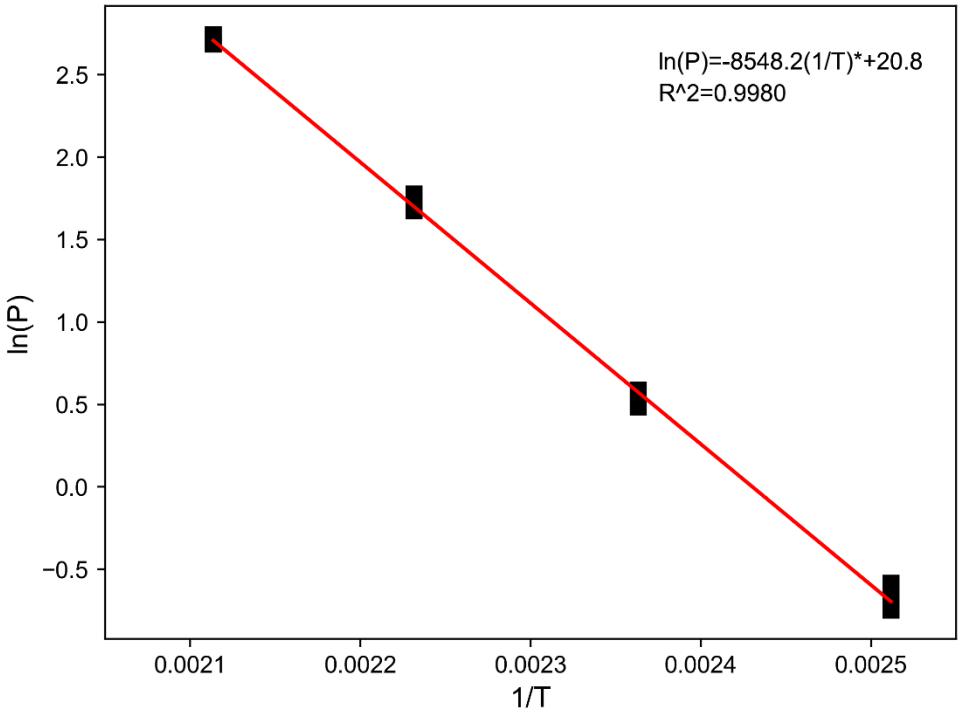

Figure 4.15. Clausius–Clapeyron plot for bulk DEET.

The same procedure was then used for evaluation of DEET vapor pressure depression in MOF-5. Generally, isothermal mass loss vs. time plots showed two distinct stages. In the first stage, mass loss proceeded at the same rate as bulk DEET at the same temperature. After this first stage, a sharp kink in the data was generally observed, followed by a second stage characterized by significantly slower mass loss (~1-10% vs. bulk, temperature dependent). Trials in which the mass loss rate in the first phase did not correspond with the bulk mass loss rate, or in which a sharp transition between the two phases was not observed, were not used for vapor pressure calculations.

These two types of evaporation data were noted to occur when adequate space was not left between the sample and the pinhole lid, and when the pan was not properly sealed.

Vapor pressure measurements were made in triplicate at 125, 150, 175, and 200 °C. Attempts to perform lower temperature measurements resulted in mass loss too slow to accurately measure with this method using our instrumentation. The Clausius–Clapeyron plot for DEET in MOF-5 is given in Figure 4.16, with measured evaporation rates for bulk DEET and DEET in MOF-5 given in Tables 4.1 and 4.2, respectively.

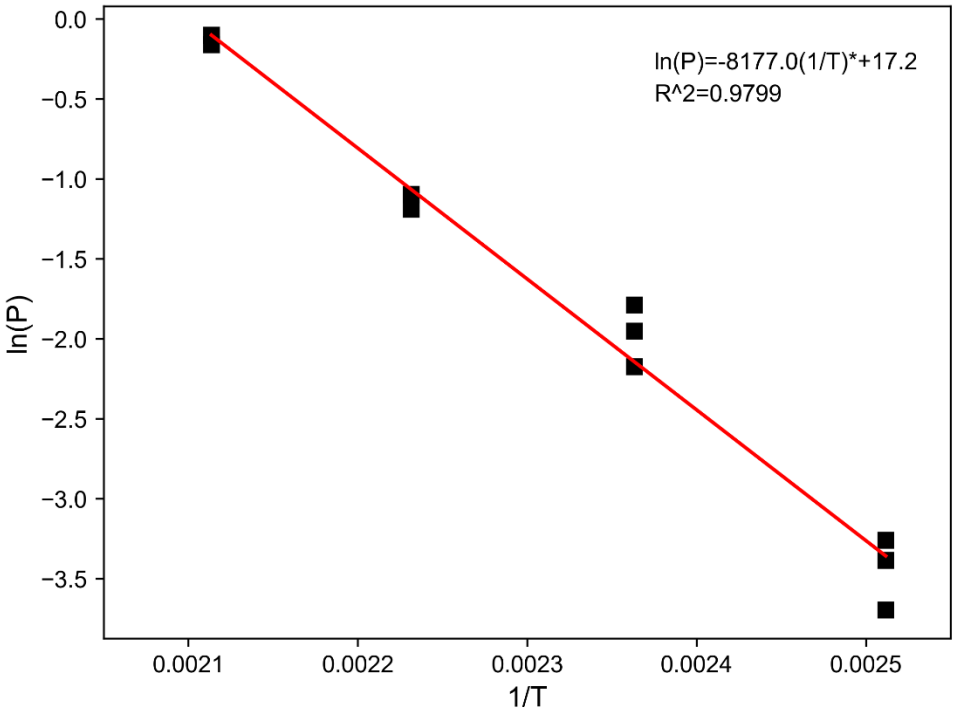

Figure 4.16. Clausius–Clapeyron plot for DEET in MOF-5.

Table 4.1. Evaporation rate data, calculated vapor pressure, and 1/T and ln(P) values used for bulk DEET vapor pressure characterization.

Temperature (°C)	Mass change (mg min^{-1})	Evaporation rate (g sec^{-1})	P_{vap} (Pa)	1/T (K^{-1})	ln(P)
125	-4.4765E-04	7.4608E-09	5.5690E-01	2.5116E-03	-5.8538E-01
125	-4.0453E-04	6.7422E-09	5.0326E-01	2.5116E-03	-6.8665E-01
125	-3.8092E-04	6.3486E-09	4.7388E-01	2.5116E-03	-7.4680E-01
150	-1.2658E-03	2.1097E-08	1.6235E+00	2.3632E-03	4.8455E-01

150	-1.3121E-03	2.1869E-08	1.6828E+00	2.3632E-03	5.2048E-01
150	-1.4027E-03	2.3379E-08	1.7990E+00	2.3632E-03	5.8726E-01
175	-4.0390E-03	6.7317E-08	5.3310E+00	2.2314E-03	1.6735E+00
175	-4.4700E-03	7.4500E-08	5.8998E+00	2.2314E-03	1.7749E+00
175	-4.1581E-03	6.9302E-08	5.4881E+00	2.2314E-03	1.7026E+00
200	-1.0832E-02	1.8053E-07	1.4690E+01	2.1135E-03	2.6872E+00
200	-1.1448E-02	1.9080E-07	1.5526E+01	2.1135E-03	2.7425E+00
200	-1.0741E-02	1.7902E-07	1.4567E+01	2.1135E-03	2.6787E+00

Table 4.2. Evaporation rate data, calculated vapor pressure, and 1/T and ln(P) values used for DEET in MOF-5 vapor pressure characterization.

Temperature (°C)	Mass change (mg min^{-1})	Evaporation rate (g sec^{-1})	P_{vap} (Pa)	1/T (K^{-1})	ln(P)
125	-3.0906E-05	5.1510E-10	3.8449E-02	2.5116E-03	-3.2584E+00
125	-2.7280E-05	4.5467E-10	3.3938E-02	2.5116E-03	-3.3832E+00
125	-2.0018E-05	3.3363E-10	2.4903E-02	2.5116E-03	-3.6928E+00
150	-1.1085E-04	1.8476E-09	1.4217E-01	2.3632E-03	-1.9507E+00
150	-8.8712E-05	1.4785E-09	1.1377E-01	2.3632E-03	-2.1735E+00
150	-1.3040E-04	2.1733E-09	1.6724E-01	2.3632E-03	-1.7883E+00
175	-2.3089E-04	3.8482E-09	3.0475E-01	2.2314E-03	-1.1883E+00
175	-2.5278E-04	4.2130E-09	3.3364E-01	2.2314E-03	-1.0977E+00
175	-2.5344E-04	4.2239E-09	3.3450E-01	2.2314E-03	-1.0951E+00
200	-6.6685E-04	1.1114E-08	9.0437E-01	2.1135E-03	-1.0052E-01
200	-6.2856E-04	1.0476E-08	8.5244E-01	2.1135E-03	-1.5965E-01
200	-6.0063E-04	1.0011E-08	8.1456E-01	2.1135E-03	-2.0510E-01

From these data, the vapor pressure at 37 °C for DEET in MOF-5 is extrapolated to be ~9% of that of the bulk liquid (1.05×10^{-4} Pa vs. 1.15×10^{-3} Pa).

4.4.5 Surface area determination

A ~30 mg sample of MOF-5 synthesized in DEET (per the first reaction described in Chapter 4.4.2) was washed 3× each with DMF, CH_2Cl_2, and hexane (~20 mL per wash, 15 minutes between washes). The sample was then evacuated under high vacuum (<0.001 Torr) for 16 hours prior to analysis. Sample surface area was calculated using the BET method from N_2 sorption

isotherms measured on a Quantachrome NOVA 4200 gas sorption analyzer. The isotherm (Figure 4.17) and BET fit (Figure 4.18) are presented below. The surface area for the MOF-5 sample was calculated to be 3255 $m^2 g^{-1}$.

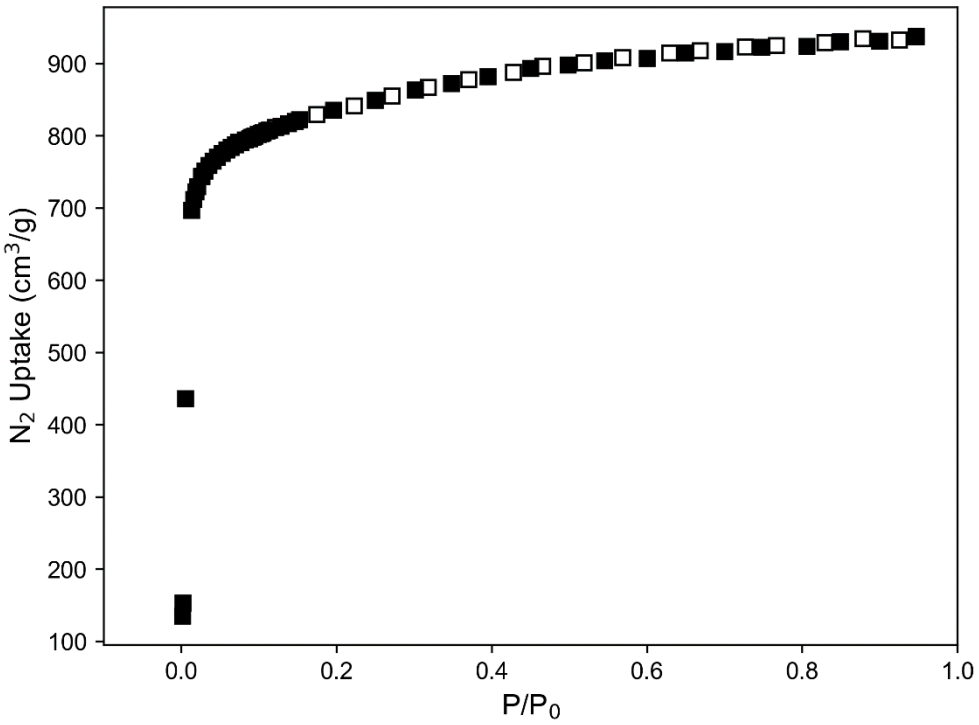

Figure 4.17. N_2 sorption isotherm for MOF-5 synthesized in DEET.

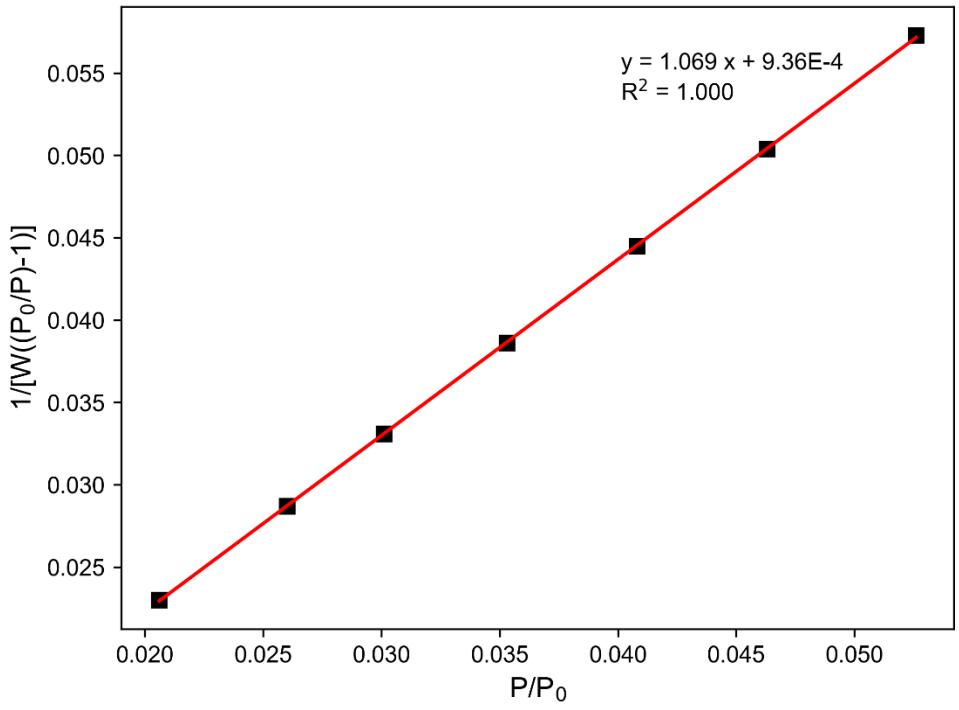

Figure 4.18. BET fit of isotherm data taken from MOF-5 synthesized in DEET.

4.4.6 Optical microscopy

MOF morphology was assessed using a digital 3D microscope (Hirox RH-2000). Optical micrographs are given in Figures 4.19 – 4.24.

MOF-5:

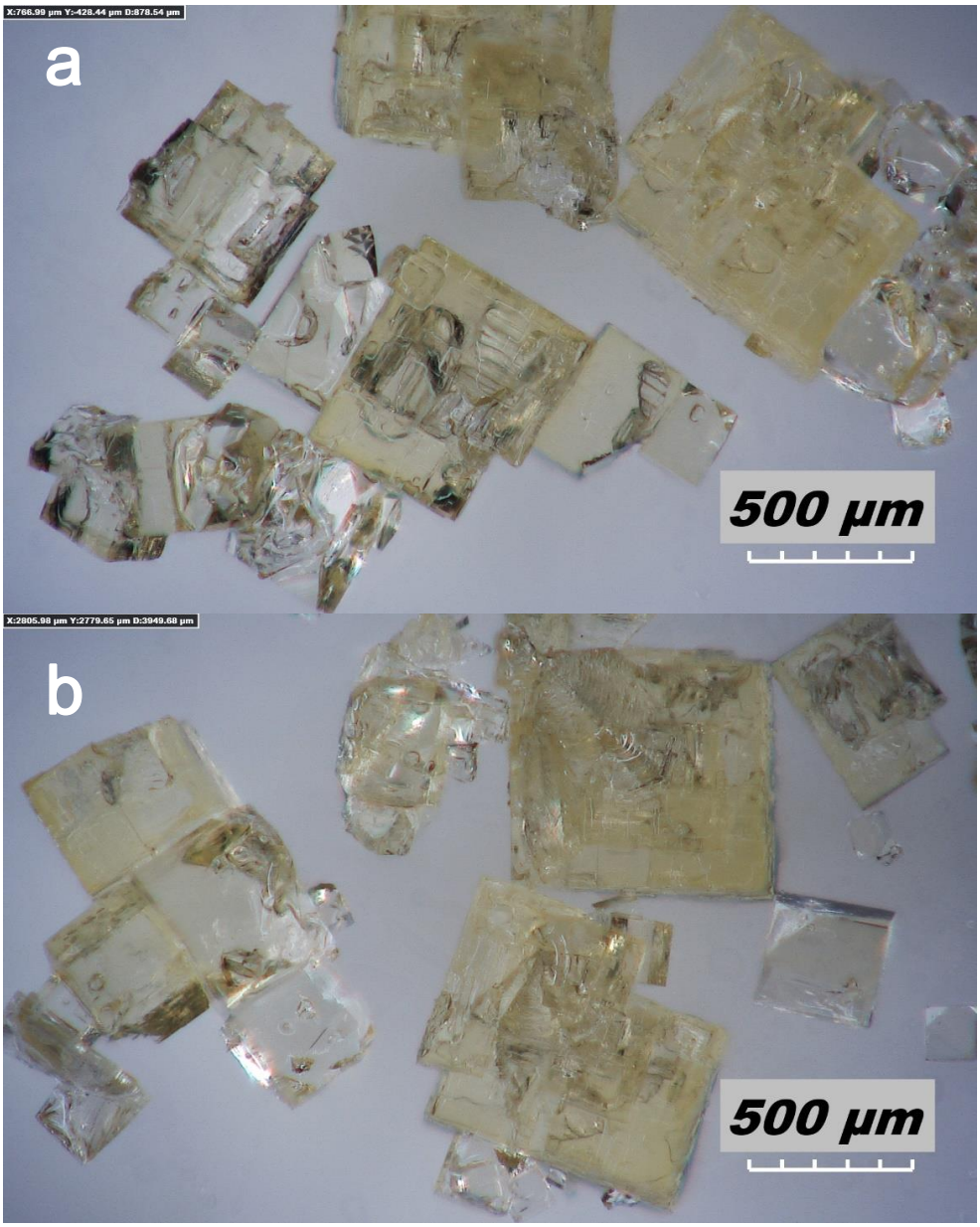

Figure 4.19. Optical micrographs of DEET-synthesized MOF-5 (a, b). The product shows the characteristic cubic morphology of the standard MOF-5 synthesis. Crystal sizes vary, but most are 200 – 600 µm in diameter.

UMCM-1:

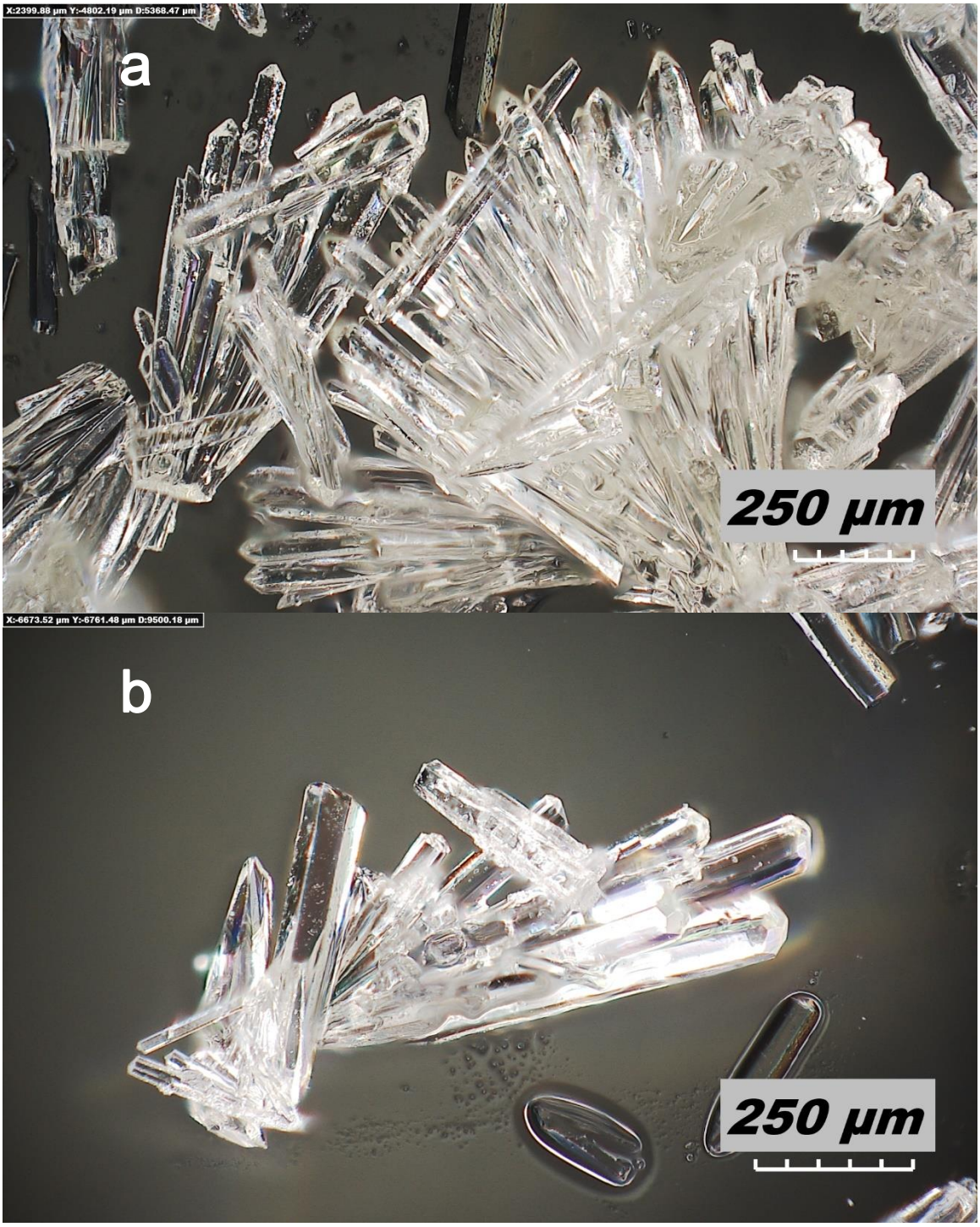

Figure 4.20. Optical micrographs of DEET-synthesized UMCM-1 (a, b). The product shows the characteristic needle morphology of the standard UMCM-1 synthesis. Crystals are as long as 1 mm, and range from 20 – 50 µm in diameter.

UMCM-9:

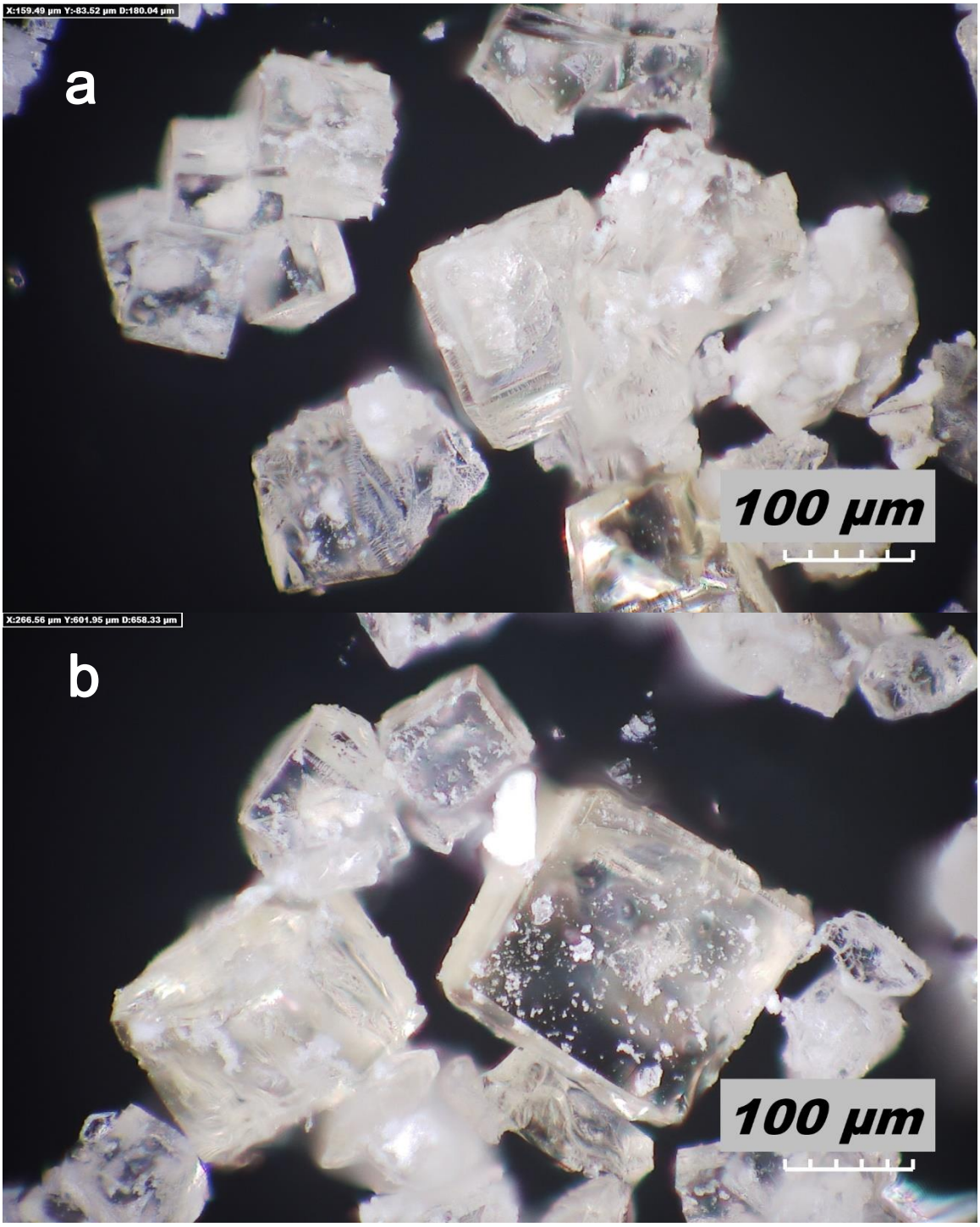

Figure 4.21. Optical micrographs of DEET-synthesized UMCM-9 (a, b). The product shows the characteristic cubic morphology of the standard UMCM-9 synthesis. Crystals are as large as ~250 µm in diameter, but most are closer to 100 µm.

MOF-177:

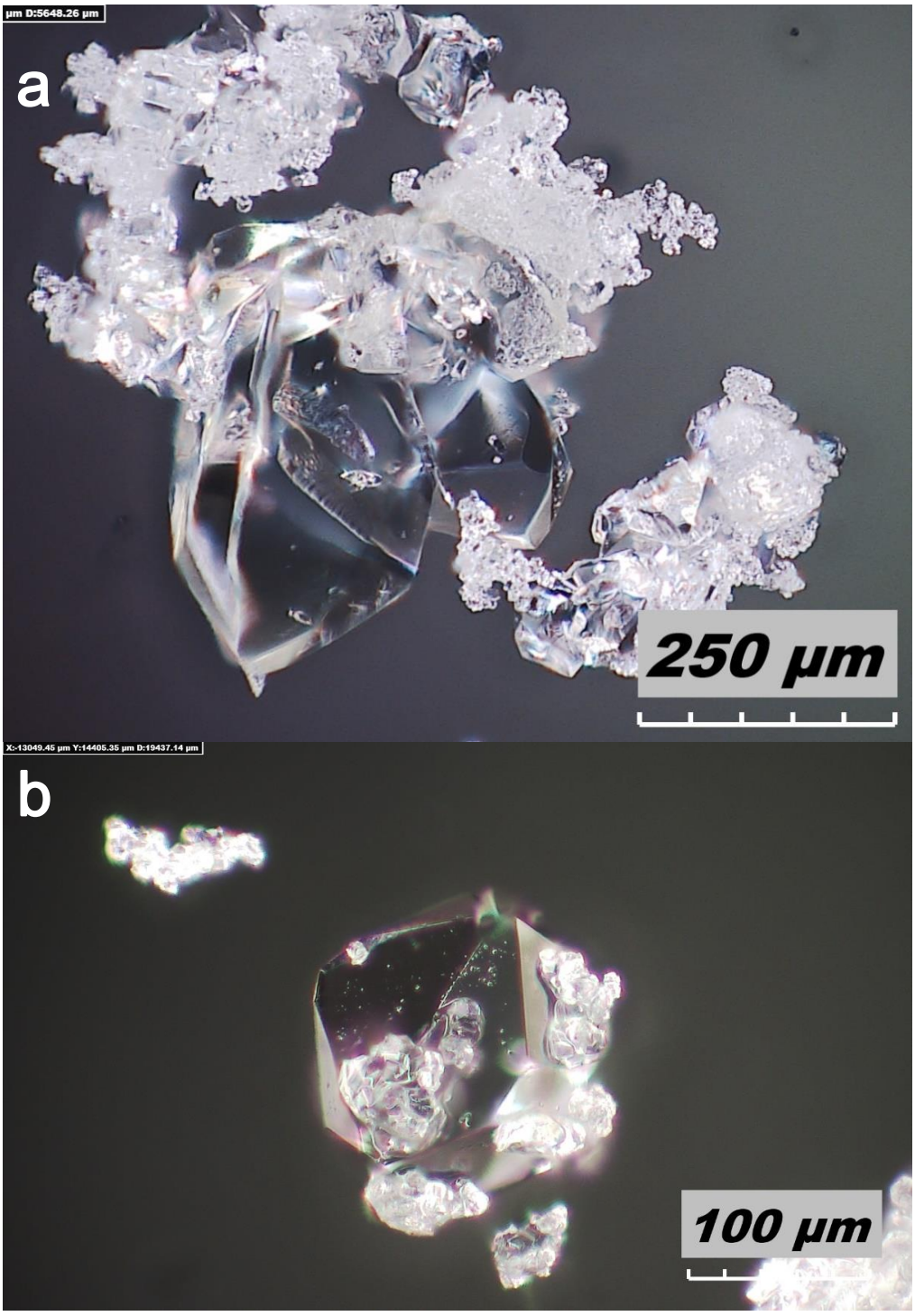

Figure 4.22. Optical micrographs of DEET-synthesized MOF-177 (a, b). Crystals appear blocky and occasionally octahedral, as the DMF-synthesis characteristically yields. Crystals are as large as ~200 µm in diameter, but most are closer to 10 – 50 µm range.

Zn/btc:

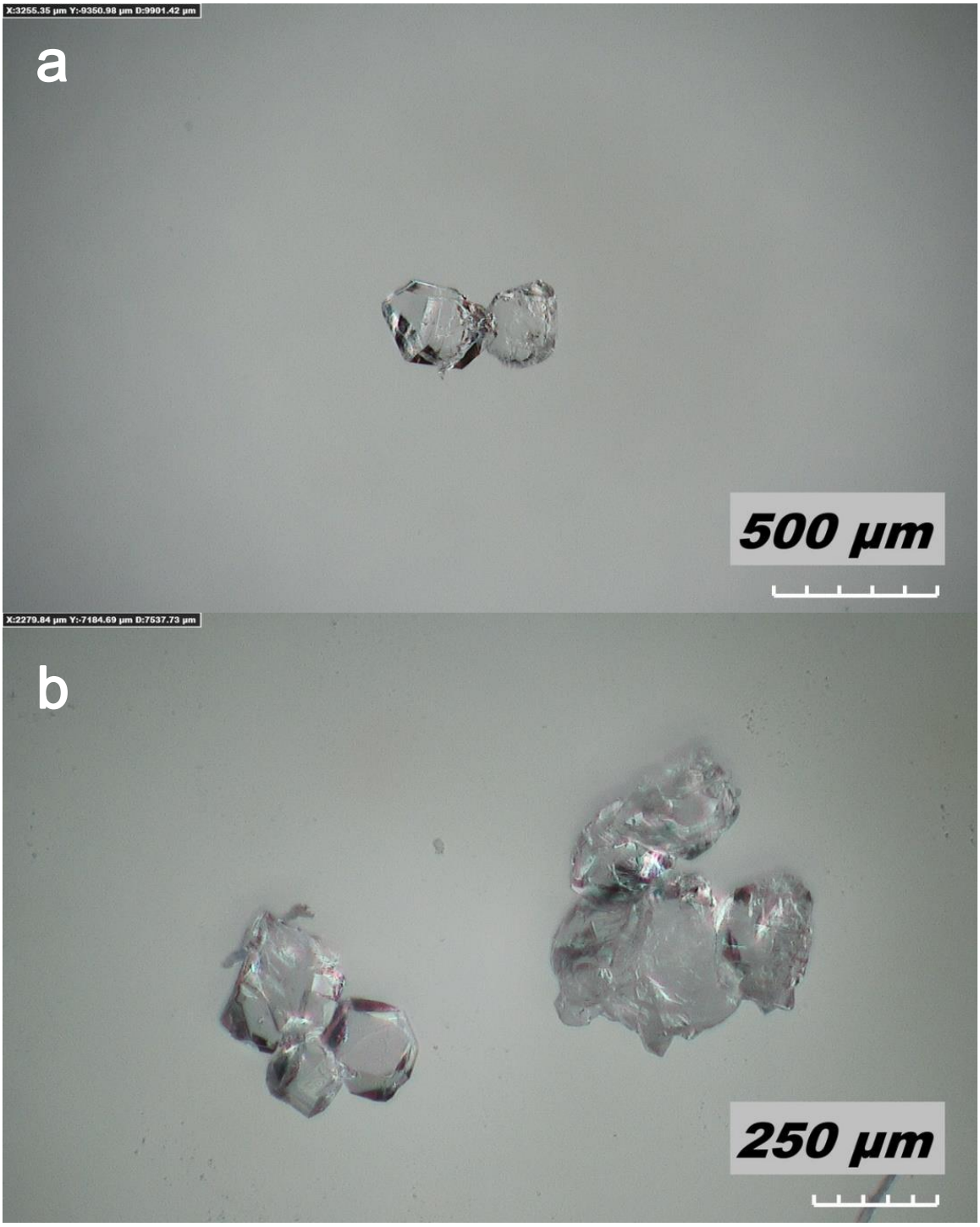

Figure 4.23. Optical micrographs of DEET-synthesized Zn/btc (a, b). The observed crystals have irregular/blocky morphologies. Crystals are 100 – 300 µm in diameter.

MOF-519:

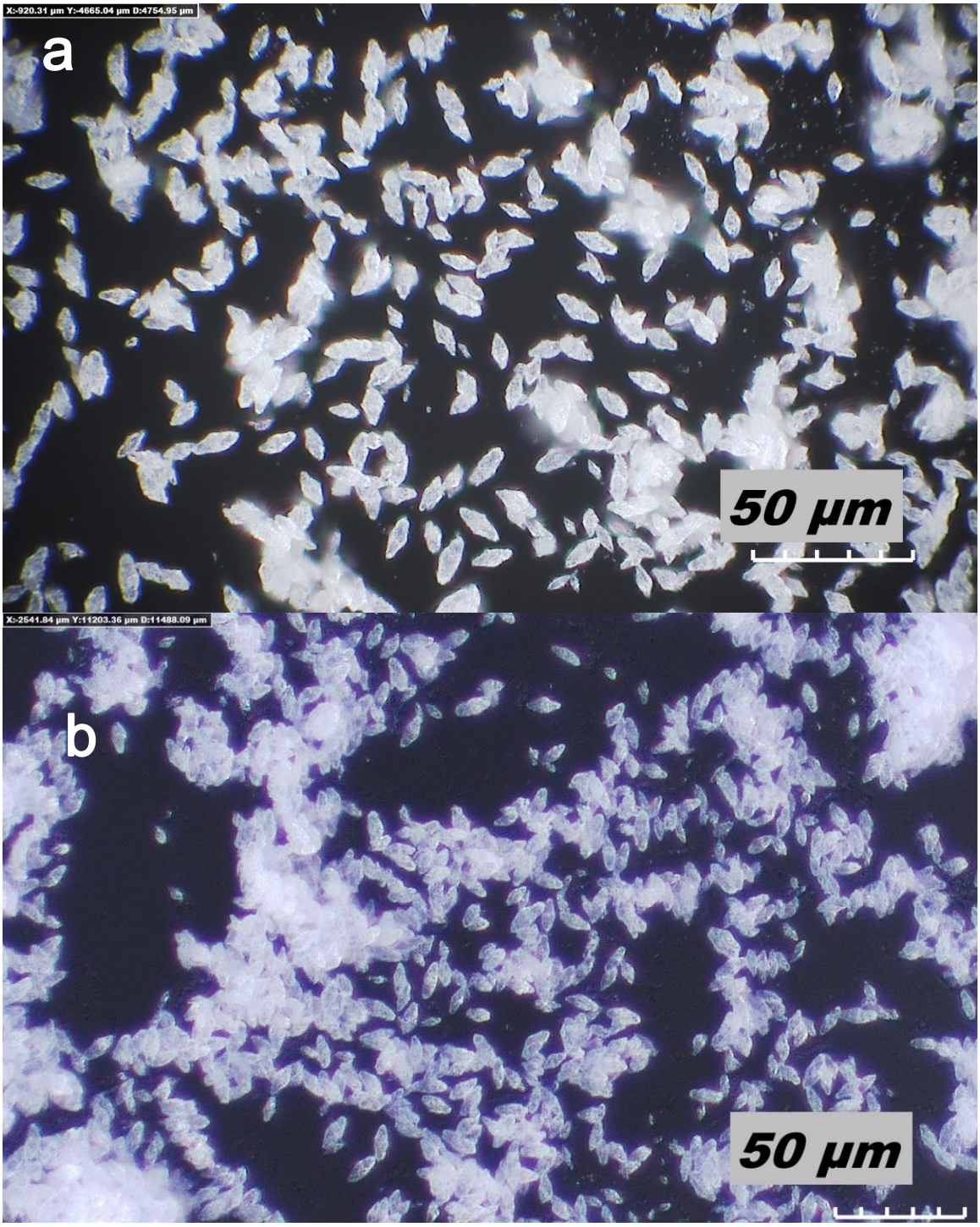

Figure 4.24. Optical micrographs of DEET-synthesized MOF-519 (a) and DMF-synthesized MOF-519 (b). Both syntheses yield crystals which appear to be elongated octahedra (approximately 5 × 5 × 10 µm).

4.4.7 Scanning electron microscopy

A JEOL JSM-7800FLV scanning electron microscope operating with an accelerating voltage of 10 kV was used to determine MOF morphology when morphology could not be determined by optical microscopy (HKUST-1, Cu/bdc). No images suitable for morphological identification could be collected for MIL-53(Al).

HKUST-1:

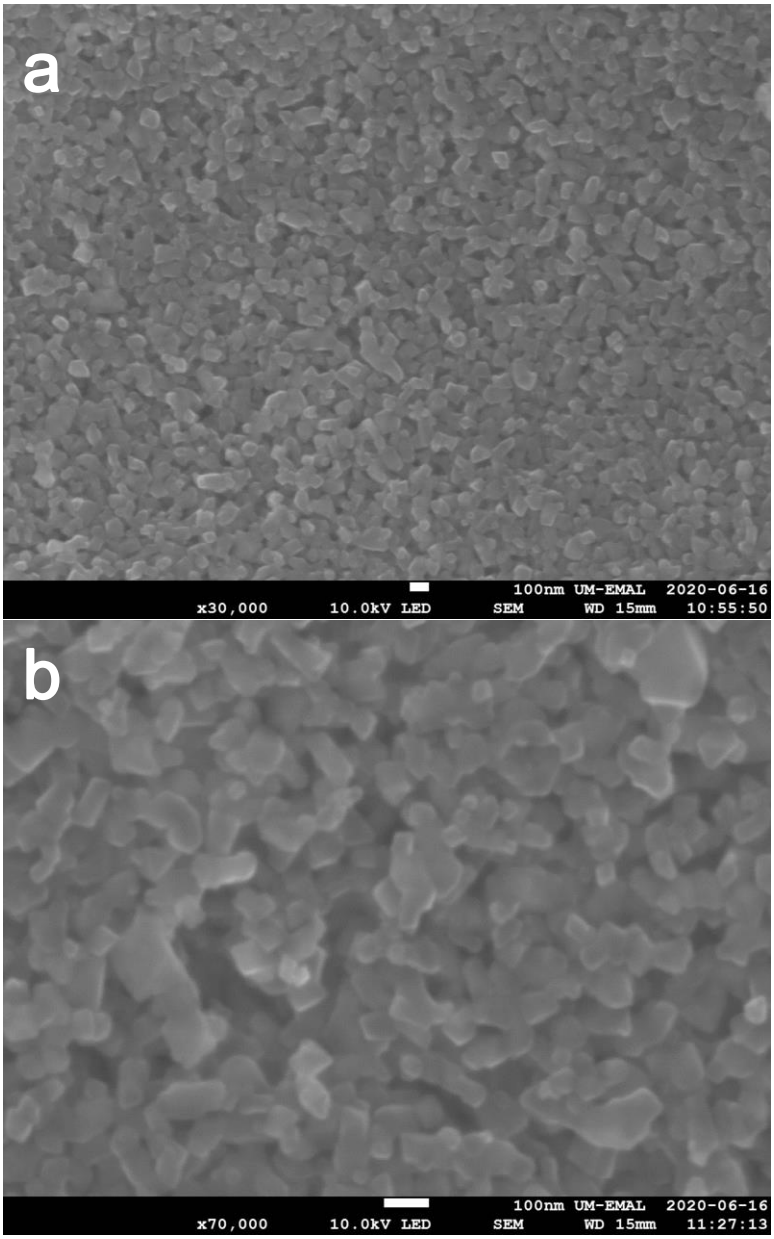

Figure 4.25. Scanning electron micrographs of DEET-synthesized HKUST-1 (a, b). Intergrown blocky crystals with sharp corners and flat faces are observed, with diameters generally ranging between 50 – 100 nm

Cu/bdc:

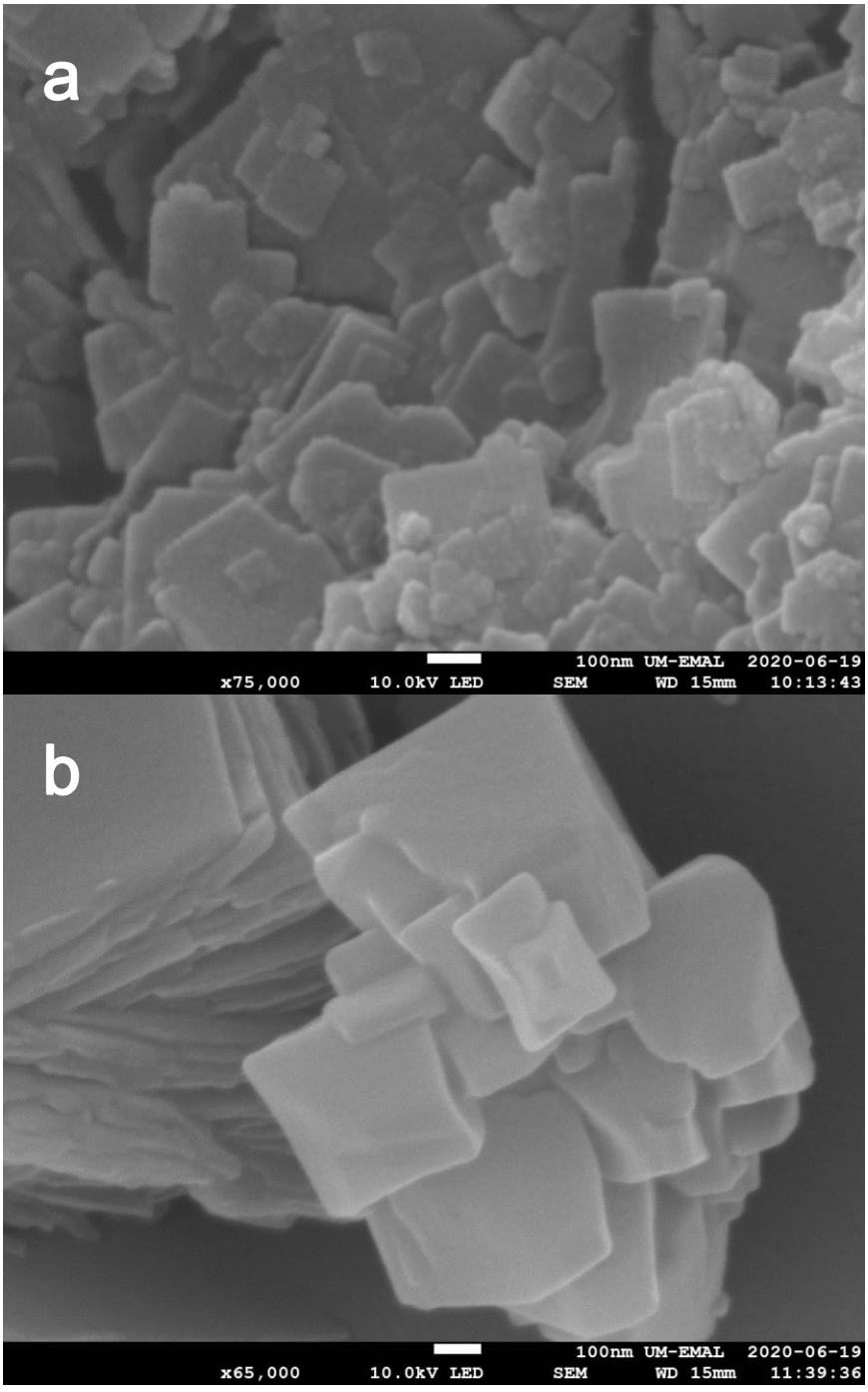

Figure 4.26. Scanning electron micrographs of DEET-synthesized Cu/bdc (a) and DMF-synthesized MOF-2 (b). Both appear to be stacked, intergrown plates.

4.4.8 ^{1}H-NMR

~10 mg of activated DEET-synthesized MOF-5 was digested using 35% DCl in D_2O (100 µL), then diluted with DMSO-d_6 (500 µL). ^{1}H-NMR measurement was performed at room temperature on a Varian Inova 500 spectrometer operating at 500 MHz. 16 scans with 2 second acquisition and a 1 second relaxation delay were collected.

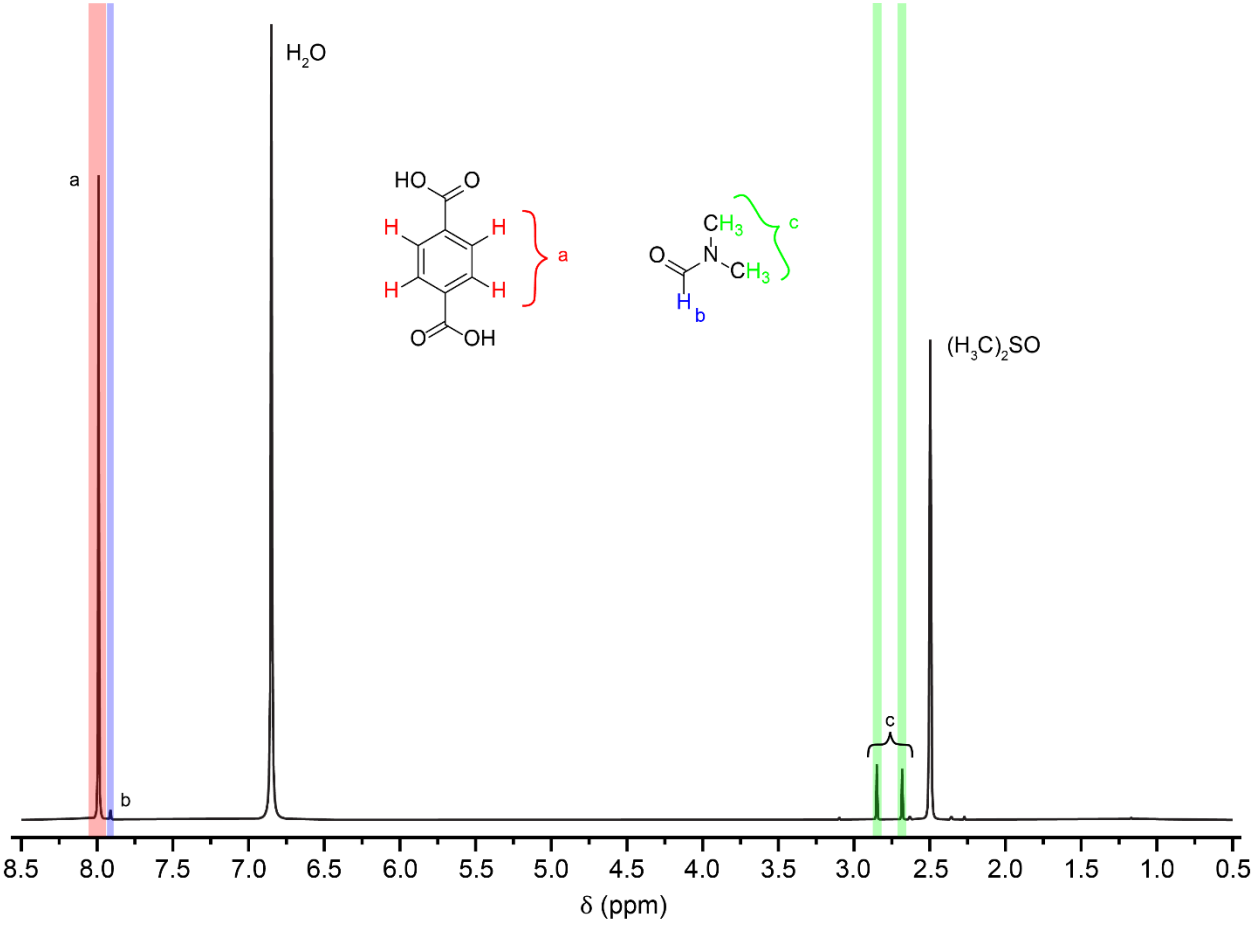

Figure 4.27. ^{1}H NMR spectrum of digested DEET-synthesized MOF-5 after solvent exchange and activation. Translucent colored overlays are for labelling only, the actual integration boundaries are given in Table 4.3. No DEET is observed in the solution.

Table 4.3. Chemical shifts, integral boundaries, integrals, and assignments for peaks in Figure S22, normalized to 100 bdc linkers (thus 400 bdc (H_a) protons).

Chemical shift (ppm)	Integration boundaries (ppm)	Integral (protons)	Assignment
7.99	8.113 – 7.937	400.00	Terephthalic acid
7.92	7.936 – 7.858	9.16	DMF formamide proton
2.85	2.899 – 2.798	34.16	DMF methyl group
2.69	2.715 – 2.656	32.31	DMF methyl group

Using DMF methyl groups (H_c) we can calculate a ratio of 1:0.11 between the amount of linker and DMF in the MOF. Per 100 bdc molecules:

$$32.31 + 34.16 = 66.47 \text{ total } H_c \text{ integral}$$

$$\frac{66.47 \text{ DMF methyl protons}}{100 \text{ linkers}} \times \frac{1 \text{ DMF molecule}}{6 \text{ methyl protons}} = \frac{0.11 \text{ DMF molecules}}{\text{linker}}$$

4.5 References

(1) Katz, T. M.; Miller, J. H.; Hebert, A. A., *J. Am. Acad. Dermatol.*, 2008, **58**, 865–871.
(2) Kennedy, G. L.; Short, R. D., *CRC Crit. Rev. Toxicol.*, 1986, **17**, 129–182.
(3) Scailteur, V.; Lauwerys, R. R., *Toxicology*, 1987, **43**, 231–238.
(4) Rutledge, L. C.; Gupta, R. K.; Mehr, Z. A.; Buescher, M. D.; Reifenrath, W. G., *J. Am. Mosq. Control Assoc.*, 1996, **12**, 39–44.
(5) Emam, H. E.; Abdelhameed, R. M., *J. Porous. Mater.*, 2017, **24**, 1175–1185.
(6) Li, H.; Eddaoudi, M.; O'Keeffe, M.; Yaghi, O. M., *Nature*, 1999, **402**, 276–279.
(7) Koh, K.; Wong-Foy, A. G.; Matzger, A. J., *Angew. Chem. Int. Ed.*, 2008, **47**, 677–680.
(8) Koh, K.; Van Oosterhout, J. D.; Roy, S.; Wong-Foy, A. G.; Matzger, A. J., *Chem. Sci.*, 2012, **3**, 2429.
(9) Furukawa, H.; Miller, M. A.; Yaghi, O. M., *J. Mater. Chem.*, 2007, **17**, 3197–3204.
(10) Chui, S. S. Y.; Lo, S. M. F.; Charmant, J. P. H.; Orpen, A. G.; Williams, I. D.; *Science*, **283**, 1999, 1148–1150.
(11) Mounfield, W. P.; Walton, K. S., *J. Colloid Interf. Sci.*, 2015, **447**, 33–39.
(12) Gándara, F.; Furukawa, H.; Lee, S.; Yaghi, O. M., *J. Am. Chem. Soc.*, 2014, **136**, 5271–5274.
(13) Kaye, S. S.; Dailly, A.; Yaghi, O. M.; Long, J. R., *J. Am. Chem. Soc.*, 2007, **129**, 14176–14177.
(14) Calza, P.; Medana, C.; Raso, E.; Giancotti V.; Minero, C., *Sci. Total Environ.*, 2011, **409**, 3894–3901.
(15) Woodrow, J. E.; Seiber J. N.; Dary, C., *J. Agric. Food Chem.*, 2001, **49**, 3841–3846.
(16) Suresh, K.; Matzger, A. J.; *Angew. Chem. Int. Ed.*, 2019, **58**, 16790–16794.

(17) Rodríguez, N. A.; Parra, R.; San Román, E.; Grela, M. A., *J. Mater. Sci.*, 2020, **55**, 6588–6597.
(18) Rubio-Martinez, M.; Avci-Camur, C.; Thornton, A. W.; Imaz, I.; Maspoch D.; Hill, M. R., *Chem. Soc. Rev.*, 2017, **46**, 3453–3480.
(19) Ren, J.; Dyosiba, X.; Musyoka, N. M.; Langmi, H. W.; Mathe M.; Liao, S., *Coord. Chem. Rev.*, 2017, **352**, 187–219.
(20) Windheuser, J. J.; Haslam, J. L.; Caldwell, L.; Shaffer, R. D., *J. Pharm. Sci*., 1982, **71**, 1211–1213.
(21) Di Lorenzo, M. L.; Longo, A., *Thermochim. Acta*, 2019, **677**, 180–185.
(22) Holsten, J. R.; Neely, N. E., US Pat., 5 207 803, 1993.
(23) Eddaoudi, M.; Kim, J.; Rosi, N.; Vodak, D.; Wachter, J.; O'Keeffe, M.; Yaghi, O. M., *Science*, 2002, **295**, 469–472.
(24) Fang, Q.; Zhu, G. S.; Xin, M.; Zhang, D.; Shi, X.; Wu, G.; Tian, G.; Tang, L.; Xue M.; Qiu, S. L., *Chem. J. Chinese U.*, 2004, **25**, 1016–1018.
(25) Park, K. S.; Ni, Z.; Cote, A. P.; Choi, J. Y.; Huang, R.; Uribe-Romo, F. J.; Chae, H. K.; O'Keeffe, M.; Yaghi, O. M., *Proc. Natl. Acad. Sci.*, 2006, **103**, 10186–10191.
(26) Banerjee, R.; Furukawa, H.; Britt, D.; Knobler, C.; O'Keeffe, M.; Yaghi, O. M., *J. Am. Chem. Soc.*, 2009, **131**, 3875–3877.
(27) Han, D.; Jiang, F.-L.; Wu, M.-Y.; Chen, L.; Chen Q.-H.; Hong, M.-C., *ChemComm*, 2011, **47**, 9861.
(28) Carson, C. G.; Hardcastle, K.; Schwartz, J.; Liu, X.; Hoffmann, C.; Gerhardt R. A.; Tannenbaum, R., *Eur. J. Inorg. Chem.*, 2009, **2009**, 2338–2343.
(29) Katz, M. J.; Brown, Z. J.; Colon, Y. J.; Siu, P. W.; Scheidt, K. A.; Snurr, R. Q.; Hupp J. T.; Farha, O. K., *ChemComm*, 2013, **49**, 9449–9451.
(30) Bon, V.; Senkovska, I.; Weiss M. S.; Kaskel, S., *CrystEngComm*, 2013, **15**, 9572.
(31) Swan, T. H.; Mack, E., *J. Am. Chem. Soc*., 1925, **47**, 2112–2116.

Chapter 5. Solvent Choice in MOF Linker Exchange Permits Microstructural Control*

5.1 Introduction

Metal–organic frameworks (MOFs) are the largest class of functional porous materials and are being pursued for myriad proposed applications. Because many MOFs with desirable chemical functionality are difficult or impossible to achieve directly, several strategies for modifying MOFs have been developed.[1] One such method is MOF linker exchange, wherein a MOF is incubated in a solution of a different linker, which replaces the original linker due to entropic and/or enthalpic forces. The process is useful for generating otherwise inaccessible materials, such as MOFs containing linkers which degrade[2–4] or generate undesired phases[5–15] under MOF synthesis conditions, and for modulating the linker distribution in MOFs.[16]

MOF linker exchange has undergone significant development and investigation in the near-decade since its discovery. The process was first reported in 2011 for the replacement of the bridging diamine linker in the pillared-sheet MOFs PPF-18 and -20 by Choe and coworkers, who accurately predicted in their report that there would be many more MOF systems to exhibit similar linker replacement.[17] Within the next year, linker exchange was reported for carboxylate[18] and

* Adapted from Dodson, R. A.; Kalenak, A. P.; Matzger, A. J. *J. Am. Chem. Soc.*, **2020**, *142*, 20806-20813.

imidazolate[5] linkers by Cohen and Farha/Hupp, respectively, who each coined terms for the process: post-synthetic exchange (PSE[18,1]) and solvent-assisted linker exchange (SALE[19,20]).

PSE is often performed in *N*,*N*-dimethylformamide (DMF), a common MOF synthesis solvent compatible with many MOFs. Other than DMF, the most often used PSE solvents are water (for water-stable MOFs such as MIL-53(Al)[21] or UiO-66[18]) or alcohols such as methanol or butanol (with Zr-MOFs[22,23] and ZIFs[5,6,24]). Other solvents used include additional amides (*N*-methyl-2-pyrrolidone,[9,17] *N*,*N*-diethylformamide,[17,25] *N*,*N*-dimethylacetamide[5]), ethers (THF,[16,26] dioxane[27]), acetonitrile,[28] DMSO,[29] and various mixtures of these. Despite the variety of solvents used in the literature, there are only a few examples of studies probing the effect of changing solvent on MOF PSE,[18,5,16,29,30] and no major effort has been made to relate the spatial distribution of exchanged linkers to the choice of PSE solvent. Developing this understanding is key to forward the purposeful design of hierarchical MOFs with tailored three dimensional architectures at length scale greatly exceeding the unit cell.[31]

MOF PSE involves the competition of two processes: linker diffusion from the high-concentration solution to the low concentration MOF interior, and linker exchange when new linker molecules have diffused to a suitable site within the framework. These two processes, diffusion and exchange, and their relative rates as a function of the PSE conditions, dictate the microstructure of the exchanged material. If diffusion is rapid relative to exchange ($k_d \gg k_e$), the new linker will reach its equilibrium concentration throughout the MOF before significant linker exchange can occur, leading to approximately uniform exchange. While characterization of the exchanged linker distribution within MOFs after PSE is still relatively uncommon, several examples of this exchange behavior have been reported.[25,22] If, instead, exchange is rapid relative

to diffusion ($k_e \gg k_d$), a core–shell MOF morphology results. This microstructure arises because the outer shell of the MOF requires less time to reach equilibrium concentration with the new linker, which is the limiting factor for PSE in this regime, and thus will undergo exchange before the MOF core. This gives rise to the core–shell morphology observed by our lab and others.[16,32–34,28,23,27,35,36]

Core–shell MOFs were first synthesized via growth of the shell phase on core seeds[37] rather than via linker exchange, but challenges associated with this method (growth of undesired phases and interfacial gaps between core and shell layers) can be bypassed with a PSE approach. Core–shell MOF materials have since been created and proposed for a range of applications. The major benefit to this type of material is the ability to modulate the overall guest uptake (or exclusion) by tuning surface linkers, while retaining desirable properties associated with the bulk phase. In the area of MOF catalysis, size-selective catalytically active core–shell MOFs have been engineered which reject undesired species by modulation of the shell pore aperture size.[36] To improve the water stability of a sensitive MOF phase, Rosi and coworkers encapsulated it in a more stable MOF phase.[38] This modification also had the effect of lowering N_2 uptake without reducing the core MOF CO_2 capacity, thus improving CO_2/N_2 selectivity relative to either of the pure component MOF phases, a concept which has subsequently been applied to additional MOF systems.[35]

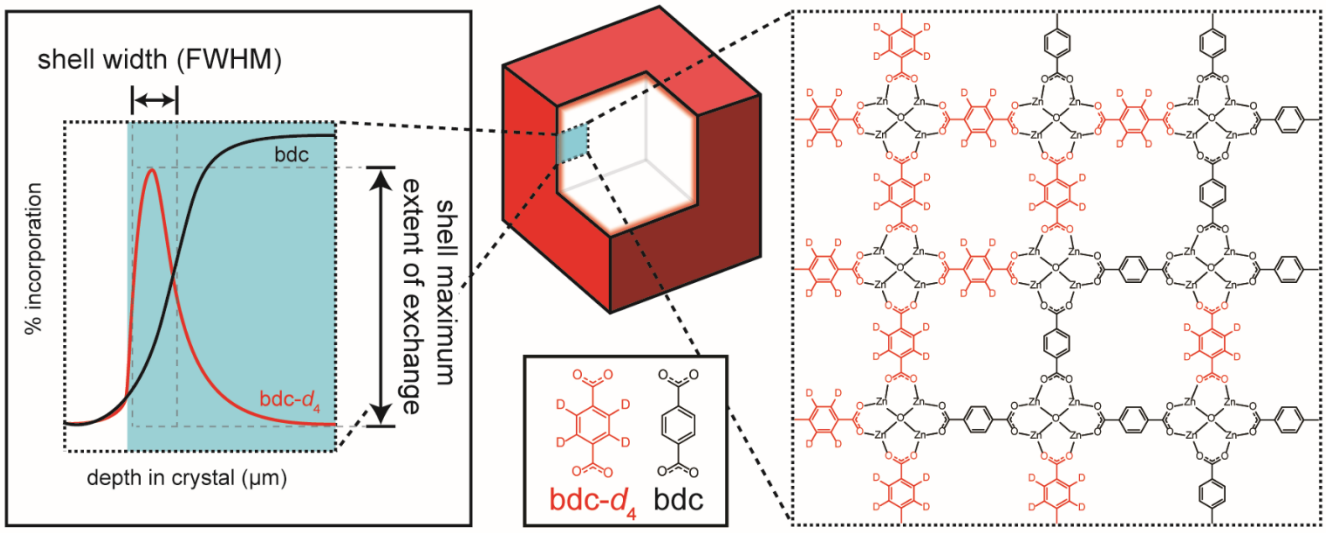

Figure 5.1. Schematic representation of the MOF-5 → MOF-5-d_4 linker exchange. Center: a partially exchanged core–shell MOF structure with a cubic region removed from the corner, with the two constituent linkers shown below. Right: an example (flattened) slice of a partially bdc-d_4 exchanged section of MOF-5. Linkers aligned perpendicular to the page have been omitted for clarity. Left: percent incorporation versus crystal depth plot for bdc and bdc-d_4 in the model system shown. Shell width, in the form of full-width at half-max, and maximum extent of exchange are both shown.

There are two main parameters that define the shell of a core–shell MOF: the thickness of the shell, and the extent of exchange (%) within that shell. (Figure 5.1) In practice, the exchanged linker distribution profile has some variability, but average shell width and maximum extent of exchange can be determined and compared between PSE conditions. It would be desirable to be able to achieve arbitrary thickness and degree of exchange within the exchanged shell, but there is currently no established roadmap for doing so.

In this work, the influence of solvent choice on PSE in the ubiquitous MOF-5 system is explored, and the extent to which the resulting core–shell morphology can be modulated by choice of solvent is characterized. In particular, this work focuses on the MOF-5 → MOF-5-d_4 linker exchange, wherein terephthalate (bdc, the linker in MOF-5) is substituted by perdeuterated terephthalate (bdc-d_4), as this system is known to generate a core-shell structure in both DMF and

THF, there are no thermodynamic factors influencing the exchange (making it purely entropically driven), and the linkers have distinct Raman signals so the resultant structures can be thoroughly characterized via mapping Raman microspectroscopy.[16]

Solvents were chosen based on their commercial availability and their similarly to reported exchange solvents. Particularly low polarity solvents (e.g. hexane, CH_2Cl_2) were purposefully excluded based on their inability to dissolve 10 mM H_2bdc-d_4 at room temperature. 30 solvents were initially screened (Figure 5.2, see Chapter 5.4 for details). The solvents include amides (DMF, *N*,*N*-diethylformamide, *N*,*N*-dibutylformamide, *N*-methyl-2-pyrrolidone, 1-formylpyrrolidine, 1-formylpiperdine, *N*-formylmorpholine, *N*,*N*-dimethylacetamide, *N*-methylformanilide, and *N*,*N*-diethyl-3-methylbenzamide), aldehydes/ketones (butanone, cyclohexanone, benzaldehyde, acetophenone), ethers (THF, 2,5-dimethyltetrahydrofuran, dioxane, dibutyl ether, methyl *t*-butyl ether, anisole, 1,2-dimethoxyethane, and 2-methoxyethanol), esters (ethyl acetate, butyl acetate, *t*-butyl acetate), carbonate esters (propylene carbonate and dimethyl carbonate), DMSO, sulfolane, and acetonitrile. Solvents were shaken over activated 4 Å molecular sieves for a minimum of 24 hours prior to analysis to remove trace water (see Chapter 5.4).

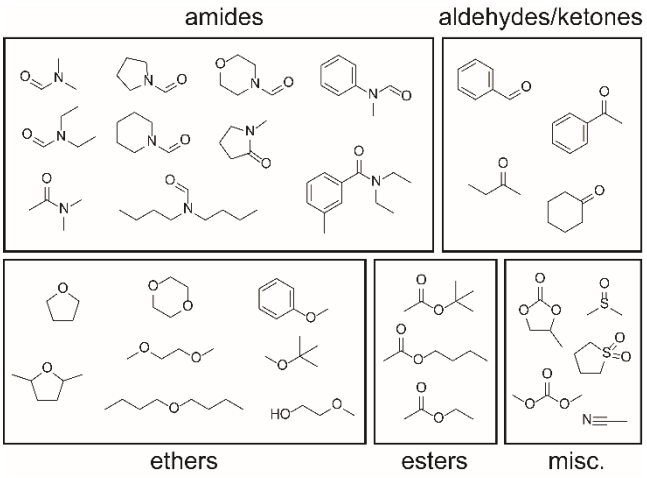

Figure 5.2. Solvents studied for their behavior in the MOF-5 → MOF-5-d4 linker exchange.

After initial screening, the solvents were narrowed down (13/30, *vide infra*) for more detailed characterization. Briefly, MOFs were synthesized and washed, then incubated in 10 mM solutions of H_2bdc-d_4 for 24 hours to allow for linker exchange (see Chapter 5.4 for full experimental details). MOF crystals were then activated, cleaved, and characterized with mapping Raman microspectroscopy to visualize the distribution of exchanged linker in the final structure. Shell maximum extent of exchange (ranging from 0%, indicating no exchange, to 100%, meaning full exchange) and thickness (in the form of shell full-width at half-max, FWHM) were extracted, and compared between different linker exchange solvents. To probe the effect of mixing solvents on the MOF-5 → MOF-5-d_4 linker exchange, several binary solvent mixtures were also tested in the same fashion.

5.2 Results and Discussion

Initial screening. The initial 30 screened solvents were divided based on their performance in three categories: a) their ability to dissolve 10 mM H_2bdc-d_4, b) their ability to maintain the

crystallinity of MOF-5 for 24 hours, and c) whether they permit linker exchange in the MOF-5 → MOF-5-d_4 linker exchange (Figure 5.3).

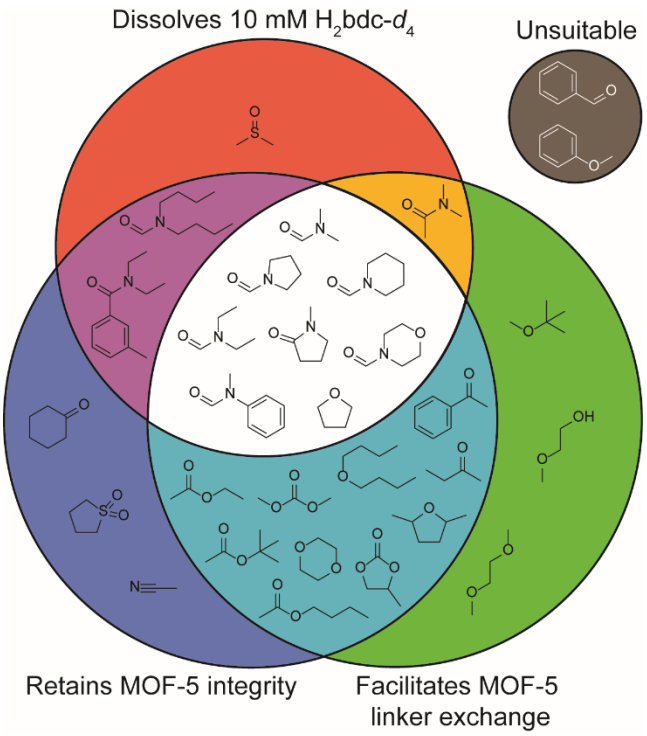

Figure 5.3. Venn diagram summarizing solvent overall performance in the MOF-5 → MOF-5-d_4 linker exchange. Solvents are separated depending on their ability to dissolve 10 mM H_2bdc-d_4, maintain the phase stability of MOF-5 for 24 hours, and facilitate the MOF-5 → MOF-5-d_4 linker exchange.

Most solvents tested (17/30) were deemed to be unsuitable for the MOF-5 → MOF-5-d_4 linker exchange. Two solvents, benzaldehyde and anisole, were wholly unsuccessful: both of these solvents cause MOF-5 degradation and fail to dissolve 10 mM H_2bdc-d_4 while accomplishing no observable linker exchange. DMSO successfully dissolves 10 mM H_2bdc-d_4 but also degrades MOF-5, obscuring the spatial distribution of any exchange process that might have occurred. *N*,*N*-Dimethylacetamide also dissolves 10 mM H_2bdc-d_4 and degrades MOF-5 (to a lesser degree than DMSO), but when the products of the exchange were characterized, linker exchange was found to occur. 1,2-Dimethoxyethane, 2-methoxyethanol, and methyl *t*-butyl ether also degrade MOF-5 and

facilitate MOF-5 linker exchange, but do not fully dissolve the linker. Cyclohexanone, sulfolane, and acetonitrile do not cause MOF-5 degradation, but they neither fully dissolve the linker, nor appear to facilitate MOF-5 linker exchange.

Many solvents were capable of performing linker exchange and did not degrade MOF-5, but could not fully dissolve 10 mM H_2bdc-d_4. Solvent functional groups that fell into this category include ketones (butanone, acetophenone), esters (ethyl acetate, butyl acetate, *t*-butyl acetate), ethers (dioxane, 2,5-dimethyltetrahydrofuran, dibutyl ether), and carbonate esters (dimethyl carbonate, propylene carbonate). Of these solvents, three (dioxane, butyl acetate, propylene carbonate) were determined to dissolve sufficient quantities of H_2bdc-d_4 to warrant further investigation. *N*,*N*-Diethyl-3-methylbenzamide and *N*,*N*-dibutylformamide both dissolve the linker and retain MOF-5 integrity, but give nearly no exchange – this is presumably due to their large sizes relative to the other solvents tested, prompting further investigation into both of these solvents. The other eight solvents (THF and the seven remaining amides) were found to successfully dissolve 10 mM H_2bdc-d_4, retain MOF-5 integrity, and facilitate MOF-5 linker exchange, and were subjected to further characterization.

Investigation of bdc-d_4 shells after linker exchange offers considerable insight into the phenomenon of MOF linker exchange, both from a fundamental perspective and from a practical one. By examining the relationship between the extent of exchange and the exchanged shell thickness, it is apparent that the two are correlated, but not linearly (Figure 5.4, Table 5.1). While holding conditions other than solvent (concentration of linker and MOF, temperature, time, agitation) constant, substantial variability in the exchanged shells are possible; these 13 solvents

allow achieving shells within a range of 8 to 70% maximum extent of exchange. All solvents give average shell thicknesses in the span of 3.6 – 56 μm, with all but four falling under 10 μm.

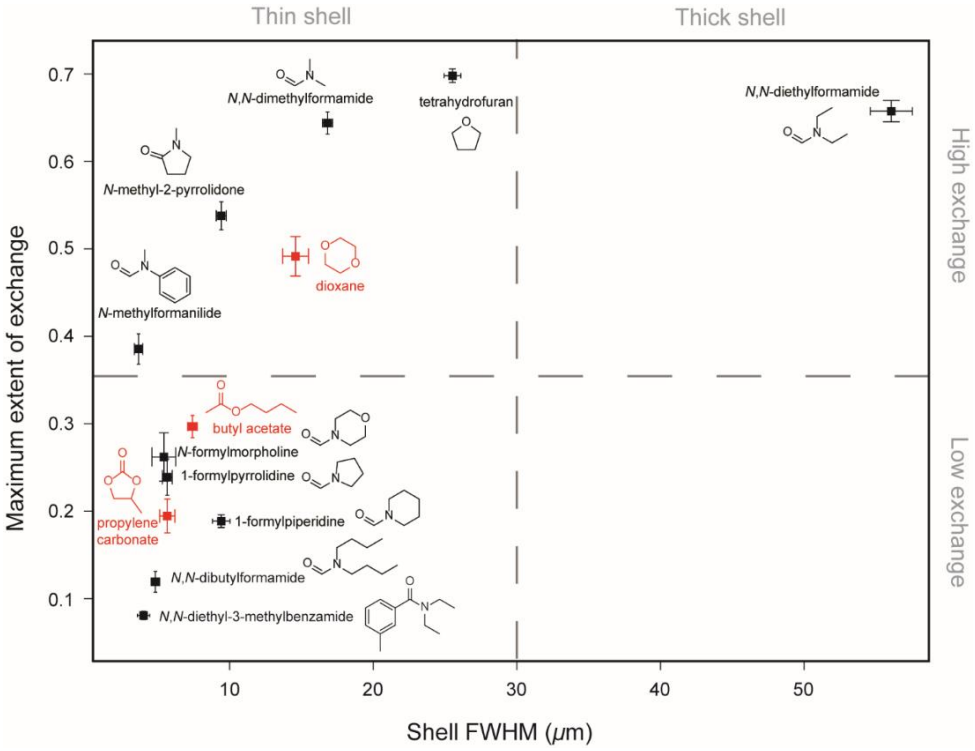

Figure 5.4. Maximum extent of exchange versus shell full-width at half-max for shells resulting from several PSE solvents. Extent of exchange and shell FWHM refer to the bdc-d_4 shells resulting from the MOF-5 → MOF-5-d_4 linker exchange after 24 hours in the presence of 10 mM H_2bdc-d_4. Error bars indicate the standard error of the mean. Solvents in red (dioxane, butyl acetate, and propylene carbonate) did not fully dissolve 10 mM H_2bdc-d_4.

Table 5.1. Measured shell parameters for individual solvents. Values are given as the average ± the standard error of the mean ($\sigma/\sqrt{n}$). Degree of shell exchange indicates the maximum degree of exchange measured in the shell. Thickness is given as shell full-width at half-max.

Solvent	Degree of shell exchange (%)	Shell thickness (μm)
tetrahydrofuran	69.8 ± 0.8	25.4 ± 0.6
N,*N*-diethylformamide	65.9 ± 1.2	56.0 ± 1.5
N,*N*-dimethylformamide	64.4 ± 1.3	16.7 ± 0.3
N-methyl-2-pyrrolidone	53.9 ± 1.6	9.4 ± 0.4
dioxane	49.1 ± 2.3	14.5 ± 0.9

N-methylformanilide	38.7 ± 1.7	3.6 ± 0.3
butyl acetate	29.8 ± 1.3	7.4 ± 0.3
N-formylmorpholine	26.3 ± 2.8	5.3 ± 0.8
1-formylpyrrolidine	24.0 ± 2.1	5.6 ± 0.3
propylene carbonate	19.4 ± 1.9	5.5 ± 0.5
1-formylpiperdine	18.9 ± 0.7	9.4 ± 0.6
N,*N*-dibutylformamide	12.0 ± 1.2	4.8 ± 0.3
N,*N*-diethyl-3-methylbenzamide	8.1 ± 0.5	4.0 ± 0.4

The landscape of possible shell types resulting from MOF PSE can be broken down into four main regimes, each with different potential applications. Specifically, shells can be classified into a) thick, high exchange shells, b) thin, high exchange shells, c) thin, low exchange shells, and d) thick, low exchange shells. Fundamentally, the MOF microstructure resulting from PSE depends on the rates of linker diffusion and exchange. The incoming linker must first diffuse through the MOF to reach a site suitable for the replacement reaction to occur. Once it has diffused into the MOF, the linker must then participate in the replacement reaction, which involves significant local bonding reorganization. If diffusion is relatively rapid, thicker shells are expected in the PSE products. If exchange is relatively rapid, shells with a greater extent of exchange should result. Changing the solvent may change both the diffusion and exchange rates through steric as well as electronic means. The use cases for each type of core-shell microstructure and the optimal PSE solvent choice for each category are as follows:

Thick shells with high exchange. This type of PSE is often utilized when complete linker replacement (e.g. the transformation of one MOF into another) is required. This is necessary when the desired MOF is composed of linkers that are unstable in the MOF synthesis conditions or when

direct synthesis with the linker being substituted in does not form the desired phase. *N*,*N*-diethylformamide is superior to the other solvents tested for achieving thick, high exchange percentage shells (Figure 5.4).

The exceptional PSE properties of *N*,*N*-diethylformamide are striking on comparison to the closest chemical analog, DMF, which gives shells with similar extents of exchange but roughly a quarter of the thickness. The sole chemical distinction between these solvents is the longer alkyl groups in *N*,*N*-diethylformamide.[39] Formamide solvents such as DMF are known to reversibly bind the Zn_4O clusters in MOF-5;[40] if a coordinating solvent with large side chains binds to the metal cluster, it leads to aperture contraction and thus slowed diffusion of H_2bdc-d_4 into the MOF. If a comparable number of solvent molecules coordinate to the framework, increasing solvent size should correlate with slowed diffusion, and thus thinner exchanged linker shells. Indeed, there is some correlation between solvent size and diffusion rate of H_2bdc-d_4 into MOF-5: *N*,*N*-diethyl-3-methylbenzamide, *N*,*N*-dibutylformamide, and *N*-methylformanilide were the largest solvents tested, and give the thinnest shells, whereas THF, DMF, and dioxane are the three smallest solvents and give rise to three of the four thickest shells. However, such size-based diffusion slowing arguments are clearly not suitable for explaining the difference between the PSE behavior of DMF and *N*,*N*-diethylformamide, as the larger solvent gives much more rapid linker diffusion into the MOF, and thus thicker exchanged shells. The differences between the PSE behavior of these solvents can instead be explained on a "shielding" basis. From a linker-framework interaction perspective, solvation of the MOF can lead to partial shielding of the polar H_2bdc-d_4 molecules from polar regions of the framework. Slow diffusion of benzoic acid through MOF-5 has been ascribed to carboxylic acid binding to the cluster that is not observed in methyl benzoate.[16] The

ethyl groups in *N*,*N*-diethylformamide seem to outperform the methyl groups of DMF at blocking unproductive linker-framework interactions, and thus at speeding H_2bdc-d_4 diffusion into MOF-5. Stated another way, *N*,*N*-diethylformamide-solvated MOF-5 has pores which are more hydrophobic than in DMF-solvated MOF-5, without suffering from an apparent loss in framework-linker reactivity.

As with the comparison between DMF and *N*,*N*-diethylformamide, the difference in PSE behavior between THF and dioxane can be understood through consideration of the differential shielding of interactions between the polar linker diacid and the polar metal cluster. When comparing the exchange behavior of the two solvents, dioxane is found to give much thinner shells than THF. Dioxane is known to solvate ion pairs less effectively than THF.[41,42] Thus, dioxane is also less effective at shielding the polar metal cluster from the polar diffusing H_2bdc-d_4 molecules, leading to slower linker diffusion into the MOF and thinner shells.

Thin shells with high exchange. This type of MOF microstructure is useful for a wide variety of applications, and is one of the more well-studied of the four regimes. In particular, this type of system is desirable for applications where guest access into the MOF needs to be modulated, whether to prevent degradation of a fragile core, to discriminate between analytes for enhanced sensitivity in molecular sensing, or to prevent undesired reagents from reaching catalyst active sites via size exclusion.

The PSE solvent most suitable for generating thin shells with a high extent of exchange is *N*-methylformanilide. This solvent gives shells with a maximum extent of exchange of ~38.7 %, a moderately high exchange fraction: it is roughly half that of the highest exchanging solvent (*N*,*N*-diethylformamide) and nearly 5× that of the lowest (*N*,*N*-diethyl-3-methylbenzamide). However,

N-methylformanilide gives the thinnest shells of the solvents tested here (3.6 μm versus 4.0 μm for *N*,*N*-diethyl-3-methylbenzamide and 4.8 μm for *N*,*N*-dibutylformamide), making it optimal for the thin, high exchange regime. If a slightly higher extent of exchange is desired, *N*-methyl-2-pyrrolidone can also be considered. This solvent gives higher degrees of exchange than *N*-methylformanilide (53.9 %, ~1.4× higher) but with the tradeoff of thicker shells (9.4 μm, ~2.6× the thickness of *N*-methylformanilide shells). These thicker shells may be ascribed to the greater bulk near the coordinating functionality in *N*-methyl-2-pyrrolidone, permitting faster linker diffusion into the MOF than occurs in *N*-methylformanilide, while also allowing for quicker linker replacement as evidenced by its higher extents of exchange.

Thin shells with low exchange. Thin shells with a low degree of exchange have potential utility in the area of catalysis. Specifically, such a MOF microstructure may be useful if surface reactivity and dilute active sites are both required (e.g. to prevent bimolecular catalyst decomposition). Two of the solvents tested are highly suitable for achieving thin, low exchange percentage shells: *N*,*N*-diethyl-3-methylbenzamide and *N*,*N*-dibutylformamide. Both give thin shells (4.0 and 4.8 μm) with low extents of exchange (8.1 and 12.0 %).

While quick linker diffusion through *N*,*N*-diethylformamide-solvated MOF-5 is attributed to its ethyl chains shielding H_2bdc-d_4/framework interactions, this enhanced diffusion is not seen in *N*,*N*-dibutylformamide, which is chemically identical to DMF and *N*,*N*-diethylformamide other than its longer alkyl chains. The much larger steric bulk of *N*,*N*-dibutylformamide relative to the other two formamide solvents significantly decreases the linker diffusion rate through the MOF, leading to its thinner, lower exchange shells. *N*,*N*-diethyl-3-methylbenzamide gives similar PSE

performance to *N*,*N*-dibutylformamide, but requires separate consideration due to its unique chemical features.

N,*N*-Diethyl-3-methylbenzamide is the only solvent other than *N*-methylformanilide with an aryl side group, and these two solvents give the thinnest shells of the solvents tested, suggesting that this bulky feature is responsible for slowing linker diffusion into MOF-5. However, *N*,*N*-diethyl-3-methylbenzamide gives substantially lower extents of exchange than *N*-methylformanilide. This makes sense when the geometries of the solvent molecules are examined. If both solvents coordinate to the Zn_4O cluster in MOF-5 through their amide oxygen, *N*-methylformanilide has one arm which extends from its carbonyl (a methylphenylamino group, 106.15 Da), whereas *N*,*N*-diethyl-3-methylbenzamide has two branching arms (a tolyl group and a diethylamino group, 91.13 and 72.13 Da), which would impose a greater barrier to H_2bdc-d_4 accessing the metal cluster to perform exchange.

Thick shells with low exchange. This regime is useful in catalysis when highly dispersed active sites are required to prevent catalyst decomposition, and pore-size selectivity is leveraged to control selective diffusing in and out of the framework to the catalytic sites. In this type of system, isolation of the active site to the MOF surface is not desirable, and high catalyst concentrations need to be avoided.

Mixed linker MOFs with homogeneous linker distributions can generally be easily achieved with direct synthesis, reducing the motivation for developing this type of PSE. The conditions used in this work were chosen such that samples could not equilibrate with the substituting linker (24 hour exchanges), which thus discourages formation of thick shells with a low exchange percentage in the relatively large MOF-5 crystals studied here (~700-1000 μm).

However, the majority of MOFs relevant to catalysis are much smaller, e.g. on the order of hundreds of nanometers for the ubiquitous UiO-66 system.[43] For such small MOF crystals, linker diffusion (and subsequent equilibration) into the MOF core takes place relatively quickly, and a low degree of exchange can be achieved by using a low exchanging solvent like *N*,*N*-diethyl-3-methylbenzamide or *N*,*N*-dibutylformamide. However, if the MOF is large, a solvent which gives thick shells (like *N*,*N*-diethylformamide) should be coupled with a lower ratio of exchanging linker:starting linker and long exchange times, such that the system can equilibrate at a high entropy, well-dispersed state. Development of specific protocols to optimize MOF PSE under equilibrating conditions remains a challenge for future work in the field.

To probe the generality of controlling shell properties in MOF PSE using solvent choice alone, a non-degenerate linker exchange (MOF-5 → IRMOF-3) was also tested. This exchange, which involves the replacement of bdc with bdc-NH_2, showed slower diffusion rates of linker into the MOF than in the MOF-5 → MOF-5-d_4 exchange, but clear differences in shell thickness and degree of exchange were still achievable upon only changing solvent (see Chapter 5.4.7).

Solvent mixtures. Solvent mixtures have been previously found to have unexpected PSE properties. Despite poor linker solubility in benzene, Bernin and coworkers found that 40.7% DMSO in benzene gave faster exchange than pure DMSO for UiO-67 PSE, which they attributed to the lower viscosity of the solvent mixture.[30] Beyond such considerations, the potential of mixing solvents on PSE outcomes is relatively unexamined. Because *N*,*N*-diethyl-3-methylbenzamide gives thin shells with very low degrees of exchange, it is apparent that the solvent does not effectively facilitate linker exchange in MOF-5 and slows linker diffusion into the MOF pores. The major disparities between its performance and that of the best PSE solvents suggests that a

wide range of PSE performance could be achieved with binary mixtures of *N*,*N*-diethyl-3-methylbenzamide and a more effective PSE solvent.

To determine the impact of mixing solvents on the MOF-5 → MOF-5-d_4 linker exchange, mixtures of *N*,*N*-diethyl-3-methylbenzamide and either DMF (Figure 5.5) or *N*,*N*-diethylformamide (see Chapter 5.4.8) were prepared and characterized. Addition of 1 part *N*,*N*-diethyl-3-methylbenzamide to 3 parts DMF results in nearly no change relative to neat DMF. However, a mixture of equal amounts of *N*,*N*-diethyl-3-methylbenzamide and DMF gives shells with slightly lower extent of exchange (~10% lower) and roughly half thickness relative to neat DMF. Further addition of *N*,*N*-diethyl-3-methylbenzamide to a 3:1 ratio also decreases the extent of exchange (~65%) and shell thickness (~24%) relative to DMF. A 9:1 *N*,*N*-diethyl-3-methylbenzamide:DMF mixture behaves nearly like pure *N*,*N*-diethyl-3-methylbenzamide, except with slightly thinner shells on average. The PSE behavior of *N*,*N*-diethylformamide is also modulated in a nonlinear fashion by addition of *N*,*N*-diethyl-3-methylbenzamide, but with a different concentration dependence than is seen in the DMF/*N*,*N*-diethyl-3-methylbenzamide system (see SI). In particular, mixtures containing 25-75 % *N*,*N*-diethylformamide in N,N-diethyl-3-methylbenzamide have approximately the same thickness, but vary in extent of exchange. This points to the possibility of further unexpected behavior of solvent mixtures in PSE.

Comparison between N,N-diethyl-3-methylbenzamide solvent mixtures and pure solvent PSE behavior reveals that in the conditions tested, these mixtures give results that can be achieved with the use of pure solvents rather than demonstrating new PSE behavior. In particular, 1:1 N,N-diethyl-3-methylbenzamide:DMF gives shells comparable to N-methyl-2-pyrrolidone and 3:1 N,N-diethyl-3-methylbenzamide:DMF gives similar shells to N-methylformanilide. It is possible

that mixtures of different solvents would allow for better modulation of shell thickness at arbitrary extents of exchange, but varying N,N-diethyl-3-methylbenzamide concentration in mixtures with DMF primarily gives control over shell extent of exchange with most mixtures giving thin shells, in a similar fashion to most pure solvents. This redundancy is valuable, as the mixed solvent approach has the potential for greater cost efficiency and for much more precise control over the process. Ultimately, both approaches are viable for controlling shell parameters using solvent alone.

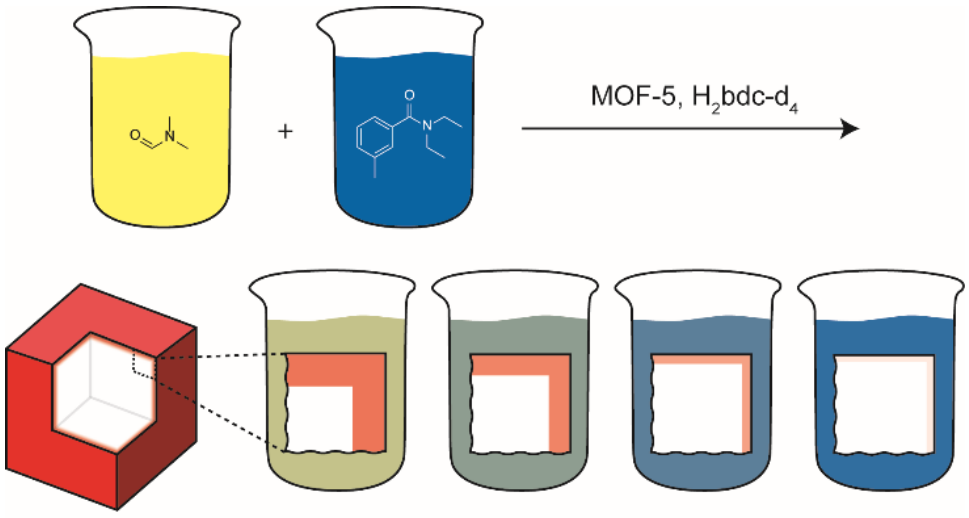

% DMF	75	50	25	10
Extent of exchange	65.8 ± 1.2	57.8 ± 1.2	41.5 ± 1.9	8.4 ± 0.7
Shell thickness	14.6 ± 0.5	9.3 ± 0.6	4.0 ± 0.2	3.1 ± 0.2

Figure 5.5. Measured shell parameters for binary mixtures of DMF and *N*,*N*-diethyl-3-methylbenzamide. Solvent composition is given as % DMF, with *N*,*N*-diethyl-3-methylbenzamide constituting the remainder of the solvent mixture. Extent of exchange indicates the maximum degree of exchange (%) measured in the shell. Thickness is given in μm as shell full-width at half-max. Values are given as the average ± the standard error of the mean ($\sigma/\sqrt{n}$).

5.3 Conclusions

The MOF linker exchange performance of a set of 30 organic solvents has been determined, and where possible, the chemical rationale for unexpected behavior was explored. While the exact

shell parameters will vary when the MOF/linker are changed, insights from this work are extensible to any PSE system. The major impact that solvent choice plays in dictating PSE behavior is demonstrated, as well as the wide variety of underutilized solvents that are suitable for this purpose. Finally, the possibility of tuning MOF core–shell microstructures using binary solvent mixtures of poor and effective PSE solvents is explored, and it is shown that these mixtures allow for equivalent control of MOF microstructure relative to pure solvents.

5.4 Supporting Information

5.4.1 Reagents

Terephthalic acid (H_2bdc, Fisher Scientific, 98%), terephthalic acid-d_4 (H_2bdc-d_4, Sigma-Aldrich, 98%, 98 atom % D), and 2-aminoterephthalic acid (H_2bdc-NH_2, Sigma-Aldrich, 99%) were used as received. Zinc nitrate hexahydrate (Fisher Scientific, ACS grade) was partially dehydrated by room temperature evacuation (~16 hr, <0.01 Torr) to yield zinc nitrate tetrahydrate. *N*,*N*-Diethylformamide (DEF, Acros Organics, 99%) was purified by storage on activated charcoal for ~1 month and passed through a silica gel column to remove impurities, followed by storage on activated 4 Å molecular sieves. Acetonitrile (Fisher, Certified ACS ≥99.9%), acetophenone (Acros Organics, 98%), anisole (Acros Organics, 99.0%), benzaldehyde (Sigma-Aldrich, 99.5%), butanone (Fisher, ACS 99+%), butyl acetate (Acros Organics, 99.5%), cyclohexanone (Acros Organics, 99.8%), dibutyl ether (Acros Organics, 99%), 1,2-dimethoxyethane (Sigma-Aldrich, 99.5%, inhibitor free), dimethyl carbonate (Acros Organics, 99%), *N*,*N*-dibutylformamide (TCI Chemicals, >98.0%), *N*,*N*-diethyl-3-methylbenzamide (Acros Organics, 98%), *N*,*N*-dimethylacetamide (Acros Organics, 99%), *N*,*N*-dimethylformamide (DMF, Fisher Scientific, 99.8%), 2,5-dimethyltetrahydrofuran (Sigma-Aldrich, 98%), dimethyl sulfoxide (DMSO, Fisher

Scientific, HPLC grade), dioxane (Fisher, Certified ACS ≥99.9%), ethyl acetate (Fisher, Certified ACS ≥99.5%), 1-formylpiperdine (Acros Organics, 99%), 1-formylpyrrolidine (Sigma-Aldrich, 97%), *N*-formylmorpholine (Acros Organics, 99+%), methylene chloride (CH_2Cl_2, Fisher scientific, ACS 99.5%), *N*-methylformanilide (Acros Organics, 99%), *N*-methyl-2-pyrrolidone (Sigma-Aldrich, 99.5%), methyl *t*-butyl ether (Oakwood Chemical, 99%), 2-methoxyethanol (Acros Organics, 99%), *t*-butyl acetate (Sigma-Aldrich, ≥99%), tetrahydrofuran (THF, Fisher Scientific, HPLC grade), propylene carbonate (Acros Organics, 99.5%), and sulfolane (Oakwood Chemical, 99%) were stored over activated 4 Å molecular sieves after shaking for a minimum of 24 hours to minimize water content prior to use.

5.4.2 Syntheses

All MOF-5 syntheses were synthesized according to a modified published procedure.[44] Specific synthetic protocols were as follows:

MOF-5

H_2bdc (100.0 mg, 0.6019 mmol, 1.0 eq.) was combined with $Zn(NO_3)_2 \cdot 4H_2O$ (500.0 mg, 1.912 mmol, 3.2 eq.) along with 15 mL DEF in a 20 mL scintillation vial and dissolved. Synthesis was performed in a 100 °C oven for 24 hours. Colorless cubic crystals 0.7 - 1.0 mm in size were obtained and washed 3 × 15 mL with DMF.

MOF-5-d_4

H_2bdc-d_4 (20.5 mg, 0.120 mmol, 1.0 eq.) was combined with $Zn(NO_3)_2 \cdot 4H_2O$ (100.0 mg, 0.3824 mmol, 3.2 eq.) along with 3 mL DEF in a 4 mL scintillation vial and dissolved. Synthesis was

performed in a 100 °C oven for 24 hours. Colorless cubic crystals 0.7 - 1.0 mm in size were obtained and were washed 3 × 3 mL with DMF.

$Zn_4O(bdc)_{1.5}(bdc\text{-}d_4)_{1.5}$

H_2bdc (10.0 mg, 0.0602 mmol, 0.5 eq.), H_2bdc-d_4 (10.2 mg, 0.0602 mmol, 0.5 eq.), and $Zn(NO_3)_2 \cdot 4H_2O$ (100.0 mg, 0.3824 mmol, 3.2 eq.) were dissolved in 3 mL DEF in a 4 mL vial. Synthesis was performed in a 100 °C oven for 24 hours after which colorless cubic crystals 0.7 - 1 mm in diameter were obtained and were washed 3 × 3 mL with DMF.

IRMOF-3[45]

H_2bdc-NH_2 (100.0 mg, 0.5520 mmol, 1.0 eq.) was combined with $Zn(NO_3)_2 \cdot 6H_2O$ (474.0 mg, 1.593 mmol, 2.9 eq.) along with 10 mL DMF in a 20 mL scintillation vial and dissolved, and then split into 2 mL aliquots in 10 separate 4 mL vials. Synthesis was performed in a 100 °C oven for 16 hours. Yellow cubic crystals were obtained and washed 3 × 3 mL with DMF.

5.4.3 Linker exchange

10 mM solutions of H_2bdc-d_4 were prepared by sonicating 17.0 mg H_2bdc-d_4 with 10 mL of solvent in a 20 mL scintillation vial until full dissolution was achieved. In cases where full dissolution did not result, the solutions were instead sonicated until no further dissolution was observed (~30-60 min.), then used without filtration of excess solid H_2bdc-d_4 in order to avoid varying the molar ratio of bdc:bdc-d_4 between experiments.

After preparation of the H_2bdc-d_4 solutions, ~18 mg aliquots (see Section 5.4.6) of MOF-5 stored in DMF were collected and transferred into fresh vials, excess DMF was removed via

pipette, and the H_2bdc-d_4 solutions were added to each. Vials were shaken on a VXR Basic Vibrax orbital shaker (IKA) at 500 RPM, keeping MOF crystals suspended in solution while minimizing mechanical abrasion. After 24 hours, aliquots of the exchanged MOF were removed and then washed 3 × 3 mL (15 minutes between washes) with DMF to remove excess linker remaining in the MOF pores.

13 solvents were chosen of the original 30 for further characterization. These included the amides (DMF, *N*,*N*-diethylformamide, *N*,*N*-dibutylformamide, *N*-methyl-2-pyrrolidone, 1-formylpiperdine, 1-formylpyrrolidine, *N*-formylmorpholine, *N*-methylformanilide, *N*,*N*-diethyl-3-methylbenzamide), THF, dioxane, butyl acetate, and propylene carbonate. These solvents were chosen because they showed evidence of bdc-d_4 incorporation after exchange (based on Raman spectra of the crystal surfaces), and because they dissolved either all or a significant fraction of the 10 mM H_2bdc-d_4. There is potential for further characterization of the other solvents that showed exchange without degrading MOF-5 or fully dissolving 10 mM H_2bdc-d_4 (ethyl acetate, *t*-butyl acetate, butanone, acetophenone, 2,5-dimethyltetrahydrofuran, dibutyl ether, dimethyl carbonate), but only dioxane, propylene carbonate, and butyl acetate were chosen from this category in this work.

For PSE with mixed solvents (DMF/*N*,*N*-diethyl-3-methylbenzamide and *N*,*N*-diethylformamide/*N*,*N*-diethyl-3-methylbenzamide) the same general protocol was utilized, but with the addition of two solvents in the linker dissolution step rather than one, to a total volume of 10 mL. Similarly, for the MOF-5 → IRMOF-3 PSE, the only adjustments to the above protocol were the use of H_2bdc-NH_2 (18.1 mg) instead of H_2bdc-d_4, and the use of either *N*,*N*-diethylformamide or *N*-methyl-2-pyrrolidone as solvents.

5.4.4 MOF activation and Raman mapping

From DMF, crystals were washed 3 × 3 mL with methylene chloride (CH_2Cl_2) at 15-minute intervals. Following the final CH_2Cl_2 exchange, excess solvent was decanted, and the material was activated under dynamic vacuum (<10 mTorr) for 16 hours at room temperature. Activated material was transferred to a desiccator for storage.

Activated MOF was transferred from the desiccator to a 20 × 20 × 0.5 mm polished steel substrate. Upon transfer, the material was sorted by crystal quality and cleaved by hand with a steel razor blade. Aligning the cleavage plane parallel to a crystal face was imperative to achieving clean edges in Raman mapping analysis. Crystals with visible defects were avoided for their tendency to crumble under the razor. The newly cleaved face of the crystal was then oriented upwards and the edges, as accurately as possible, were aligned with the X and Y axes of the instrument mapping stage. Raman mapping microspectroscopy was carried out on a Renishaw InVia Qontor confocal Raman microscope equipped with a Renishaw Centrus 2957 detector, a Leica 50× long working distance objective, and a 785 nm laser. The stage enclosure was supplied with positive pressure of dry air to mitigate MOF degradation during collection, resulting in a relative humidity consistently <1 %. Preliminary spectra were acquired with a 510 – 1650 cm^{-1} window (Raman shift) at 10 accumulations of 0.5 s exposures, typically one near the crystal edge and another ~100 µm from the edge to confirm the cleaved face was exposed. Maps were collected with similar spectral parameters (510 – 1650 cm^{-1} window, 0.5 s exposure, single accumulation) in an array spanning ~100 × 15 µm with 0.1 and 2 µm resolution in the orthogonal and parallel axis (respective to the edge).

5.4.5 Data processing

Raw spectral data were converted to 1D extent of exchange versus depth profiles using WiRE 5.3 (Renishaw) followed by data normalization with custom-written Python code. First, spectra saturated by cosmic rays were removed, subjected to a zero-order background subtraction, then deconvoluted into MOF-5 and MOF-5-d_4 signals using Non-Negative Least Squares (NNLS) component analysis as implemented in WiRE 5.3. Briefly, for a two-component system, NNLS minimizes the difference (via the method of least squares) between the spectrum and the sum of two scaled reference spectra, with the constraint that the scaling factors cannot be negative. The reference spectra used in NNLS were experimentally measured Raman spectra of MOF-5 and MOF-5-d_4. These spectra were previously scaled relative to one another such that the difference between their adjusted sum and the measured Raman spectrum of $Zn_4O(bdc)_{1.5}(bdc\text{-}d_4)_{1.5}$ was minimized. Thus, $Zn_4O(bdc)_{1.5}(bdc\text{-}d_4)_{1.5}$ acts as the basis for the calibration.

After NNLS, line maps were normalized based on several facts about the system. Because it is a mixed isostructural material, the products of the MOF-5 → MOF-5-d_4 linker exchange should spectroscopically appear as a linear combination of MOF-5 and MOF-5-d_4. Put another way, for any Raman scan S_i of the system, $S_{i,\text{total}} = (a_i \times S_{i,\text{bdc}}) + (b_i \times S_{i,\text{bdc-}d4})$. The crystal should have effectively uniform density, so for every scan (assuming the same volume of sample is probed), $a_i + b_i = c$, where c is a constant defined here as unity. Deviations from this prediction result from surface inhomogeneities, which the data must be normalized to correct for. This can be simply done by dividing each a_i and b_i by $(a_i + b_i)$; however, care must be taken near the crystal edges.

The exchanged linker bdc-d_4 should be most concentrated at the crystal surface, as this is where the least diffusion (and thus time) is required for exchange. This would ideally translate to the maximum bdc-d_4 Raman signal occurring exactly at the crystal edge. However, in practice the bdc-d_4 signal is highest at the closest position to the crystal edge where irradiation of the crystal surface is maximized (Figure S1). As the laser scans further from this point, is begins to transition off of the crystal, and less of the sample is irradiated and therefore detected. Thus, away from the crystal center from the point of maximum bdc-d_4 intensity (e.g. at points 1 and 2 in Figure 5.6 A), the assumption that $a_i + b_i = c$ is no longer true. To address this boundary condition, the assumption is made that the scaling factor ($a_i + b_i$) for scans earlier than the maximum bdc-d_4 point is equal to the scaling factor at that point, ($a_{d4\text{-max}} + b_{d4\text{-max}}$). This simplification is reasonable because the remaining surface can be assumed to be nearly homogeneous over such a small region.

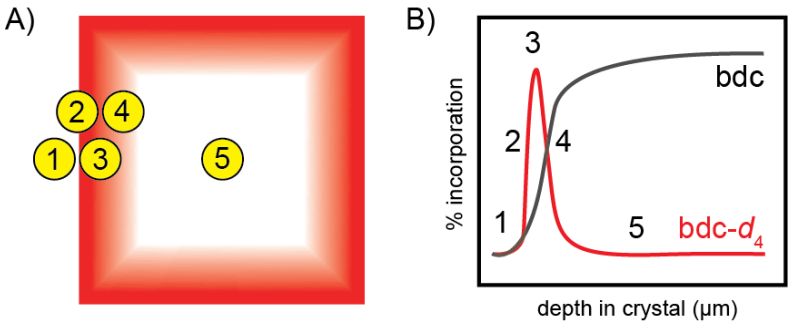

Figure 5.6. Relationship between laser position on sample and observed linker incorporation for a model core-shell system. A) Model MOF-5 → MOF-5-d_4 core-shell system (higher bdc-d_4 density shown in red) with five example laser spot locations indicated. B) Idealized percent incorporation versus depth in the crystal for the model in (A). Each of the five sample laser spot locations are shown on the plot.

5.4.6 Linker solution concentration calculations

Because PSE involves exchanging linker molecules between the solution and the MOF, it is important to consider the maximum degree to which the solution composition can vary over the course of the exchange. Particularly, if PSE in a particular solvent depletes solution H_2bdc-d_4 (and

thus equilibrates with the solution linker) more rapidly than PSE in other solvents, there is the potential for underestimating the exchange rate in the fast conditions, as the process will be slowed by the decreased exchanging linker concentration in solution. Upper, middle, and lower estimates for the percentage of bdc-d_4 incorporated in the MOF (and H_2bdc-d_4 lost from the solution) are as follows:

In these PSE studies, 10 mL quantities of 10 mM H_2bdc-d_4 solutions were used. An estimate for the quantity of MOF-5 used in each experiment was determined by transferring three aliquots of DMF-solvated MOF into three empty vials, and then washing and activating the material according to the protocol described above in Section 5.4.4. This yielded an average mass of MOF-5 of 18.1 ± 0.9 mg. This can be converted into moles of bdc in MOF-5 added at the start of the exchange.

$$18.1 \pm 0.9 \text{ mg MOF} - 5 \times \frac{1 \text{ mmol } Zn_4O(bdc)_3}{769.46 \text{ mg MOF} - 5} \times \frac{3 \text{ mmol bdc}}{1 \text{ mmol } Zn_4O(bdc)_3}$$

$$= 0.0706 \pm 0.0035 \text{ mmol bdc}$$

To make each of the 10 mM 10 mL solutions, 17.0 mg of H_2bdc-d_4 was used, corresponding to 0.100 mmol of H_2bdc-d_4. Thus, at the extreme case of 19.0 mg of MOF-5 added, the starting H_2bdc-d_4:bdc ratio in the system is

$$\frac{0.100 \text{ mmol } H_2bdc - d_4}{0.0741 \text{ mmol bdc}} = 1.35 \text{ } H_2bdc - d_4 \text{ per bdc}$$

Of the solvents tested, *N*,*N*-diethylformamide gave the highest overall extent of exchange. The MOF-5 crystals ranged from 700-1000 μm in diameter, but the greatest perturbation to the linker solution composition would occur with the smallest sized crystals, so a worst-case scenario for H_2bdc-d_4 depletion can be calculated with the assumption that all crystals are 700 μm in diameter. *N*,*N*-Diethylformamide gave 56 μm shells on average, with maximum extents of exchange of ~66 %: for these calculations, it will be assumed that 60 μm shells with uniform 70 % exchange resulted. Such an exchange would result in the crystals being 30.2 % bdc-d_4 overall, and 22.4 % of all H_2bdc-d_4 in solution would be replaced by H_2bdc, decreasing [H_2bdc-d_4] from 10 mM to 7.76 mM.

DMF is a more representative example of a high exchanging solvent. Assuming 18.1 mg of 850 μm MOF-5 crystals, 20 μm thick shells, and uniform 65% exchange, 8.8 % of the linkers in the MOFs would be bdc-d_4, and 6.2 % of H_2bdc-d_4 in solution would be replaced with H_2bdc, giving a final [H_2bdc-d_4] of 9.38 mM.

A low exchanging solvent such as 1-formylpyrrolidine, with 17.2 mg of 1000 μm MOF-5 crystals, 6 μm thick shells, and uniform 25% exchange, would give an exchanged product with 0.9 % bdc-d_4, and would use 0.6 % of all H_2bdc-d_4 in the starting solution, resulting in a final [H_2bdc-d_4] of 9.99 mM.

5.4.7 MOF-5 → IRMOF-3 linker exchange data

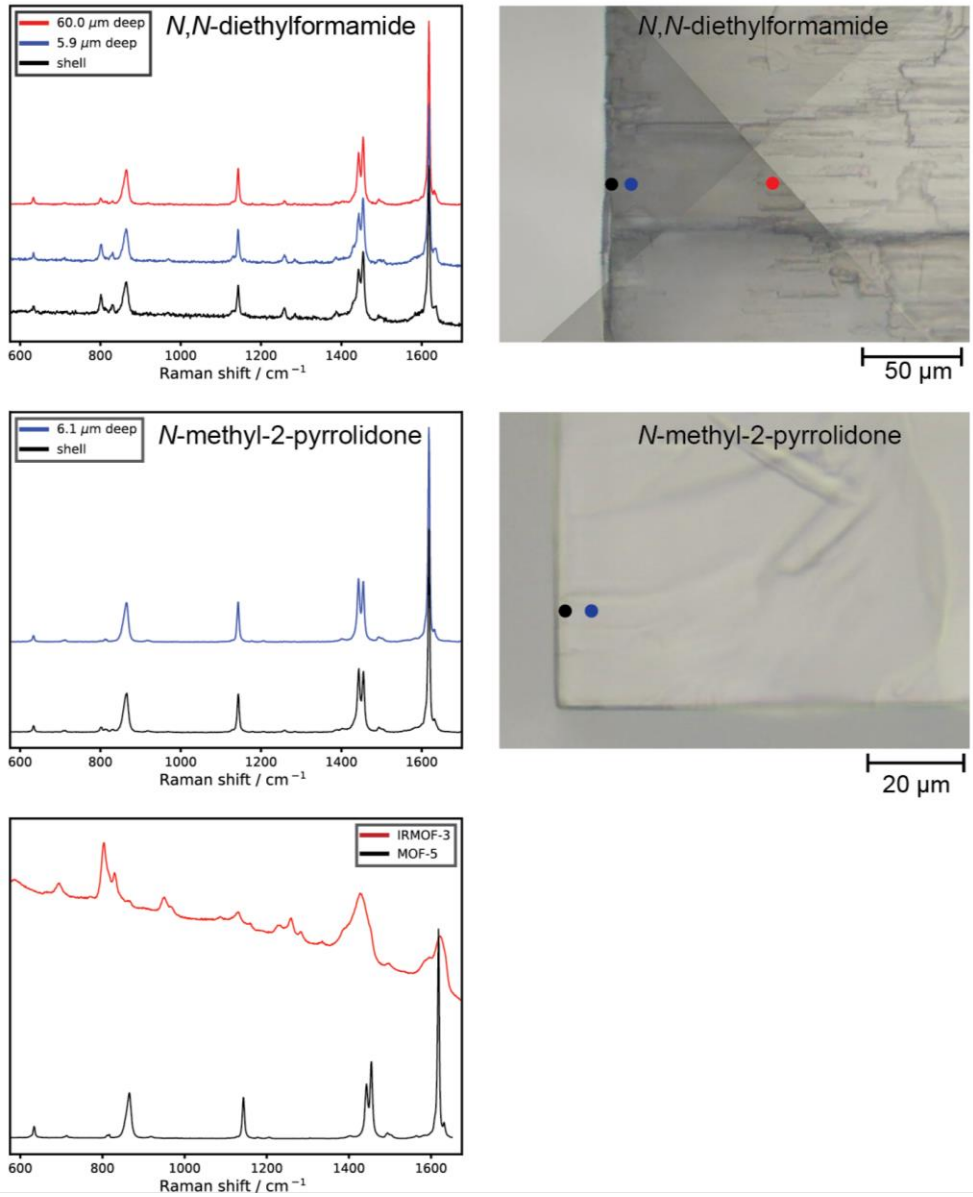

Figure 5.7. Comparison of *N*,*N*-diethylformamide and *N*-methyl-2-pyrrolidone in facilitating the MOF-5 → IRMOF-3 linker exchange. Left, above: Raman spectra of cross-sectioned MOF resulting from the MOF-5 → IRMOF-3 linker exchange in *N*,*N*-diethylformamide. Spectra taken at the far edge of the shell, 5.9 μm deep in the crystal, and 60.0 μm deep in the crystal are shown. Left, middle: Raman spectra of cross-sectioned MOF resulting from the MOF-5 → IRMOF-3 linker exchange in *N*-methyl-2-pyrrolidone. Spectra taken at the far edge of the shell and 6.1 μm deep in the crystal are shown. Left, below: Raman spectra of pure phase MOF-5 and IRMOF-3. Right, above: locations of Raman spectra collected of the sample resulting from the MOF-5 → IRMOF-3 linker exchange in *N*,*N*-diethylformamide. Visual artifacts

in the image (discontinuities in image brightness) result from the automated image stitching process in WiRE 5.3 rather than from the sample itself. Right, below: locations of Raman spectra collected of the sample resulting from the MOF-5 → IRMOF-3 linker exchange in *N*-methyl-2-pyrrolidone.

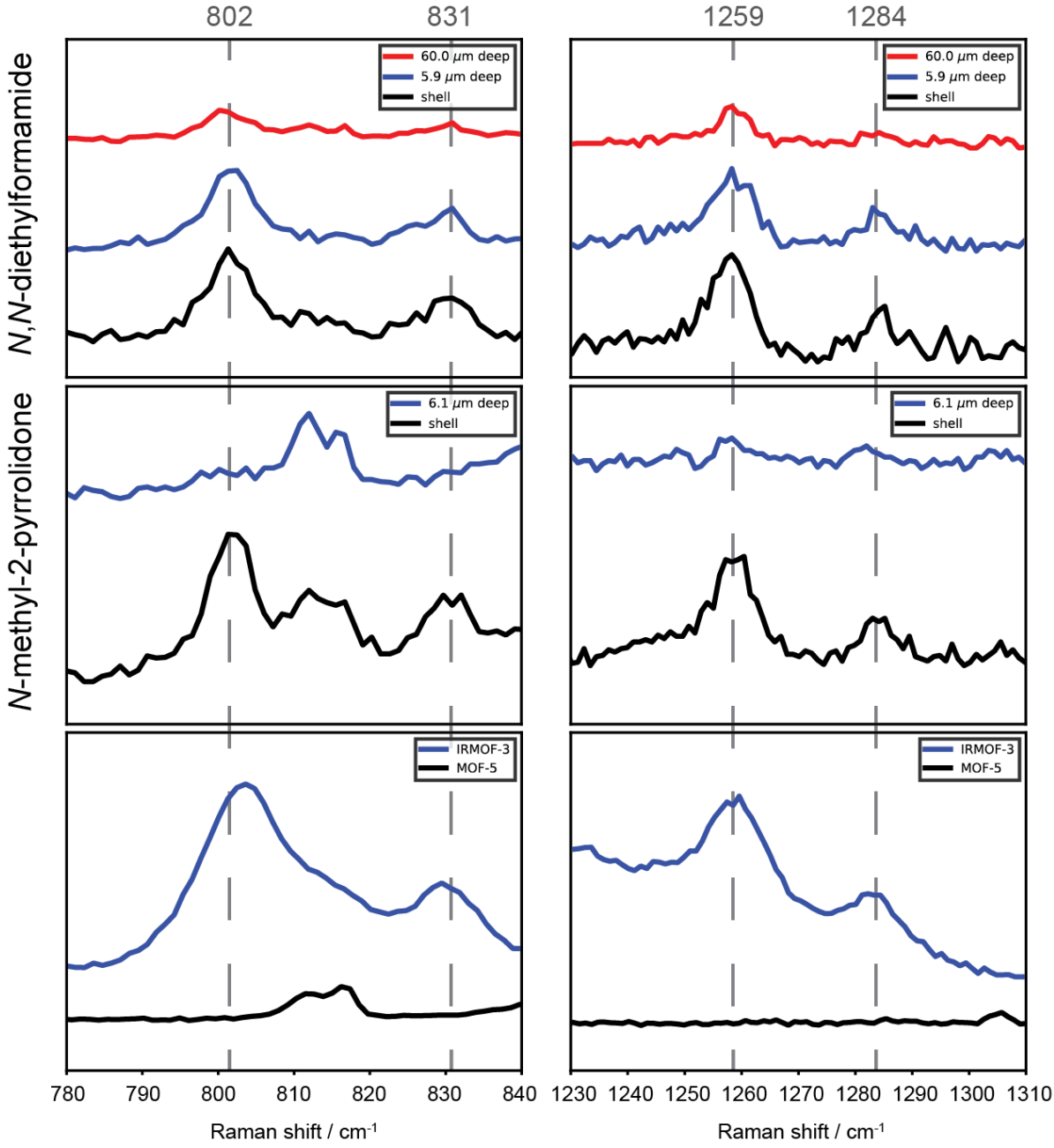

Figure 5.8. Magnified regions of interest from Raman spectra given in Figure S2 of the MOF-5 → IRMOF-3 linker exchange. Left: 780 – 840 cm^{-1} region. Right: 1230 – 1310 cm^{-1} region. Above: Raman spectra of cross-sectioned MOF resulting from the MOF-5 → IRMOF-3 linker exchange in *N*,*N*-diethylformamide. Spectra taken at the far edge of the shell, 5.9 μm deep in the crystal, and 60.0 μm deep in the crystal are

shown. Exchange at least as deep as 60 μm is observed. Middle: Raman spectra of cross-sectioned MOF resulting from the MOF-5 → IRMOF-3 linker exchange in *N*-methyl-2-pyrrolidone. Spectra taken at the far edge of the shell and 6.1 μm deep in the crystal are shown. Exchange is observed at the surface, but is minimal 6.1 μm deep in the crystal. Below: Raman spectra of phase pure MOF-5 and IRMOF-3.

5.4.8 Mixed solvent data

Table 5.2. Measured shell parameters for mixed solvents. Degree of shell exchange indicates the maximum degree of exchange measured in the shell. Thickness is given as shell full-width at half-max. Values are given as the average ± the standard error of the mean ($\sigma/\sqrt{n}$).

Solvent	Degree of shell exchange (%)	Shell thickness (μm)
1:3 *N*,*N*-diethyl-3-methylbenzamide:DMF	65.8 ± 1.2	14.6 ± 0.5
1:1 *N*,*N*-diethyl-3-methylbenzamide:DMF	57.8 ± 1.2	9.3 ± 0.6
3:1 *N*,*N*-diethyl-3-methylbenzamide:DMF	41.5 ± 1.9	4.0 ± 0.2
9:1 *N*,*N*-diethyl-3-methylbenzamide:DMF	8.4 ± 0.7	3.1 ± 0.2
1:3 *N*,*N*-diethyl-3-methylbenzamide: *N*,*N*-diethylformamide	41.1 ± 1.3	4.0 ± 0.4
1:1 *N*,*N*-diethyl-3-methylbenzamide: *N*,*N*-diethylformamide	16.3 ± 2.9	6.0 ± 0.6
3:1 *N*,*N*-diethyl-3-methylbenzamide: *N*,*N*-diethylformamide	6.9 ± 0.5	4.3 ± 0.4

5.5 References

(1) Cohen, S. M. *J. Am. Chem. Soc.* **2017,** *139*, 2855.
(2) Madrahimov, S. T.; Atesin, T. A.; Karagiaridi, O.; Sarjeant, A. A.; Farha, O. K.; Hupp, J. T.; Nguyen, S. T. *Cryst. Growth Des.* **2014,** *14*, 6320.
(3) Nickerl, G.; Senkovska, I.; Kaskel, S. *Chem. Commun.* **2015,** *51*, 2280.
(4) Zhang, X.; Sun, J.; Wei, G.; Liu, Z.; Yang, H.; Wang, K.; Fei, H. *Angew. Chem. Int. Ed.* **2019,** *58*, 2844.
(5) Karagiaridi, O.; Bury, W.; Sarjeant, A. A.; Stern, C. L.; Farha, O. K.; Hupp, J. T. *Chem. Sci.* **2012,** *3*, 3256.

(6) Karagiaridi, O.; Lalonde, M. B.; Bury, W.; Sarjeant, A. A.; Farha, O. K.; Hupp, J. T. *J. Am. Chem. Soc.* **2012,** *134*, 18790.
(7) Jeong, S.; Kim, D.; Song, X.; Choi, M.; Park, N.; Lah, M. S. *Chem. Mater.* **2013,** *25*, 1047.
(8) Bury, W.; Fairen-Jimenez, D.; Lalonde, M. B.; Snurr, R. Q.; Farha, O. K.; Hupp, J. T. *Chem. Mater.* **2013,** *25*, 739.
(9) Li, T.; Kozlowski, M. T.; Doud, E. A.; Blakely, M. N.; Rosi, N. L. *J. Am. Chem. Soc.* **2013,** *135*, 11688.
(10) Fei, H.; Shin, J.; Meng, Y. S.; Adelhardt, M.; Sutter, J.; Meyer, K.; Cohen, S. M. *J. Am. Chem. Soc.* **2014,** *136*, 4965.
(11) Karagiaridi, O.; Vermeulen, N. A.; Klet, R. C.; Wang, T. C.; Moghadam, P. Z.; Al-Juaid, S. S.; Stoddart, J. F.; Hupp, J. T.; Farha, O. K. *Inorg. Chem.* **2015,** *54*, 1785.
(12) Xu, Y.; Howarth, A. J.; Islamoglu, T.; da Silva, C. T.; Hupp, J. T.; Farha, O. K. *Inorg. Chem. Commun.* **2016,** *67*, 60.
(13) Pereira, C. F.; Howarth, A. J.; Vermeulen, N. A.; Almeida Paz, F. A.; Tomé, J. P. C.; Hupp, J. T.; Farha, O. K. *Mater. Chem. Front.* **2017,** *1*, 1194.
(14) Nguyen, H. T. T.; Tu, T. N.; Nguyen, M. V.; Lo, T. H. N.; Furukawa, H.; Nguyen, N. N.; Nguyen, M. D. *ACS Appl. Mater. Interfaces* **2018,** *10*, 35462.
(15) Tan, C.; Han, X.; Li, Z.; Liu, Y.; Cui, Y. *J. Am. Chem. Soc.* **2018,** *140*, 16229.
(16) Boissonnault, J. A.; Wong-Foy, A. G.; Matzger, A. J. *J. Am. Chem. Soc.* **2017,** *139*, 14841.
(17) Burnett, B. J.; Barron, P. M.; Hu, C.; Choe, W. *J. Am. Chem. Soc.* **2011,** *133*, 9984.
(18) Kim, M.; Cahill, J. F.; Su, Y.; Prather, K. A.; Cohen, S. M. *Chem. Sci.* **2012,** *3*, 126.
(19) Karagiaridi, O.; Bury, W.; Mondloch, J. E.; Hupp, J. T.; Farha, O. K. *Angew. Chem. Int. Ed.* **2014,** *53*, 4530.
(20) Islamoglu, T.; Goswami, S.; Li, Z.; Howarth, A. J.; Farha, O. K.; Hupp, J. T. *Acc. Chem. Res.* **2017,** *50*, 805.
(21) Kim, M.; Cahill, J. F.; Fei, H.; Prather, K. A.; Cohen, S. M. *J. Am. Chem. Soc.* **2012**, *134*, 18082.
(22) Fluch, U.; Paneta, V.; Primetzhofer, D.; Ott, S. *Chem. Commun.* **2017**, *53*, 6516.
(23) Marreiros, J.; Caratelli, C.; Hajek, J. *Chem. Mater.* **2019,** *31*, 1359.
(24) Fei, H.; Cahill, J. F.; Prather, K. A.; Cohen, S. M. *Inorg. Chem.* **2013,** *52*, 4011.
(25) Gross, A. F.; Sherman, E.; Mahoney, S. L.; Vajo, J. J. *J. Phys. Chem. A* **2013,** *117*, 3771.
(26) Fluch, U.; McCarthy, B. D.; Ott, S. *Dalton Trans.* **2019,** *48*, 45.
(27) Mutruc, D.; Goulet-Hanssens, A.; Fairman, S.; Wahl, S.; Zimathies, A.; Knie, C.; Hecht, S. *Angew. Chem. Int. Ed.* **2019,** *58*, 12862.
(28) Shao, Z.; Huang, C.; Dang, J.; Wu, Q.; Liu, Y.; Ding, J.; Hou, H. *Chem. Mater.* **2018,** *30*, 7979.
(29) Taddei, M.; Wakeham, R. J.; Koutsianos, A.; Andreoli, E.; Barron, A. R. *Angew. Chem. Int. Ed.* **2018,** *57*, 11706.
(30) Yuan, N.; Church, T. L.; Brandt, E. G.; Hedin, N.; Zou, X.; Bernin, D. *Sci Rep* **2018,** *8*, 17530.
(31) Luo, Y.; Ahmad, M.; Schug, A.; Tsotsalas, M. Rising Up: *Adv. Mater.* **2019,** *31*, 1901744.

(32) Liu, C.; Zeng, C.; Luo, T.-Y.; Merg, A. D.; Jin, R.; Rosi, N. L. *J. Am. Chem. Soc.* **2016,** *138*, 12045.
(33) Jayachandrababu, K. C.; Sholl, D. S.; Nair, S. *J. Am. Chem. Soc.* **2017,** *139*, 5906.
(34) Park, H.; Kim, S.; Jung, B.; Park, M. H.; Kim, Y.; Kim, M. *Inorg. Chem.* **2018,** *57*, 1040.
(35) He, Y.; Sun, M.; Zhao, Q.; Shang, J.; Tian, Y.; Xiao, P.; Gu, Q.; Li, L.; Webley, P. A. *ACS Appl. Mater. Interfaces* **2019,** *11*, 30234.
(36) Kim, S.; Lee, J.; Jeoung, S.; Moon, H. R.; Kim, M. *Chem. Eur. J.* **2020,** *26*, 7568.
(37) Koh, K.; Wong-Foy, A. G.; Matzger, A. J. *Chem. Commun.* **2009,** *41*, 6162.
(38) Li, T.; Sullivan, J. E.; Rosi, N. L. *J. Am. Chem. Soc.* **2013,** *135*, 9984.
(39) The diffusion rate of small molecules in organic solvents has been previously reported to correlate negatively with solvent molecular weight: Wilke, C. R.; Chang, P. *AIChE J.* **1955,** *1*, 264.
(40) Brozek, C. K.; Michaelis, V. K.; Ong, T.-C.; Bellarosa, L.; López, N.; Griffin, R. G.; Dincă, M. *ACS Cent. Sci.* **2015,** *1*, 252.
(41) Bhattacharyya, D. N.; Smid, J.; Szwarc, M. *J. Phys. Chem.* **1965,** *69*, 624.
(42) Beylen, M. van; Bhattacharyya, D. N.; Smid, J.; Szwarc, M. *J. Phys. Chem.* **1966**, *70*, 157.
(43) Cho, K. Y.; Seo, J. Y.; Kim, H.-J.; Pai, S. J.; Do, X. H.; Yoon, H. G.; Hwang, S. S.; Han, S. S.; Baek, K.-Y. *Appl. Catal. B: Environ.* **2019,** *245*, 635.
(44) Li, H.; Eddaoudi, M.; O'Keeffe, M.; Yaghi, O. M. *Nature* **1999,** *402*, 276.
(45) Eddaoudi, M.; Kim, J.; Rosi, N.; Vodak, D.; Wachter, J.; O'Keeffe, M.; Yaghi, O. M. *Science* **2002,** *295*, 469.

Chapter 6. Conclusions and Future Directions

6.1 Summary of Work

The work described in Chapters 2 – 5 underscores the importance of correctly utilizing solvent choice in MOF synthesis, modification, activation, and handling.

Chapter 2 examines solvent-dependence in the MOF activation process, a process central to the production of these materials. It was found that intermediate MOF collapse can occur, as can structural damage in the absence of loss of function. Particularly, MOFs can undergo macroscopic damage (cracking) during activation, leading to an apparent decrease in crystallinity, without a measurable decrease in accessible surface area. In addition to these fundamental findings, this work highlights the importance of utilizing multiple complementary methods when characterizing MOF activation and other MOF processing steps.

Chapter 3 pertains to MOF resolvation, a process relevant to many MOF applications including catalysis, chemical sensing, and pollutant capture. It was found that resolvation-induced MOF collapse is a legitimate concern, particularly for frameworks also sensitive to activation, and a stepwise method for bypassing this degradation route was developed. These concepts are broadly extensible to other fragile MOF systems, and inform best practices for handling MOFs when it is necessary to change their solvation state.

Chapter 4 centers on the use of a novel MOF synthesis solvent, DEET, which offers health, safety, and cost benefits relative to commonly-used formamide solvents such as DMF and DEF. It was shown that this solvent is also capable of phase direction during MOF synthesis, and the crystal structure of a novel MOF synthesized in this solvent was reported. The potential of MOFs

to act as vapor-pressure reducing excipients in controlled release insect repellent formulations was also demonstrated.

Chapter 5 details a study relating solvent choice and its role in dictating microstructural outcomes in MOF linker exchange. It was found that significant variations in exchanged shell thickness and extent of exchange can result from treatment conditions that are identical except for the solvent used. These results serve to reveal the important role of solvent in this process from a fundamental perspective, as well as to offer practical guidance for creating and elaborating hierarchical MOF architectures.

6.2 Future Directions

While trends relating solvent surface tension to activation efficacy have been utilized for choosing better activation solvents, researchers lack a detailed understanding of the process of MOF collapse. Due to the complexity of the process, developing this understanding will benefit from the use of advanced computational modeling techniques, such as Grand-Canonical Monte Carlo simulation. Investigation into the process of MOF collapse during activation and resolvation, using experimental data collected here and elsewhere for validation, will be an important phase in developing realistic models of these materials with predictive power and is a logical next step for the continuation of this research.

Another potential area of research deriving from the work in this thesis relates to the process of solvent degradation during MOF synthesis. The ability of DEET to act as a MOF synthesis solvent was an unexpected finding, as the slow degradation of formamide solvents (and the subsequent increase in reaction pH) is thought to be necessary for controlled growth of highly crystalline MOFs, and DEET is expected to be significantly more thermally stable than these solvents. Nevertheless, MOF synthesis occurs in DEET, suggesting that solvent degradation may

be catalyzed by species in the reaction mixture. Developing a better understanding of solvent degradation during the process of MOF synthesis, in formamide solvents as well as in other amides, should allow for further expansion of the scope of safer MOF synthesis solvents and may allow for creation of as-yet-unknown MOF phases.

A final research direction branching from this work is further exploration into mixed solvent systems in MOF PSE. Several pairs of high- and low-exchanging solvent were tested in Chapter 5, and it was found that the PSE behavior of these mixtures was not linearly related to the solvent composition. Additional investigation into mixed solvents in MOF linker exchange may reveal methods for achieving thick, low extent of exchange shells in large MOF crystals, a useful microstructure which currently lacks an appropriate PSE solvent system for its creation.

APPENDICES

APPENDIX A

Raw isotherm data from Chapter 3

UMCM-9

Pristine samples

Table A.1. N_2 isotherm data for pristine UMCM-9 samples used. Samples are labelled with their BET surface areas, given in parentheses.

Pristine (4886.229)		Pristine (4887.313)		Pristine (4743.236)	
P/P_0	N_2 uptake (cc g^{-1})	P/P_0	N_2 uptake (cc g^{-1})	P/P_0	N_2 uptake (cc g^{-1})
0.001338	121.448	0.001667	131.7486	0.00176	132.4987
0.002227	151.4731	0.002027	143.9085	0.002258	147.6816
0.002434	158.4382	0.002215	149.4989	0.002489	154.3302
0.002647	166.0549	0.002424	155.555	0.002756	161.6113
0.002896	174.3455	0.002626	162.3281	0.00303	169.7847
0.003174	183.2304	0.002864	169.4083	0.003355	178.2203
0.003508	192.4386	0.003146	176.9069	0.00368	187.1035
0.003886	202.9771	0.004163	206.4162	0.004033	196.6306
0.004284	214.1292	0.005108	233.8595	0.005317	230.0782
0.005117	238.6288	0.010238	357.4244	0.010426	342.4005
0.011792	391.098	0.015267	441.095	0.015361	419.7723
0.015869	455.8534	0.020375	512.339	0.02057	487.6923
0.020402	518.9627	0.025021	584.1923	0.026695	574.925
0.02611	610.403	0.030339	685.0366	0.030043	631.5458
0.030849	703.6158	0.035418	803.4431	0.036175	754.4304
0.035212	802.0498	0.040266	906.0776	0.040454	844.6796
0.041317	936.8083	0.045252	992.517	0.045252	936.6118
0.045765	1015.6574	0.051522	1059.2762	0.051341	1021.5338
0.050547	1071.114	0.055403	1083.7811	0.056247	1061.4844
0.055159	1103.3843	0.062228	1108.1532	0.060793	1082.6519
0.060994	1127.6688	0.065879	1117.3331	0.0665	1099.8375
0.065655	1140.7897	0.072466	1130.3423	0.07085	1109.5605
0.070508	1151.5048	0.077149	1137.6071	0.07637	1119.2653

0.076244	1161.8573	0.082726	1145.1743	0.081644	1127.0826
0.082727	1171.6665	0.088231	1151.8151	0.088556	1135.8774
0.089417	1180.6207	0.095915	1159.8022	0.095453	1143.4412
0.096974	1189.4729	0.100208	1164.0295	0.101918	1149.9186
0.103236	1195.6401	0.145027	1195.4763	0.147905	1183.2412
0.148019	1229.6373	0.197097	1221.1212	0.199578	1209.5826
0.197805	1257.7205	0.251244	1241.0785	0.254419	1231.4049
0.251071	1281.8148	0.305132	1258.3115	0.307917	1250.1376
0.3064	1303.1857	0.359576	1273.9275	0.361127	1267.4528
0.360477	1322.7224	0.412663	1287.5156	0.414424	1282.5343
0.41153	1340.4115	0.466371	1301.6736	0.466212	1297.697
0.46567	1357.9423	0.519025	1313.8212	0.516413	1311.5906
0.517755	1374.2007	0.568462	1325.7159	0.569118	1325.322
0.567982	1389.3346	0.619233	1337.0569	0.620402	1338.8806
0.619034	1405.2467	0.670336	1348.6359	0.67105	1352.3676
0.671403	1420.6644	0.721389	1360.2335	0.724138	1366.1984
0.723616	1436.2327	0.773928	1372.2263	0.776965	1379.6136
0.774149	1452.7494	0.82234	1382.9275	0.827072	1391.7034
0.826254	1467.8889	0.873154	1394.8068	0.877447	1404.5657
0.877029	1481.1389	0.922425	1407.1571	0.926732	1417.2649
0.929946	1498.0494	0.971493	1418.876	0.975909	1430.0822
0.975156	1513.5253	0.920585	1404.9961	0.923464	1413.4832
0.922623	1494.8191	0.870636	1389.6353	0.869013	1396.0789
0.870653	1477.1871	0.820096	1376.083	0.820731	1382.1304
0.820675	1461.4185	0.770767	1364.5555	0.769627	1369.6467
0.771238	1444.6801	0.719635	1353.2362	0.718214	1356.9501
0.720548	1425.8158	0.672226	1342.7072	0.66973	1344.6071
0.669496	1409.9517	0.622393	1331.7408	0.619608	1331.754
0.622599	1395.52	0.572055	1321.2172	0.56839	1319.4004
0.57043	1380.5144	0.526558	1311.3014	0.523931	1309.1381
0.520594	1366.1115	0.471407	1300.083	0.474185	1297.1906
0.47105	1351.2609	0.421069	1288.1792	0.420116	1282.8218
0.423172	1336.4841	0.371993	1275.9668	0.372902	1269.5531
0.372105	1320.5203	0.322131	1262.0203	0.320002	1252.4147
0.321714	1303.703	0.271504	1245.4595	0.272853	1235.2401
0.269772	1285.9353	0.222774	1228.7693	0.221562	1216.1527
0.221652	1265.5547	0.175784	1209.3253	0.172905	1194.2622
0.173247	1242.52	0.123101	1179.8625	0.127494	1168.1511
		0.07694	1135.6134	0.074537	1114.1841
		0.029372	669.6445	0.029841	630.2878
		0.01922	496.0755	0.019184	470.5441

Table A.1 cont.

Pristine (4639.937)	
P/P_0	N_2 uptake (cc g^{-1})
0.001562	127.3639
0.002145	147.0902
0.002318	151.9786
0.00252	157.3182
0.002729	163.2837
0.002959	169.4219
0.003211	175.9539
0.004219	201.8158
0.005169	225.6803
0.010864	342.5211
0.01648	422.0432
0.020972	477.8545
0.02581	542.0718
0.030526	614.5441
0.035998	714.7361
0.040843	805.2365
0.045076	874.7419
0.050677	944.2665
0.055076	980.8764
0.061189	1008.3234
0.066221	1022.0355
0.07026	1030.0784
0.075465	1038.6124
0.082744	1048.5162
0.088821	1055.4229
0.094271	1060.9299
0.099937	1066.1846
0.14597	1096.9416
0.195438	1119.5641
0.250191	1138.7201
0.305397	1155.2965
0.35989	1169.9951
0.413656	1182.6891
0.465996	1195.0244
0.516076	1205.8235
0.569201	1216.6313
0.620239	1227.1788
0.672075	1237.4052
0.724653	1247.3395

0.775748	1257.1487
0.827117	1266.1825
0.87886	1275.9797
0.926802	1285.3129
0.976039	1295.8752
0.922518	1284.5959
0.869177	1272.9109
0.822185	1263.1678
0.768038	1252.5958
0.721594	1242.8612
0.668728	1231.7773
0.620692	1221.0613
0.573953	1210.8254
0.5237	1200.0452
0.472764	1189.0085
0.420589	1176.7872
0.372309	1165.4791
0.319868	1151.9561
0.270515	1138.6896
0.22109	1122.9647
0.175704	1105.7451
0.12165	1077.8994
0.076322	1035.9994
0.029885	607.1306
0.019741	461.2468

Hexane resolvated samples

Table A.2. N_2 isotherm data for hexane resolvated UMCM-9 samples used.

Hexane resolvation 1		Hexane resolvation 2		Hexane resolvation 3	
P/P_0	N_2 uptake (cc g^{-1})	P/P_0	N_2 uptake (cc g^{-1})	P/P_0	N_2 uptake (cc g^{-1})
0.000854	102.8176	0.002183	142.8976	0.002304	151.7099
0.001576	126.0468	0.002405	151.3999	0.002803	165.4619
0.00204	138.7709	0.002676	160.6224	0.003331	180.0053
0.002275	144.3276	0.003025	170.6378	0.003895	195.7011
0.002504	150.3606	0.003375	181.0182	0.004387	212.185
0.002739	156.94	0.003753	191.8324	0.005022	228.7104
0.00299	164.1782	0.004167	203.4925	0.005664	245.8678
0.003269	171.9515	0.004538	216.2154	0.006356	263.6201
0.004271	201.7715	0.005373	239.6053	0.007097	281.6356
0.005243	230.4159	0.010182	349.2979	0.010065	343.4959

0.010611	363.1591	0.016083	441.8339	0.016128	438.8759
0.016045	454.1748	0.020243	499.0471	0.020251	498.2961
0.021398	530.5004	0.025417	578.5092	0.025986	581.5939
0.025713	600.8777	0.030105	666.2097	0.030986	672.2932
0.031037	706.9827	0.035999	793.3056	0.035551	767.4641
0.035808	818.4945	0.041693	908.5762	0.040017	864.5951
0.040624	928.0124	0.045025	959.7186	0.046158	983.8399
0.045027	1008.0267	0.051547	1023.3932	0.05093	1048.8754
0.051448	1081.0383	0.055129	1043.8704	0.056644	1096.3799
0.055277	1105.5306	0.060609	1064.8115	0.061117	1118.5179
0.062302	1131.7946	0.065718	1077.9871	0.067101	1138.3868
0.065837	1140.9774	0.071234	1089.0662	0.073179	1153.3052
0.072191	1153.6509	0.07802	1100.0099	0.080248	1167.5341
0.076116	1160.0041	0.083749	1107.9565	0.085997	1177.2659
0.081204	1167.3536	0.090557	1116.479	0.093472	1187.7766
0.085799	1173.4076	0.098213	1124.9332	0.101597	1198.1506
0.09194	1180.326	0.104856	1131.5743	0.107575	1205.2135
0.098066	1186.5663	0.152757	1168.3876	0.158163	1252.6407
0.147961	1221.6937	0.205474	1199.004	0.210284	1294.0204
0.197458	1244.5177	0.259847	1225.3652	0.262784	1329.8661
0.248369	1262.0239	0.313063	1247.9872	0.315455	1365.8298
0.299685	1276.8252	0.365031	1269.3193	0.36702	1400.2544
0.351325	1289.3098	0.416607	1289.4387	0.420233	1435.0269
0.397781	1299.9332	0.469388	1309.6719	0.472006	1469.5714
0.447631	1309.9238	0.521606	1328.7511	0.523521	1502.9099
0.495457	1319.3661	0.571968	1349.2615	0.573039	1534.6053
0.548592	1328.7982	0.622438	1368.2021	0.621858	1568.723
0.596469	1337.2408	0.674556	1387.0991	0.673937	1603.4269
0.64559	1345.708	0.728293	1406.1283	0.722671	1636.1168
0.697429	1354.412	0.775509	1423.9126	0.773237	1673.5481
0.746757	1360.7208	0.822732	1440.688	0.820573	1723.9731
0.801003	1369.3944	0.873387	1460.229	0.868286	1770.1322
0.850861	1377.776	0.923007	1478.8687	0.917619	1812.5326
0.895314	1382.8784	0.974076	1498.9982	0.968264	1861.0565
0.95258	1393.2075	0.918312	1474.7521	0.918268	1812.8109
0.922876	1389.141	0.868342	1452.9658	0.869292	1772.6744
0.869373	1384.1262	0.819892	1433.3514	0.81717	1727.0983
0.814766	1379.0367	0.76726	1412.6122	0.768537	1688.8796
0.765394	1371.5704	0.716427	1397.7942	0.719896	1655.6594
0.729062	1367.7914	0.666385	1385.0977	0.667831	1619.7104
0.666024	1359.8364	0.619377	1371.1547	0.617999	1583.8662
0.61934	1353.0647	0.572867	1354.0813	0.571113	1550.6398
0.570225	1344.2137	0.523468	1333.9296	0.523813	1519.3781

0.516671	1335.9393	0.47135	1314.7498	0.470458	1484.2147
0.470105	1326.3214	0.42091	1294.4144	0.418414	1447.3853
0.421116	1316.218	0.370711	1274.2072	0.367513	1411.9352
0.370308	1303.1281	0.31915	1253.03	0.317745	1377.6047
0.319706	1288.5687	0.270436	1232.3655	0.26782	1342.5273
0.269708	1273.9653	0.219274	1207.7245	0.220577	1309.527
0.22407	1259.2203	0.172166	1181.9984	0.169889	1268.6157
		0.125992	1150.9061	0.121063	1223.2394
		0.07919	1103.1774	0.075732	1161.7749
		0.029141	655.7994	0.028804	635.9639
		0.018973	484.3526	0.019794	492.3433

CH_2Cl_2 resolvated samples

Table A.3. N_2 isotherm data for CH_2Cl_2 resolvated UMCM-9 samples used.

CH_2Cl_2 resolvation 1		CH_2Cl_2 resolvation 2		CH_2Cl_2 resolvation 3	
P/P_0	N_2 uptake (cc g^{-1})	P/P_0	N_2 uptake (cc g^{-1})	P/P_0	N_2 uptake (cc g^{-1})
0.000862	102.8932	0.002319	152.0882	0.002789	158.6394
0.001694	128.57	0.002447	157.6814	0.003053	165.4709
0.002231	143.0098	0.002626	163.8124	0.003338	172.9295
0.002452	149.0254	0.002847	170.5885	0.003545	181.5152
0.002695	155.5455	0.003083	177.7026	0.00388	190.3519
0.002938	162.6803	0.003354	185.3816	0.004244	199.6416
0.003203	170.2931	0.003603	193.6359	0.004644	209.4696
0.003498	178.5759	0.004217	213.3924	0.005072	220.3801
0.004197	199.3481	0.005266	243.0668	0.005485	231.4812
0.00528	231.0876	0.011431	381.3405	0.011577	353.7755
0.011494	378.6632	0.016583	460.7737	0.015051	405.2699
0.015044	437.5925	0.020265	512.0027	0.020272	476.0619
0.021811	534.9156	0.025517	593.1702	0.02533	545.6231
0.025183	589.8244	0.030754	695.7355	0.031314	643.8457
0.030691	698.0439	0.035528	800.7624	0.035837	732.9795
0.035389	807.6776	0.041008	916.1349	0.040987	839.4541
0.040808	928.0407	0.045553	990.8456	0.045631	928.2318
0.045072	1004.1877	0.051169	1049.9519	0.05011	993.4976
0.052531	1082.5494	0.05555	1076.6555	0.055481	1042.4773
0.055638	1100.979	0.060202	1094.3204	0.060275	1068.146
0.060719	1120.7368	0.06661	1110.8649	0.066716	1089.0593
0.066764	1136.9105	0.071134	1119.7275	0.071452	1100.0516
0.070483	1144.2551	0.076471	1128.5031	0.077323	1110.8387
0.075659	1153.3846	0.081238	1135.2599	0.082744	1118.9944

0.080608	1160.7408	0.088074	1143.915	0.08992	1128.1615
0.087839	1170.0844	0.094153	1150.6183	0.09696	1135.9308
0.09289	1175.73	0.101053	1157.3872	0.103131	1142.1672
0.097993	1181.1528	0.146264	1189.9762	0.150052	1176.9056
0.146827	1217.6013	0.196441	1215.3428	0.201368	1204.5005
0.198982	1243.0977	0.252426	1237.1938	0.255145	1228.1053
0.248435	1261.2	0.306006	1255.1195	0.30942	1248.9187
0.299427	1277.7407	0.360215	1271.5609	0.361827	1268.2865
0.351457	1292.1747	0.411826	1285.3213	0.414506	1285.4808
0.395778	1304.3525	0.466127	1300.2947	0.465786	1302.8896
0.450636	1317.7058	0.518473	1313.5702	0.517358	1319.4102
0.500516	1329.2615	0.570984	1326.4771	0.569294	1335.465
0.545823	1339.0441	0.622395	1339.1943	0.619447	1351.6321
0.598751	1349.1234	0.673871	1351.3484	0.670292	1367.4854
0.649434	1360.2971	0.725867	1363.0801	0.724183	1383.9773
0.698482	1368.9886	0.777293	1374.9161	0.775092	1401.8612
0.745998	1378.6843	0.829047	1386.0182	0.824082	1422.269
0.795459	1386.8618	0.881136	1398.1121	0.873129	1440.8667
0.854661	1396.4567	0.929101	1409.3427	0.92289	1459.2701
0.89714	1406.2837	0.97795	1421.4518	0.973542	1477.8174
0.945975	1413.1907	0.922215	1406.2854	0.920993	1458.5731
0.928192	1413.4556	0.868891	1392.5129	0.86947	1440.4224
0.866545	1405.6105	0.82149	1380.9882	0.818076	1423.2783
0.826083	1398.7559	0.76776	1368.5099	0.770063	1409.1954
0.771159	1391.7783	0.729677	1364.4794	0.719582	1393.9813
0.723289	1385.6958	0.669183	1353.5685	0.668231	1377.5588
0.666665	1374.3826	0.619591	1342.9594	0.619041	1361.2412
0.61741	1365.8076	0.570727	1330.6841	0.570842	1345.4741
0.570417	1357.2842	0.522819	1318.6428	0.52315	1330.2721
0.517481	1347.2904	0.474319	1305.8749	0.471107	1313.1487
0.478875	1338.4475	0.423093	1291.5664	0.419242	1294.573
0.421712	1322.9772	0.371867	1277.3898	0.369524	1277.083
0.367112	1306.4189	0.321134	1261.8463	0.320006	1258.5531
0.317755	1290.8397	0.271941	1246.0698	0.27011	1239.7473
0.273721	1275.2151	0.221964	1227.2643	0.221177	1218.0822
0.224003	1256.4882	0.175719	1206.9617	0.172928	1193.8359
		0.129538	1180.7417	0.126442	1164.1814
		0.076956	1130.4816	0.07335	1106.1719
		0.029463	677.6927	0.029467	616.5276
		0.019723	507.097	0.019259	464.2281

THF resolvated samples

Table A.4. N_2 isotherm data for THF resolvated UMCM-9 samples used.

THF resolvation 1		THF resolvation 2		THF resolvation 3	
P/P_0	N_2 uptake (cc g^{-1})	P/P_0	N_2 uptake (cc g^{-1})	P/P_0	N_2 uptake (cc g^{-1})
0.001119	96.5602	0.002348	138.4489	0.002097	118.894
0.001833	113.5284	0.002505	143.4323	0.002446	125.782
0.00218	120.5519	0.002697	148.9138	0.002854	133.5293
0.002555	128.189	0.002961	154.9165	0.003269	141.7052
0.002945	136.3503	0.003218	161.2355	0.003713	150.4104
0.003365	145.085	0.003518	168.0051	0.004201	159.7925
0.003807	154.2796	0.00381	175.2662	0.004703	169.5387
0.004278	164.256	0.004103	183.4794	0.00522	179.5252
0.004757	174.7995	0.005409	211.2484	0.005817	190.7634
0.005272	185.5421	0.01106	306.6071	0.011146	277.6443
0.010191	271.1646	0.015263	357.0137	0.015274	326.7872
0.015861	339.4452	0.021949	428.9156	0.020289	376.6397
0.020647	388.1961	0.025909	477.418	0.025262	426.3637
0.025124	438.4272	0.030569	543.4325	0.031537	500.585
0.030396	509.9272	0.035114	612.2186	0.035825	559.9279
0.036722	605.4405	0.040458	686.8381	0.040885	632.8437
0.040661	661.3959	0.047194	753.489	0.045646	697.8566
0.044991	706.5098	0.050769	775.9655	0.050203	747.3752
0.050609	744.3038	0.056142	796.2482	0.055758	788.2574
0.055771	764.3315	0.060024	805.8008	0.060657	809.3951
0.063009	780.7942	0.067516	818.6036	0.065433	822.3434
0.067832	788.5477	0.072154	824.6355	0.070078	830.8224
0.072633	794.7545	0.078391	831.5286	0.075596	839.1374
0.079157	801.7437	0.083521	836.4448	0.08332	848.1032
0.083656	805.9816	0.0905	842.465	0.089938	854.1811
0.088325	810.0668	0.09837	848.4166	0.096118	859.7447
0.095578	815.6649	0.105085	852.9067	0.100872	863.2542
0.099782	818.8013	0.151094	876.4299	0.146656	888.2487
0.148653	844.6412	0.204247	895.7127	0.199058	906.5652
0.199638	863.4519	0.257107	911.171	0.246924	920.4383
0.247368	877.6379	0.31128	924.9681	0.295919	931.3466
0.296106	889.5927	0.36496	937.5987	0.351276	943.2972
0.352496	903.3121	0.417784	948.915	0.40073	951.9452
0.399084	912.8175	0.468767	959.6913	0.448297	961.1887
0.445481	923.4951	0.520029	970.4811	0.50134	969.5233
0.504271	933.7878	0.570006	980.437	0.551019	977.3798

0.546824	942.0367	0.623665	991.052	0.596759	983.1662
0.601903	952.8238	0.674434	1000.5923	0.648848	992.3586
0.647321	961.7704	0.727216	1010.6331	0.698534	1000.5761
0.703445	972.6344	0.777856	1020.2665	0.751016	1005.8195
0.750468	981.632	0.828354	1030.2831	0.79905	1012.0954
0.800046	987.9322	0.880001	1040.344	0.847513	1021.9186
0.847827	998.2308	0.929828	1048.7811	0.897862	1029.3704
0.8996	1009.0509	0.9784	1058.3204	0.947177	1035.0281
0.947786	1016.6848	0.922201	1046.507	0.926581	1035.7018
0.92669	1016.52	0.868984	1035.5343	0.878832	1031.1727
0.866045	1006.9503	0.819506	1024.7167	0.817141	1024.7407
0.826842	1003.3141	0.76624	1015.6906	0.779015	1025.646
0.766623	996.7147	0.72987	1012.5099	0.720272	1018.8304
0.729423	990.5378	0.670296	1003.9662	0.666932	1015.1146
0.67042	982.9404	0.620654	995.061	0.616226	1007.7674
0.618117	973.5067	0.571169	984.7311	0.567464	1000.9124
0.567494	966.5584	0.523226	975.08	0.519249	995.6926
0.518674	955.7685	0.471793	963.9265	0.477592	987.8376
0.478109	948.341	0.421388	953.1143	0.418289	976.0176
0.421646	936.4407	0.371361	942.3337	0.37977	970.8312
0.370212	922.0687	0.320377	929.9971	0.316012	955.7488
0.321186	909.1228	0.269273	917.0856	0.267782	943.1533
0.27247	896.8976	0.220252	902.7191	0.219945	928.129
0.221566	878.2913	0.173828	887.3293	0.17392	911.0368
		0.12729	867.4968	0.123047	885.7618
		0.073282	828.319	0.076928	846.7618
		0.029955	542.927	0.028196	459.693
		0.018966	400.0949	0.019489	369.0791

DMF resolvated samples

Table A.5. N_2 isotherm data for DMF resolvated UMCM-9 samples used.

DMF resolvation 1		DMF resolvation 2		DMF resolvation 3	
P/P_0	N_2 uptake (cc g^{-1})	P/P_0	N_2 uptake (cc g^{-1})	P/P_0	N_2 uptake (cc g^{-1})
0.002128	89.6953	0.002212	77.7682	0.003888	73.7443
0.002431	93.2838	0.002697	82.5872	0.004412	76.9833
0.002864	97.0049	0.003304	87.5176	0.005023	80.4062
0.003362	100.9949	0.004017	92.6359	0.005729	84.0529
0.003947	105.3123	0.004774	97.6528	0.006465	87.8291
0.004581	109.746	0.005566	102.6186	0.007265	91.8198
0.005267	114.1105	0.006451	107.7039	0.008132	95.7403

0.006003	118.6068	0.007271	113.2735	0.008998	99.6093
0.00684	123.2605	0.008277	118.289	0.009923	103.3434
0.010974	141.8924	0.010646	128.5363	0.012056	110.9315
0.015353	156.7374	0.016112	147.1975	0.016693	124.8061
0.021731	176.2013	0.021043	162.8644	0.020158	134.0575
0.02518	187.9136	0.025716	179.0682	0.026252	150.6862
0.030923	208.9781	0.030882	198.8399	0.030911	165.1534
0.036428	229.9688	0.035385	216.6276	0.035745	181.5511
0.040223	242.535	0.040551	233.8976	0.040426	197.2712
0.045771	255.7691	0.046402	247.5531	0.046592	214.8041
0.05075	263.4886	0.05119	254.8529	0.052606	226.9351
0.057041	269.4146	0.058354	261.5247	0.057578	233.2891
0.062892	273.1582	0.064783	265.6796	0.062099	237.055
0.069883	276.53	0.071305	268.7529	0.069211	241.0115
0.075663	278.9028	0.077306	271.248	0.074926	243.4167
0.082113	281.1406	0.084113	273.6938	0.082425	246.2158
0.086968	282.7378	0.089008	275.3486	0.088402	248.2411
0.094219	284.9153	0.096044	277.6046	0.092122	249.3209
0.102379	287.1859	0.104221	280.1453	0.098834	251.3832
0.108115	288.8067	0.109452	281.742	0.103726	252.6233
0.158295	299.4373	0.163931	294.5049	0.14654	261.0122
0.212912	308.8545	0.214629	305.6728	0.19528	268.1155
0.265479	318.2703	0.268252	315.7811	0.250441	275.4769
0.318134	327.232	0.321162	326.3183	0.301212	281.1794
0.36858	336.2042	0.370383	335.8712	0.349937	287.5742
0.4178	344.6321	0.420082	345.5601	0.399863	292.9127
0.46847	352.0472	0.470394	355.8271	0.447286	299.3399
0.519682	359.8893	0.5207	365.6162	0.496717	304.2738
0.569811	368.3905	0.573574	376.3062	0.551295	309.8639
0.620582	376.9749	0.623943	387.0473	0.597589	315.2426
0.672674	386.3687	0.672286	396.9943	0.647254	320.2307
0.72496	395.9441	0.72596	407.8312	0.698221	325.324
0.775969	405.6761	0.776229	418.6252	0.748766	332.8745
0.826531	414.5491	0.82859	431.7307	0.798081	336.6064
0.873825	424.3697	0.877404	443.811	0.848765	341.5308
0.924445	432.0753	0.927131	456.0046	0.901837	347.1574
0.972871	443.316	0.978143	472.1187	0.95054	353.283
0.925051	430.6322	0.919339	452.8603	0.9268	351.7759
0.870073	420.4393	0.868549	439.4963	0.862437	347.1733
0.817318	408.7946	0.819599	426.6182	0.824697	347.6305
0.768956	399.9407	0.766668	412.9311	0.765591	343.4467
0.718726	390.8578	0.7285	408.7925	0.726555	341.0682
0.667154	382.1121	0.66899	399.7185	0.666335	337.7727

0.618158	374.1427	0.61765	390.9779	0.628959	333.8852
0.570597	367.2858	0.571219	381.5359	0.567625	331.1576
0.520649	360.0216	0.523147	371.9851	0.528705	326.5955
0.469906	353.2606	0.471722	361.7091	0.469322	319.1716
0.421198	346.7237	0.419632	350.7703	0.428743	316.3339
0.371647	338.4703	0.368706	340.7114	0.365232	307.2409
0.318725	328.554	0.317516	330.8017	0.326735	302.0163
0.269902	319.9749	0.267831	320.711	0.267192	293.5903
0.218063	311.2129	0.216805	310.9397	0.228782	287.3873
0.167898	302.6229	0.16899	300.4805	0.168431	277.3046
0.121398	293.6887	0.12104	289.3611	0.117675	266.3263
0.073628	280.5242	0.071605	274.1087	0.070129	250.6287
0.027496	201.0551	0.029598	201.754	0.029972	170.2466
0.019812	175.5842	0.01973	166.4008	0.018884	138.5911

DMSO resolvated samples

Table A.6. N_2 isotherm data for DMSO resolvated UMCM-9 samples used.

DMSO resolvation 1		DMSO resolvation 2		DMSO resolvation 3	
P/P_0	N_2 uptake (cc g^{-1})	P/P_0	N_2 uptake (cc g^{-1})	P/P_0	N_2 uptake (cc g^{-1})
0.002915	45.5737	0.003072	33.9917	0.003895	26.9798
0.003701	49.6327	0.003866	37.3792	0.004892	29.8461
0.004531	53.4695	0.004783	40.7255	0.005948	32.7158
0.00544	57.4738	0.005751	44.0725	0.00704	35.4089
0.006472	61.3567	0.006741	47.3499	0.008117	37.9817
0.007503	65.1279	0.00779	50.6556	0.00926	40.4996
0.008586	68.6403	0.008831	53.6604	0.010367	42.7822
0.009718	72.0494	0.009915	56.5289	0.011437	44.8551
0.010945	75.3692	0.010986	59.228	0.012471	46.7384
0.014228	82.8551	0.01373	65.0131	0.015528	51.5374
0.018326	91.1964	0.017312	71.7835	0.019423	57.1504
0.022395	99.7505	0.021585	79.5165	0.023471	62.9599
0.02632	108.8474	0.02532	87.0857	0.027591	69.486
0.030512	119.1824	0.031559	100.4469	0.031887	76.9591
0.036933	134.6579	0.035097	108.5044	0.036626	85.4342
0.041832	144.4291	0.041664	120.5084	0.041365	93.6933
0.047308	151.9148	0.046257	126.6811	0.046243	100.6428
0.053296	157.0684	0.05262	131.7746	0.052271	106.7858
0.060951	161.1894	0.058379	134.8208	0.058735	110.6178
0.068563	164.2671	0.064669	137.0248	0.064756	113.0329
0.073873	166.183	0.070871	138.8776	0.071679	115.1636

0.07927	167.8858	0.078064	140.5953	0.078472	116.9968
0.085937	169.7558	0.084084	142.0383	0.084572	118.2104
0.091759	171.3303	0.090229	143.0935	0.08921	119.4542
0.097084	172.6952	0.09558	144.2495	0.09424	120.6878
0.104948	174.6029	0.10053	145.0547	0.100515	121.7984
0.110193	176.0178	0.103988	145.9505	0.1046	122.5509
0.164947	187.3255	0.148658	150.9241	0.148666	128.9885
0.218893	198.9951	0.196918	155.7864	0.196743	135.4845
0.268979	209.97	0.245548	160.2726	0.246793	140.9586
0.318509	219.7628	0.298307	164.1656	0.299493	147.4995
0.370608	230.5688	0.349485	168.6874	0.349485	152.6462
0.420636	240.9561	0.398174	172.0485	0.400249	158.8889
0.471162	251.1471	0.447897	175.272	0.449171	163.7635
0.523715	261.863	0.495589	179.8828	0.497008	168.3879
0.574529	271.9518	0.546483	183.396	0.545639	172.7038
0.626563	282.7978	0.599147	186.6741	0.597414	178.3247
0.67828	294.1155	0.648848	192.1257	0.64622	184.0473
0.728878	304.8744	0.698447	195.2846	0.698978	189.0152
0.779844	317.675	0.751009	198.5936	0.750696	193.4206
0.830759	328.9391	0.800098	205.0492	0.800455	199.2649
0.880484	339.0574	0.849544	208.6855	0.848146	204.7916
0.929603	349.6408	0.897585	212.3324	0.900592	210.5757
0.977676	365.6869	0.946572	215.4484	0.947315	214.4152
0.920296	343.8183	0.924987	218.4416	0.926858	211.6868
0.86871	330.3495	0.863682	213.8614	0.87897	215.9443
0.819165	319.0846	0.828519	212.7282	0.815248	210.2278
0.769988	308.7444	0.777785	213.2376	0.774793	206.8161
0.718229	295.3847	0.717499	209.5869	0.729088	206.3237
0.668576	286.1585	0.671416	209.8096	0.667012	203.6007
0.618079	276.7387	0.616386	205.842	0.626425	202.2337
0.571918	268.389	0.566212	202.089	0.567392	194.8206
0.523268	260.5709	0.528742	201.8258	0.527752	191.006
0.468442	251.2205	0.470167	196.1332	0.467677	187.4231
0.420607	242.5379	0.429813	192.6361	0.415399	180.588
0.369121	232.1056	0.367402	188.4928	0.366135	173.9126
0.316489	219.9827	0.317104	183.7109	0.316077	167.3653
0.268625	210.8223	0.266391	178.1732	0.266056	161.0449
0.216303	200.2458	0.218117	172.6197	0.216472	153.879
0.167508	190.3915	0.171911	166.4982	0.170302	146.0339
0.118129	181.1118	0.117114	158.1271	0.116539	135.8172
0.069681	170.2035	0.068163	147.8646	0.06742	123.5587
0.027741	122.2911	0.026652	99.47	0.0231	71.3708
0.018246	101.7412	0.018622	83.0035	0.019773	65.4987

CH_2Cl_2 RSE samples

Table A.7. N_2 isotherm data for CH_2Cl_2 RSE UMCM-9 samples used.

CH_2Cl_2 RSE 1		CH_2Cl_2 RSE 2		CH_2Cl_2 RSE 3	
P/P_0	N_2 uptake (cc g^{-1})	P/P_0	N_2 uptake (cc g^{-1})	P/P_0	N_2 uptake (cc g^{-1})
0.001447	116.4523	0.001588	130.2948	0.000972	108.0439
0.002178	134.982	0.002066	144.8337	0.001772	133.5725
0.002395	138.9366	0.002283	151.476	0.002103	143.3374
0.002591	143.2571	0.00253	158.7704	0.002248	147.8403
0.002786	148.1131	0.002827	166.8092	0.002435	152.7775
0.003025	153.3894	0.003139	175.2291	0.002637	157.9219
0.003271	159.2954	0.003472	184.0833	0.00286	163.7222
0.00351	165.4601	0.004306	205.1881	0.00309	169.8648
0.004147	180.9345	0.005147	226.4746	0.00402	193.9257
0.005239	208.3784	0.010591	340.5368	0.005403	227.8658
0.011087	331.8874	0.016832	429.893	0.010633	334.1795
0.016007	405.6018	0.020761	479.2364	0.015747	407.3836
0.02108	469.1804	0.025132	537.6119	0.020934	471.0472
0.026037	533.6008	0.030272	615.476	0.025364	529.1401
0.030314	598.3585	0.03639	727.1491	0.031177	621.1502
0.03559	693.0795	0.040159	799.5146	0.035867	706.1994
0.04038	788.479	0.046053	899.4316	0.040391	788.9645
0.045091	878.0828	0.051417	961.2317	0.045498	871.1676
0.050902	965.6228	0.05539	992.0528	0.051628	941.2669
0.056424	1019.6191	0.061029	1017.3038	0.055129	966.1048
0.06018	1040.1055	0.065255	1029.1007	0.060777	989.9886
0.067691	1064.2009	0.072316	1044.3492	0.065294	1002.6435
0.0711	1071.9806	0.077318	1052.8585	0.071093	1014.6445
0.07516	1079.4438	0.082247	1060.0554	0.075869	1022.4883
0.081644	1089.2881	0.089184	1068.701	0.081329	1030.1948
0.086731	1095.9117	0.097274	1077.4867	0.086976	1037.089
0.092224	1102.3259	0.104074	1084.1897	0.092509	1043.0523
0.096754	1106.995	0.150047	1118.4231	0.09928	1049.6664
0.146759	1142.2896	0.202566	1147.1212	0.147047	1085.1042
0.199391	1166.0869	0.25581	1172.2727	0.196594	1111.3895
0.246943	1181.8256	0.307749	1193.6108	0.246212	1132.5595
0.297585	1196.0929	0.359326	1212.5533	0.299037	1152.9087
0.347843	1209.0797	0.412171	1231.3989	0.3531	1171.6065
0.401278	1221.7197	0.46698	1249.5584	0.406796	1188.347
0.445783	1230.7123	0.520021	1266.5393	0.45962	1204.6405

0.501469	1241.3553	0.56864	1285.4033	0.510203	1219.9316
0.550751	1249.6068	0.620275	1302.5096	0.564094	1234.5798
0.599381	1258.0658	0.672555	1318.4553	0.612942	1248.2764
0.646238	1266.776	0.721913	1334.2355	0.66524	1262.8638
0.707807	1277.5717	0.770924	1350.9305	0.71488	1275.847
0.750214	1285.1656	0.822188	1368.5023	0.765219	1288.6657
0.802708	1296.0333	0.87059	1385.0077	0.81684	1301.8901
0.855051	1305.6711	0.921877	1400.3138	0.867114	1314.9498
0.895677	1312.4655	0.973011	1417.6119	0.918641	1327.9665
0.953136	1320.6001	0.91997	1397.8789	0.969456	1339.1775
0.926925	1319.7297	0.86822	1380.9257	0.923072	1326.1903
0.869025	1307.6254	0.819202	1363.2927	0.872884	1309.9276
0.823506	1298.8751	0.76951	1345.3165	0.820132	1292.9453
0.767386	1292.5609	0.718136	1326.8456	0.770211	1277.4286
0.72634	1290.1339	0.667705	1309.1104	0.721313	1263.3955
0.669641	1280.64	0.619209	1293.3367		
0.618536	1272.7917	0.57133	1277.0107		
0.568415	1265.6826	0.522392	1257.563		
0.517325	1258.5258	0.469278	1239.6799		
0.473869	1248.9706	0.419166	1223.2373		
0.422814	1238.9174	0.372511	1207.4994		
0.368721	1227.4534	0.322015	1189.2333		
0.322153	1215.8574	0.268648	1169.3812		
0.274312	1202.0764	0.221145	1149.0713		
0.225211	1186.4379	0.174425	1126.7898		
0.179526	1166.9921	0.129068	1100.1506		
0.1218	1133.1608	0.075361	1046.9547		
0.078344	1087.9042	0.029482	610.8469		
		0.019014	457.6094		

THF RSE samples

Table A.8. N_2 isotherm data for THF RSE UMCM-9 samples used.

THF RSE 1		THF RSE 2		THF RSE 3	
P/P_0	N_2 uptake (cc g^{-1})	P/P_0	N_2 uptake (cc g^{-1})	P/P_0	N_2 uptake (cc g^{-1})
0.000832	99.5942	0.001508	126.247	0.001225	115.5137
0.002301	142.05	0.002233	147.1904	0.001628	128.298
0.002504	146.4827	0.002428	153.3263	0.00219	143.9659
0.002735	151.5184	0.00266	159.6984	0.00232	147.8017
0.002974	156.9191	0.002921	166.819	0.002471	152.045
0.003213	162.8312	0.003197	174.3096	0.002658	156.4689
0.003481	169.4519	0.003509	182.1718	0.002838	161.506

0.00377	176.3008	0.004284	201.4355	0.00304	166.9016
0.004067	183.4526	0.005024	219.6065	0.004214	196.9355
0.005326	214.096	0.011569	351.5347	0.005079	218.2344
0.011817	342.8071	0.015187	402.611	0.010957	337.6479
0.01524	391.7376	0.021515	481.4713	0.015387	400.515
0.02184	472.7428	0.025328	532.3002	0.02053	463.5185
0.025408	518.2547	0.030482	609.8063	0.026308	540.0511
0.030416	591.0793	0.035107	692.3314	0.030608	607.8764
0.036096	691.2939	0.04124	804.4949	0.035651	698.0826
0.040033	763.7047	0.045437	875.5155	0.041061	797.1176
0.046271	866.5284	0.050997	942.608	0.045419	867.0708
0.05185	935.0442	0.05523	976.9294	0.050749	929.6936
0.056106	967.6193	0.061551	1004.3724	0.056303	968.9416
0.061142	990.4816	0.065357	1015.0627	0.061058	988.0252
0.065846	1004.0999	0.071598	1028.3234	0.065531	1000.1297
0.070174	1013.3777	0.076781	1037.0227	0.070704	1010.7242
0.075189	1022.0157	0.082972	1045.663	0.075364	1018.1973
0.081955	1031.5663	0.089489	1053.4387	0.080378	1025.2689
0.087701	1038.323	0.097173	1061.4764	0.086141	1032.203
0.093533	1044.5742	0.103313	1067.1537	0.09168	1038.145
0.098179	1049.0431	0.14843	1098.7998	0.098128	1044.3316
0.149082	1082.8901	0.198876	1124.4697	0.145816	1078.3292
0.201764	1105.5728	0.254215	1147.252	0.197005	1104.1534
0.248383	1121.4027	0.307408	1166.1899	0.245975	1123.6337
0.299452	1136.2158	0.361529	1183.7816	0.298525	1142.0713
0.351056	1148.9348	0.413439	1199.5353	0.350831	1158.0488
0.395699	1160.2825	0.466524	1215.4054	0.403331	1172.9423
0.449076	1172.6844	0.5166	1229.0845	0.456745	1187.0121
0.500507	1182.1654	0.569307	1242.7775	0.509951	1200.3883
0.550208	1192.3834	0.621978	1257.4718	0.560276	1212.3104
0.596218	1199.5045	0.671105	1271.2526	0.613518	1224.9671
0.650963	1210.6653	0.723377	1284.4856	0.666976	1236.9481
0.699311	1219.92	0.776527	1299.3412	0.719015	1247.757
0.745619	1232.2783	0.826915	1315.703	0.768064	1259.3813
0.801579	1241.449	0.876672	1330.6743	0.819649	1270.2222
0.846273	1250.1346	0.925581	1345.275	0.86898	1280.0681
0.897566	1260.4004	0.974164	1360.0936	0.920875	1290.441
0.949207	1271.8713	0.922341	1342.5945	0.970284	1302.6122
0.92699	1268.9264	0.86906	1325.3928	0.92323	1287.8065
0.869018	1253.6173	0.820528	1309.954	0.873288	1274.6669
0.814902	1244.4093	0.769358	1292.3944	0.822048	1261.6045
0.778487	1242.1168	0.719622	1277.4959	0.77217	1248.8852
0.718213	1233.9232	0.669532	1263.4927	0.721911	1235.7479

0.668766	1225.1033	0.61913	1248.7251		
0.628696	1219.4821	0.571612	1235.0824		
0.571259	1211.4343	0.523436	1221.8756		
0.52111	1202.3354	0.472091	1207.5101		
0.46902	1190.5912	0.419992	1192.3002		
0.419797	1181.14	0.372352	1177.8616		
0.368344	1168.615	0.319818	1161.6589		
0.321617	1156.5123	0.269373	1144.9363		
0.272785	1142.8503	0.22108	1127.7397		
0.224314	1125.7228	0.174172	1107.4753		
0.178781	1105.8773	0.129148	1082.9753		
0.129224	1078.1875	0.075397	1032.7118		
0.076839	1027.8474	0.029453	600.4489		
		0.019841	462.0487		

DMF RSE samples

Table A.9. N_2 isotherm data for DMF RSE UMCM-9 samples used.

DMF RSE 1		DMF RSE 2		DMF RSE 3	
P/P_0	N_2 uptake (cc g^{-1})	P/P_0	N_2 uptake (cc g^{-1})	P/P_0	N_2 uptake (cc g^{-1})
0.000753	106.6805	0.00166	139.8508	0.001253	134.8667
0.00212	151.286	0.002269	157.4192	0.001693	149.7097
0.002258	154.2108	0.002457	162.5536	0.002132	162.597
0.002417	157.6062	0.002653	167.9156	0.002298	167.0458
0.002576	161.2743	0.002878	173.9339	0.002485	171.9515
0.00275	165.2883	0.003139	180.2535	0.002709	177.0466
0.002924	169.8004	0.0034	186.9513	0.002925	182.841
0.003126	174.4722	0.004067	202.6221	0.003184	189.0045
0.004284	203.841	0.005154	227.2196	0.004193	212.9794
0.005131	223.9892	0.011221	338.4932	0.005165	234.578
0.010884	340.0609	0.016202	401.4953	0.011266	341.3101
0.015269	402.5985	0.021327	459.5968	0.016741	407.0125
0.020523	464.6953	0.026118	517.9801	0.020264	444.8359
0.025531	525.8939	0.030337	576.1373	0.026099	512.7076
0.030777	602.4045	0.035991	666.0779	0.030399	571.3599
0.035271	678.0693	0.041116	748.6905	0.036227	660.6899
0.040771	776.6685	0.045444	808.1713	0.040081	718.726
0.045157	846.0088	0.051272	866.5035	0.045131	783.0338
0.051633	922.8174	0.055375	893.0149	0.050894	836.2141
0.05549	952.1767	0.060616	912.3021	0.055259	860.7835
0.060346	973.3549	0.066502	926.3175	0.06167	881.3915
0.066939	990.7773	0.070779	933.8923	0.065351	889.5507

0.071375	998.9802	0.075825	941.5056	0.07128	899.6696
0.075377	1005.0114	0.08158	948.6484	0.076683	907.1129
0.081246	1012.9382	0.088235	955.6933	0.081545	912.963
0.086058	1018.3647	0.096216	962.9786	0.087978	919.6337
0.090885	1023.1976	0.102479	968.1114	0.095232	926.3111
0.097629	1029.3949	0.146278	995.1508	0.100426	930.6285
0.155327	1062.9012	0.198927	1018.3929	0.146781	961.3499
0.199789	1079.5764	0.252802	1037.2521	0.19645	985.7715
0.24564	1092.5482	0.305277	1053.1692	0.247689	1006.6193
0.297975	1105.3011	0.358485	1067.7812	0.299094	1025.1682
0.348697	1115.6143	0.411091	1080.6901	0.353496	1043.244
0.401293	1125.5665	0.464219	1093.4642	0.405794	1059.205
0.446008	1131.8226	0.517158	1105.1432	0.45766	1075.1533
0.501491	1139.6519	0.570112	1117.3403	0.511997	1090.5348
0.548486	1146.5498	0.620318	1128.4684	0.563791	1105.8026
0.598845	1153.7507	0.674128	1139.7833	0.613619	1119.692
0.648163	1160.6776	0.726219	1150.7067	0.666025	1133.9014
0.703132	1168.9252	0.776708	1161.7095	0.718597	1147.5649
0.747044	1174.2314	0.828104	1172.8937	0.770946	1161.3206
0.80226	1183.0555	0.879543	1183.9877	0.820838	1174.1542
0.847937	1188.7726	0.928596	1194.1884	0.869801	1187.0037
0.897508	1196.176	0.977332	1203.5571	0.919333	1200.2642
0.957427	1202.4419	0.921579	1191.5598	0.969938	1213.5154
0.925753	1197.2561	0.8698	1179.5453	0.922323	1197.0596
0.868171	1188.0707	0.819999	1167.7549	0.873093	1180.0527
0.826293	1184.6471	0.769698	1156.1365	0.822005	1163.321
0.766033	1179.7196	0.720072	1144.1981	0.77302	1148.4971
0.725327	1175.2516	0.669517	1132.8591	0.72052	1133.4366
0.668353	1171.0487	0.622145	1122.2969		
0.620953	1165.5941	0.573048	1110.9485		
0.568748	1159.8817	0.52179	1098.5947		
0.519105	1151.9012	0.471047	1087.303		
0.471691	1146.1461	0.418912	1074.8542		
0.423133	1138.4492	0.370728	1063.1659		
0.370609	1130.0868	0.318978	1049.5388		
0.322413	1120.8896	0.270047	1036.326		
0.275658	1109.5636	0.221015	1021.2796		
0.227172	1095.7021	0.174483	1004.3187		
0.171805	1075.6411	0.129641	983.1228		
0.121742	1050.0608	0.076252	940.1655		
		0.029851	575.9409		
		0.019188	436.1349		

DMSO RSE samples

Table A.10. N_2 isotherm data for DMSO RSE UMCM-9 samples used.

DMSO RSE 1		DMSO RSE 2		DMSO RSE 3	
P/P_0	N_2 uptake (cc g^{-1})	P/P_0	N_2 uptake (cc g^{-1})	P/P_0	N_2 uptake (cc g^{-1})
0.001288	96.0082	0.00166	107.9172	0.001059	77.7508
0.002164	114.0716	0.00224	120.2242	0.001563	89.4876
0.002308	116.4553	0.002523	125.8568	0.002226	101.5963
0.002475	119.1109	0.00282	131.6187	0.002392	104.5363
0.002656	121.9861	0.003168	138.0065	0.002586	107.7763
0.00283	125.1624	0.003545	144.658	0.002817	111.1439
0.003032	128.6833	0.003951	151.5927	0.00304	114.9969
0.003249	132.32	0.004386	158.8397	0.003292	119.0131
0.004197	148.4951	0.005277	172.7401	0.004301	133.6643
0.005167	164.3745	0.011627	252.2136	0.005331	147.7923
0.010623	236.6508	0.01544	286.3076	0.011223	211.291
0.016782	293.0219	0.020884	330.3972	0.016223	249.7377
0.021008	326.5128	0.026249	377.508	0.021056	283.6839
0.025328	362.7814	0.030866	424.2672	0.025681	318.728
0.030821	416.0493	0.035303	471.5812	0.030075	355.7841
0.035829	470.4579	0.040246	520.6962	0.036328	411.6847
0.040569	520.2985	0.045676	564.2274	0.040585	446.8318
0.045099	558.3901	0.050656	590.5933	0.046103	480.7905
0.051112	592.6505	0.055622	606.33	0.050526	499.5286
0.055404	607.6891	0.060239	615.5448	0.057096	515.2463
0.061555	620.1567	0.066002	623.8464	0.060287	520.2543
0.065021	625.1736	0.071787	630.4708	0.066835	527.8772
0.0711	631.7344	0.078811	636.7833	0.071064	531.7761
0.075927	636.1233	0.085538	641.8764	0.076711	536.1888
0.080797	639.8948	0.091946	646.1163	0.081617	539.545
0.086239	643.6499	0.098333	650.1694	0.088453	543.6298
0.09218	647.2247	0.105292	653.9594	0.094274	546.7723
0.098121	650.5894	0.156209	676.0826	0.100382	549.7729
0.148069	669.5587	0.20809	693.1686	0.148387	568.453
0.201164	682.6027	0.261276	708.1066	0.19668	582.8725
0.24729	691.455	0.315034	721.64	0.248669	595.7963
0.300573	699.8193	0.367336	734.1447	0.302084	607.6104
0.346598	706.3364	0.418528	745.5418	0.354144	618.4812
0.398564	713.4916	0.470924	756.6505	0.406111	628.4979
0.450921	718.9785	0.522805	767.8853	0.459483	638.9483
0.49966	724.5897	0.572685	778.1657	0.510852	648.3237
0.545027	729.0024	0.625704	789.1121	0.562963	657.6418

0.601407	734.6564	0.674903	799.1848	0.617019	667.5389
0.646151	739.8237	0.728002	810.2742	0.6681	676.5011
0.698458	745.2098	0.777817	821.0779	0.718626	684.8661
0.748318	751.8749	0.829488	832.4011	0.768986	693.513
0.803526	757.3835	0.881261	843.5163	0.821558	702.8256
0.849688	761.1869	0.930894	853.7081	0.869253	711.964
0.903167	766.769	0.978477	862.9576	0.919729	720.8604
0.947781	770.9336	0.920246	849.9786	0.968246	730.0968
0.929241	766.778	0.86964	838.4755	0.920442	718.1959
0.86668	761.4622	0.820115	826.4901	0.871652	707.0812
0.828406	758.142	0.769525	814.7048	0.821465	695.6078
0.767032	754.7618	0.718202	802.5684	0.77199	685.6299
0.729119	752.9872	0.667379	791.4996	0.721947	676.278
0.66598	747.6656	0.618325	780.9702		
0.629065	744.766	0.570706	770.385		
0.573068	740.038	0.521986	759.848		
0.517455	734.8794	0.472642	748.8486		
0.472566	730.004	0.419739	737.8431		
0.421664	724.28	0.371112	727.0612		
0.367063	717.9954	0.31926	715.2783		
0.321422	711.4879	0.268017	703.355		
0.27374	703.878	0.218296	690.9037		
0.223322	694.3383	0.171134	677.3193		
0.177855	683.5868	0.125031	660.6889		
0.129803	668.6545	0.078971	635.1545		
		0.02875	404.7621		
		0.019282	318.8458		

IRMOF-3

Pristine samples

Table A.11. N_2 isotherm data for pristine IRMOF-3 samples used. Samples are labelled with their BET surface areas, given in parentheses.

Pristine (2846.728)		Pristine (2723.582)		Pristine (2758.320)	
P/P_0	N_2 uptake (cc g^{-1})	P/P_0	N_2 uptake (cc g^{-1})	P/P_0	N_2 uptake (cc g^{-1})
0.000856	186.6838	0.001553	301.3788	0.001525	315.5685
0.0015	283.985	0.002041	381.5295	0.00205	402.8175
0.002092	383.5995	0.002056	386.0941	0.002035	404.6269
0.002027	386.4686	0.002092	391.1812	0.002057	406.6476
0.002041	389.5788	0.002135	396.5203	0.002086	408.7935

0.00207	393.0332	0.002207	402.6256	0.002107	411.2892
0.0021	396.8442	0.003364	478.1078	0.003035	474.6723
0.003256	493.3278	0.004205	506.9238	0.004236	518.9852
0.00417	530.8211	0.005096	527.8423	0.005099	538.9257
0.005077	554.2401	0.012578	595.5035	0.010141	593.5232
0.012115	623.6217	0.015971	606.9885	0.017506	620.9821
0.015912	637.1946	0.020614	617.7178	0.02021	626.9193
0.021728	650.1838	0.026493	627.1177	0.025287	635.2256
0.026345	657.2733	0.030734	632.5758	0.031185	642.3717
0.031898	663.8951	0.036067	638.1304	0.036047	647.0881
0.035651	667.5847	0.042098	643.4355	0.041398	651.3784
0.040392	671.5142	0.047675	647.7037	0.045238	654.0895
0.045249	674.9889	0.052951	651.3242	0.051122	657.7059
0.051014	678.58	0.059319	655.1876	0.056127	660.4324
0.05664	681.6474	0.064415	658.2393	0.060615	662.6427
0.062888	684.6675	0.070323	661.3358	0.065844	664.9982
0.068002	686.9179	0.075685	663.9828	0.071044	667.1672
0.07234	688.7151	0.081392	666.6849	0.07651	669.2589
0.077893	690.7998	0.087624	669.5057	0.082558	671.4055
0.084507	693.0999	0.093827	672.1678	0.088909	673.461
0.08954	694.7747	0.101028	675.0586	0.095166	675.3439
0.096139	696.7136	0.106606	677.2594	0.101035	676.9879
0.100156	697.9298	0.152348	691.6379	0.145007	686.9564
0.146086	707.9977	0.201511	704.6813	0.195856	695.4618
0.195886	716.0574	0.252679	717.1183	0.246467	702.7219
0.249526	722.6945	0.30297	728.9453	0.29674	708.8449
0.301324	728.2996	0.353607	740.7395	0.347581	714.4917
0.348439	732.6804	0.40374	752.4312	0.399486	720.1123
0.395319	737.1478	0.454405	763.8578	0.451133	725.0294
0.450467	741.5918	0.505839	776.171	0.501909	730.0079
0.49756	745.2385	0.55754	788.3908	0.552657	735.8967
0.545129	748.7983	0.608729	800.7709	0.606188	741.2461
0.602786	752.8481	0.659272	813.0172	0.658129	746.4482
0.645226	755.8998	0.708378	824.7012	0.709502	751.314
0.696753	759.4926	0.757699	836.9116	0.760494	756.589
0.748455	762.9728	0.808285	849.5768	0.81048	761.8195
0.798899	766.572	0.857182	862.1201	0.85853	767.2512
0.846555	769.8096	0.907402	874.8718	0.909616	773.0703
0.901308	772.6852	0.957571	886.5629	0.956933	779.3196
0.945796	776.0291	0.923567	877.0425	0.920526	775.5751
0.927419	775.5742	0.87605	864.5355	0.871857	771.0773
0.867479	772.6751	0.825931	850.8779	0.822944	766.4503
0.828558	771.0573	0.775761	837.6851	0.772333	761.6368

0.766262	767.8973	0.725247	825.0805	0.722534	756.8789
0.72658	765.6781	0.675531	813.2606	0.67201	752.2485
0.669267	762.3526	0.625584	801.8733	0.623966	748.0349
0.620096	760.2639	0.575293	790.8622	0.576599	743.7758
0.57015	756.2864	0.528207	780.7929	0.52811	738.899
0.516875	752.7338	0.477901	769.5461	0.477895	732.3249
0.472993	749.2807	0.426654	755.666	0.428262	724.582
0.420128	744.8826	0.376377	744.7269	0.375572	719.4034
0.368792	740.3433	0.324361	733.1467	0.327673	714.1079
0.321713	735.1476	0.275579	721.6042	0.276055	708.1308
0.272689	729.8566	0.224051	709.2468	0.226019	701.4277
0.222787	723.1833	0.175858	697.3744	0.171482	692.9409
0.175225	715.6951	0.128722	684.0579	0.122662	683.3801
0.12525	705.7328	0.071128	662.3439	0.075503	669.7415
0.078142	692.0454	0.028707	630.6712	0.029524	641.2546
0.026616	657.5483	0.017229	610.0887	0.019038	625.1136

CH_2Cl_2 resolvated samples

Table A.12. N_2 isotherm data for CH_2Cl_2 resolvated IRMOF-3 samples used.

CH_2Cl_2 resolvation 1		CH_2Cl_2 resolvation 2		CH_2Cl_2 resolvation 3	
P/P_0	N_2 uptake (cc g^{-1})	P/P_0	N_2 uptake (cc g^{-1})	P/P_0	N_2 uptake (cc g^{-1})
0.001569	338.4936	0.000792	175.8427	0.001555	275.9629
0.002117	417.7809	0.001713	332.0263	0.002027	351.1375
0.002117	422.1602	0.002166	391.2234	0.002056	356.9337
0.002167	426.7111	0.002202	397.131	0.002115	362.9989
0.002217	431.9087	0.002281	403.4106	0.002194	369.7578
0.002304	437.4185	0.00236	410.313	0.002274	377.0309
0.003276	488.6112	0.002461	417.7493	0.003328	437.121
0.004305	520.0953	0.003023	449.28	0.004135	462.4313
0.005277	539.7979	0.004325	492.6904	0.005341	487.238
0.013722	603.152	0.005153	510.1216	0.010834	536.9028
0.016199	610.6912	0.011047	564.5229	0.015354	553.4458
0.020843	620.6934	0.016048	581.875	0.020847	565.4153
0.025105	627.5081	0.020302	591.1249	0.025534	572.5602
0.032031	635.788	0.025109	598.6034	0.031311	579.3698
0.037258	640.8804	0.030996	605.5414	0.037458	585.0612
0.043248	645.6309	0.037329	611.4366	0.043838	589.8942
0.049029	649.5041	0.043806	616.3894	0.049891	593.8176
0.054306	652.7418	0.049981	620.3121	0.055064	596.8377
0.061095	656.3474	0.055407	623.3171	0.06196	600.4754

0.066041	658.6459	0.062107	626.6713	0.067497	603.0772
0.071556	661.032	0.067634	629.1838	0.073615	605.7578
0.076725	663.0923	0.07324	631.5652	0.078375	607.725
0.0817	665.0273	0.078342	633.5996	0.084515	610.1065
0.087352	667.0994	0.084639	635.9718	0.088911	611.7842
0.09584	669.9767	0.089324	637.6635	0.095145	613.9935
0.10255	672.0931	0.09601	639.9949	0.100261	615.7503
0.108173	673.7773	0.100832	641.6157	0.105631	617.4175
0.15777	686.3387	0.107503	643.666	0.157105	630.986
0.210514	697.6058	0.158398	656.5054	0.210607	642.6088
0.263459	707.0687	0.212142	667.5662	0.261958	652.3807
0.31508	715.9657	0.263288	676.8102	0.313905	661.4153
0.365347	724.3108	0.315363	685.3171	0.367763	670.4456
0.418681	732.8501	0.365444	693.7751	0.420197	679.1678
0.469315	740.9766	0.416879	701.5796	0.472057	687.9391
0.520914	748.7346	0.469364	710.1993	0.520705	695.9149
0.571037	756.1835	0.522144	718.138	0.571061	704.4914
0.623918	764.6137	0.571066	727.221	0.621721	712.9328
0.675236	772.4561	0.621666	735.9577	0.673378	721.7628
0.72623	780.0464	0.671437	744.5289	0.722345	729.8644
0.776375	788.05	0.721727	752.9969	0.773319	737.7946
0.828154	796.8931	0.77219	762.02	0.824808	745.0756
0.87616	805.7294	0.821206	770.8575	0.875156	752.392
0.92665	814.9212	0.871914	780.487	0.926144	759.556
0.976334	826.1446	0.921225	789.9267	0.976936	763.4883
0.921236	813.9349	0.971097	799.5429	0.92331	758.5491
0.868205	803.4054	0.923168	790.5648	0.872729	750.6476
0.820292	793.2141	0.870244	780.0911	0.822802	742.0405
0.767246	784.0593	0.819825	769.9959	0.771742	734.2088
0.720276	775.7193	0.771629	761.5547	0.720449	725.9019
0.669325	767.4773	0.720871	752.1813	0.669774	718.4359
0.619533	759.191	0.670358	742.7482	0.620711	710.8016
0.570864	751.0447	0.620672	733.6319	0.57271	703.6739
0.521116	743.6111	0.570361	724.5036	0.523517	696.7141
0.4692	735.5685	0.522698	715.8205	0.472529	688.4866
0.419739	727.5466	0.473566	707.9447	0.422784	678.1921
0.372374	720.1584	0.419311	697.8353	0.370735	670.4722
0.317967	711.6029	0.369179	690.1627	0.320837	662.5975
0.268319	703.5771	0.318594	681.6603	0.270642	654.1259
0.218095	695.3698	0.270658	674.3046	0.219676	644.6062
0.170362	686.2289	0.219	667.6457	0.17094	634.4542
0.123709	675.9309	0.168494	658.8879	0.123339	622.7377
0.075703	661.3364			0.074945	606.726

0.027243	629.6801			0.025003	572.0439
0.01874	615.9101			0.017991	559.9057

THF resolvated samples

Table A.13. N_2 isotherm data for THF resolvated IRMOF-3 samples used.

THF resolvation 1		THF resolvation 2		THF resolvation 3	
P/P_0	N_2 uptake (cc g^{-1})	P/P_0	N_2 uptake (cc g^{-1})	P/P_0	N_2 uptake (cc g^{-1})
0.0015	278.2234	0.000936	202.5886	0.001533	274.8725
0.002059	365.8123	0.00167	320.6308	0.002173	359.6135
0.002074	369.548	0.002152	376.5596	0.002187	364.26
0.00211	373.6219	0.002188	382.174	0.002253	369.0916
0.002147	378.149	0.002274	388.4389	0.00234	374.4931
0.002176	383.1598	0.002375	394.9733	0.00242	380.1977
0.003118	463.8061	0.002476	402.4081	0.003074	414.2841
0.004235	512.4102	0.003008	429.244	0.004076	447.0426
0.005301	542.5121	0.004404	470.3538	0.005108	467.4171
0.011831	605.4714	0.005124	483.6363	0.010384	515.1585
0.016735	622.7297	0.010917	533.1635	0.016342	535.0582
0.021191	632.52	0.016099	549.6676	0.020171	542.6353
0.026632	641.0571	0.020496	558.3068	0.026864	551.9581
0.03064	645.954	0.025397	565.2557	0.031841	557.1686
0.035434	650.7918	0.031406	571.6547	0.037879	562.2263
0.040713	655.1829	0.037833	577.1534	0.044048	566.5449
0.046103	658.9309	0.044396	581.7259	0.049389	569.7708
0.052463	662.8617	0.050362	585.1929	0.054418	572.5128
0.058669	665.9534	0.055515	587.9114	0.06079	575.601
0.062993	667.9966	0.061553	590.7589	0.065971	577.899
0.069382	670.9146	0.067447	593.3175	0.072133	580.4217
0.074184	672.8306	0.073355	595.6232	0.076965	582.2879
0.079699	674.8859	0.078184	597.4908	0.083476	584.7247
0.085485	677.0021	0.082963	599.2427	0.087872	586.3683
0.08986	678.4141	0.087777	600.9603	0.094615	588.6631
0.096971	680.4915	0.09442	603.1564	0.099832	590.3282
0.102471	682.006	0.100091	604.9431	0.10728	592.5599
0.149118	692.4185	0.10715	607.0453	0.156335	605.211
0.200096	700.8367	0.15911	619.6735	0.20701	616.8854
0.246875	706.8791	0.210537	629.8205	0.260607	627.9705
0.295272	712.7815	0.264807	639.517	0.312212	637.6506
0.353302	718.0992	0.316479	648.1444	0.364733	647.4196
0.399486	722.7275	0.367013	656.2806	0.415183	656.7446

0.446316	726.4294	0.418915	664.4807	0.465851	666.0242
0.496765	730.7949	0.467219	673.0191	0.515539	675.0664
0.552089	735.9099	0.519315	681.175	0.56697	684.1724
0.599964	738.435	0.572174	690.4234	0.620217	694.2511
0.649147	742.175	0.620593	699.5052	0.670493	703.5922
0.697787	745.9285	0.672553	708.7762	0.720253	712.3759
0.74539	750.2803	0.723555	717.896	0.772113	723.0559
0.804405	752.45	0.775198	727.692	0.823297	732.4781
0.848037	756.0748	0.824661	733.9395	0.872678	740.59
0.896133	759.2975	0.875973	749.8828	0.921559	748.8166
0.957317	763.7646	0.923103	760.9373	0.969655	760.5616
0.928383	761.7976	0.971464	770.761	0.923136	749.0519
0.864214	760.2758	0.92432	761.1854	0.873434	739.927
0.8135	756.5492	0.871856	748.347	0.822861	730.0485
0.77439	755.7045	0.819198	733.6837	0.771248	720.0308
0.715228	751.5026	0.77083	727.3405	0.720042	708.8027
0.677199	749.1099	0.720202	717.4515	0.671031	700.6623
0.617611	746.2068	0.669645	707.4074	0.62175	691.9382
0.567302	743.5198	0.618621	697.8549	0.57162	683.1346
0.515339	738.8293	0.568914	688.3286	0.523909	675.5869
0.468309	735.0803	0.522302	680.1564	0.473859	666.3657
0.422677	731.1867	0.471623	671.5258	0.423838	656.7089
0.367177	725.6696	0.420117	661.3842	0.370495	647.728
0.316934	720.608	0.367992	653.1938	0.320598	638.8817
0.268199	714.4371	0.317695	645.0954	0.270874	629.9747
0.219655	707.7146	0.26978	637.3734	0.219908	619.3949
0.174507	700.4185	0.21854	631.3325	0.170744	608.5022
0.123581	689.4715			0.124538	597.1846
0.074956	674.3414			0.076507	582.131
0.02739	641.9386			0.02658	551.5751
0.017382	623.8947			0.01919	540.7043

DMF resolvated samples

Table A.14. N_2 isotherm data for DMF resolvated IRMOF-3 samples used.

DMF resolvation 1		DMF resolvation 2		DMF resolvation 3	
P/P_0	N_2 uptake (cc g^{-1})	P/P_0	N_2 uptake (cc g^{-1})	P/P_0	N_2 uptake (cc g^{-1})
0.001662	180.1611	0.000885	128.5276	0.00162	207.5796
0.002154	218.9357	0.001655	203.3457	0.002144	250.2977
0.002199	222.8566	0.002029	230.3619	0.002209	254.947
0.002279	227.1467	0.002173	238.1408	0.002296	260.0791

0.002353	231.8916	0.002353	246.6368	0.002434	265.781
0.002456	237.336	0.002591	255.3613	0.002565	271.8167
0.003176	265.8267	0.002915	265.0928	0.003016	286.5162
0.004	288.2216	0.003325	274.6969	0.004062	309.091
0.005493	307.8072	0.004455	292.7894	0.005086	322.5855
0.011897	339.5245	0.005361	302.4174	0.011168	357.1743
0.016529	348.5803	0.01299	334.7081	0.016204	368.0979
0.020684	353.9413	0.017826	342.5648	0.020724	374.2558
0.025412	358.4455	0.023403	348.5971	0.026115	379.673
0.03111	362.5414	0.029384	353.3444	0.031928	384.2192
0.037559	366.1274	0.035307	357.1951	0.038635	388.4137
0.044176	369.1537	0.041553	360.6304	0.045364	391.9648
0.0495	371.1823	0.048145	363.8331	0.051446	394.8297
0.054875	373.1438	0.053816	366.2299	0.056387	396.9683
0.061662	375.2206	0.058422	368.0753	0.062527	399.396
0.065904	376.416	0.065144	370.5275	0.067875	401.3583
0.071368	377.9843	0.070275	372.4059	0.073753	403.4332
0.077162	379.4887	0.075744	374.2612	0.079886	405.4549
0.082941	380.8139	0.079703	375.6277	0.08426	406.887
0.087463	381.8527	0.086122	377.7592	0.089536	408.5668
0.092875	382.9979	0.090044	379.1548	0.094048	409.9361
0.099147	384.1296	0.096744	381.2909	0.099643	411.5536
0.105265	385.2043	0.102091	382.9609	0.106851	413.5122
0.147743	392.1646	0.10805	384.8068	0.156429	425.4857
0.202677	398.6947	0.161161	398.3148	0.209503	437.0048
0.252684	403.9098	0.215107	410.862	0.261573	448.3271
0.296368	408.3912	0.267189	422.6899	0.313905	458.8164
0.353096	413.0034	0.319559	434.3219	0.365307	469.2386
0.402022	417.8574	0.368402	445.4304	0.415445	479.6883
0.448684	421.641	0.418649	456.8078	0.466462	490.1745
0.496147	425.9421	0.468291	468.1273	0.517115	500.632
0.546633	430.5416	0.520316	481.3311	0.563896	513.161
0.595956	433.597	0.572606	494.617	0.614223	525.0263
0.647809	437.4732	0.624429	507.079	0.66723	536.6924
0.702471	441.9353	0.675367	521.1078	0.719918	548.5602
0.750824	445.839	0.726233	534.9535	0.770456	560.0189
0.801464	449.3042	0.775249	548.2406	0.818944	571.5144
0.849677	453.4377	0.827201	563.538	0.868987	583.0411
0.896214	457.5089	0.876023	577.2838	0.918907	594.1128
0.946192	461.2641	0.922794	590.9225	0.967112	607.9591
0.926023	460.3612	0.971299	603.9374	0.923768	596.1741
0.863714	456.92	0.921945	590.3328	0.873732	583.3185
0.827008	454.5021	0.870201	574.0363	0.823442	570.0721

0.769206	452.7374	0.818097	558.8508	0.772948	556.9815
0.729243	450.3658	0.770485	545.3809	0.7205	544.258
0.665942	445.8383	0.719892	530.6158	0.66957	533.1418
0.629699	443.0821	0.669307	515.4485	0.620566	522.4835
0.567868	439.5304	0.619348	500.6916	0.571649	512.1232
0.516861	435.4732	0.56972	488.4525	0.522311	500.3482
0.468677	431.9687	0.523597	477.1262	0.472384	489.9293
0.416515	426.865	0.470033	464.0813	0.42112	479.7355
0.379	423.7849	0.421355	452.9155	0.368977	469.954
0.315441	417.0367	0.367603	440.6591	0.317509	459.8841
0.266177	412.2584	0.316846	429.355	0.270605	450.6246
0.218184	406.478	0.266973	420.7146	0.218498	439.3749
0.17364	400.5197	0.218972	412.4112	0.171594	429.1576
0.120132	392.0191			0.1236	418.1889
0.071029	381.0157			0.074058	404.2661
0.027529	362.3257			0.029596	383.3769
0.017846	352.6046			0.018907	372.7968

DMSO resolvated samples

Table A.15. N_2 isotherm data for DMSO resolvated IRMOF-3 samples used.

DMSO resolvation 1		DMSO resolvation 2		DMSO resolvation 3	
P/P_0	N_2 uptake (cc g^{-1})	P/P_0	N_2 uptake (cc g^{-1})	P/P_0	N_2 uptake (cc g^{-1})
0.001625	116.3307	0.001101	100.6516	0.001715	152.5715
0.002162	141.1628	0.001511	129.1903	0.002107	172.8787
0.002184	143.422	0.002109	158.8034	0.002216	177.0995
0.00225	145.8737	0.002253	163.848	0.002369	181.7205
0.002346	148.5828	0.002454	169.2408	0.002543	186.7786
0.002426	151.564	0.002706	175.0832	0.002768	192.1293
0.00325	170.7839	0.003037	181.3358	0.003074	198.0708
0.00439	186.5834	0.003498	187.7246	0.004672	217.3727
0.005132	192.5459	0.004066	194.2263	0.005333	222.6763
0.011691	214.2551	0.005585	205.4214	0.01151	244.3525
0.01686	220.7427	0.01019	221.1301	0.015623	250.5002
0.020485	223.9988	0.015206	228.4626	0.020883	255.6029
0.025184	226.9503	0.021036	233.4706	0.027329	260.0302
0.030757	229.5774	0.027477	237.2262	0.033832	263.5125
0.036875	231.8846	0.033839	240.0931	0.040394	266.4542
0.043125	233.8023	0.041071	242.7318	0.046984	269.0137
0.04864	235.3273	0.047663	244.786	0.052739	271.0836
0.055191	236.8124	0.0535	246.413	0.057745	272.7734

0.060971	238.1046	0.058429	247.6797	0.062796	274.3494
0.067228	239.2691	0.063301	248.8706	0.068827	276.1478
0.072985	240.3227	0.06908	250.1861	0.074945	277.8433
0.077934	241.231	0.075025	251.4348	0.079871	279.2115
0.082529	241.9762	0.080264	252.5608	0.084224	280.3581
0.088096	242.8038	0.086417	253.8288	0.089187	281.6414
0.091816	243.37	0.092275	254.9991	0.095291	283.1702
0.097743	244.1431	0.098219	256.145	0.103349	284.9993
0.102949	244.785	0.10538	257.4633	0.109235	286.283
0.147103	248.8019	0.109266	258.2541	0.1593	296.2751
0.201022	252.8054	0.161809	265.9125	0.212242	306.203
0.250066	255.5191	0.21451	272.7506	0.26384	315.4551
0.298375	258.0419	0.266649	279.2921	0.316267	324.4273
0.347515	260.5659	0.319444	285.7021	0.366768	333.6887
0.396155	262.5364	0.370396	292.0236	0.415983	342.5959
0.445287	264.824	0.421197	298.2267	0.465757	352.3089
0.496552	266.6354	0.471717	304.5285	0.517123	361.651
0.550015	268.8653	0.522957	311.7137	0.568902	372.3114
0.596669	271.3735	0.573542	318.5832	0.619214	382.5042
0.646794	273.0032	0.625106	325.9982	0.669854	392.6416
0.698118	274.0413	0.674913	333.2522	0.720609	402.7234
0.75028	275.3335	0.725794	340.5952	0.772192	412.8546
0.798787	276.5626	0.774443	348.3696	0.821589	422.7591
0.848692	278.3721	0.823955	356.1399	0.872446	433.3597
0.904979	279.0742	0.873346	364.5073	0.920462	445.0219
0.949684	282.2099	0.921916	373.7509	0.965361	459.4611
0.928706	281.1589	0.970788	385.8022	0.926667	448.502
0.867265	280.1439	0.925946	375.1129	0.874052	433.8221
0.826964	280.1258	0.873447	364.5311	0.821138	421.0546
0.770361	279.0532	0.820688	354.9453	0.770717	409.9062
0.714927	279.2856	0.770189	346.5994	0.720594	399.739
0.675993	278.4192	0.720432	338.2409	0.669657	389.402
0.615456	276.8795	0.670221	329.9955	0.619367	379.6011
0.569184	275.3206	0.619866	322.3939	0.569506	370.6825
0.528537	274.2235	0.570188	315.2271	0.522056	361.6745
0.469927	271.6785	0.524288	309.2653	0.474077	352.6
0.413361	269.7094	0.469896	301.7328	0.420735	343.0904
0.379875	268.1011	0.418599	295.354	0.369384	334.5185
0.318912	265.3591	0.367121	289.0394	0.319479	325.8983
0.267309	262.3832	0.318796	283.171	0.268404	317.2887
0.218302	259.5263	0.269305	279.5297	0.217605	308.2139
0.173743	256.2175	0.221217	274.9926	0.170119	299.479
0.120228	251.2956			0.122358	290.3051

0.071375	244.9935			0.07283	279.1377
0.028221	233.9145			0.027489	262.6388
0.018434	228.0562			0.016996	254.519

THF RSE samples

Table A.16. N_2 isotherm data for THF RSE IRMOF-3 samples used.

THF RSE 1		THF RSE 2		THF RSE 3	
P/P_0	N_2 uptake (cc g^{-1})	P/P_0	N_2 uptake (cc g^{-1})	P/P_0	N_2 uptake (cc g^{-1})
0.002153	336.0491	0.000947	214.6897	0.001565	287.81
0.002182	340.9833	0.001608	321.0983	0.002121	367.7562
0.002233	346.5504	0.002093	373.3325	0.002188	373.268
0.002292	352.7055	0.00213	378.2264	0.00224	379.5833
0.002365	359.8325	0.002196	383.6106	0.002314	386.5822
0.002452	367.5786	0.002269	389.5445	0.002388	394.1159
0.003102	414.3866	0.002372	395.9398	0.003056	440.6198
0.004182	454.4485	0.003121	435.0774	0.004198	485.5865
0.005583	482.9213	0.004017	462.7153	0.005414	513.2454
0.01094	529.1996	0.005229	487.1484	0.010917	566.1671
0.016231	546.9528	0.010591	533.9703	0.015359	583.6472
0.020063	554.7376	0.017451	555.4393	0.022026	598.4071
0.025069	562.0879	0.020741	561.4924	0.026024	604.3971
0.030623	568.238	0.025419	568.1292	0.031564	610.9189
0.036841	573.4077	0.030891	574.0306	0.036711	615.8163
0.043001	577.6481	0.03612	578.5205	0.042392	620.2519
0.048942	581.0937	0.04215	582.7675	0.048458	624.3411
0.05516	584.004	0.048511	586.7978	0.053835	627.7504
0.061633	587.0252	0.054158	589.6902	0.059783	631.1309
0.065677	588.589	0.060695	592.6429	0.065486	634.1714
0.070756	590.4254	0.066284	594.8123	0.070893	636.9054
0.075515	592.1821	0.072138	597.0448	0.075802	639.1415
0.081076	593.8859	0.076523	598.5518	0.080578	641.0356
0.086798	595.4786	0.082655	600.6113	0.087171	643.4482
0.090709	596.723	0.08845	602.3198	0.092689	645.3442
0.098175	598.7194	0.093709	603.991	0.099074	647.3987
0.102073	599.7921	0.099195	605.4869	0.102938	648.5342
0.146971	608.6805	0.104307	606.9232	0.14536	659.7101
0.201394	617.0623	0.146729	615.8678	0.199469	670.7612
0.249548	622.6682	0.199014	624.8418	0.247668	678.7069
0.296015	627.505	0.246996	630.5939	0.296593	685.585
0.347417	632.471	0.296014	637.7493	0.353476	692.4227

0.398884	637.7339	0.346184	643.0043	0.399383	697.3568
0.448125	641.5112	0.396428	648.3101	0.448894	702.0233
0.497293	645.4165	0.445768	654.7043	0.499021	706.8129
0.549395	649.1943	0.496908	659.6954	0.550342	711.0496
0.600212	653.4532	0.549745	668.0101	0.60015	715.4678
0.648373	657.1551	0.59979	672.5937	0.649024	720.0297
0.700818	661.161	0.649263	678.6118	0.698654	722.4406
0.751102	663.2847	0.69936	686.5641	0.747794	726.05
0.800322	667.193	0.750691	694.8319	0.7987	729.7762
0.850241	671.8789	0.796183	701.6008	0.847121	732.8277
0.906058	676.3328	0.851223	710.8892	0.897448	737.0994
0.952788	680.3253	0.895319	717.3279	0.947767	741.6566
0.916735	679.0518	0.957659	727.2491	0.926468	741.3436
0.877245	680.3015	0.927995	726.7494	0.8667	736.1825
0.813473	676.6527	0.866	715.7516	0.825028	734.703
0.776092	674.5958	0.828198	712.1823	0.777281	732.1276
0.713181	673.5366	0.770403	707.0701	0.716297	729.0649
0.679543	671.5985	0.726865	706.207	0.665243	725.1905
0.618027	667.2744	0.668388	700.4927	0.61703	722.4497
0.578244	666.4128	0.617278	698.1651	0.56826	717.5941
0.515597	660.9572	0.569127	690.5891	0.529139	716.0071
0.467808	655.668	0.516871	683.4295	0.468006	708.5866
0.428127	651.4841	0.478657	679.8327	0.420764	703.1791
0.367509	645.1309	0.421664	672.9671	0.369377	697.2643
0.318749	639.9587	0.370957	666.309	0.319539	690.8801
0.267625	633.5225	0.322858	661.4533	0.268077	682.9757
0.218078	626.2482	0.269507	652.84	0.21933	674.9806
0.17253	618.3156	0.221246	644.1741	0.173245	665.8208
0.12018	606.9327	0.172868	634.4782	0.121464	652.8097
0.070887	591.3418	0.122793	619.7231	0.07337	635.6486
0.028514	564.2675			0.022991	595.2245
0.018705	549.4815			0.018378	585.9238

DMF RSE samples

Table A.17. N_2 isotherm data for DMF RSE IRMOF-3 samples used.

DMF RSE 1		DMF RSE 2		DMF RSE 3	
P/P_0	N_2 uptake (cc g^{-1})	P/P_0	N_2 uptake (cc g^{-1})	P/P_0	N_2 uptake (cc g^{-1})
0.001992	297.2275	0.000867	186.649	0.001609	278.1537
0.002036	301.3062	0.001594	292.7418	0.002069	337.1375
0.002095	305.9058	0.002027	344.1209	0.002114	342.563

0.00216	310.9679	0.002042	348.9767	0.002188	348.3981
0.002204	316.545	0.002108	354.3122	0.00224	354.8318
0.00227	322.951	0.002181	360.1399	0.002329	362.1072
0.003299	384.0099	0.002262	366.4507	0.003041	407.2222
0.004313	416.1372	0.003378	422.8767	0.004294	450.3633
0.005101	431.5091	0.004252	446.7949	0.005132	467.8469
0.010561	478.1471	0.005031	461.9792	0.010702	518.3123
0.015275	493.5019	0.010451	510.347	0.015441	534.926
0.022449	506.0423	0.017091	531.1786	0.021834	547.2863
0.026792	511.1758	0.020374	537.2101	0.026328	553.2234
0.032025	515.99	0.02774	546.7379	0.031994	559.0228
0.037703	520.1992	0.032793	551.5255	0.037415	563.4919
0.043964	523.9042	0.037788	555.282	0.043141	567.4141
0.04938	526.8033	0.043663	559.15	0.04937	571.1518
0.055817	529.5624	0.048687	562.2364	0.054873	574.2006
0.061677	532.0298	0.054974	564.9103	0.061333	577.4133
0.065604	533.5961	0.061173	567.5782	0.067184	580.152
0.070617	535.3784	0.065109	569.2931	0.071849	582.2767
0.076507	537.3189	0.071829	571.6218	0.076944	584.2976
0.081755	538.776	0.078226	573.816	0.082291	586.1708
0.08717	540.3886	0.083324	575.1668	0.088662	588.2839
0.093308	542.0037	0.089162	577.1969	0.093557	589.7249
0.099496	543.4839	0.092225	578.023	0.099742	591.4318
0.104138	544.5902	0.098725	579.8535	0.103242	592.2468
0.147387	553.1906	0.10214	580.817	0.151664	603.6407
0.200978	561.1253	0.147236	589.7182	0.201464	613.1317
0.245271	566.5176	0.202092	598.2694	0.24634	619.5118
0.302927	573.4507	0.248223	604.4965	0.300168	626.6739
0.350183	578.6074	0.296616	610.2349	0.346008	632.1976
0.399635	583.5928	0.347212	615.0975	0.404552	638.3534
0.449336	588.0449	0.39573	621.5311	0.449636	642.3791
0.495563	592.0809	0.447524	625.7798	0.497864	646.1415
0.54511	596.2957	0.495601	632.2579	0.546931	650.3192
0.602095	600.045	0.546491	637.3763	0.603013	654.706
0.646621	604.1661	0.595714	643.4907	0.652732	657.694
0.70262	609.1344	0.650196	650.9399	0.697726	662.1694
0.749103	613.4664	0.698633	657.9734	0.750197	665.9512
0.798242	616.4755	0.745755	665.0342	0.799998	669.3784
0.847453	621.0927	0.795199	671.8312	0.851511	671.9625
0.8963	625.7416	0.853037	678.9205	0.904605	676.2267
0.945483	628.9581	0.895202	685.8105	0.949696	679.1222
0.926405	629.5519	0.952291	694.8168	0.925756	677.3068
0.866567	625.6659	0.929853	693.532	0.867063	673.9807

0.82769	622.9211	0.864883	683.9901	0.827697	673.2714
0.763502	621.8822	0.827816	679.2393	0.76385	669.0172
0.728639	619.6847	0.762258	676.7507	0.727889	667.3616
0.667764	614.5703	0.728422	674.9084	0.667913	662.8793
0.614152	611.8513	0.679265	673.3261	0.628799	659.7817
0.566086	607.9277	0.617917	665.9523	0.568942	655.5734
0.515137	603.6722	0.570912	658.7189	0.516413	651.9185
0.479346	601.4576	0.515468	653.5934	0.477833	648.7009
0.416553	594.659	0.478378	650.1229	0.420364	643.5643
0.366151	588.9484	0.418535	643.6967	0.366366	637.4416
0.329514	584.645	0.366396	639.2495	0.320355	631.4934
0.268851	576.7859	0.32158	633.5384	0.266668	624.1602
0.219005	569.4714	0.271725	625.8121	0.219189	616.7059
0.1735	561.9103	0.220806	617.1911	0.17501	608.4371
0.120793	551.3548	0.174095	607.9672	0.123037	596.6381
0.071676	537.0038	0.120546	593.2684	0.072954	580.4229
0.029631	513.0324			0.02951	552.9354
0.019552	500.2157			0.017925	535.5542

DMSO RSE samples

Table A.18. N_2 isotherm data for DMSO RSE IRMOF-3 samples used.

DMSO RSE 1		DMSO RSE 2		DMSO RSE 3	
P/P_0	N_2 uptake (cc g^{-1})	P/P_0	N_2 uptake (cc g^{-1})	P/P_0	N_2 uptake (cc g^{-1})
0.002131	294.6091	0.000984	183.6272	0.001602	274.2739
0.002138	298.6055	0.001557	256.9007	0.002158	340.1241
0.002204	303.0772	0.002123	311.5657	0.002195	346.1451
0.002262	308.0261	0.002174	316.6591	0.002277	352.6394
0.002328	313.7605	0.002247	322.2112	0.002358	360.1766
0.002408	319.9992	0.00235	328.3485	0.002462	368.2809
0.003051	358.5619	0.002482	335.0712	0.003004	399.4894
0.004269	396.3096	0.00307	360.4033	0.004568	447.7699
0.005087	411.5046	0.004062	386.3524	0.005377	462.5552
0.011101	457.8983	0.00506	402.9339	0.011688	511.6286
0.016209	472.2386	0.011421	447.4154	0.016331	525.7411
0.02242	481.9895	0.016922	461.1919	0.020558	533.7332
0.026908	486.8136	0.020719	467.1249	0.025549	540.6367
0.03209	491.3204	0.026022	473.1832	0.031586	546.9406
0.037761	495.1809	0.031963	478.285	0.037423	551.6746
0.043877	498.6788	0.037523	482.0859	0.043482	555.8147
0.049621	501.3914	0.044052	485.6331	0.050023	559.7631
0.05597	504.0538	0.049627	488.4011	0.055496	562.8157

0.062283	506.2812	0.055716	490.8509	0.061763	565.9904
0.065844	507.7122	0.062318	493.1158	0.067881	568.931
0.070727	509.2171	0.066306	494.588	0.071182	570.6154
0.075989	510.7322	0.07169	496.2925	0.076952	572.9882
0.081521	512.3406	0.075986	497.4715	0.080912	574.4736
0.087411	513.7351	0.081935	499.4141	0.087283	576.699
0.091403	514.7025	0.088913	501.0884	0.092407	578.1663
0.098519	516.2456	0.092049	501.7493	0.09906	580.207
0.103423	517.5253	0.098725	503.494	0.105148	581.8795
0.148883	525.3434	0.102566	504.2838	0.147911	592.7761
0.197263	531.3251	0.147537	512.1932	0.201798	604.1666
0.252087	537.5227	0.195408	518.27	0.248217	612.1457
0.300854	542.041	0.245748	524.2439	0.300539	620.3532
0.348716	546.1488	0.297093	529.0074	0.348352	627.3945
0.398446	549.9331	0.34506	534.7039	0.398011	634.2961
0.450153	553.3713	0.395737	539.119	0.445943	640.746
0.498475	556.4057	0.449587	545.0054	0.504406	648.2607
0.549103	560.2529	0.496365	549.6652	0.550572	653.7989
0.59584	562.9208	0.548019	554.4058	0.597043	659.3956
0.646169	565.9712	0.600025	562.1267	0.649765	665.0773
0.698767	570.3647	0.646017	567.1153	0.700174	670.9545
0.751745	573.1523	0.696327	572.9683	0.748076	676.7368
0.800197	576.4363	0.747511	581.7336	0.797847	681.4171
0.847271	579.9305	0.796932	587.6982	0.849242	686.7862
0.904321	584.1713	0.853485	594.999	0.896521	692.592
0.950767	587.7524	0.899696	604.577	0.950259	697.8272
0.927267	586.9693	0.946981	610.2365	0.9254	697.6157
0.866173	583.9642	0.927848	607.9395	0.87218	691.3291
0.82342	583.9773	0.866433	598.9949	0.829158	687.1118
0.77731	581.8821	0.826692	595.9246	0.779773	683.6642
0.716239	579.0092	0.773767	593.9343	0.717521	677.549
0.676872	578.3063	0.727063	593.557	0.677762	672.4506
0.618173	574.4708	0.668748	588.5503	0.618105	665.451
0.566509	571.065	0.619224	583.6949	0.56763	660.5938
0.528595	570.1062	0.569061	577.5218	0.514996	654.4188
0.46799	564.8257	0.513845	571.751	0.478641	650.0303
0.420618	560.5903	0.476931	568.6789	0.420661	641.7841
0.378317	557.0984	0.418594	564.1545	0.366292	633.4677
0.316706	551.0197	0.364979	558.3785	0.329329	628.1516
0.266472	545.535	0.321073	553.1884	0.269664	617.6184
0.217735	539.913	0.271013	546.3282	0.219167	608.5179
0.171771	533.2518	0.219785	538.8369	0.174276	599.1159
0.119172	523.4331	0.17098	529.3345	0.122273	586.1127

0.071581	510.7324			0.072131	568.6362
0.029113	488.1494			0.028167	539.5181
0.019129	475.9723			0.016605	520.8652

FJI-1

Pristine samples

Table A.19. N_2 isotherm data for pristine FJI-1 samples used. Samples are labelled with their BET surface areas, given in parentheses.

Pristine (4736.240)		Pristine (4922.309)		Pristine (4512.863)	
P/P_0	N_2 uptake (cc g^{-1})	P/P_0	N_2 uptake (cc g^{-1})	P/P_0	N_2 uptake (cc g^{-1})
0.001526	207.8972	0.000972	156.3222	0.001073	144.9805
0.002178	294.6489	0.001502	198.9866	0.001628	190.612
0.002149	300.6988	0.00204	245.9087	0.002138	237.2355
0.002149	307.7027	0.002076	250.1191	0.002175	241.4341
0.002192	315.0204	0.002143	254.8657	0.002249	246.038
0.002228	322.9532	0.002157	260.3267	0.002308	251.3225
0.003102	495.9367	0.002209	266.004	0.002353	257.0678
0.004255	614.345	0.003004	394.3553	0.003004	360.7419
0.005194	652.0475	0.004065	590.6368	0.004224	546.3065
0.011161	733.0936	0.005316	672.0308	0.005171	598.577
0.016047	771.396	0.011928	769.8162	0.012436	696.7001
0.020324	801.3021	0.015176	794.8428	0.015365	718.8778
0.025854	839.6839	0.020219	830.5734	0.020677	754.1662
0.030196	870.2867	0.025285	866.1451	0.026115	789.9651
0.035454	909.2764	0.030447	902.408	0.03099	822.0793
0.040297	949.9116	0.035528	939.8503	0.035288	851.2169
0.046945	1005.8856	0.040954	984.9285	0.041687	901.2347
0.050176	1028.7483	0.045792	1028.7626	0.045438	933.7219
0.055148	1050.583	0.051668	1070.123	0.051645	973.1037
0.060929	1066.6178	0.055909	1089.4194	0.055307	989.0392
0.065406	1075.7897	0.062543	1107.303	0.062704	1007.8018
0.070278	1083.7483	0.066033	1114.1071	0.065323	1012.8107
0.076066	1091.3788	0.072115	1123.412	0.070539	1020.6096
0.082757	1098.7362	0.076489	1128.7545	0.075569	1026.5918
0.090473	1106.0057	0.082144	1134.5321	0.081081	1032.5103
0.09816	1112.354	0.087541	1139.3625	0.086637	1037.5477
0.104005	1116.7386	0.092394	1143.3624	0.092037	1041.9736
0.150456	1141.6581	0.098513	1147.9969	0.098554	1046.4351
0.200087	1161.9001	0.147206	1172.1654	0.150599	1070.3871

0.250929	1179.0438	0.196414	1187.259	0.198559	1083.8384
0.304809	1195.4268	0.247022	1199.136	0.250352	1095.203
0.356783	1210.5081	0.30053	1210.2786	0.298563	1103.381
0.408141	1225.054	0.345159	1217.8383	0.347959	1111.5244
0.461619	1240.7404	0.40176	1226.7402	0.395601	1118.1348
0.514997	1255.5475	0.445888	1233.3501	0.450834	1125.2118
0.564571	1270.5828	0.501134	1241.2034	0.496627	1130.17
0.614045	1285.0652	0.550129	1249.0629	0.550506	1135.8177
0.666134	1300.1024	0.59542	1254.7095	0.596298	1139.1899
0.716274	1314.3259	0.647235	1261.1316	0.651117	1144.9194
0.768333	1329.6711	0.695141	1267.8237	0.700475	1149.8992
0.816023	1343.7367	0.747714	1273.2496	0.747726	1154.2919
0.865583	1358.2772	0.79601	1280.0435	0.799888	1158.1755
0.916662	1373.8811	0.852817	1288.5479	0.848899	1162.6521
0.967368	1389.7856	0.896569	1296.1731	0.897118	1167.7919
0.920867	1376.1389	0.944982	1313.7137	0.946588	1170.8273
0.870512	1360.4611	0.928165	1311.2595	0.92907	1170.4009
0.820286	1345.0776	0.868309	1301.9583	0.86908	1165.568
0.770941	1330.3965	0.81712	1295.1616	0.828673	1161.4366
0.721331	1315.7517	0.769686	1291.8516	0.76733	1157.4995
0.67064	1301.2595	0.728761	1288.1531	0.721892	1152.5447
0.622935	1288.4014	0.671556	1281.4229	0.667481	1148.2212
0.574028	1275.2964	0.619638	1275.934	0.629863	1143.6779
0.525499	1260.8765	0.569288	1270.2753	0.568956	1137.7734
0.474328	1247.1973	0.516538	1263.2681	0.515758	1131.996
0.421494	1232.3782	0.468545	1256.1656	0.479109	1129.0575
0.37106	1218.0991	0.419594	1248.739	0.417314	1119.6521
0.321594	1203.5607	0.369656	1239.3542	0.36706	1112.2667
0.27106	1188.3894	0.323607	1229.9819	0.320861	1104.98
0.221006	1171.739	0.271512	1218.4546	0.269002	1096.0868
0.172678	1153.9443	0.223113	1206.1355	0.222099	1086.9113
0.127166	1133.0337	0.178227	1192.2717	0.176454	1076.0946
0.073587	1092.3856	0.128319	1171.5857	0.127784	1059.7125
0.029515	878.3228			0.075636	1026.4409
0.019722	804.1403				

Table A.19 cont.

Pristine (4756.530)	
P/P_0	N_2 uptake (cc g^{-1})
0.001613	214.4736
0.002102	274.8794
0.002124	285.3504

0.002182	296.9449
0.002261	309.172
0.002333	323.0916
0.003269	504.1606
0.004046	582.2675
0.005213	630.1589
0.010987	707.4757
0.01543	740.5037
0.020095	772.0238
0.026863	817.5121
0.031039	846.2365
0.035258	876.2746
0.040118	916.198
0.046094	967.3579
0.050386	994.4775
0.056578	1019.2365
0.061509	1030.8011
0.067737	1041.3965
0.073771	1049.5272
0.080395	1056.8744
0.087386	1063.6128
0.094457	1069.5006
0.10247	1075.4576
0.108165	1079.3307
0.159645	1106.6254
0.213314	1128.1368
0.268005	1147.1764
0.319665	1164.0852
0.370843	1180.1199
0.42171	1195.7563
0.471628	1212.6685
0.524325	1227.8154
0.574012	1243.1613
0.625211	1259.3719
0.678455	1275.345
0.729632	1290.2459
0.781299	1306.058
0.831815	1314.2697
0.88269	1346.1471
0.92684	1368.8513
0.973194	1400.595
0.922844	1382.8718
0.870291	1359.4294

0.817638	1335.1436
0.767245	1323.1193
0.71758	1305.9381
0.668519	1290.3993
0.617673	1273.6865
0.568353	1258.0624
0.522647	1245.4655
0.474537	1198.2246
0.420314	1178.3545
0.369626	1164.4252
0.31708	1149.4373
0.268344	1134.7251
0.216957	1117.2601
0.168617	1100.2544
0.121464	1079.6688
0.075549	1046.4597
0.028418	826.4085
0.017546	751.7759

Hexane resolvated samples

Table A.20. N_2 isotherm data for hexane resolvated FJI-1 samples used.

Hexane resolvation 1		Hexane resolvation 2		Hexane resolvation 3	
P/P_0	N_2 uptake (cc g^{-1})	P/P_0	N_2 uptake (cc g^{-1})	P/P_0	N_2 uptake (cc g^{-1})
0.000837	151.9327	0.000976	133.1055	0.001558	191.1914
0.002152	288.6482	0.001576	183.9089	0.002063	233.7902
0.002195	296.9886	0.002116	237.2547	0.002129	239.8164
0.002274	306.0971	0.002123	241.9789	0.002211	246.6396
0.002324	316.4015	0.00216	247.5004	0.002315	254.2434
0.002388	327.2531	0.002204	253.5951	0.002389	262.3884
0.002445	339.6888	0.002256	260.1445	0.003153	381.0689
0.003168	501.3763	0.003092	400.8251	0.004073	531.1381
0.004469	644.6486	0.004216	539.9586	0.005238	606.1764
0.005298	677.2376	0.005015	580.2446	0.011404	699.767
0.010804	759.1033	0.012405	674.9375	0.015707	731.6341
0.016153	801.8651	0.01623	700.929	0.020322	761.6082
0.020185	831.8626	0.020202	725.7217	0.025553	794.9451
0.026006	874.7159	0.025646	759.4123	0.03068	827.4411
0.030167	906.0178	0.031202	794.4332	0.035199	857.2173
0.035909	951.8882	0.036077	827.1707	0.040712	897.5609
0.040771	997.3436	0.040544	860.7187	0.04546	942.2631

0.045784	1044.2948	0.045153	897.1861	0.05101	981.2085
0.050739	1078.4296	0.05025	930.098	0.056315	1005.1951
0.056609	1102.2096	0.056419	953.9139	0.061398	1020.1146
0.061379	1114.2421	0.061479	966.3092	0.065115	1027.4429
0.067321	1125.4177	0.065717	973.4398	0.070034	1034.9058
0.072955	1133.7209	0.0702	979.2144	0.076133	1042.161
0.079691	1141.9907	0.076288	985.7825	0.081668	1046.3665
0.085039	1147.7395	0.082509	991.2303	0.08793	1050.5354
0.092311	1154.8121	0.087931	995.3005	0.094883	1055.2085
0.100219	1161.7646	0.094278	999.8199	0.101865	1059.0513
0.106805	1166.8368	0.099013	1002.6472	0.147095	1080.0779
0.155256	1197.3275	0.151237	1025.0531	0.200264	1095.3242
0.208061	1223.0037	0.196804	1037.8518	0.24755	1104.9076
0.261331	1244.1584	0.247897	1048.4005	0.296134	1114.693
0.313987	1263.3682	0.298554	1057.0729	0.348643	1123.098
0.365591	1280.3474	0.345926	1064.1581	0.397019	1128.0938
0.419705	1297.6909	0.395429	1071.5117	0.453475	1136.9414
0.471931	1314.1328	0.448208	1078.6771	0.500761	1143.6168
0.524743	1329.4392	0.495499	1083.7493	0.546688	1150.9734
0.573366	1343.0721	0.545653	1088.4938	0.598782	1154.4835
0.62492	1358.8084	0.599912	1094.3795	0.646023	1162.667
0.674715	1373.7584	0.650087	1100.118	0.695735	1168.0396
0.72426	1389.2225	0.700603	1104.4828	0.754179	1172.1301
0.773347	1405.7621	0.750202	1108.8464	0.799499	1179.3962
0.82257	1424.6473	0.798336	1113.9985	0.848491	1188.9095
0.869605	1444.5802	0.846781	1119.1371	0.89824	1193.0045
0.919086	1467.5315	0.902667	1122.574	0.947788	1210.6816
0.962231	1509.3495	0.948996	1127.4613	0.927956	1208.4474
0.922411	1485.1783	0.928284	1125.8282	0.8677	1199.1499
0.87381	1455.1412	0.868299	1123.8513	0.813366	1190.7102
0.821133	1428.5061	0.826638	1123.5189	0.769145	1188.88
0.771037	1407.2159	0.765869	1118.5387	0.729005	1182.3428
0.71771	1387.7776	0.728824	1115.7428	0.669477	1177.2045
0.669753	1369.9359	0.666687	1112.2971	0.615098	1173.8385
0.619035	1349.301	0.616903	1109.1649	0.566076	1168.1089
0.57102	1328.5187	0.567815	1103.7993	0.527672	1163.9895
0.521597	1308.776			0.471349	1153.3727
0.47123	1282.928			0.416466	1145.4243
0.418418	1264.2198			0.365092	1135.3431
0.369016	1249.4172			0.329886	1131.0231
0.320593	1233.9745			0.27127	1118.9985
0.26871	1219.1473			0.22098	1107.5637
0.217242	1204.2541			0.171283	1093.3538

0.167797	1185.5651			0.12563	1073.4066
				0.079724	1042.2501
				0.029144	817.3602
				0.018987	748.9588

CH_2Cl_2 resolvated samples

Table A.21. N_2 isotherm data for CH_2Cl_2 resolvated FJI-1 samples used.

CH_2Cl_2 resolvation 1		CH_2Cl_2 resolvation 2		CH_2Cl_2 resolvation 3	
P/P_0	N_2 uptake (cc g^{-1})	P/P_0	N_2 uptake (cc g^{-1})	P/P_0	N_2 uptake (cc g^{-1})
0.002073	192.2444	0.001001	106.9938	0.000978	111.7791
0.002051	195.878	0.002031	175.2183	0.001522	142.212
0.00208	199.9054	0.002102	181.153	0.002037	175.6468
0.002108	204.461	0.002167	187.7095	0.002081	178.7941
0.002158	209.2806	0.002238	195.0235	0.002148	182.2087
0.002208	214.853	0.00231	202.7706	0.002192	185.9917
0.003041	323.6409	0.002395	211.5545	0.002236	190.1239
0.004623	412.1578	0.003218	326.2233	0.003037	283.2949
0.005029	421.8055	0.004262	405.9665	0.004155	427.0558
0.012635	483.4973	0.005348	436.348	0.005479	485.8457
0.0151	495.5254	0.010575	486.9402	0.010186	541.6765
0.020064	517.2411	0.016274	516.7559	0.016636	578.9854
0.025905	542.6412	0.020572	537.3584	0.02007	596.4547
0.030349	562.0692	0.026757	566.8781	0.025424	623.321
0.035777	587.6574	0.030475	585.2203	0.030521	649.6567
0.040756	614.2443	0.036259	614.9669	0.035125	674.0743
0.045342	639.1647	0.040464	640.3153	0.041361	712.1793
0.050663	662.8555	0.045584	671.2219	0.046465	745.0123
0.056261	678.0465	0.05001	691.6805	0.050702	766.5646
0.060977	685.8995	0.055794	707.9177	0.055931	783.4675
0.065585	691.4324	0.060542	716.2512	0.060512	792.8899
0.070485	696.2957	0.066527	723.8746	0.066256	800.9733
0.076675	701.3066	0.072254	729.6578	0.071493	806.614
0.083099	705.6993	0.079083	735.3177	0.07506	809.7383
0.089802	709.6871	0.086126	740.5502	0.080737	813.9717
0.097743	713.817	0.093169	745.2451	0.085797	817.2532
0.103385	716.5191	0.098561	748.4833	0.092137	820.9806
0.148278	732.1229	0.105975	752.5082	0.098822	824.2389
0.197488	745.0589	0.154112	773.5446	0.14892	840.5583
0.249968	756.56	0.20741	789.8936	0.198335	850.1262
0.302924	767.1202	0.261246	806.2961	0.249037	857.6395

0.354471	776.8522	0.315316	820.2479	0.301033	863.3267
0.405711	786.2768	0.366084	832.9313	0.35083	868.1129
0.45683	795.7105	0.417352	845.1272	0.397001	872.1378
0.509686	804.929	0.470515	855.3375	0.446894	876.3922
0.55869	813.2269	0.521061	865.2678	0.497242	879.6066
0.609467	822.4908	0.572322	876.4006	0.545811	883.5632
0.662352	831.6868	0.624963	887.1	0.598454	886.7615
0.714105	840.7343	0.67641	898.7399	0.646097	890.4675
0.763322	850.8333	0.727978	910.2678	0.695489	894.094
0.814007	859.9349	0.776264	922.6285	0.746992	896.8578
0.866842	868.7599	0.825337	934.4485	0.798165	900.4993
0.915895	877.1062	0.876927	949.1701	0.845094	904.041
0.961444	887.7598	0.923791	965.2716	0.901826	906.8977
0.919727	878.2084	0.964305	996.4536	0.952653	910.911
0.870069	869.4971	0.920988	983.4266	0.929059	909.76
0.821842	861.7629	0.873223	968.4198	0.864965	906.7061
0.772795	853.2968	0.818623	951.0449	0.827965	905.1765
0.722787	844.1483	0.769243	938.1302	0.763849	901.002
0.672644	836.147	0.719769	924.9738	0.725819	898.9051
0.622708	828.0434	0.670968	911.9127	0.664858	895.5468
0.576169	820.6992	0.617991	896.3981	0.623599	892.0252
0.526838	812.611	0.571442	882.9533	0.568411	888.7578
0.474266	803.9286	0.523056	868.5564	0.516768	884.8063
0.425084	795.5359	0.472975	835.4877	0.469303	881.4809
0.373345	786.5641	0.421035	824.0798	0.419734	877.7969
0.323509	777.3699	0.369674	812.6953	0.36737	872.9348
0.275908	768.5219	0.317805	800.1506	0.321287	868.5917
0.226356	757.8551	0.26678	789.697	0.271402	862.6356
0.176135	745.9007	0.21687	778.529	0.222252	855.9057
0.129681	732.3221	0.168462	766.2231	0.171535	846.7725
0.074901	706.317				
0.028319	562.8373				
0.019523	523.1446				

THF resolvated samples

Table A.22. N_2 isotherm data for THF resolvated FJI-1 samples used.

THF resolvation 1		THF resolvation 2		THF resolvation 3	
P/P_0	N_2 uptake (cc g^{-1})	P/P_0	N_2 uptake (cc g^{-1})	P/P_0	N_2 uptake (cc g^{-1})
0.001535	99.4	0.001187	66.4379	0.000853	77.7864
0.002181	123.6515	0.002074	99.1526	0.001743	117.0078

0.002321	128.9942	0.002195	104.6877	0.002029	130.5963
0.002461	135.1701	0.002317	110.7663	0.00211	134.2426
0.002571	142.0449	0.002417	117.5935	0.002198	138.435
0.002681	149.5272	0.002517	124.8154	0.002279	143.0039
0.003048	178.7138	0.002646	132.9753	0.002353	148.1006
0.004106	254.2664	0.003032	163.2031	0.003162	218.8742
0.005119	282.5518	0.005027	229.7147	0.004096	298.7592
0.011766	328.3297	0.005742	237.2635	0.005022	329.8499
0.016092	342.7237	0.011727	265.6517	0.013838	393.6106
0.021557	358.6699	0.015059	275.6288	0.015412	399.7972
0.026368	372.4202	0.021287	292.427	0.021051	419.996
0.031135	386.269	0.026585	306.5981	0.026316	438.5206
0.036004	400.5461	0.030167	316.3686	0.030095	451.8682
0.040367	414.976	0.036059	333.1559	0.035029	469.8148
0.046566	436.9253	0.041	349.4403	0.041102	495.0338
0.051472	450.8665	0.046005	365.642	0.045463	514.2061
0.055248	458.3276	0.05219	379.5676	0.050735	533.1323
0.060382	465.4396	0.058054	387.2566	0.056477	545.9399
0.066625	471.0816	0.063981	392.5247	0.062852	554.3821
0.074153	475.8947	0.070982	397.3347	0.06697	558.3603
0.079823	478.7985	0.077088	400.7634	0.071411	561.8886
0.084575	480.9607	0.082958	403.7506	0.076087	564.8985
0.091494	483.5896	0.089458	406.8423	0.08269	568.6577
0.098259	485.8234	0.095457	409.6029	0.087433	570.9273
0.102291	487.1512	0.10097	411.8961	0.094374	574.0942
0.148005	496.7677	0.107191	414.3137	0.100249	576.3259
0.197075	503.3286	0.158338	431.8017	0.146998	589.0316
0.248636	508.5381	0.210542	446.664	0.195696	598.153
0.299844	512.6049	0.264435	461.6436	0.249754	605.5605
0.348679	515.8542	0.317776	474.6356	0.296003	611.7783
0.402046	518.752	0.369874	487.0565	0.349083	616.9043
0.451638	520.9014	0.419347	498.139	0.396649	622.5385
0.501282	523.5961	0.470093	509.9836	0.446332	627.7256
0.551608	526.2691	0.521812	522.3054	0.501066	632.8038
0.600143	528.3829	0.570642	535.2892	0.546529	636.8782
0.649838	528.4185	0.620244	546.4153	0.597139	640.5432
0.703043	529.485	0.674922	557.2164	0.651572	645.4377
0.753421	529.6149	0.726369	568.2493	0.699497	651.3873
0.805437	531.3127	0.777487	580.3022	0.748629	656.1694
0.855315	530.1478	0.825838	591.8029	0.79918	660.1942
0.903791	530.6296	0.876184	603.2642	0.847672	664.5084
0.952112	531.2421	0.928124	616.8057	0.898083	670.7524
0.928815	530.8903	0.973614	633.9718	0.948531	682.4633

0.863145	534.9543	0.921967	617.4456	0.925318	680.0511
0.825172	536.2861	0.871908	605.2487	0.875642	674.0383
0.76673	536.3122	0.819495	591.7262	0.828819	670.809
0.727465	537.8343	0.770086	579.4321	0.766166	666.3308
0.679408	536.6839	0.718304	565.9728	0.728843	663.7526
0.618424	536.2325	0.670532	553.607	0.666263	660.1935
0.567201	535.498	0.619014	539.9462		
0.516221	533.2805	0.57052	526.2281		
0.477646	531.0718	0.522584	511.3804		
0.416398	527.8442	0.473146	495.0053		
0.364331	524.8655	0.422407	478.1979		
0.313997	521.35	0.369573	465.8208		
0.265771	516.9645	0.317404	453.9284		
0.217053	511.9765	0.265807	444.0652		
0.171545	505.7096	0.216556	433.3089		
0.119052	495.3866	0.167376	422.0198		
0.072427	478.0843				
0.029541	384.1942				
0.018494	351.2871				

DMF resolvated samples

Table A.23. N_2 isotherm data for DMF resolvated FJI-1 samples used.

DMF resolvation 1		DMF resolvation 2		DMF resolvation 3	
P/P_0	N_2 uptake (cc g^{-1})	P/P_0	N_2 uptake (cc g^{-1})	P/P_0	N_2 uptake (cc g^{-1})
0.001843	105.5009	0.002182	86.877	0.001634	122.1731
0.002095	118.2418	0.002277	90.5662	0.002146	150.1643
0.002124	121.0206	0.00235	94.696	0.002174	154.9531
0.002196	124.1723	0.002467	99.3932	0.002239	160.2841
0.002268	127.5195	0.002576	104.6533	0.002318	166.2816
0.002333	131.0926	0.002693	110.3316	0.002405	172.6652
0.003017	164.537	0.003095	132.9367	0.003067	226.0465
0.004262	197.5685	0.004496	190.5133	0.004565	283.8396
0.005522	210.2387	0.005189	201.8112	0.005321	295.2847
0.011008	231.9419	0.01248	236.7818	0.011174	331.9411
0.016494	244.7543	0.015093	243.9116	0.015394	347.1534
0.020756	253.5825	0.020705	256.8804	0.022003	368.032
0.025191	262.3623	0.02677	270.0746	0.025978	380.4869
0.031635	274.4598	0.031617	280.7146	0.030298	393.5916
0.035587	282.2498	0.03666	291.9409	0.03528	408.9428
0.040987	294.0439	0.041061	302.9602	0.04014	425.7575

0.045083	302.8046	0.045476	314.3448	0.046447	447.9984
0.051743	313.2715	0.050819	325.6587	0.050746	459.6217
0.056106	317.8363	0.055453	332.2785	0.055469	467.9309
0.06098	321.4524	0.060825	337.4977	0.060653	474.2263
0.066675	324.6858	0.067641	342.1564	0.066881	479.7084
0.072384	327.273	0.072925	345.0182	0.073094	484.0906
0.078684	329.6148	0.079596	347.9852	0.080237	488.2573
0.085415	331.8643	0.085106	350.0965	0.086018	491.2665
0.092989	334.144	0.091835	352.492	0.09324	494.5093
0.100037	335.9786	0.096601	354.1372	0.101462	497.8228
0.106596	337.6137	0.101674	355.748	0.107553	500.085
0.157158	346.2179	0.151259	365.8076	0.158623	513.8784
0.208765	352.9464	0.198924	372.5741	0.213998	524.882
0.263481	358.9941	0.251071	378.624	0.26874	534.1788
0.31495	364.1947	0.299335	383.6443	0.321904	541.9192
0.366153	369.2328	0.349344	388.3457	0.37378	549.697
0.418818	374.0665	0.397265	392.7112	0.42377	556.4325
0.472634	379.1476	0.44747	397.2994	0.474825	563.657
0.525695	383.5604	0.496136	400.777	0.52647	570.4149
0.577013	388.3978	0.545436	404.3236	0.579477	577.2065
0.625862	392.7725	0.597642	407.813	0.630661	583.8881
0.674458	396.8519	0.65092	412.7683	0.68186	590.4355
0.726223	401.1845	0.698483	414.9958	0.733549	596.6363
0.777764	405.7158	0.74609	418.8673	0.783114	602.884
0.827815	410.1487	0.797026	422.3629	0.831793	608.5571
0.876787	414.7934	0.852464	428.3757	0.881696	615.6213
0.926154	419.7018	0.905895	431.0733	0.93152	624.1067
0.973814	426.4112	0.950291	437.1119	0.979083	635.829
0.922885	420.2292	0.929126	435.3372	0.925638	622.4951
0.868853	414.8594	0.86409	433.7423	0.86937	612.3805
0.821084	409.8422	0.825686	431.7118	0.817544	605.3024
0.768499	404.6545	0.766219	428.0843	0.767706	598.4019
0.720391	400.1205	0.728231	427.1409	0.717169	591.2368
0.667468	395.551	0.667874	425.8639	0.667136	584.1506
0.620289	391.4812	0.61769	421.4505	0.617248	576.6991
0.571707	387.2426	0.578695	419.3212	0.568043	570.361
0.522239	382.642	0.517936	414.9362	0.522294	565.0627
0.469654	378.4847	0.467169	412.1688	0.472218	557.8211
0.417234	373.7252	0.421955	408.0376	0.419867	551.032
0.367615	369.6366	0.37191	403.9538	0.369431	545.2798
0.316153	365.0395	0.321537	398.4438	0.317519	538.4686
0.265641	360.5829	0.265026	392.5736	0.270352	532.0743
0.218433	355.9782	0.21755	386.083	0.217195	523.7164

0.171032	350.7755	0.172169	379.133	0.168473	515.4057
0.124804	344.2573	0.120781	368.5778	0.121709	505.1357
0.077582	333.5765	0.074348	353.8803	0.076226	488.3389
0.027315	273.5468	0.028018	282.3004	0.026129	386.5906
0.019201	258.1363	0.017334	257.7118	0.017806	360.96

DMSO resolvated samples

Table A.24. N_2 isotherm data for DMSO resolvated FJI-1 samples used.

DMSO resolvation 1		DMSO resolvation 2		DMSO resolvation 3	
P/P_0	N_2 uptake (cc g^{-1})	P/P_0	N_2 uptake (cc g^{-1})	P/P_0	N_2 uptake (cc g^{-1})
0.001194	182.7782	0.001494	101.8151	0.001593	182.182
0.002231	271.0053	0.001657	106.5779	0.002048	212.0695
0.00226	276.2863	0.002034	120.3136	0.002172	219.9595
0.00231	282.1266	0.002205	126.2344	0.002304	228.9807
0.002367	288.6637	0.002375	132.9979	0.002429	238.9566
0.00241	295.6199	0.002523	140.4455	0.002561	249.8512
0.002474	303.5332	0.002678	148.2294	0.003053	307.2515
0.003017	369.8882	0.003018	167.8419	0.004125	416.3678
0.004562	471.655	0.004024	217.4802	0.005548	473.6187
0.005113	485.9919	0.005815	247.4341	0.010979	537.6948
0.011848	556.9438	0.011474	277.6571	0.015243	564.6497
0.016381	584.4628	0.016113	292.1469	0.0203	590.9799
0.02143	611.6127	0.021469	306.7794	0.025445	616.1368
0.025241	631.4401	0.02502	316.0127	0.031441	645.0292
0.030568	658.7178	0.031078	331.1965	0.03569	666.4329
0.036052	686.6638	0.03696	345.8659	0.040138	688.7286
0.040285	710.1234	0.040318	354.7939	0.046126	720.7272
0.045848	739.2612	0.046141	370.5483	0.050537	740.0429
0.051483	760.3092	0.050283	379.7928	0.057575	760.5698
0.055937	770.564	0.055795	388.4689	0.061671	768.3044
0.061543	779.7903	0.061691	394.588	0.067953	776.6087
0.067013	786.5272	0.068771	400.0138	0.073281	782.101
0.072662	792.2086	0.073572	403.075	0.079967	787.8111
0.079355	797.8935	0.080481	406.7052	0.086404	792.5243
0.084446	801.8207	0.086851	410.1313	0.090403	795.0911
0.091746	806.9634	0.09166	412.3065	0.097288	799.282
0.097688	810.5867	0.098044	415.3505	0.102528	802.1899
0.104388	814.3807	0.104295	417.737	0.148852	821.5743
0.153196	836.182	0.146182	431.1873	0.200336	836.5777
0.207825	853.8012	0.200912	444.035	0.248562	848.1207

0.260237	867.291	0.245743	453.3145	0.298512	857.9769
0.31561	878.905	0.298216	461.9812	0.348388	865.6654
0.369037	889.1745	0.348225	469.8575	0.397972	873.7139
0.419504	897.7117	0.396571	476.8926	0.447085	881.154
0.470351	906.2589	0.451884	484.6936	0.499288	888.3274
0.522241	913.7651	0.496723	489.1829	0.54733	894.4666
0.576233	922.8646	0.552932	495.2327	0.59739	897.5685
0.627458	931.3682	0.597341	499.9036	0.646952	903.9473
0.678018	939.2852	0.646737	504.8536	0.697122	910.9775
0.729544	948.0156	0.696362	510.514	0.748958	915.1849
0.778853	956.8928	0.74666	516.1556	0.799026	920.2993
0.827511	966.7899	0.796078	521.1843	0.848308	927.189
0.876019	977.7419	0.854063	528.4504	0.895506	935.8611
0.92565	991.5732	0.89879	534.8665	0.951063	945.5508
0.96951	1012.8243	0.945737	544.8519	0.926352	942.8245
0.928424	998.8966	0.927494	541.9094	0.86714	938.0795
0.872458	985.6812	0.86857	533.88	0.826812	936.2086
0.820732	974.4836	0.827356	530.8848	0.76448	933.389
0.770129	964.5755	0.774498	523.8409	0.724504	931.0665
0.718268	953.9378	0.722647	516.8517	0.666393	922.948
0.670704	943.7743	0.6643	513.4155	0.615408	917.8532
0.619507	931.9305	0.623182	507.0351	0.574287	914.9234
0.570877	920.2847	0.568801	500.7508	0.518436	909.2845
0.52302	908.8976	0.518525	496.652	0.469741	897.2615
0.47537	893.6193	0.470616	486.7854	0.418037	887.0951
0.423795	878.1179	0.419393	476.7433	0.365907	878.468
0.36943	868.9553	0.369428	469.004	0.314496	867.7056
0.318541	860.679	0.314928	459.9644	0.265141	857.2428
0.266387	852.5112	0.267411	452.5316	0.218875	846.1921
0.221146	843.4249	0.219022	443.5633	0.172741	832.6379
		0.173754	433.607	0.122321	812.7501
		0.12316	419.9548	0.074507	781.9907
		0.073986	400.5178	0.027103	621.5972
		0.029059	324.1093	0.017827	573.0786

CH_2Cl_2 RSE samples

Table A.25. N_2 isotherm data for CH_2Cl_2 RSE FJI-1 samples used.

CH_2Cl_2 RSE 1		CH_2Cl_2 RSE 2		CH_2Cl_2 RSE 3	
P/P_0	N_2 uptake (cc g^{-1})	P/P_0	N_2 uptake (cc g^{-1})	P/P_0	N_2 uptake (cc g^{-1})
0.000869	144.9106	0.001762	201.2521	0.000905	121.0356
0.001671	213.1819	0.002052	232.5175	0.001589	172.8371

0.002157	257.1107	0.00211	240.4373	0.002096	211.5266
0.002216	261.0222	0.002175	249.4153	0.002118	215.1526
0.002261	265.466	0.00224	258.9105	0.002148	219.1605
0.002312	270.2891	0.002313	269.6948	0.002206	223.5986
0.002319	275.5709	0.00303	399.4659	0.002265	228.3745
0.003048	394.6068	0.004125	526.8072	0.003037	336.0391
0.004087	585.9756	0.005466	576.7866	0.004045	504.5173
0.005324	662.2448	0.011339	644.4868	0.005244	572.9031
0.011258	755.5151	0.01508	669.588	0.011377	656.287
0.015595	789.3096	0.021068	706.2518	0.015694	685.6537
0.020404	822.8378	0.025056	730.5659	0.020482	714.5815
0.025212	855.9459	0.030972	767.0045	0.025579	745.6003
0.030042	889.8796	0.035452	796.1495	0.030595	776.1283
0.036698	938.5084	0.040636	834.1822	0.035044	804.5115
0.040446	970.2141	0.04574	873.4727	0.04117	849.0341
0.045954	1018.7546	0.051388	905.4422	0.045804	885.4125
0.051211	1056.4351	0.055296	919.1713	0.0514	919.1725
0.056005	1078.5371	0.062582	935.893	0.055916	936.4054
0.061866	1094.9707	0.0677	943.5919	0.060505	947.2994
0.067042	1104.7163	0.073268	950.4177	0.066168	956.7775
0.070473	1109.8087	0.079482	956.6752	0.070044	961.9503
0.076924	1117.9965	0.08568	962.0739	0.076839	969.1145
0.081761	1122.9998	0.09243	967.2875	0.082039	973.5953
0.085877	1126.9545	0.09844	971.5121	0.086525	977.0651
0.092048	1131.9899	0.104037	975.0795	0.091747	980.5672
0.096907	1135.6051	0.152402	998.9428	0.098292	984.577
0.148759	1161.0536	0.201804	1016.8568	0.147898	1004.6138
0.195383	1175.3787	0.253663	1033.0431	0.197011	1016.7227
0.245733	1187.6145	0.304384	1047.5642	0.24797	1025.9401
0.298395	1197.769	0.356519	1062.1794	0.300768	1033.7214
0.351764	1206.5123	0.408878	1075.502	0.345476	1039.5475
0.395884	1213.0098	0.458997	1090.9355	0.402046	1046.3
0.450173	1220.2767	0.510798	1104.5641	0.447467	1051.3531
0.504374	1226.8685	0.564151	1118.7623	0.501464	1056.7881
0.547022	1232.3408	0.615488	1134.114	0.548738	1061.2953
0.599176	1238.7592	0.666195	1146.9523	0.598925	1065.1213
0.649378	1244.9949	0.717402	1161.5262	0.645913	1069.0441
0.696812	1249.7391	0.768108	1176.6283	0.69568	1073.1938
0.745881	1255.6348	0.816074	1189.0067	0.747257	1077.2639
0.797114	1262.1182	0.865947	1206.6393	0.797091	1080.2247
0.849997	1268.4786	0.910237	1227.7894	0.846998	1083.7308
0.90204	1276.9884	0.957819	1252.4851	0.900318	1088.1472
0.948554	1290.4202	0.925034	1240.4166	0.947909	1091.0764

0.927605	1288.8036	0.873588	1216.7278	0.926721	1090.851
0.867956	1279.132	0.821221	1195.6902	0.864053	1087.0275
0.828121	1276.6202	0.772306	1185.0444	0.825266	1084.9209
0.764524	1271.1572	0.722998	1170.1017	0.771748	1082.301
0.727612	1269.9059	0.673401	1154.4656	0.715295	1078.4882
0.669016	1264.295	0.623231	1139.7428	0.667204	1074.6821
0.616833	1259.6711	0.573112	1124.6141	0.617355	1070.4659
0.569428	1254.0264	0.52611	1111.3406	0.567485	1066.9717
0.517311	1248.3279	0.47415	1096.8984	0.515518	1062.126
0.470783	1241.4028	0.423175	1080.8223	0.472627	1058.1346
0.418342	1234.1581	0.371838	1066.9349	0.420785	1052.3376
0.369627	1225.8427	0.320986	1053.3618	0.36979	1046.1184
0.321199	1216.2683	0.270229	1039.1361	0.316345	1038.9817
0.271711	1205.5701	0.222771	1024.8262	0.268019	1031.6616
0.224151	1193.8911	0.174587	1008.3885	0.222038	1023.4851
0.179103	1180.5044	0.127158	988.4124	0.177853	1013.8079
0.129424	1160.6016	0.071753	949.2584		
0.07766	1123.3379	0.028993	756.0954		
		0.019517	696.4122		

THF RSE samples

Table A.26. N_2 isotherm data for THF RSE FJI-1 samples used.

THF RSE 1		THF RSE 2		THF RSE 3	
P/P_0	N_2 uptake (cc g^{-1})	P/P_0	N_2 uptake (cc g^{-1})	P/P_0	N_2 uptake (cc g^{-1})
0.001535	182.3229	0.000772	106.4441	0.001605	200.8439
0.002166	236.3549	0.001544	165.7249	0.002113	244.0178
0.002188	241.2293	0.002191	220.6822	0.002158	247.8574
0.002247	246.753	0.002213	225.6445	0.002224	252.3132
0.002299	252.8673	0.002287	231.3021	0.002283	257.2134
0.002344	259.4762	0.002323	237.6319	0.002334	262.4584
0.003056	379.4238	0.002404	244.3639	0.003078	371.4006
0.004279	559.6526	0.003037	336.2885	0.004013	545.485
0.005051	601.0975	0.004228	517.3994	0.005228	642.2209
0.010657	686.5416	0.005338	578.0984	0.010251	734.7576
0.016071	725.8309	0.011963	666.5942	0.017062	787.2959
0.020365	753.507	0.015639	693.9434	0.02	807.3572
0.02503	783.4073	0.020139	722.9889	0.025163	842.6915
0.031245	823.7968	0.025007	753.197	0.030074	875.3109
0.035925	855.7778	0.03097	790.554	0.036481	920.0952
0.040278	889.1393	0.036073	824.2997	0.041186	966.1349
0.046582	940.2556	0.040624	857.5499	0.045958	1008.5301

0.050001	962.8062	0.04547	896.3201	0.051282	1046.1095
0.055652	986.8439	0.050632	930.5431	0.055723	1066.7407
0.060614	1000.187	0.057132	956.8892	0.061526	1082.8157
0.067511	1012.2955	0.060065	965.1164	0.06668	1092.6122
0.071968	1018.0699	0.066433	976.4553	0.070215	1097.7917
0.076032	1022.5468	0.070528	982.5298	0.076828	1105.752
0.082128	1028.3251	0.077389	990.403	0.082388	1111.0746
0.087631	1032.6671	0.083183	995.3699	0.086335	1114.561
0.094128	1037.2271	0.088124	999.613	0.092491	1119.2744
0.100528	1041.1971	0.09466	1004.121	0.097042	1122.4153
0.146739	1061.8629	0.100785	1008.1136	0.145651	1144.6128
0.198371	1076.5372	0.147049	1028.0883	0.20239	1159.9677
0.247312	1086.6464	0.199049	1042.4504	0.248489	1167.8738
0.301466	1096.0112	0.246048	1052.671	0.299859	1175.8037
0.346475	1102.6329	0.302856	1062.1525	0.347467	1181.1495
0.400963	1110.0598	0.347708	1069.3831	0.396636	1186.9139
0.446922	1115.306	0.396222	1076.2952	0.447381	1191.631
0.502359	1122.524	0.445508	1083.0597	0.495166	1195.9402
0.547428	1127.6791	0.496566	1089.4083	0.552516	1200.5768
0.595878	1132.8875	0.551573	1097.196	0.598659	1204.4969
0.65024	1138.9189	0.598859	1102.0975	0.647069	1209.0868
0.697652	1143.2468	0.648506	1107.8867	0.699147	1210.6692
0.749596	1148.0798	0.69924	1113.7131	0.747992	1215.4491
0.80085	1152.6409	0.748004	1119.5137	0.79842	1220.4927
0.848426	1156.7876	0.799423	1124.1636	0.847994	1224.1757
0.897885	1161.3101	0.848789	1128.9988	0.901125	1228.2305
0.948346	1167.8605	0.899531	1137.8254	0.945353	1241.1752
0.924985	1165.3181	0.947354	1143.4777	0.929373	1238.3121
0.872981	1160.6075	0.926707	1143.1312	0.869894	1229.5812
0.828973	1156.6378	0.863216	1139.266	0.829216	1226.3491
0.770599	1152.8451	0.827378	1135.9111	0.770054	1223.4913
0.729142	1148.7817	0.766386	1131.9056	0.726489	1220.8113
0.66686	1143.423	0.725549	1130.7014	0.668439	1218.0002
0.628406	1140.8831			0.617083	1213.3268
0.569372	1134.4578			0.568599	1208.8099
0.518511	1129.225			0.528326	1206.2513
0.470862	1123.4624			0.472558	1199.6836
0.422507	1116.0465			0.420864	1194.5415
0.364623	1107.7861			0.379802	1190.4824
0.320266	1100.7645			0.319182	1183.2144
0.271941	1092.415			0.267355	1174.2433
0.221903	1082.1974			0.221073	1165.8156
0.175996	1070.6313			0.176322	1155.2343

0.125803	1052.7997			0.12744	1138.5342
0.073792	1017.4614			0.076828	1105.4358
0.028723	801.5673			0.028911	870.475
0.01883	735.8391			0.019816	805.8362

DMF RSE samples

Table A.27. N_2 isotherm data for DMF RSE FJI-1 samples used.

DMF RSE 1		DMF RSE 2		DMF RSE 3	
P/P_0	N_2 uptake (cc g^{-1})	P/P_0	N_2 uptake (cc g^{-1})	P/P_0	N_2 uptake (cc g^{-1})
0.002083	264.7953	0.001551	192.291	0.00162	230.5477
0.002054	267.3467	0.002156	254.662	0.002117	293.2907
0.002061	270.1726	0.002178	260.2812	0.002095	295.9899
0.002075	273.3235	0.002223	266.6719	0.002117	298.9921
0.002097	276.8842	0.002274	273.8261	0.002138	302.3972
0.002104	280.6009	0.002326	281.3679	0.002153	306.0447
0.003038	468.6271	0.003064	418.8617	0.003038	484.5482
0.004144	586.1218	0.004135	554.8927	0.004133	613.2234
0.005513	634.6876	0.005184	602.7428	0.00522	659.7482
0.010577	698.8628	0.011947	687.7316	0.010894	739.359
0.016754	742.1859	0.016097	716.3025	0.016294	780.1926
0.020177	764.1716	0.02038	744.4138	0.021319	815.0885
0.026097	801.9724	0.026368	782.3812	0.025639	845.2242
0.030704	831.8817	0.031101	813.0072	0.030226	877.1441
0.03524	862.6147	0.03534	842.0678	0.036115	921.4629
0.04141	910.6229	0.040531	882.4495	0.041148	965.1177
0.045175	941.7403	0.045589	924.2341	0.045943	1006.8843
0.051944	983.1604	0.051267	959.6166	0.050558	1037.5962
0.055603	997.1359	0.055203	975.0876	0.05503	1056.475
0.060303	1008.7639	0.060748	989.2214	0.060429	1070.392
0.066394	1019.146	0.066589	999.7262	0.065851	1080.3301
0.070901	1024.9648	0.071654	1006.4565	0.070884	1087.3451
0.076293	1030.6963	0.07779	1012.604	0.075139	1092.296
0.080266	1034.3364	0.083173	1018.3118	0.080143	1097.2168
0.086435	1039.3074	0.088903	1022.3619	0.085665	1101.9874
0.091884	1043.1865	0.095579	1026.5819	0.092477	1107.1632
0.097654	1046.834	0.100607	1029.3478	0.098345	1111.1588
0.148956	1069.2197	0.145317	1049.96	0.14598	1132.6626
0.196571	1081.7429	0.196392	1065.3804	0.196437	1146.8229
0.24778	1092.8751	0.2478	1076.6194	0.249134	1157.8087
0.29742	1101.4547	0.298845	1086.3588	0.303832	1166.9723
0.345655	1109.4773	0.347395	1093.0027	0.358437	1175.3383

0.397043	1117.7875	0.395421	1099.9775	0.410198	1182.6469
0.450299	1124.8096	0.446983	1105.8363	0.464313	1188.751
0.501579	1131.6493	0.497859	1112.1667	0.516902	1194.7672
0.552896	1138.6382	0.548587	1117.5389	0.569145	1200.3966
0.601994	1145.6323	0.596753	1122.7767	0.619249	1205.8208
0.651334	1152.4739	0.649142	1129.4834	0.673552	1211.4233
0.701117	1159.6505	0.698084	1134.4274	0.724614	1216.6818
0.749794	1166.509	0.747438	1140.486	0.776727	1222.4092
0.798764	1173.759	0.79536	1147.4038	0.825918	1227.1097
0.847755	1181.4056	0.847358	1152.7528	0.87603	1233.5425
0.899913	1188.5674	0.899445	1160.5803	0.925832	1240.5527
0.94864	1196.0598	0.947729	1166.5249	0.966361	1253.1782
0.917979	1192.351	0.927911	1166.9775	0.922081	1247.1144
0.872418	1187.3215	0.866321	1160.3065	0.870349	1239.7775
0.824362	1180.8674	0.828928	1156.6244	0.819618	1233.645
0.774201	1174.3966	0.765691	1151.6769	0.770881	1228.5225
0.724154	1167.3201	0.727701	1146.7703	0.718055	1222.1968
0.675662	1160.9226	0.664198	1144.396	0.669779	1216.6943
0.62655	1154.0848	0.628342	1140.6165	0.620063	1210.8489
0.579249	1147.9271	0.568612	1133.0107	0.571139	1205.7172
0.528675	1140.6802	0.51623	1126.8617	0.523533	1200.6841
0.476253	1133.6453	0.478166	1121.2869	0.474832	1185.3737
0.425193	1126.641	0.420681	1112.8522	0.4222	1179.532
0.376859	1119.3867	0.36965	1105.1984	0.373737	1173.7726
0.325842	1110.6116	0.322016	1097.6135	0.321076	1165.7828
0.278106	1101.7905	0.267508	1084.4019	0.274068	1158.5696
0.228694	1092.1434	0.220449	1073.9969	0.22366	1149.47
0.173362	1078.1007	0.175355	1059.7216	0.177062	1139.2722
0.126055	1061.8915	0.124583	1039.8478	0.122781	1121.8374
0.071208	1024.3174	0.073028	1003.7943	0.072173	1087.8386
0.029791	822.3125	0.029913	801.2363	0.029182	870.3054
0.019592	754.9392	0.018615	726.1517	0.019296	800.5732

DMSO RSE samples

Table A.28. N_2 isotherm data for DMSO RSE FJI-1 samples used.

DMSO RSE 1		DMSO RSE 2		DMSO RSE 3	
P/P_0	N_2 uptake (cc g^{-1})	P/P_0	N_2 uptake (cc g^{-1})	P/P_0	N_2 uptake (cc g^{-1})
0.000869	131.121	0.00103	124.6889	0.001528	151.4394
0.001524	179.2103	0.00164	164.2211	0.002167	197.8713
0.002187	231.9364	0.00214	199.5647	0.002248	204.9084

0.002224	236.6431	0.002206	203.2615	0.002359	212.861
0.002275	242.0457	0.00225	207.3293	0.002463	221.7717
0.002297	247.9041	0.002309	211.8364	0.002575	231.2417
0.002349	254.2601	0.002375	216.8711	0.003012	284.4106
0.003144	372.7437	0.003082	307.0381	0.004059	425.1827
0.004109	517.897	0.004111	442.5896	0.005105	486.2153
0.005059	582.1251	0.005494	508.3938	0.013036	582.29
0.012422	693.2261	0.010973	572.9513	0.01619	601.6815
0.015706	718.0737	0.015812	602.8269	0.020456	624.7291
0.020948	752.166	0.021122	631.7404	0.025316	649.9211
0.026073	784.4592	0.025939	657.0793	0.030094	675.522
0.031242	817.9498	0.030933	683.9539	0.036149	708.2744
0.036124	850.6786	0.0355	709.1949	0.041491	741.35
0.040984	887.2243	0.041192	744.9642	0.045698	772.9135
0.045497	923.2094	0.045223	772.1351	0.051292	804.9429
0.050225	954.6838	0.052003	807.5397	0.056375	824.5592
0.056535	981.1003	0.055997	821.0007	0.060723	835.2303
0.061004	993.3001	0.061116	831.6889	0.0653	843.1642
0.065938	1002.8864	0.06658	839.8558	0.071058	850.3308
0.072609	1012.2228	0.070492	844.4086	0.077832	856.1341
0.077513	1018.0887	0.075486	849.2436	0.085905	860.1937
0.082888	1023.4689	0.081414	854.062	0.090921	862.8665
0.087865	1027.7866	0.086488	857.6321	0.097576	866.7142
0.092482	1031.4115	0.093071	861.684	0.103771	870.115
0.098167	1035.5341	0.099646	865.2483	0.150011	888.0184
0.149687	1061.6733	0.148854	883.3126	0.195746	899.747
0.198712	1076.9551	0.19554	894.7459	0.246288	909.3829
0.247375	1089.0079	0.248485	903.7646	0.296891	916.0774
0.300655	1100.4734	0.299407	911.564	0.345801	923.6879
0.34845	1109.4686	0.347138	917.2921	0.399237	930.5933
0.39637	1116.6212	0.401451	923.5388	0.44935	936.1876
0.449562	1125.9209	0.447313	928.4464	0.499767	940.0232
0.500221	1134.984	0.502243	933.7645	0.547067	946.0948
0.54697	1142.9274	0.546885	938.5574	0.597625	952.0197
0.595825	1145.9629	0.598182	942.0143	0.647655	954.7691
0.651823	1153.5006	0.645641	946.0782	0.697145	957.4207
0.696532	1160.0045	0.697673	949.5361	0.749082	962.2063
0.747964	1166.4342	0.75128	954.7514	0.801406	962.4742
0.797563	1173.5105	0.806144	957.3516	0.850183	966.5148
0.854584	1182.3998	0.848278	961.3093	0.904279	972.1477
0.905309	1188.1936	0.895317	965.0455	0.952114	976.4901
0.948708	1196.6942	0.954888	970.8543	0.927332	973.7441
0.925963	1196.1644	0.928177	969.0175	0.867166	970.6229

0.866358	1193.1174	0.868863	966.3304	0.825037	973.0392
0.828592	1192.4664	0.813624	961.6224	0.763862	972.0514
0.770886	1186.7369	0.777918	960.0528	0.728559	974.9474
0.717989	1183.9153	0.715802	955.9575	0.664661	970.3545
0.67967	1180.4277	0.677897	953.1222	0.628661	969.8063
0.619432	1173.1696	0.617142	949.0406	0.567033	966.1333
0.57149	1168.3765	0.566926	945.1307	0.51632	959.114
0.518659	1160.769	0.514739	940.504	0.479592	955.3912
0.470083	1152.329	0.474804	935.369	0.417297	947.3987
0.42206	1143.7167	0.422175	930.4109	0.363415	940.4114
0.372064	1134.1661	0.36773	923.7932	0.317324	931.6031
0.320823	1123.0796	0.321206	918.3904	0.268585	922.9334
0.269988	1110.2961	0.271019	910.5769	0.218079	912.3029
0.223172	1097.2108	0.221693	902.0933	0.175282	900.77
0.175127	1081.7739	0.174977	892.2562	0.123315	881.0806
0.125771	1060.3378			0.077135	851.7094
				0.026421	653.189
				0.018289	608.1123

UiO-66

Pristine samples

Table A.29. N_2 isotherm data for pristine UiO-66 samples used. Samples are labelled with their BET surface areas, given in parentheses.

Pristine (1648.81)		Pristine (1544.766)	
P/P_0	N_2 uptake (cc g^{-1})	P/P_0	N_2 uptake (cc g^{-1})
0.002938	216.7104	0.001761	200.7243
0.003555	222.7127	0.002163	207.7869
0.004304	228.9196	0.002293	209.8184
0.005163	235.4742	0.002473	211.9499
0.006059	241.607	0.002638	214.2853
0.007139	248.082	0.002868	216.89
0.008219	254.3458	0.003112	219.6385
0.009365	260.0793	0.00414	229.3341
0.010532	265.3442	0.005376	238.8598
0.013412	276.4538	0.011457	269.115
0.01715	288.3472	0.015913	285.3063
0.021271	299.9169	0.020959	301.1307
0.026023	312.0817	0.025753	315.1251
0.030569	323.2985	0.030914	328.128
0.036173	335.7427	0.03537	337.0929

0.041461	347.0021	0.041738	346.8474
0.04636	356.0132	0.046101	351.9967
0.052802	366.1554	0.050989	356.8105
0.058619	373.4695	0.055553	360.3582
0.064781	379.6046	0.061116	364.245
0.0704	384.0757	0.065946	366.9864
0.077627	388.7356	0.070927	369.5344
0.083077	391.8799	0.076979	372.1947
0.087006	393.9419	0.082815	374.4933
0.093279	396.6494	0.089147	376.7411
0.099683	398.999	0.096809	379.1248
0.104142	400.5673	0.102523	380.774
0.1512	412.2884	0.146806	390.2991
0.199668	420.6237	0.195883	398.1253
0.251243	427.7198	0.248402	405.5077
0.301886	434.214	0.299082	412.0729
0.349135	440.1493	0.348691	418.3297
0.397316	446.0227	0.401059	424.5107
0.448231	452.624	0.450847	431.19
0.499879	458.0694	0.501297	437.4467
0.54682	464.1263	0.552573	443.8763
0.599886	468.6935	0.60193	450.6916
0.649536	475.02	0.650755	457.1011
0.698636	482.2197	0.702103	463.9814
0.750777	486.312	0.751647	471.0137
0.80092	492.5435	0.801615	478.2235
0.849403	499.8122	0.85039	485.5353
0.898033	509.2918	0.900667	496.6621
0.947412	517.223	0.948119	508.9101
0.924503	515.8483	0.925277	502.1623
0.879678	509.3445	0.878989	491.4983
0.821948	502.0055	0.829424	479.9225
0.779591	499.0551	0.77914	473.4005
0.717013	493.5852	0.728144	465.6208
0.677674	489.6619	0.677673	458.5453
0.6178	484.5073	0.62575	451.7275
0.566717	479.8353	0.577334	445.5444
0.514253	473.6493	0.527977	439.4277
0.477426	469.1308	0.473977	433.3356
0.423163	462.4883	0.424958	427.2081
0.365455	454.675	0.374666	421.2119
0.313696	446.5221	0.327056	415.6129
0.266616	439.4718	0.274953	409.1849

0.217024	430.7812	0.225115	402.2708
0.168725	420.9124	0.177159	395.3254
0.123209	409.4842	0.121822	385.4583
0.070789	385.2401	0.074995	371.9686
0.025508	308.9412	0.029189	326.2901
0.019699	291.8843	0.019148	296.7492

EtOH resolvated samples

Table A.30. N_2 isotherm data for EtOH resolvated UiO-66 samples used.

EtOH resolvation 1		EtOH resolvation 2		EtOH resolvation 3	
P/P_0	N_2 uptake (cc g^{-1})	P/P_0	N_2 uptake (cc g^{-1})	P/P_0	N_2 uptake (cc g^{-1})
0.001854	206.3747	0.000827	175.846	0.001153	203.3106
0.002251	212.3593	0.001547	198.4167	0.001574	215.6336
0.002764	218.6912	0.002065	206.9809	0.002299	228.0148
0.003391	224.9926	0.002353	210.9609	0.002516	231.5761
0.004099	231.2256	0.002705	214.9926	0.002821	235.2695
0.004892	237.4981	0.003123	219.3833	0.003183	239.1382
0.005867	243.9046	0.003619	223.8601	0.003604	243.5079
0.00692	250.0238	0.004187	228.4298	0.004119	248.0045
0.008082	256.1658	0.004835	233.0923	0.004685	252.6755
0.010687	268.031	0.005626	238.1045	0.005337	257.4665
0.016034	288.5891	0.01121	264.0041	0.01095	286.1538
0.021294	306.3652	0.016469	282.3591	0.015736	303.8608
0.026901	322.1881	0.020124	293.8657	0.021392	322.147
0.031216	331.8495	0.025714	310.0291	0.025018	332.6796
0.036245	340.6806	0.03029	320.7651	0.030152	344.9318
0.042494	348.7491	0.035801	330.9811	0.035598	354.9859
0.048585	354.605	0.040593	337.7509	0.040116	361.3971
0.055663	359.9106	0.045572	343.2325	0.045148	367.0558
0.06158	363.6904	0.050579	347.6488	0.050355	371.7708
0.068638	367.4807	0.056918	352.1296	0.05707	376.6264
0.073833	369.9511	0.064149	356.3452	0.062581	380.0136
0.078971	372.1403	0.070286	359.2913	0.068477	383.058
0.085097	374.5304	0.075862	361.6052	0.074474	385.7689
0.08934	375.8574	0.08128	363.689	0.081384	388.4741
0.09574	377.6822	0.086604	365.4508	0.088049	390.8468
0.101975	379.541	0.093799	367.7109	0.094698	393.0353
0.10808	381.1396	0.099475	369.311	0.099941	394.6911
0.159659	394.0309	0.106411	371.128	0.105525	396.3785
0.213302	405.1084	0.156537	382.8336	0.155285	407.8639

0.264809	415.2713	0.20934	393.2907	0.20944	417.8372
0.318055	425.5337	0.261553	402.807	0.261862	426.5241
0.369742	435.7633	0.313319	411.3442	0.312739	434.4246
0.422353	445.5701	0.364388	419.5036	0.365762	442.7817
0.474776	455.2865	0.415198	427.5283	0.418989	450.6761
0.526255	465.2723	0.467806	435.7062	0.471352	458.9047
0.576059	474.5344	0.519113	443.491	0.520221	466.1785
0.626252	484.4568	0.568706	450.7203	0.570771	474.5713
0.67514	494.3028	0.619286	458.3041	0.62072	482.81
0.725211	504.6229	0.670498	465.5954	0.670771	491.0011
0.774697	515.4197	0.721143	472.1541	0.719588	498.7291
0.824718	527.0497	0.774291	480.674	0.768979	507.0543
0.873945	539.7574	0.82233	487.5899	0.819442	515.8666
0.921887	553.1544	0.872162	495.0663	0.868709	525.3276
0.969866	574.4597	0.921828	503.9381	0.918136	536.1963
0.927155	553.6141	0.966011	518.3292	0.963792	550.014
0.871679	536.5826	0.92808	501.5455	0.926446	537.6813
0.820425	522.3981	0.875363	488.8062	0.875345	525.4321
0.770483	510.4491	0.823086	479.2901	0.822343	515.1664
0.717779	498.3336	0.771247	470.6799	0.772822	506.086
0.668306	489.3371	0.719366	461.3862	0.721415	497.1557
0.619332	480.7845	0.669678	454.019	0.670524	489.0974
0.571022	472.0006	0.621149	446.0977	0.620546	481.1416
0.523123	463.4614	0.570246	440.2263	0.57323	473.3164
0.472561	453.7315	0.521998	435.2037	0.523941	465.0881
0.420838	443.8894	0.472548	428.5171	0.470003	456.9856
0.369129	436.4757	0.42017	420.4151	0.420439	449.2489
0.319137	428.9619	0.371756	412.4773	0.368061	441.6353
0.267031	419.8664	0.31868	404.16	0.319562	434.0573
0.217963	408.6025	0.267172	396.6887		
0.169025	396.4654	0.21765	388.8363		
0.121133	384.1444	0.170244	380.8334		
0.07327	367.9239	0.123506	371.7868		
0.026417	320.139	0.075776	358.5822		
0.018732	296.7393	0.02752	314.8941		

DMF resolvated samples

Table A.31. N_2 isotherm data for DMF resolvated UiO-66 samples used.

DMF resolvation 1		DMF resolvation 2		DMF resolvation 3	
P/P_0	N_2 uptake (cc g^{-1})	P/P_0	N_2 uptake (cc g^{-1})	P/P_0	N_2 uptake (cc g^{-1})

0.001652	209.5393	0.001072	199.3837	0.001073	200.1529
0.002143	217.9328	0.001583	214.1244	0.001617	215.25
0.002504	222.8206	0.002158	223.7468	0.002175	224.9534
0.002951	228.1085	0.002461	227.9166	0.002451	229.3485
0.003442	233.5323	0.002835	232.3746	0.002828	233.8445
0.004041	239.349	0.003295	237.2173	0.003256	238.5464
0.004777	245.2411	0.003828	242.1624	0.003793	243.7674
0.005585	251.0581	0.004439	247.1862	0.004416	249.0871
0.006523	256.8963	0.00513	252.3668	0.005134	254.5198
0.010153	274.7454	0.005957	257.6033	0.005917	259.6926
0.016719	299.0385	0.010404	279.4924	0.010479	282.706
0.020919	312.7076	0.01603	300.1378	0.016331	304.3078
0.025479	326.2354	0.020433	314.3824	0.020203	316.9206
0.030769	339.6877	0.025038	328.4921	0.02504	331.1613
0.036736	351.2491	0.030657	342.8275	0.030544	344.6591
0.042069	358.7654	0.036636	354.6761	0.036794	356.2206
0.047683	364.9721	0.041298	361.5251	0.041784	363.0235
0.052957	369.6425	0.046457	367.6267	0.046831	368.6148
0.059812	374.5067	0.051572	372.4652	0.052146	373.3515
0.0656	378.0091	0.058062	377.517	0.058564	378.0707
0.071589	381.137	0.065055	382.0243	0.064234	381.6108
0.077044	383.6056	0.070193	384.8458	0.070543	385.0273
0.08361	386.3465	0.076351	387.8076	0.076178	387.6555
0.090134	388.612	0.082949	390.6082	0.08269	390.3576
0.096202	390.6211	0.08782	392.3798	0.088549	392.6233
0.101131	391.9727	0.094698	394.7057	0.095249	395.0327
0.107473	393.7621	0.100504	396.5199	0.100906	396.9999
0.159009	406.0377	0.107088	398.4475	0.108193	399.3901
0.214759	416.211	0.155516	411.1001	0.157997	412.269
0.267457	426.204	0.206498	422.2852	0.20944	423.9029
0.318877	435.6107	0.260531	433.1677	0.26366	434.577
0.369446	445.2115	0.31373	443.7086	0.315929	444.9601
0.419279	454.3371	0.36323	453.1302	0.367981	455.2453
0.471067	462.2606	0.415407	462.6559	0.418836	465.1319
0.520583	470.4561	0.465036	472.4563	0.46851	475.32
0.574197	480.3931	0.515019	482.3631	0.518625	485.3548
0.62403	489.4941	0.566195	491.1528	0.568632	495.5241
0.674678	499.7988	0.616509	500.7611	0.618762	506.5148
0.726062	510.1438	0.668426	510.5314	0.670045	517.7354
0.776372	521.5237	0.720128	519.6678	0.721401	528.6529
0.825404	531.6139	0.772125	528.7592	0.770364	539.6442
0.872119	544.4741	0.82305	538.3667	0.821596	551.8773
0.919773	556.3182	0.871622	548.3598	0.868601	565.1094

0.967116	577.359	0.923533	560.1649	0.917657	578.9857
0.929125	558.6648	0.969385	573.4446	0.96443	597.5979
0.873649	543.0988	0.925965	556.6053	0.926649	581.2092
0.821096	528.6692	0.876025	542.3325	0.874569	565.4745
0.769589	517.1929	0.822223	529.6755	0.82061	550.2737
0.718991	505.8943	0.771888	519.1619	0.771872	538.102
0.667397	496.5554	0.720819	509.305	0.721742	526.5015
0.617485	487.6653	0.669175	499.0312	0.66919	515.4423
0.569737	479.2529	0.620826	488.2794	0.618617	504.4488
0.523953	470.9637	0.569706	481.5098	0.571127	494.1578
0.472128	462.4533	0.522933	475.2039	0.522969	484.1916
0.422562	454.3886	0.473483	466.1182	0.473549	474.1884
0.368992	446.9795	0.421457	455.4327	0.421897	463.8138
0.318459	438.7951	0.371482	446.0045	0.3716	454.1028
0.267839	429.8966	0.317313	436.0369	0.320846	444.1382
0.218396	418.932	0.268489	427.3233		
0.16953	408.4162	0.218226	418.5243		
0.12153	397.1053	0.169553	409.343		
0.073956	380.5706	0.122477	398.9382		
0.025479	324.8989	0.075035	383.9945		
0.01923	305.5477	0.027052	334.3427		

DMSO resolvated samples

Table A.32. N_2 isotherm data for DMSO resolvated UiO-66 samples used.

DMSO resolvation 1		DMSO resolvation 2		DMSO resolvation 3	
P/P_0	N_2 uptake (cc g^{-1})	P/P_0	N_2 uptake (cc g^{-1})	P/P_0	N_2 uptake (cc g^{-1})
0.001523	207.1343	0.003123	227.7704	0.000885	193.6255
0.002049	216.5733	0.003605	233.4583	0.001849	219.1487
0.002345	220.787	0.004223	239.0395	0.002125	223.9352
0.002692	225.3874	0.004972	244.6233	0.002306	226.8072
0.003103	230.1531	0.005821	250.2694	0.002545	229.9729
0.003601	235.2533	0.006828	256.0483	0.002814	233.3198
0.004185	240.5042	0.007878	261.462	0.003147	237.0847
0.004842	245.8117	0.008958	266.6134	0.003546	240.9564
0.0056	251.1342	0.010044	271.3682	0.004336	247.9458
0.010268	275.214	0.011238	276.2166	0.005294	254.9943
0.015774	295.8163	0.014541	288.4471	0.012117	288.3554
0.020067	309.7182	0.018181	300.7328	0.016127	302.9117
0.026554	329.2481	0.022131	313.601	0.020812	317.8525
0.031223	340.6304	0.02657	327.0567	0.025946	332.7246

0.035105	348.0743	0.031312	339.4847	0.030087	342.5404
0.041592	357.8152	0.036953	351.2447	0.037106	355.0728
0.046434	363.1946	0.043601	361.6952	0.041029	360.2448
0.052741	368.8085	0.049644	369.1616	0.045409	365.0378
0.059062	373.2672	0.055565	375.035	0.050232	369.3914
0.064972	376.7843	0.062379	380.9115	0.056243	373.7512
0.070809	379.7543	0.067451	384.6971	0.061377	376.9561
0.076178	382.1206	0.074027	389.0684	0.067802	380.3461
0.082759	384.6424	0.079539	392.1782	0.073988	383.1308
0.089239	386.7802	0.084273	394.7556	0.07984	385.4756
0.095156	388.5695	0.090633	397.892	0.085532	387.5155
0.103281	390.7803	0.097094	400.7993	0.092494	389.8582
0.108671	392.0785	0.102339	402.9532	0.098295	391.6611
0.157718	402.865	0.109527	405.9964	0.10567	393.7766
0.208633	412.0988	0.161027	427.0103	0.154081	404.7014
0.262723	420.9548	0.214902	447.5239	0.207098	414.2582
0.315919	429.5759	0.265719	466.5928	0.260991	422.7812
0.36809	437.5547	0.316356	485.152	0.313232	430.834
0.418435	444.7409	0.365784	503.3248	0.363021	438.2206
0.470216	452.9029	0.417112	522.3699	0.413985	445.3846
0.52129	460.913	0.468799	541.8887	0.465261	453.1067
0.57157	467.7585	0.521062	562.3364	0.517298	461.0641
0.620249	475.7116	0.569915	580.2299	0.568436	468.2938
0.671922	484.3409	0.621157	598.1553	0.618943	476.2239
0.723097	493.0775	0.673808	617.2155	0.670234	484.2956
0.772699	501.6379	0.726668	635.597	0.72151	492.3939
0.823852	511.2097	0.77655	652.3803	0.770683	500.1715
0.871657	520.9002	0.826158	670.6594	0.819101	508.2822
0.919982	532.1971	0.875601	689.2794	0.866984	517.1739
0.964439	548.297	0.926173	709.2095	0.914829	526.9179
0.928324	534.1407	0.975285	725.9282	0.960493	540.1003
0.87577	520.275	0.927037	698.7527	0.924612	528.8583
0.822265	508.8952	0.873083	671.5869	0.875577	518.1628
0.772843	499.4699	0.82082	648.5256	0.82256	508.1928
0.719727	490.3001	0.770031	628.0054	0.773228	499.5125
0.669107	482.8346	0.719898	608.9294	0.72222	491.2537
0.618019	475.0268	0.6687	588.2436	0.671249	483.3461
0.570134	467.7274	0.622193	565.6982	0.62167	475.4395
0.521528	461.0072	0.568411	555.8337	0.571279	467.6092
0.471688	453.0673	0.521141	541.7245	0.522947	460.7098
0.422714	445.2969	0.472886	523.1293	0.472788	452.9844
0.371596	439.8958	0.418745	501.7958	0.419917	445.122
0.319786	432.8837	0.369504	482.8197	0.371672	438.3586

0.270848	425.1633	0.316169	464.2354	0.319577	430.7284
0.219017	414.9917	0.279648	452.4936		
0.170165	405.4757	0.218996	433.6161		
0.122374	394.9524	0.169128	417.8026		
0.075218	380.3479	0.120657	401.2111		
0.02776	331.7619	0.070912	379.0206		
0.019461	307.0171				

H_2O resolvated samples

Table A.33. N_2 isotherm data for H_2O resolvated UiO-66 samples used.

H_2O resolvation 1		H_2O resolvation 2		H_2O resolvation 3	
P/P_0	N_2 uptake (cc g^{-1})	P/P_0	N_2 uptake (cc g^{-1})	P/P_0	N_2 uptake (cc g^{-1})
0.001616	201.3387	0.001223	199.4368	0.001218	203.8998
0.002129	209.7235	0.001554	207.5004	0.001726	216.0363
0.002497	214.696	0.002058	215.7701	0.002052	222.1101
0.002973	220.0083	0.002338	219.6397	0.002277	225.6725
0.003492	225.4698	0.002684	223.5668	0.002589	229.6124
0.004142	231.1886	0.003065	227.8922	0.002944	233.7099
0.0049	236.9697	0.003554	232.2803	0.003336	237.9555
0.005765	242.6751	0.004079	236.8058	0.003836	242.6536
0.00674	248.2531	0.004727	241.5937	0.004416	247.5124
0.010622	266.2654	0.005439	246.2804	0.005054	252.3962
0.015586	283.9461	0.011526	274.7234	0.010544	281.4232
0.020847	300.2849	0.01549	288.4733	0.015359	299.4306
0.026042	314.7145	0.021318	306.6858	0.020892	317.3767
0.030191	324.2175	0.025182	317.5815	0.02504	329.5601
0.036772	335.6971	0.030528	329.9337	0.030159	342.0033
0.042018	342.3491	0.035988	339.5846	0.035794	352.6853
0.047444	347.6389	0.040701	345.8811	0.041755	361.0192
0.052871	351.95	0.045766	351.2531	0.046722	366.3131
0.060015	356.4669	0.051069	355.6942	0.051791	370.7837
0.065722	359.4879	0.057925	360.2344	0.057425	374.9184
0.071762	362.2177	0.064055	363.5791	0.063284	378.4846
0.077246	364.3908	0.070488	366.5337	0.069673	381.8441
0.083899	366.7331	0.076373	368.8234	0.07567	384.5499
0.09004	368.6515	0.081481	370.526	0.082262	387.2167
0.097184	370.6828	0.08705	372.1657	0.08728	389.1247
0.102054	371.8865	0.093878	374.0556	0.095663	392.0544
0.107827	373.2769	0.102339	376.1203	0.102907	394.3989
0.161867	384.909	0.108886	377.5991	0.108672	396.1669

0.2153	395.1966	0.160228	387.1772	0.156837	407.924
0.268799	404.9267	0.211599	394.6783	0.207308	418.0084
0.319837	412.9857	0.264085	401.3731	0.259563	427.5638
0.369634	420.961	0.318514	407.6257	0.31176	436.7131
0.421292	429.088	0.369094	413.1968	0.363021	445.4721
0.472366	436.6736	0.420947	418.7279	0.415718	454.4455
0.522026	444.149	0.472368	424.0642	0.46761	463.1895
0.574962	451.9511	0.524185	429.0313	0.518886	472.3494
0.625805	460.0464	0.5758	434.1315	0.567167	480.9253
0.676367	468.4515	0.626625	438.7568	0.617573	489.6348
0.726055	476.3277	0.679096	442.9372	0.670082	499.2787
0.774928	486.449	0.730849	446.9914	0.722249	508.9332
0.826067	496.0831	0.780637	450.8806	0.771248	518.1093
0.877733	505.8923	0.831518	455.3908	0.822495	528.1791
0.926686	517.2628	0.879774	460.096	0.870283	538.2521
0.970602	539.0277	0.927389	466.2547	0.919688	549.7045
0.927847	516.7437	0.973537	474.0941	0.965373	565.1727
0.87344	502.6831	0.918842	460.756	0.924459	550.6321
0.822084	492.4342	0.872816	453.0896	0.872502	537.9214
0.770079	482.1671	0.821978	446.7852	0.820341	526.4641
0.717988	471.6027	0.770945	441.8425	0.771676	516.6518
0.669411	465.2086	0.719761	436.7765	0.721909	507.1537
0.617788	457.806	0.669937	431.4301	0.669552	497.4564
0.56986	450.4789	0.619185	427.31	0.62196	488.4761
0.520872	443.201	0.567526	424.5767	0.571525	479.8475
0.46987	435.2778	0.521098	420.8727	0.52323	471.1393
0.419892	429.1885	0.472677	416.0114	0.473905	462.3363
0.371012	423.2674	0.420731	409.9564	0.419714	453.3865
0.31729	415.5065	0.370885	404.6518	0.368554	444.6458
0.266576	406.8402	0.318939	399.4781	0.318177	436.0436
0.218021	396.1763	0.267697	394.6431		
0.169342	385.9977	0.219118	389.7131		
0.12	375.1064	0.169618	383.8973		
0.073306	360.6757	0.121376	376.6235		
0.029094	320.1844	0.075135	365.2761		
0.01874	291.9583				

DMF RSE samples

Table A.34. N_2 isotherm data for DMF RSE UiO-66 samples used.

DMF RSE 1		DMF RSE 2		DMF RSE 3	
P/P_0	N_2 uptake (cc g^{-1})	P/P_0	N_2 uptake (cc g^{-1})	P/P_0	N_2 uptake (cc g^{-1})

0.002288	217.1789	0.001614	212.3994	0.00125	204.1998
0.002638	222.0843	0.002047	219.7736	0.001561	212.0072
0.003089	227.4048	0.002253	223.0132	0.002197	222.8863
0.003604	232.8919	0.00251	226.4157	0.002426	226.2812
0.004233	238.729	0.002767	230.1167	0.002722	230.101
0.004969	244.5807	0.003082	234.0856	0.003062	234.2159
0.005756	250.4795	0.003471	238.4315	0.003462	238.5032
0.006657	256.2727	0.004337	246.825	0.003928	243.1313
0.007665	262.0558	0.005342	255.0011	0.004468	247.8759
0.010031	273.4788	0.010398	282.7042	0.005089	252.7408
0.015201	292.5409	0.015366	301.6552	0.010896	283.4783
0.020528	308.6212	0.020305	318.1811	0.016022	302.3424
0.025826	322.9442	0.026051	335.2045	0.021312	319.404
0.031874	338.0135	0.030732	346.4949	0.025321	331.3118
0.036279	347.838	0.035957	356.1729	0.030136	343.9457
0.040948	357.9423	0.041013	363.3188	0.035581	355.3486
0.045524	366.7299	0.045284	367.9535	0.041047	364.1366
0.051215	375.7571	0.050252	372.3048	0.045271	369.3745
0.057528	383.7859	0.055477	376.0177	0.053135	376.5072
0.063013	389.6464	0.061414	379.5785	0.057847	379.6609
0.06899	394.9872	0.067534	382.6012	0.063483	382.8478
0.074788	399.3221	0.072817	384.9015	0.068018	385.139
0.081595	403.768	0.079715	387.4132	0.073381	387.4524
0.08808	407.2057	0.085894	389.5274	0.078293	389.3438
0.09493	410.2594	0.090972	391.0443	0.085823	391.791
0.100314	412.4781	0.097562	392.841	0.091497	393.328
0.106927	414.9526	0.102141	394.0244	0.097711	395.2537
0.156991	430.3254	0.150287	402.6848	0.10155	396.0818
0.211524	443.908	0.198279	408.6308	0.150483	406.2414
0.265356	456.782	0.246395	413.4043	0.200022	413.3226
0.316514	468.2912	0.296317	418.0487	0.247454	419.0163
0.366099	479.9908	0.347171	421.8038	0.29524	424.3148
0.416384	491.8514	0.395728	425.8807	0.355365	429.614
0.467721	504.3882	0.451711	429.5751	0.399623	433.615
0.518328	515.9221	0.500628	432.673	0.445604	438.7047
0.570673	529.6899	0.545435	436.0053	0.495129	442.5089
0.61885	541.6147	0.599774	440.4693	0.550587	447.6832
0.670601	554.4229	0.649505	443.2194	0.595555	450.2192
0.722002	567.792	0.696235	447.4365	0.647417	454.8773
0.773989	581.8063	0.749944	451.2204	0.699124	458.3985
0.824089	595.5532	0.802992	455.0473	0.746037	463.3424
0.873953	611.1694	0.845905	459.8853	0.796657	466.7771
0.921385	628.3661	0.898513	466.1537	0.854015	473.2985

0.968461	655.1918	0.94638	473.8162	0.896749	478.5074
0.928964	630.196	0.924556	470.8493	0.951704	489.4335
0.874632	607.5441	0.868867	464.9855	0.925732	484.736
0.822788	589.5834	0.816963	461.1154	0.869224	477.4908
0.770522	573.6094	0.77697	458.7807	0.827481	474.4899
0.720107	558.9412	0.729213	456.3099	0.766106	470.0291
0.671051	546.2081	0.664813	451.8745	0.716862	465.6952
0.622189	534.4182	0.628922	448.8728	0.665577	461.6121
0.572232	522.2364	0.568748	445.674	0.627082	461.0792
0.52259	509.729	0.517564	441.572	0.570078	456.4354
0.472812	498.5951	0.471429	438.0162	0.516152	451.5152
0.421268	487.162	0.414712	434.062		
0.367815	475.3783	0.364548	429.6603		
0.31828	464.3036	0.31624	425.6864		
0.26891	454.0433	0.267933	420.4925		
0.218109	442.7047	0.220506	415.5875		
0.168903	431.0345	0.175354	409.4443		
0.121428	417.8354	0.123363	400.4988		
0.075167	397.991	0.075701	387.1375		
0.027506	327.9935	0.029213	344.252		
0.019634	306.1631	0.01938	315.5485		

DMSO RSE samples

Table A.35. N_2 isotherm data for DMSO RSE UiO-66 samples used.

DMSO RSE 1		DMSO RSE 2		DMSO RSE 3	
P/P_0	N_2 uptake (cc g^{-1})	P/P_0	N_2 uptake (cc g^{-1})	P/P_0	N_2 uptake (cc g^{-1})
0.00216	210.547	0.001504	204.6585	0.000999	194.4961
0.002584	216.1561	0.002011	214.3003	0.00159	209.143
0.003051	222.2265	0.002157	216.8747	0.002034	217.0137
0.003598	228.5204	0.002363	219.6239	0.002241	220.338
0.004211	235.0291	0.002576	222.6181	0.002515	224.1095
0.005014	242.0073	0.002825	225.8539	0.002855	228.1488
0.00586	248.6573	0.003104	229.4381	0.00321	232.3873
0.006714	255.2849	0.004418	242.6841	0.003662	236.965
0.007846	262.3035	0.005232	249.2606	0.004172	241.65
0.010108	273.5397	0.010655	278.1803	0.005311	250.6617
0.016209	295.8638	0.016306	299.0605	0.011281	280.699
0.02188	312.5927	0.02029	311.8166	0.016193	298.0977
0.02539	322.1657	0.026197	329.3159	0.021541	315.0666
0.031638	338.1394	0.030057	338.7501	0.026172	328.4817
0.035754	347.7475	0.036361	351.0424	0.030151	338.3587

0.040483	357.913	0.040507	357.1241	0.035581	349.2935
0.045322	366.9672	0.045739	363.1375	0.041062	357.8551
0.051357	375.7078	0.052072	368.6691	0.045271	362.873
0.057846	383.1324	0.056402	371.7128	0.050006	367.2479
0.062495	387.7696	0.061318	374.6357	0.055443	371.0991
0.068377	392.3449	0.066015	377.1134	0.061715	374.8752
0.073799	396.1018	0.071181	379.429	0.066923	377.4894
0.079806	399.3439	0.078123	382.1291	0.073218	380.0789
0.086608	402.3589	0.08436	384.1993	0.078004	381.8494
0.092614	405.0554	0.089834	385.8336	0.084862	383.9268
0.099161	407.3483	0.096336	387.6314	0.090698	385.8111
0.103875	408.9085	0.102566	389.1885	0.097503	387.5745
0.148146	419.7028	0.147814	397.2725	0.103873	389.0125
0.195512	428.5284	0.200979	403.6902	0.146207	397.2727
0.245592	435.6804	0.24889	408.3095	0.200925	404.9095
0.296738	442.1317	0.295326	412.3516	0.245959	409.8343
0.345242	449.6349	0.345659	416.4348	0.298569	414.9604
0.396278	455.6088	0.400344	420.6974	0.346	419.5496
0.448526	460.7012	0.449253	424.0052	0.396361	424.013
0.499168	465.6067	0.495131	427.5629	0.447542	427.4713
0.546701	470.9648	0.551393	431.4914	0.503185	431.7129
0.599679	476.7263	0.599055	434.0463	0.549048	434.8965
0.650832	482.1131	0.645704	437.6612	0.597034	438.8575
0.698993	485.4662	0.698796	441.709	0.648386	442.1209
0.750708	489.3412	0.746311	445.2055	0.696727	446.3196
0.795906	495.2897	0.801098	449.3354	0.748449	449.7525
0.848533	499.7098	0.845994	453.3471	0.799009	454.1377
0.898957	502.3092	0.90092	459.1652	0.849074	458.1292
0.947256	518.4755	0.946439	466.4926	0.901617	466.2842
0.926763	511.5555	0.927837	465.1625	0.949729	474.8132
0.867925	507.7288	0.87743	459.9633	0.927781	470.7636
0.829222	503.9205	0.821469	454.0166	0.867256	464.3081
0.764889	498.8694	0.765148	451.268	0.829013	460.5128
0.727383	501.2963	0.728068	448.5528	0.769213	456.2076
0.669523	496.0455	0.66744	444.7434	0.728654	454.6698
0.617428	492.6927	0.62912	442.1659	0.667227	451.1119
0.567224	489.5302	0.569453	438.0171	0.616763	447.3042
0.519523	483.5341	0.51774	434.8219	0.569161	443.7685
0.473873	477.463	0.469506	431.4933		
0.428967	473.9998	0.429858	428.0812		
0.364407	465.4443	0.369105	423.3039		
0.329193	460.345	0.318706	418.6982		
0.268757	450.3834	0.268762	414.3331		

0.218815	441.3949	0.220778	409.1544		
0.171858	431.6461	0.17564	403.408		
0.11899	417.5945	0.12508	395.3986		
0.071574	396.4043	0.077961	382.9888		
0.028843	331.7714	0.029089	337.5387		
0.017428	296.7115	0.019138	308.548		

H_2O RSE samples

Table A.36. N_2 isotherm data for H_2O RSE UiO-66 samples used.

H_2O RSE 1		H_2O RSE 2		H_2O RSE 3	
P/P_0	N_2 uptake (cc g^{-1})	P/P_0	N_2 uptake (cc g^{-1})	P/P_0	N_2 uptake (cc g^{-1})
0.002545	175.1699	0.001651	205.094	0.000851	194.0369
0.003175	182.4433	0.002121	213.2436	0.001857	218.2992
0.003975	189.9229	0.002334	216.6383	0.002049	222.1557
0.004876	197.0922	0.002605	220.2342	0.002204	224.3693
0.005913	204.0872	0.002928	224.1131	0.002382	226.92
0.007071	210.6729	0.003288	228.2514	0.002589	229.6962
0.008251	217.0108	0.00372	232.7804	0.002826	232.6347
0.009509	222.8304	0.004227	237.4573	0.003099	235.8622
0.010832	228.3076	0.005328	246.2561	0.004239	247.2045
0.014178	240.5482	0.011029	275.6219	0.005178	254.6003
0.018032	252.7786	0.015858	293.1683	0.010127	280.9145
0.022665	265.7282	0.021163	309.8397	0.015164	300.4341
0.027463	277.7086	0.025354	321.4332	0.020912	319.3253
0.032854	289.5397	0.030622	333.3431	0.025047	331.7043
0.038717	300.7515	0.035972	342.5356	0.03004	344.3516
0.04438	310.2954	0.042195	350.2949	0.035736	355.5984
0.049914	318.3617	0.046656	354.5772	0.040323	362.449
0.056191	325.7566	0.050839	357.8636	0.046359	369.2989
0.062505	332.1637	0.056402	361.4583	0.052417	374.2408
0.06766	336.8051	0.06214	364.6052	0.056471	376.8115
0.073144	341.3626	0.068003	367.3565	0.061745	379.7863
0.078263	345.1491	0.07336	369.4378	0.066753	382.2262
0.084777	349.497	0.080508	372.0061	0.072323	384.5838
0.090776	353.0489	0.086429	373.847	0.077006	386.184
0.097154	356.2961	0.090289	374.9774	0.083441	388.3
0.104261	359.7298	0.09682	376.7096	0.088479	389.6884
0.109637	362.0112	0.102302	378.0835	0.095477	391.4228
0.160874	382.8919	0.149509	386.5029	0.101823	392.9903
0.212675	401.4724	0.20219	393.2482	0.147036	400.7622
0.266858	421.1277	0.245368	397.3567	0.197944	406.562

0.319145	440.2717	0.298335	402.1574	0.246869	410.8801
0.370239	459.5949	0.34519	406.1527	0.298436	415.4457
0.420217	478.6945	0.397262	410.1606	0.347376	419.0683
0.471732	498.2328	0.448093	413.9706	0.395281	421.5043
0.52284	519.5067	0.497524	417.0231	0.445508	424.4807
0.571331	538.3366	0.552303	421.0888	0.503074	427.9679
0.622975	557.4315	0.597507	424.8589	0.547598	430.5444
0.67369	578.8417	0.645734	427.6534	0.596812	432.2061
0.724905	601.3077	0.69782	430.1858	0.652906	435.2099
0.775762	621.7194	0.751294	432.666	0.697829	437.7748
0.825111	644.3082	0.796857	436.8188	0.749107	440.1714
0.873145	666.6182	0.852025	439.7418	0.797478	444.2521
0.923059	692.0793	0.900127	444.8408	0.850642	448.4073
0.970377	720.0563	0.94729	452.5811	0.900648	452.188
0.926154	690.7042	0.927572	449.2316	0.946503	459.6793
0.87391	659.9841	0.869013	445.7231	0.92929	457.7776
0.819792	633.4317	0.820669	442.8323	0.87333	451.2028
0.7706	608.3919	0.779906	441.095	0.821763	447.675
0.721037	584.8852	0.72015	439.1412	0.764249	445.2909
0.670844	563.026	0.678785	435.8444	0.727574	444.4219
0.619014	542.0896	0.619382	433.5869	0.669209	441.0631
0.571395	524.8843	0.565974	430.2443	0.618042	438.0937
0.521546	506.4053	0.516926	425.9859	0.578718	437.1727
0.471446	486.8114	0.469235	422.6419		
0.417993	468.0119	0.427906	420.0932		
0.36961	451.1666	0.368555	414.5163		
0.320539	433.8956	0.317921	410.3812		
0.269968	417.084	0.268138	405.0063		
0.219289	399.8438	0.215699	398.9047		
0.169053	382.2726	0.167216	392.4108		
0.120498	363.7943	0.121154	384.0087		
0.071378	337.8868	0.074138	370.6617		
0.023502	267.8795	0.027225	326.4956		
0.018168	252.8002	0.019344	304.2083		